

**NATURE AND ORIGIN OF ULTRAMAFIC LAMPROPHYRES AND
CARBONATITES FROM THE BORDERS OF THE LABRADOR SEA: INSIGHTS
FROM PETROLOGY, GEOCHEMISTRY, AND GEOCHRONOLOGY**

*

Dissertation

zur Erlangung des Grades

Doktor der Naturwissenschaften

am Fachbereich

Chemie, Pharmazie und Geowissenschaften

der Johannes Gutenberg-Universität Mainz

*

Sebastian Tappe

geboren am 30. April 1976 in der Hansestadt Stralsund

*

Mainz, 16. Juni 2005

A dissertation submitted to the
Geosciences Institute of the Johannes Gutenberg University Mainz
in fulfilment of the requirements for the degree of
Doctor rerum naturalium

Dekan: xxx

1. Berichterstatter: xxx

2. Berichterstatter: xxx

Tag der mündlichen Prüfung: 18/11/2005

CURRICULUM VITAE

Name: Sebastian Tappe

Date and place of birth: 30th of April 1976 in the Hansestadt Stralsund (Germany)

Nationality: German

Address: Kirchstrasse 10, 55124 Mainz, Germany

Phone: (+49)-06131-39-24759

Fax: (+49)-06131-39-23070

Email: tappes@uni-mainz.de

Education:

- Graduated from high-school, August 1994 (Johann Gottfried Herder–Gymnasium, Stralsund).
- Military Service, October 1994-September 1995 (trained as a tank driver in Basepohl and Stadtallendorf).
- University of Greifswald, October 1995-February 2001 (Diploma program, German M.Sc. equivalent, with courses in geology, oceanography, mineralogy, inorganic chemistry and remote sensing; diploma thesis on “Petrology and Geochemistry of mafic alkaline volcanics from southern Sweden”).
- Universities of Greifswald/Memorial-Newfoundland/Mainz, May 2001-present (Ph.D. program; preparation of thesis on “Ultramafic lamprophyre, carbonatite and lamproite intrusions from Labrador and New Quebec, Canada”).

Awards:

- Best oral presentation by a young scientist at 8th International Kimberlite Conference held in Victoria, Canada, 2003.

Publications:

Peer-reviewed journal articles

Tappe, S., Foley, S. F. & Pearson, D. G. (2003a). The Kamafugites of Uganda: a mineralogical and geochemical comparison with their Italian and Brazilian analogues. *Periodico di Mineralogia* 72, 51-77.

Tappe, S., Jenner, G. A., Foley, S. F., Heaman, L. M., Besserer, D., Kjarsgaard, B. A. & Ryan, A. B. (2004a). Torngat ultramafic lamprophyres and their relation to the North Atlantic Alkaline Province. *Lithos* 76, 491-518.

Tappe, S. (2004). Mesozoic mafic alkaline magmatism of southern Scandinavia. *Contributions to Mineralogy and Petrology* 148, 312-334.

Tappe, S., Foley, S. F., Jenner, G. A. & Kjarsgaard, B. A. (2005). Integrating ultramafic lamprophyres into the IUGS classification of igneous rocks: rationale and implications. *Journal of Petrology* 46, 1893-1900.

Extended abstracts

Tappe, S., Obst, K. & Solyom, Z. (2001). Geochemie und Genese der mesozoischen Schlotbasalte am SW-Rand des Fennoskandischen Schildes (Schonen, Schweden). *Terra Nostra* 5/01, 65-68.

Tappe, S., Foley, S. F., Jenner, G. A., Ryan, B., Besserer, D. & Kjarsgaard, B. A. (2003b). Ultramafic lamprophyre dyke swarm, Torngat Mountains, Quebec and Labrador: Mineralogy and Geochemistry. *Extended Abstracts of the 8th International Kimberlite Conference* (7.2.)

PREAMBLE

This doctoral thesis embodies selected results of my research at the Universities of Greifswald and Mainz, as well as at Memorial University of Newfoundland and the University of Alberta between 2001-2005. It consists of three articles, which have been prepared for publication in the following international peer-review journals:

Part I (Journal of Petrology, published in September 2005, volume 46, pp. 1893-1900):

- *“Integrating ultramafic lamprophyres into the IUGS classification of igneous rocks: rationale and implications”*

Part II (Journal of Petrology, revised version submitted in June 2005):

- *“Genesis of ultramafic lamprophyres and carbonatites, Aillik Bay, Canada: implications for incipient rifting in the Labrador Sea area”*

Part III (Lithos, published in October 2004, volume 76, pp. 491-518):

- *“Torngat ultramafic lamprophyres and their relation to the North Atlantic Alkaline Province”*

These manuscripts have co-authors, as listed in the table of contents, and their contributions are indicated in the acknowledgments of this thesis.

S. Tappe

University of Mainz

June 2005

TABLE OF CONTENTS

CURRICULUM VITAE	III
PREAMBLE	V
SUMMARY	VII
ACKNOWLEDGMENTS.....	X

**PART I: “INTEGRATING ULTRAMAFIC LAMPROPHYRES INTO THE IUGS
CLASSIFICATION OF IGNEOUS ROCKS: RATIONALE AND IMPLICATIONS”1**

(S. Tappe; S.F. Foley; G.A. Jenner & B.A. Kjarsgaard)

**PART II: “GENESIS OF ULTRAMAFIC LAMPROPHYRES AND CARBONATITES,
AILLIK BAY, CANADA: IMPLICATIONS FOR INCIPIENT RIFTING IN THE
LABRADOR SEA AREA”19**

(S. Tappe; S.F. Foley; G.A. Jenner; L.M. Heaman; B.A. Kjarsgaard; R.L. Romer; A. Stracke
& J. Hoefs)

**PART III: “TORNGAT ULTRAMAFIC LAMPROPHYRES AND THEIR RELATION
TO THE NORTH ATLANTIC ALKALINE PROVINCE”116**

(S. Tappe; G.A. Jenner; S.F. Foley; L.M. Heaman; D. Besserer; B.A. Kjarsgaard & B. Ryan)

SUMMARY

The ultramafic lamprophyre (UML) group of igneous rocks comprises potassic, silica undersaturated members with essential phlogopite/biotite phenocrysts or macrocrysts and > 90 vol.% mafic minerals (including carbonate and apatite), some of which are characteristically enriched in Al and Ti. UML are globally widespread but represent only a minor component of continental extension-related magmatism. They are commonly associated with carbonatites forming dyke swarms or central complexes at rift margins. However, volumetrically significant UML magma production occurred at the borders of the Labrador Sea predominantly during the Late Neoproterozoic (~ 610-550 Ma), making it an ideal area for studying the genesis of this poorly understood magma type and the geodynamic conditions under which melting occurred.

Previous attempts to decipher the genesis of UML were often hampered by cumbersome nomenclature systems which caused confusion with other ultramafic rock groups such as kimberlites. As a consequence, UML were commonly regarded as varieties of kimberlites and their potential as an indicator of ancient rifting episodes became lost. For this reason, a simplified UML classification is introduced enabling the correct identification and subdivision of UML within the IUGS nomenclature system from which they were omitted entirely in the year 2002. As a first result, the new classification mechanism allows a more rigorous classification of the Late Neoproterozoic alkaline ultramafic intrusives from northern Labrador/Quebec and West Greenland as UML and shows that they are not kimberlites as often referred to in the literature. The existence of a large UML province to either side of the Labrador Sea remained unrecognized in previous studies because of an inconsistently applied nomenclature to the dyke rocks from the widespread UML localities and, more importantly, the lack of detailed petrologic and geochemical characterization and the poorly known age distribution of rock types. Any genetic model for this UML province has to include a geodynamic scenario of incipient rifting in an area of thick cratonic lithosphere, which is in stark contrast to kimberlite magma production within the interior of stable Archean cratons.

A model is developed for the Aillik Bay intrusive suite (central-east Labrador), which is one of the best exposed and compositionally most diverse UML occurrences at the Labrador Sea coast. It comprises a variety of UML (aillikite, mela-aillikite, damtjernite) and dolomite-bearing carbonatite types ranging in age between ~ 590-555 Ma (U-Pb perovskite ages). On

the basis of their overlapping $^{87}\text{Sr}/^{86}\text{Sr}_i$ ratios (0.70369-0.70662) and initial ϵ_{Nd} values (+0.1 to +1.9) all of these coeval rock types can be related to a single parental magma type. The carbonate-rich aillikite variety is closest to this primary magma composition, which most likely formed in a metasomatized garnet peridotite mantle at the base of the cratonic lithosphere (4-6 GPa, as indicated by the presence of diamonds and relevant published experimental studies).

Since the geochemical data indicate disequilibrium between the volatile-rich “metasomatic” component and fertile garnet peridotite under the above outlined pressure conditions, the volatiles are best considered part of a vein assemblage stabilized within a comparatively cold lithospheric mantle. The metasomatic incompatible element enriched component was introduced as small melt fractions from the upwelling asthenosphere into the cratonic lithosphere where it solidified due to heat death forming carbonate-phlogopite dominated veins. This veined lithospheric mantle portion was successively replaced by convecting upper mantle during rift propagation, thereby causing combined volatile-fluxed melting of the veins and the host peridotite which gave rise to the proto-aillikite magma. Such a multi-stage veined mantle melting model can account for the chemical (incompatible element-enriched but highly magnesian) and isotopic (long-term depleted) composition of type aillikite and for the long time span of UML magma production during initiation of a continental rift zone in the Labrador Sea area.

Proto-aillikite magma reached the surface only after coating the upper mantle and crustal conduits with “glimmerite” material, which caused minor alkali-loss. At intrusion level, carbonate separation from this slightly modified aillikite magma occasionally occurred resulting in fractionated dolomite-bearing carbonatites and carbonate-poor mela-aillikite residues. Where alkali-loss by glimmerite precipitation did not occur, CO_2 -saturated proto-aillikite magma was prone to unmix into conjugate damtjernite and calciocarbonatite liquid presumably at uppermost mantle depths (< 1.5 GPa?). It is speculated that calciocarbonatite forms minor intrusions in a central complex, which is currently sea covered as inferred from the convergence of the satellite dykes.

Abundant clinopyroxene- or olivine-bearing micaceous inclusions occur exclusively in the aillikites. They share similar crystallization ages (~ 573 Ma; Ar-Ar phlogopite), identical mineral compositions and a common Sr-Nd isotope signature with their hosts implying an

origin as low-pressure cumulates ($\sim 0.4\text{-}1.5$ GPa). These are thought to line conduits and are most likely derived from blind UML magma injections consistent with the multi-stage model for Aillik Bay UML magmatism.

The Torngat UML dyke swarm (aillikite, mela-aillikite, dolomite carbonatite) is situated about 500 km to the north of Aillik Bay at the Labrador/Quebec border and its general north-south orientation is parallel to the Labrador Sea coast. Mineral assemblage, bulk rock chemical composition and emplacement age (~ 584 Ma; U-Pb perovskite) of the Torngat aillikites are similar to the type rocks from Aillik Bay reflecting melting of a similar source material triggered by the same extension-induced lithospheric thinning in the periphery of the Labrador Sea precursor rift zone. However, subtle differences in the mineral composition (i.e. greater Al depletion of the Torngat UML spinels, phlogopites and clinopyroxenes) indicate slightly different mantle source signatures in keeping with magma derivation from distinct lithospheric blocks (Saglek block affinity in the north vs. Hopedale block affinity in the south). This re-emphasises the role of cold lithospheric mantle in UML magma generation, which is important in storing the asthenosphere-derived metasomatic agents as carbonate-phlogopite dominated vein assemblages thus enabling later re-melting together with the lithospheric wall-rock. Low-pressure devolatilization processes can also account for some of the compositional variation between Torngat aillikites and mela-aillikites but there is no indication for liquid immiscibility having occurred, because the damtjernite UML variety is absent. This may reflect contrasting structural controls during magma ascent through the shallow lithosphere between the Torngat and Aillik Bay UML occurrences, which have emplaced as massive dyke swarm and central complex, respectively.

Deep-seated potassic carbonate-rich magmas were produced throughout the North Atlantic region on both the Laurentia (i.e. Saguenay aillikites of the St. Lawrence valley rift system; ~ 564 Ma) and Baltica side (i.e. the Fen, $\sim 600\text{-}560$ Ma; and Alnö, $\sim 584\text{-}550$ Ma; UML-carbonatite complexes) during the Late Neoproterozoic ($\sim 610\text{-}550$ Ma) in response to continental stretching associated with the breakup of the supercontinent Rodinia. The Labrador/New Quebec and the majority of the West Greenland UML occurrences are an integral part of this North Atlantic Alkaline Province. Although distal to the newly formed Iapetus ocean basin, this deep-seated volatile-rich magmatism indicates enhanced upwelling of the asthenosphere and progressive thinning and replacement of the cratonic lithospheric mantle as a consequence of plate reorganization. The large UML province in Labrador/New

Quebec and West Greenland is one of the strongest indications of ancient incipient continental rifting in the present-day Labrador Sea area. This early rifting episode failed to proceed to completion but the reactivation of the continental rift structure during the Mesozoic/Cenozoic opening of the Central/North Atlantic caused the breakup of the Archean North Atlantic craton with final production of new oceanic crust in the Labrador Sea.

ACKNOWLEDGMENTS

I am greatly indebted to many people for technical and mental support, provision of information and discussion during the research for this thesis. The following deserve special acknowledgments:

Stephen Foley, for his guidance through these years. His inspiring way of supervising led to many suggestions, which pointed to new directions of interpretation and made data presentation clearer. His groundwork in alkaline rock petrogenesis and his support in selecting and organizing the various laboratory programs were essential for obtaining our new broader view on the origin of UML.

George Jenner, for his helpful advice at all stages (often over long distance but so concise to the point), many useful debates (often loud) and strong mental support. This project would not have been possible without his perfect organization of field work in Labrador in the summer of 2003.

Bruce Kjarsgaard, for his help in working out the differences and discrimination criteria between the plethora of ultramafic alkaline rock types. Bruce is furthermore thanked for enabling the Ar-Ar dating at the Geological Survey of Canada in Ottawa. Additionally, his criticisms and clarifications of the prepared manuscripts helped to tackle the problems.

Larry Heaman, for invitation to Edmonton, where I learned about the difficult U-Pb perovskite dating technique. The high quality data obtained from his laboratory are the key to understanding UML genesis in a geodynamic context.

Dejan Prelevic, for introducing me to the zoo of alkaline rock types and the many valuable follow-up discussions about their genesis. Having Dejan around through all these years often prevented me from losing my mind.

Bruce Ryan and Dean Besserer, for sample donation at an early stage of the project, which saved time and costs during our own field work.

Andreas Stracke, for organization of isotope work in his clean laboratory. In spite of being occupied by his own research, he taught me the principles of ion exchange chromatography and tracer isotope analysis.

Rolf Romer and Jochen Hoefs are thanked for enabling isotope measurements at their mass spectrometer facilities.

Andreas Kronz and Dr. Burkhard Schulz-Dobrick, for maintaining functional microprobes and efficient introduction into their laboratories.

My colleagues in the Geoscience Departments of Greifswald, Mainz and St. John's, who have assisted with a variety of tasks: Max Sommer, Tatjana Rehfeldt, Franziska Nehring, Anja Rosenthal, Dorrit Jacob, Matthias Guru Barth, Mike Bishop, Mike Tubrett, Jürgen Eidam and Dieter Mertz.

Silvana Herzog, for allowing me to leave home and, more importantly, waiting for me over long time periods during the course of this study.

Part I

**INTEGRATING ULTRAMAFIC LAMPROPHYRES INTO THE IUGS
CLASSIFICATION OF IGNEOUS ROCKS: RATIONALE AND IMPLICATIONS**

S. Tappe; S.F. Foley; G.A. Jenner & B.A. Kjarsgaard

ABSTRACT	1
1. STATEMENT OF THE PROBLEM.....	2
2. PREVIOUS TERMINOLOGY OF ULTRAMAFIC LAMPROPHYRES	4
3. INTEGRATING ULTRAMAFIC LAMPROPHYRES INTO THE IUGS CLASSIFICATION.....	6
4. APPLICATION OF THE REVISION	7
4.1. West Greenland	8
4.2. Aillik Bay, Labrador.....	8
5. COMMENTS	9
ACKNOWLEDGMENTS.....	11
REFERENCES	11
TABLES	16
FIGURES	17

ABSTRACT

We introduce a modification to the current IUGS classification system for igneous rocks to include ultramafic lamprophyres, which are currently entirely omitted. This is done by including a new step in the sequential system, after the assignment of pyroclastic rocks and carbonatites, that considers ultramafic inequigranular textured rocks with olivine and

phlogopite macrocrysts and/or phenocrysts. At this step ultramafic lamprophyres are considered together with kimberlites, orangeites (former Group 2 kimberlites) and olivine lamproites.

This proposal enables the correct identification and classification of ultramafic lamprophyres within the IUGS scheme. Only three end-members are required for describing the petrographic and compositional continuum of ultramafic lamprophyres: alnöite (essential groundmass melilite), aillikite (essential primary carbonate) and damtjernite (essential groundmass nepheline and/or alkali feldspar). It is argued that all ultramafic lamprophyre rock types can be related to a common magma type which differs in important petrogenetic aspects from kimberlites, orangeites, olivine lamproites and the remainder of lamprophyres such as alkaline and calc-alkaline varieties. Ultramafic lamprophyres can be readily distinguished from olivine lamproites by the occurrence of primary carbonates, and from kimberlites by the presence of groundmass clinopyroxene. In other cases distinction between aillikites, kimberlites and orangeites must rely on mineral compositions in order to recognize their petrogenetic affinities.

1. STATEMENT OF THE PROBLEM

The International Union of Geological Sciences (IUGS) has played an important role in establishing a systematic classification scheme for igneous rocks and simplifying their nomenclature (Streckeisen, 1978; Le Maitre, 1989, 2002). The main principle in their hierarchical approach is to deal with "exotic" or "special" rocks first, thus clearing the way for the classification of the "normal", or majority of, igneous rocks. Included amongst the "special" rocks are pyroclastics, carbonatites, kimberlites, lamproites and lamprophyres.

Unfortunately, a widely recognized group of exotic alkaline rocks, the ultramafic lamprophyres (UML; Rock, 1986, 1991), were never integrated into IUGS classification schemes. Some of the group members (*e.g.* alnöite and polzenite) were considered within early versions of the IUGS system (Streckeisen, 1978; Le Maitre, 1989), while others were ignored from the beginning (*e.g.* aillikite and damtjernite). In the most recent IUGS classification scheme (Le Maitre, 2002) all ultramafic lamprophyre group members have been entirely omitted.

Several lines of evidence point to the exclusion of UML from the IUGS classification scheme as having been a serious omission. First, the term ultramafic lamprophyre continues to be used as a collective term for melanocratic to holomelanocratic, silica-undersaturated potassic rocks, with essential hydrous phenocrysts (*e.g.* Foley *et al.*, 2002; Coulson *et al.*, 2003; Riley *et al.*, 2003; Upton *et al.*, 2003; Tappe *et al.*, 2004). Second, many inequigranular textured, ultramafic olivine-phlogopite rocks do not fulfill the criteria for being kimberlites, orangeites or lamproites (see Mitchell, 1986) and would erroneously be classified as "mica peridotites". Third, the close association and even gradation between ultramafic lamprophyres and carbonatites in rift tectonic settings is in strong contrast to macroscopically similar kimberlites, orangeites and olivine lamproites and points to important differences in their petrogenesis. Fourth, no satisfactory explanation has been given (*e.g.* Woolley *et al.*, 1996) for the dismissal of most of the chemical and mineralogical arguments cited by Rock (1986, 1987) for treating the UML as a separate group of rocks.

Our own recent experience with trying to apply the IUGS classification scheme to the numerous carbonate-rich, melilite-free, ultramafic alkaline rocks of West Greenland, northern Quebec and Labrador also highlights the shortcomings of the current scheme. These rocks have been variably described as kimberlites (Emeleus & Andrews, 1975; Andrews & Emeleus, 1976; Collerson & Malpas, 1977; Scott, 1981; Larsen & Rønso, 1993; Davis *et al.*, 2001; Jensen *et al.*, 2002; Wilton *et al.*, 2002), ultramafic lamprophyres (Malpas *et al.*, 1986; Foley, 1989; Larsen & Rex, 1992; Wardle *et al.*, 1994; Pearce & Leng, 1996; Mitchell *et al.*, 1999; Digonnet *et al.*, 2000; Tappe *et al.*, 2004) and more vaguely as carbonatitic lamprophyres or meimechites (Dimroth, 1970; Walton & Arnold, 1970; Hansen, 1980). We have extensively investigated the petrography, mineral and whole rock composition of these rocks in Labrador and New Quebec in an attempt to understand their petrogenesis (*e.g.* Tappe *et al.*, 2004; and in preparation). Using the current IUGS scheme, we were led to point 12 of Le Maitre (2002): "if you get to this point, either the rock is not igneous or you have made a mistake". The result of this shortcoming is that many UML occurrences are arbitrarily termed "kimberlites" or worse "kimberlitic" by non-specialists. This gap in classification severely hampers systematic attempts to decipher the petrogenesis of alkaline rocks. Furthermore, the correct identification of ultramafic lamprophyres is also of practical importance during exploration programs, since they may also be diamond-bearing (Hamilton, 1992; Janse, 1994; Mitchell *et al.*, 1999; Digonnet *et al.*, 2000; Birkett *et al.*, 2004).

Herein, we provide a mechanism by which to integrate and correctly identify ultramafic lamprophyres within the IUGS system and distinguish them from other inequigranular textured olivine- and phlogopite-bearing ultramafic rocks.

2. PREVIOUS TERMINOLOGY OF ULTRAMAFIC LAMPROPHYRES

Kranck (1939) observed that carbonate-rich varieties of lamprophyres are highly abundant in the Aillik Bay area of Labrador. He defined this so far unknown or unreported rock type as "aillikite". These rocks could not be classified as alnöite because they lack melilite. Unfortunately, this important distinction became lost. For example, in one of the most successful classification schemes of igneous rocks, devised by Streckeisen (1978), aillikites were not included but the term "melilitic lamprophyres" was introduced, including alnöites and polzenites.

Rock (1986) introduced the term ultramafic lamprophyre and included melilitic lamprophyres (*i.e.* alnöite) as well as the melilite-free carbonate-rich and feldspar-/foid-bearing varieties such as aillikite and damtjernite/ouachitite, respectively. All of these rocks have in common an ultramafic, silica-undersaturated nature. Rock (1986) noted that there are strong textural and petrographic similarities between ultramafic lamprophyres and kimberlites.

A new classification concept for all "lamprophyres" was presented by Rock (1987, 1991), where he included kimberlites and lamproites with ultramafic, alkaline and calc-alkaline lamprophyres into his "lamprophyre clan". Mitchell (1994a, b) disputed the concept of a lamprophyre clan and suggested its use be discontinued. The similarities between ultramafic lamprophyres, olivine lamproites, orangeites and kimberlites are best explained by hypabyssal crystallization from volatile-rich magmas, which nonetheless strongly differ in important aspects of their petrogenesis [the lamprophyric facies concept of Mitchell (1994a)]. Nevertheless, although Rock's UML group (Rock, 1986) was a great improvement on previous lamprophyre classification schemes and recognized that such rocks were being confused with kimberlites, it was not accepted by the IUGS subcommittee on classification (Le Maitre, 1989, 2002; Woolley *et al.*, 1996).

Woolley *et al.* (1996) removed alnöites and polzenites from the lamprophyre classification of Le Maitre (1989) and assigned them to the melilitic rocks. Aillikites were considered for the first time by the IUGS, but classified as silicocarbonatites, despite the fact that the modal

carbonate content is less than the 50 vol.% required to classify them as carbonatites, as Rock (1986) had previously noted. In the most recent IUGS scheme (Le Maitre, 2002) alnöites and polzenites were included into the melilite-bearing group of rocks following Woolley *et al.* (1996), whereas aillikite and damtjernite were simply overlooked.

The use of the acronym "melnoite" (melilite plus alnöite) as a stem name for all ultramafic lamprophyres was suggested by Mitchell (1994b), a collective term that was until then only used by exploration geologists for potentially diamondiferous rocks different from kimberlites and lamproites. Mitchell (1994b) favoured "melnoite" over type locality names, because the latter have an inherent petrographic connotation. However, because melnoite implies "melilite-bearing", which is not true for many carbonate-rich or feldspathoid-bearing ultramafic lamprophyres, we suggest the widely used collective term "ultramafic lamprophyre" as a group name for these genetically related rock types.

In this study, we introduce a simplified version of Rock's (1986) classification of ultramafic lamprophyres. This scheme is illustrated in Table 1. Alnöite is used to describe all melilite-bearing ultramafic lamprophyres. Melilite-free ultramafic lamprophyres are split into aillikite and damtjernite. Ouachitites and polzenites are subtle, more felsic (nepheline-bearing) variants of damtjernite and alnöite, respectively, and as such are dropped to simplify matters. Brief definitions of the three UML end-members are described as follows:

Alnöites are melilite-bearing UML, characterized by olivine, phlogopite and clinopyroxene macrocrysts/phenocrysts, and groundmass melilite, clinopyroxene, phlogopite, spinel, ilmenite, perovskite, Ti-rich garnet, apatite and minor primary carbonate. Monticellite may occur in rare instances.

Aillikites are carbonate-rich UML, characterized by olivine and phlogopite macrocrysts/phenocrysts, and groundmass primary carbonate, phlogopite, spinel, ilmenite, rutile, perovskite, Ti-rich garnet and apatite. Mela-aillikites are more melanocratic (colour index > 90%) as a result of the presence of clinopyroxene and/or richteritic amphibole in the groundmass (at the expense of carbonate). Monticellite may occur in rare instances.

Damtjernites are feldspathoid- and/or alkali feldspar-bearing UML, characterized by olivine, phlogopite and clinopyroxene macrocrysts/phenocrysts and groundmass phlogopite/biotite,

clinopyroxene, spinel, ilmenite, rutile, perovskite, Ti-rich garnet, titanite, apatite, primary carbonate, with essential minor nepheline and/or alkali feldspar.

3. INTEGRATING ULTRAMAFIC LAMPROPHYRES INTO THE IUGS CLASSIFICATION

Strict application of the modified classification system requires following the flow chart in Figure 1, which is mainly adopted from Le Maitre (2002). Our revision to the IUGS sequential system is highlighted in bold and the quotation marks refer to sections in Le Maitre (2002):

(1) If the rock is considered to be of pyroclastic origin, go to the section on “Pyroclastic Rocks and Tephra, p.7”.

(2) If the rock contains > 50 modal % of primary carbonate, go to the section on “Carbonatites, p.10”.

(3) If the rock is ultramafic with M > 90% (as defined in the section on “Principles, p.4”), inequigranular textured and contains olivine and phlogopite macrocrysts and/or phenocrysts, use the following:

(a) if it does not contain primary carbonate, check to see if the rock is a lamproite as described in the section on “Lamproites, p.16”;

(b) if melilite-bearing, it is an alnöite (see Table 1 and Figure 2);

(c) if nepheline- and/or alkali feldspar-bearing, it is a damtjernite (see Table 1 and Figure 2);

(d) if it is carbonate-rich and contains melanite/schorlomite- or kimzeyite garnets, it is an aillikite (see Table 1 and Figure 2);

(e) if carbonate-bearing, the rock may be an aillikite, orangeite (former Group 2 kimberlite) or archetypal kimberlite, and discrimination must rely on differences in mineral composition (see Figure 2).

(4) If the rock contains >10 modal % of melilite, go to the section on “Melilite-bearing Rocks, p.11”. **If the rock is also kalsilite-bearing, go to the section on “Kalsilite-bearing Rocks, p.12”.**

(5) If the rock contains modal kalsilite, go to the section on “Kalsilite-bearing Rocks, p.12”.

(6) Check to see if the rock is a kimberlite as described in the section on “Kimberlites, p.13”.

- (7) Check to see if the rock is a lamproite as described in the section on “Lamproites, p.16”.
- (8) If the rock contains modal leucite, go to the section on “Leucite-bearing Rocks, p.18”.
- (9) Check to see if the rock is a lamprophyre as described in the section on “Lamprophyres, p.19”.
- (10) Check to see if the rock is a charnockite as described in the section on “Charnockites, p.20”.
- (11) If the rock is plutonic as defined in the section on "Principles, p.3", go to the section on “Plutonic Rocks, p.21”.
- (12) If the rock is volcanic as defined in the section on "Principles, p.3", go to the section on “Volcanic Rocks, p.30”.

4. APPLICATION OF THE REVISION

Our new Step 3 considers ultramafic (melanocratic to holomelanocratic) inequigranular rocks with olivine and phlogopite macrocrysts and/or phenocrysts. At this step, ultramafic lamprophyres, orangeites and the majority of kimberlites and olivine lamproites are directed to a more appropriate classification scheme. Lamproites are sifted out by the absence of primary carbonate and directed to the existing lamproite classification. The remaining rocks are evaluated in a separate flow chart (Figure 2). Most ultramafic lamprophyres are identified and sifted out by the presence of groundmass melilite, nepheline, alkali feldspar or Ti- and/or Zr-rich primary garnets. The remaining carbonate-bearing rocks may be aillikite, orangeite or archetypal kimberlite, and discrimination must rely on mineral compositional differences (see also Mitchell, 1986, 1995), as follows.

Kimberlite spinels show variations in atomic $Ti/(Ti+Cr+Al)$ at a fixed high Mg-number [magnesian ulvöspinel trend of Mitchell, (1986)]. Phlogopites in kimberlite show Ba and Al enrichment leading to kinoshitalite. Spinel in orangeite and aillikite show similar variation in atomic $Ti/(Ti+Cr+Al)$ with decreasing Mg-number [titanomagnetite trend of Mitchell, (1986)], but $Cr/(Cr+Al)$ is higher in orangeite (> 0.85) than in aillikite spinels (< 0.85 ; Tappe *et al.*, in preparation). In contrast to kimberlite, phlogopite in orangeite and aillikite is Ti-rich but Ba-poor and evolves by Al depletion to tetraferriphlogopite. Groundmass clinopyroxene is absent from kimberlite, occurs as nearly pure diopside in orangeite, but if present in aillikite/mela-aillikite, it shows Al and Ti enrichment.

It should be noted that it is important to examine a suite of samples, as individual samples may not be representative of the whole rock series. Additionally, it should be noted that some kimberlites and almost all leucite lamproites pass Step 3 and are picked up at the original steps in the IUGS scheme (now Steps 6 and 7). We now consider two test cases where the criteria in Step 3 (Figure 1) and Figure 2 allow for a more rigorous classification.

4.1. West Greenland

Many carbonate-rich ultramafic alkaline dykes from western Greenland have long been regarded as kimberlites (*e.g.* Emeleus & Andrews, 1975; Scott, 1981; Thy *et al.*, 1987; Larsen & Rønso, 1993). They are characterized by an inequigranular texture and contain both abundant olivine and phlogopite as macrocrysts and phenocrysts. These rocks are directed at Step 3 in Figure 1 to the flow chart in Figure 2. Because they do not contain melilite, nepheline, alkali feldspar or Ti-rich primary garnets, one must decide between aillikite, orangeite or kimberlite based on mineral compositions. The spinels are compositionally diverse, but evolve at comparably high Fe/Mg ratios towards titanomagnetite/magnetite. The magnesian ulvöspinel component is low (< 15 wt.% and 12 wt.% MgO for Sarfartoq and Nigerdlikasik/Pyramidefjeld spinels, respectively) and Al is enriched [$\text{Cr}/(\text{Cr}+\text{Al}) < 0.85$]. The mica compositions are Ba-poor and trend from aluminous titanian phlogopite toward either aluminous magnesian biotite or to Ti- and Al-depleted tetraferriphlogopite. The western Greenland ultramafic dyke occurrences also contain groundmass clinopyroxenes enriched in Al_2O_3 and TiO_2 (up to 10 and 5 wt.%, respectively, Mitchell *et al.*, 1999). These criteria eliminate kimberlites and orangeites and clearly identify these rocks as ultramafic lamprophyres, namely the carbonate-rich variety aillikite. This is in agreement with Mitchell *et al.* (1999), who considered that these rocks are not kimberlite but rather ultramafic lamprophyres.

4.2. Aillik Bay, Labrador

At the type locality of aillikites at Aillik Bay in Labrador (Kranck, 1939; Foley, 1984; Malpas *et al.*, 1986; Rock, 1986), a variety of Late Neoproterozoic lamprophyric dykes occur that can now all be classified as ultramafic lamprophyres. Many dykes have olivine and aluminous titanian phlogopite phenocrysts and their groundmass is dominated by primary carbonates including rare Ti-rich garnets. Others have olivine, Ti-Al-enriched diopside and aluminous titanian phlogopite phenocrysts and contain minor alkali feldspar, nepheline and primary

carbonate in the groundmass (Tappe *et al.*, in preparation). Using the new classification, the first type is aillikite, whereas the second classifies as damtjernite. These damtjernites include more evolved types with more nepheline and alkali feldspar [the “sannaite” of Foley, (1984)], thus violating the M=90% screen of Step 3 in Figure 1. However, they are clearly genetically related to the damtjernites and so we recommend referring to them as “evolved damtjernites” and not sannaite (see below).

5. COMMENTS

The introduction of the ultramafic lamprophyre group at an early stage in the IUGS classification scheme does not compromise the existing lamprophyre classification in “Section 2.9., p.19” (Le Maitre, 2002) in any way. The “Section 2.9.” considers those lamprophyres termed calc-alkaline and alkaline lamprophyres by Rock (1987, 1991), and is herein retained entirely as Step 9 in Figure 1. This further illustrates the point that the ultramafic lamprophyres were simply omitted in the current IUGS scheme (Le Maitre, 2002), and that there is no genetic relationship between UML and the remainder of lamprophyres.

The prefix “mela-” can be added to ultramafic lamprophyre rock names to indicate a colour index > 90% as suggested by Rock (1986) and applied by Tappe *et al.* (2004) for the first time to aillikites. This is an important qualifier, especially for aillikites, to indicate the gradation into carbonate-poor varieties, which by definition have < 10 vol.% modal carbonate. It therefore has a meaning essentially equivalent to “carbonate-poor aillikite” and allows the correct identification of the petrogenetic affinity of the magma series for degassed varieties. It does not, however, indicate which mafic mineral is common; this can also be done by the use of mineral qualifiers as in the section on lamproites [Section 2.7., p.17 of Le Maitre, (2002)] - for example, “clinopyroxene mela-aillikite” or “richterite clinopyroxene mela-aillikite”.

The reintroduction of the term “damtjernite” for nepheline- and/or alkali feldspar-bearing ultramafic lamprophyres follows the description of dykes associated with the Fen Complex in southern Norway. Although earlier usage of the term damtjernite has been inconsistent [even in spelling: damtjernite vs. damkjernite (Griffin & Taylor, 1975; Rock, 1986, 1987, 1991; Dahlgren, 1994; Le Maitre, 2002); a problem that stems from Brøgger (1921)], a more recent compilation of the dykes in the Fen province indicates that the majority have feldspathoids and/or alkali feldspar in the groundmass [the “F-damtjernites” of Dahlgren (1994)]. Dahlgren's (1994) “C-damtjernites” are nepheline- and alkali feldspar-free with 25-50 vol.%

modal carbonate and therefore correspond to aillikites. This confirms the co-occurrence of distinct ultramafic lamprophyre types together with carbonatites within a single province, with prime examples being the Fen and Aillik Bay areas.

The new definition of damtjernite as an ultramafic lamprophyre with feldspathoids and/or alkali feldspar in the groundmass could potentially cause confusion with other lamprophyre types belonging to the calc-alkaline and alkaline groups. At Aillik Bay, the coexistence of aillikites and sannaites has been described (Foley, 1984; Malpas *et al.*, 1986), implying the existence of both ultramafic and alkaline lamprophyre magmas. However, recent work has shown that damtjernites also occur which are petrogenetically linked to both the aillikites and these "sannaites", forming a strong mineral compositional and geochemical continuum. Age determinations confirm the genetic relationship (Tappe *et al.*, in preparation). In this case, ultramafic lamprophyres grade into more evolved rocks that have more than 10 vol.% felsic minerals, but are clearly related by fractionation. Hence, mineralogical definitions based on rigid boundaries of percentage modal minerals introduce arbitrary delimiters that risk being carried over into petrogenetic arguments. We therefore suggest that the term sannaites should be reserved for rocks that not only have the mineralogical characteristics described by the IUGS classification (Le Maitre, 2002, p.19), but also pass an extra chemical screen ($\text{SiO}_2 > 41$ wt.%). This greatly restricts the chemical variation amongst rocks hitherto called sannaites (Rock, 1991, p.82), making it more likely that those remaining as sannaites are related to a specific alkaline lamprophyre magma type. Hence, the former Aillik Bay sannaites are more appropriately referred to as "evolved damtjernites", similar to the usage by Mitchell (1995), who describes "evolved orangeites". This reiterates the message that genetic considerations cannot be left out of classification schemes (Foley *et al.*, 1987; Mitchell, 1994b, 1995) and removes the confusion of a petrogenetic relation between ultramafic and alkaline lamprophyre groups, which is no longer justified on petrogenetic grounds. A strict application of this genetic concept obviates the need for the former UML types "polzenite" and "ouachitite", which are, according to our extensive literature survey, equivalent to evolved alnöites and evolved damtjernites, respectively.

It should be noted that if one were to recover only the evolved damtjernites or evolved orangeites at a locality, then they would not be recognized at Step 3 in the new classification. This re-emphasizes the importance of considering geochemical and, more importantly, mineral compositional data from larger sample suites wherever available.

ACKNOWLEDGMENTS

This paper is dedicated to Nicolas Rock, who recognized ultramafic lamprophyres as an independent group of igneous rocks and systematically classified them. Although sometimes in error, he greatly improved our understanding of lamprophyres.

We are grateful to Bruce Ryan and Dejan Prelevic for discussions that ensued during this study. Thoughtful comments by Lotte Larsen, Roger Mitchell, Teal Riley and Marjorie Wilson on an early version of this manuscript are gratefully acknowledged. This study was carried out within the DFG project Fo 181/15 (Germany) and this publication is Geological Survey of Canada Contribution 200502.

REFERENCES

- Andrews, J. R. & Emeleus, C. H. (1976). Kimberlites of West Greenland. In: Escher, A. & Watt, W. S. (eds.) *Geology of Greenland*. Copenhagen, Denmark: Geological Survey of Greenland, pp. 575-589.
- Birkett, T. C., McCandless, T. E. & Hood, C. T. (2004). Petrology of the Renard igneous bodies: host rocks for diamond in the northern Otish Mountains region, Quebec. *Lithos* 76, 475-490.
- Brøgger, W. C. (1921). *Die Eruptivgesteine des Kristianiagebietes: IV. Das Fengebiet in Telemark, Norwegen*. Kristiania (Oslo): Skrifter udgit av Videnskabselskabet i Kristiania I. Math.-Nat. Klasse No.9, 408 pp.
- Collerson, K. D. & Malpas, J. (1977). Partial melts in upper mantle nodules from Labrador kimberlites. *Extended abstracts of the 2nd International Kimberlite Conference, Santa Fe*
- Coulson, I. M., Goodenough, K. M., Pearce, N. J. G. & Leng, M. J. (2003). Carbonatites and lamprophyres of the Gardar Province: a "window" to the sub-Gardar mantle? *Mineralogical Magazine* 67, 855-872.
- Dahlgren, S. (1994). Late Proterozoic and Carboniferous ultramafic magmatism of carbonatitic affinity in Southern Norway. *Lithos* 31, 141-154.

- Davis, D. W., Roy, R. R. & Coates, H. J. (2001). The eastern Arctic Torngat and Jackson inlet diamond projects of Twin Mining Corporation. In: Kerr, A. & Kean, B. (eds.) *North Atlantic Minerals Symposium*. St. John's: Memorial University of Newfoundland, pp. 13-15.
- Digonnet, S., Goulet, N., Bourne, J., Stevenson, R. & Archibald, D. (2000). Petrology of the Abloviak aillikite dykes, New Québec: evidence for a Cambrian diamondiferous alkaline province in northeastern North America. *Canadian Journal of Earth Sciences* 37, 517-533.
- Dimroth, E. (1970). Meimechites and carbonatites of the Castignon Lake Complex, New Quebec. *Neues Jahrbuch für Mineralogie Abhandlungen* 112, 239-278.
- Emeleus, C. H. & Andrews, J. R. (1975). Mineralogy and petrology of kimberlite dyke and sheet intrusions and included peridotite xenoliths from South-west Greenland. *Physics and Chemistry of the Earth* 9, 179-197.
- Foley, S. F. (1984). Liquid immiscibility and melt segregation in alkaline lamprophyres from Labrador. *Lithos* 17, 127-137.
- Foley, S. F. (1989). Emplacement features of lamprophyre and carbonatitic lamprophyre dykes at Aillik Bay, Labrador. *Geological Magazine* 126, 29-42.
- Foley, S. F., Andronikov, A. V. & Melzer, S. (2002). Petrology of ultramafic lamprophyres from the Beaver Lake area of Eastern Antarctica and their relation to the breakup of Gondwanaland. *Mineralogy and Petrology* 74, 361-384.
- Foley, S. F., Venturelli, G., Green, D. H. & Toscani, L. (1987). The Ultrapotassic Rocks: Characteristics, Classification, and Constraints for Petrogenetic models. *Earth-Science Reviews* 24, 81-134.
- Griffin, W. L. & Taylor, P. N. (1975). The Fen damkjernite: petrology of a "central-complex kimberlite". *Physics and Chemistry of the Earth* 9, 163-177.
- Hamilton, R. (1992). Geology and structural setting of ultramafic lamprophyres from Bulljah Pool, central Western Australia. *Journal of the Royal Society of Western Australia* 75, 51-56.

Hansen, K. (1980). Lamprophyres and carbonatitic lamprophyres related to rifting in the Labrador Sea. *Lithos* 13, 145-152.

Janse, A. J. A. (1994). Review of supposedly non-kimberlitic and non-lamproitic diamond host rocks. In: Meyer, H. O. A. & Leonardos, O. H. (eds.) *Diamonds: characterization, genesis and exploration*. Rio de Janeiro, Brazil: Companhia de Pesquisa de Recursos Minerais, pp. 144-159.

Jensen, S. M., Hansen, H., Secher, K., Steenfelt, A., Schjoth, F. & Rasmussen, T. M. (2002). Kimberlites and other ultramafic alkaline rocks in the Sisimiut-Kangerlussuaq region, southern West Greenland. *Geology of Greenland Survey Bulletin* 191, 57-66.

Kranck, E. H. (1939). The rock-ground of the coast of Labrador and the connection between the pre-Cambrian of Greenland and North America. *Bulletin de la Commission Geologique de Finlande* 22, 65-86.

Larsen, L. M. & Rex, D. C. (1992). A review of the 2500 Ma span of alkaline-ultramafic, potassic and carbonatitic magmatism in West Greenland. *Lithos* 28, 367-402.

Larsen, L. M. & Rønsbo, J. (1993). Conditions of origin of kimberlites in West Greenland: new evidence from the Sarfartoq and Sukkertoppen regions. *Report - Geological Survey of Greenland* 159, 115-120.

Le Maitre, R. W. (1989). *A Classification of Igneous Rocks and Glossary of Terms: Recommendations of the International Union of Geological Sciences, Subcommittee on the Systematics of Igneous Rocks*. Oxford: Blackwell, 193 pp.

Le Maitre, R. W. (2002). *Igneous Rocks: A Classification and Glossary of Terms: Recommendations of the International Union of Geological Sciences Subcommittee on the Systematics of Igneous Rocks*. Cambridge: Cambridge University Press, 236 pp.

Malpas, J., Foley, S. F. & King, A. F. (1986). Alkaline mafic and ultramafic lamprophyres from the Aillik Bay area, Labrador. *Canadian Journal of Earth Sciences* 23, 1902-1918.

Mitchell, R. H. (1986). *Kimberlites: mineralogy, geochemistry and petrology*. New York: Plenum Press, 442 pp.

Mitchell, R. H. (1994a). The lamprophyre facies. *Mineralogy and Petrology* 51, 137-146.

Mitchell, R. H. (1994b). Suggestions for revisions to the terminology of kimberlites and lamprophyres from a genetic viewpoint. In: Meyer, H. O. A. & Leonardos, O. H. (eds.) *Kimberlites, related rocks and mantle xenoliths*. Rio de Janeiro, Brazil: Companhia de Pesquisa de Recursos Minerais, pp. 15-26.

Mitchell, R. H. (1995). *Kimberlites, orangeites, and related rocks*. New York: Plenum Press, 410 pp.

Mitchell, R. H., Scott-Smith, B. H. & Larsen, L. M. (1999). Mineralogy of ultramafic dikes from the Sarfartoq, Sisimiut and Maniitsoq areas, West Greenland. In: Gurney, J. J., Gurney, J. L., Pascoe, M. D. & Richardson, S. H. (eds.) *Proceedings of the VIIth international kimberlite conference*. Cape Town: Red Roof Design, pp. 574-583.

Pearce, N. J. G. & Leng, M. J. (1996). The origin of carbonatites and related rocks from the Igaliko dyke swarm, Gardar Province, South Greenland: field, geochemical and C-O-Sr-Nd isotope evidence. *Lithos* 39, 21-40.

Riley, T. R., Leat, P. T., Storey, B. C., Parkinson, I. J. & Millar, I. L. (2003). Ultramafic lamprophyres of the Ferrar large igneous province: evidence for a HIMU mantle component. *Lithos* 66, 63-76.

Rock, N. M. S. (1986). The nature and origin of ultramafic lamprophyres: alnöites and allied rocks. *Journal of Petrology* 27, 155-196.

Rock, N. M. S. (1987). The nature and origin of lamprophyres: an overview. In: Fitton, J. G. & Upton, B. G. J. (eds.) *Alkaline igneous rocks*. London, United Kingdom: Geological Society of London, pp. 191-226.

Rock, N. M. S. (1991). *Lamprophyres*. Glasgow: Blackie & Son, 285 pp.

Scott, B. H. (1981). Kimberlite and lamproite dykes from Holsteinsborg, West Greenland. *Meddelelser om Grønland, Geoscience* 4, 3-24.

Streckeisen, A. (1978). Classification and nomenclature of volcanic rocks, lamprophyres, carbonatites and melilitic rocks: recommendations and suggestions, IUGS Subcommittee on the Systematics of Igneous Rocks. *Neues Jahrbuch für Mineralogie Abhandlungen* 134, 1-14.

Tappe, S., Jenner, G. A., Foley, S. F., Heaman, L. M., Besserer, D., Kjarsgaard, B. A. & Ryan, A. B. (2004). Torngat ultramafic lamprophyres and their relation to the North Atlantic Alkaline Province. *Lithos* 76, 491-518.

Thy, P., Stecher, O. & Korstgard, J. A. (1987). Mineral chemistry and crystallization sequences in kimberlite and lamproite dikes from the Sisimiut area, central West Greenland. *Lithos* 20, 391-417.

Upton, B. G. J., Emeleus, C. H., Heaman, L. M., Goodenough, K. M. & Finch, A. A. (2003). Magmatism of the mid-Proterozoic Gardar Province, South Greenland: chronology, petrogenesis and geological setting. *Lithos* 68, 43-65.

Walton, B. J. & Arnold, A. R. (1970). Plutonic nodules in lamprophyric carbonatite dykes near Frederikshåb, South-West Greenland. *Grønlands Geologiske Undersøgelse Bulletin* 91, 1-26.

Wardle, R. J., Bridgwater, D., Mengel, F., Campbell, L., van Kranendonk, M. J., Hauman, A., Churchill, R. & Reid, L. (1994). Mapping in the Torngat Orogen, northernmost Labrador: Report 3, the Nain Craton (including a note on ultramafic dyke occurrences in northernmost Labrador). *Current Research, Newfoundland Department of Mines and Energy* 94-1, 399-407.

Wilton, D. H. C., Taylor, R. C., Sylvester, P. J. & Penney, G. T. (2002). A review of kimberlitic and ultramafic lamprophyre intrusives from northern Labrador. *Current Research, Newfoundland Department of Mines and Energy* 02-1, 343-352.

Woolley, A. R., Bergman, S. C., Edgar, A. D., Le Bas, M. J., Mitchell, R. H., Rock, N. M. S. & Scott-Smith, B. H. (1996). Classification of Lamprophyres, Lamproites, Kimberlites, and the Kalsilitic, Melilitic and Leucitic rocks. *The Canadian Mineralogist* 34, 175-186.

TABLES

Table 1: Classification of ultramafic lamprophyres based on their diagnostic mineralogy

	melilite (<i>grdm.</i>)	carbonate (<i>grdm., primary</i>)	nepheline (<i>grdm.</i>)	alkali feldspar (<i>grdm.</i>)
alnöite	MN	m	m	-
aillikite	-	MN	-	-
damtjernite	-	m	mN*	mN*

Note: olivine and phlogopite are common to all three rock types; Ti-rich primary garnets may occur

- M** = major constituent
- m** = minor constituent
- N** = necessary
- N*** = presence of only one "star" phase necessary
- = absent

FIGURES

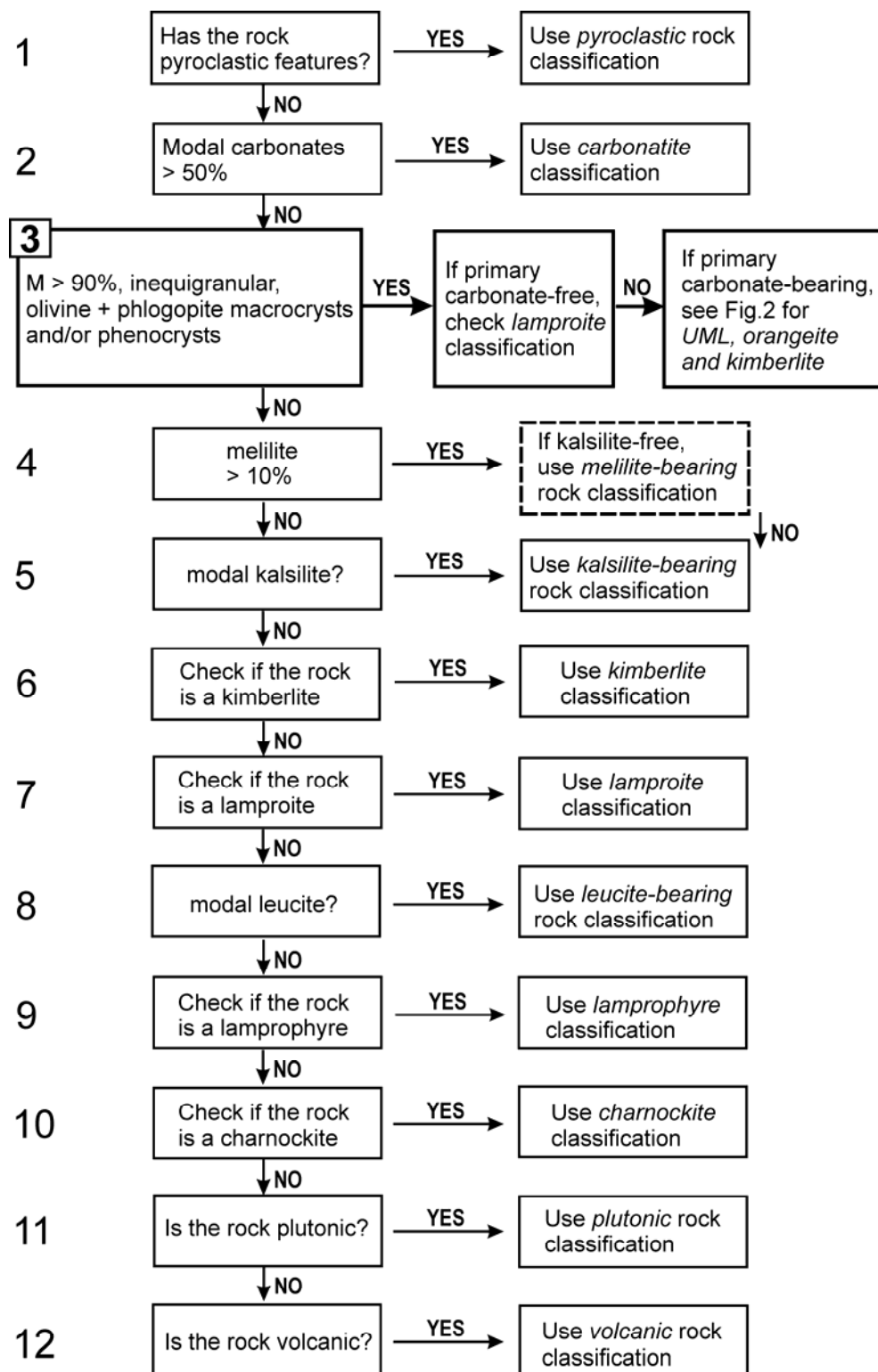


Figure 1: Flow chart illustrating the sequential system for the classification of igneous rocks following the IUGS scheme devised by Le Maitre (2002). The new “Step 3” is integrated to distinguish between ultramafic lamprophyres (UML), kimberlite, orangeite and olivine lamproite. (See text for further explanation.) “M” is defined as mafic and related minerals (i.e. including primary carbonate and apatite).

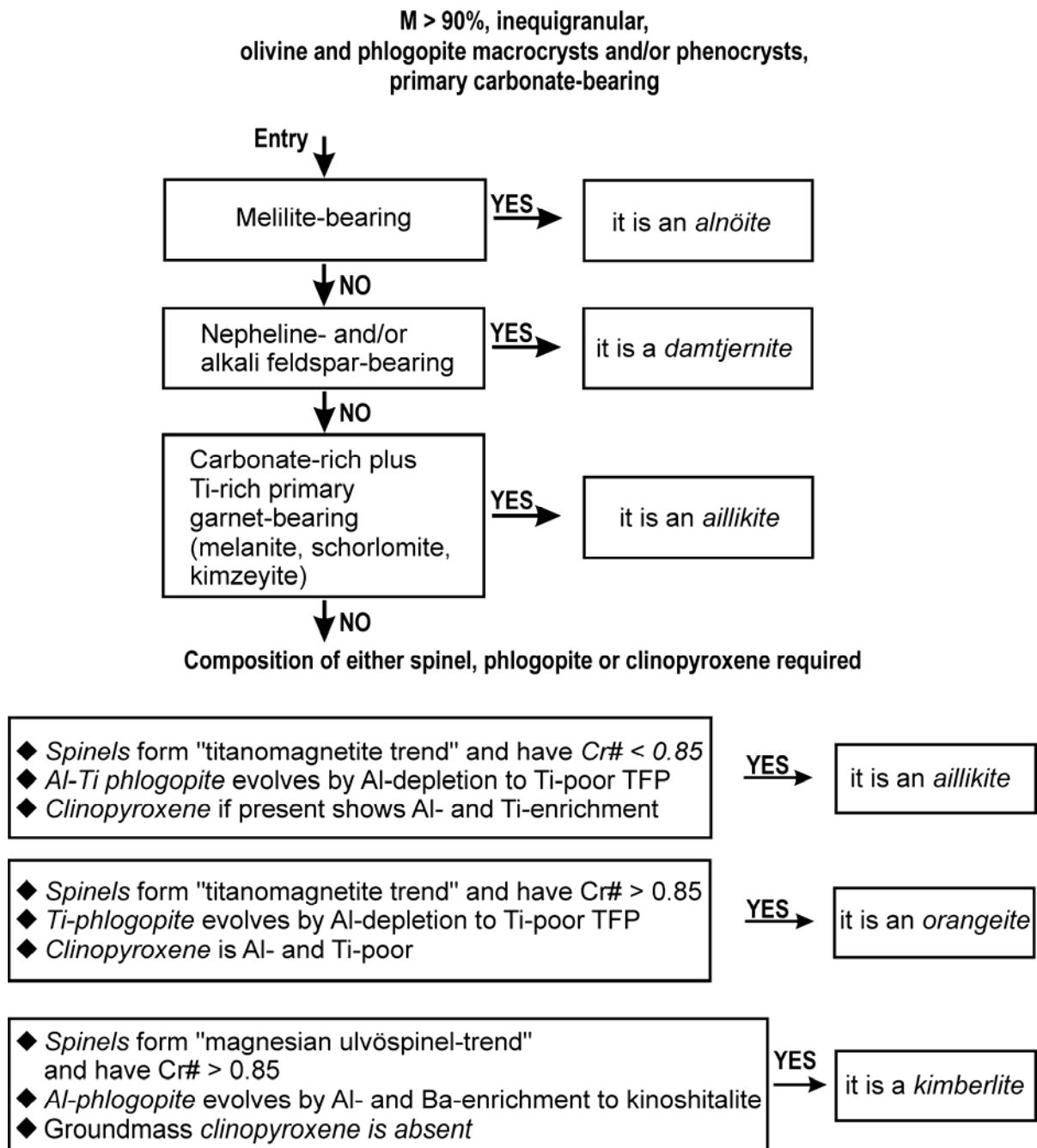


Figure 2: Flow chart illustrating how to distinguish between the three UML end-members (alnöite, damtjernite, aillikite), orangeite and kimberlite. Discrimination criteria that rely on mineral composition after Mitchell (1986, 1995) and Tappe *et al.* (2004, and in preparation).

Cr# (Cr-number) = atomic Cr/(Cr+Al); **TFP** = tetraferriphlogopite

Part II

**GENESIS OF ULTRAMAFIC LAMPROPHYRES AND CARBONATITES, AILLIK
BAY, CANADA: IMPLICATIONS FOR INCIPIENT RIFTING IN THE LABRADOR
SEA AREA**

S. Tappe; S.F. Foley; G.A. Jenner; L.M. Heaman; B.A. Kjarsgaard; R.L. Romer; A. Stracke &
J. Hoefs

ABSTRACT	22
1. INTRODUCTION	23
2. GEOLOGICAL FRAMEWORK OF THE AILLIK BAY AREA	25
2.1. Makkovik-Ketilidian belt	25
2.2. Alkaline magmatism and previous age constraints	26
3. GEOCHRONOLOGY	26
3.1. U-Pb dating of ultramafic lamprophyres	26
3.2. Ar-Ar dating of cognate inclusion ST162I	27
4. PETROGRAPHY	28
4.1. Carbonatite dykes	28
4.2. Aillikite dykes	28
4.3. Damtjernite dykes.....	29
4.4. Cognate inclusions.....	30
5. MINERAL COMPOSITIONS	31
5.1. Olivine	31
5.2. Phlogopite.....	32
5.3. Clinopyroxene and amphibole.....	33
5.4. Spinel.....	34

5.5. Ilmenite and rutile.....	35
5.6. Perovskite, titanite and Ti-rich primary garnet.....	36
5.7. Apatite and carbonate	37
5.8. Alkali feldspar, feldspathoids and pectolite	37
6. PRESSURE ESTIMATES FOR COGNATE INCLUSIONS	38
7. MINERALOGICAL CONSTRAINTS ON CRYSTALLIZATION CONDITIONS AND THEIR IMPLICATIONS FOR MANTLE SOURCE CHARACTERISTICS.....	38
7.1. Oxygen fugacity estimates from olivine-spinel and ilmenite-magnetite pairs.....	38
7.2. Hydrogen fluoride fugacity estimates from phlogopite-apatite pairs.....	40
8. GEOCHEMISTRY AND ISOTOPIC COMPOSITION	41
8.1. Major and compatible trace elements.....	41
8.2. Incompatible trace elements	42
8.3. Sr-Nd isotope composition	43
8.4. Carbon and oxygen isotope composition of the bulk rock carbonate fraction.....	44
9. DISCUSSION.....	44
9.1. Modification of the parental UML magma.....	44
9.1.1. Role of contamination and fractionation processes	44
9.1.2. Linking aillikites, mela-aillikites and carbonatites by a devolatilization process.....	46
9.1.3. A role for liquid immiscibility in the genesis of damtjernites?.....	48
9.1.4. Petrogenetic significance of cognate inclusions in aillikites.....	50
9.2. Mantle source characteristics and melting processes	51
9.2.1. Identification of the parental UML magma	51
9.2.2. Constraints on the mineralogy and location of the source region	51
9.2.3. Isotopic constraints on the age and style of mantle metasomatism.....	54
10. PETROGENESIS OF PARENTAL AILLIK BAY UML MAGMA AS PART OF THE NORTH ATLANTIC ALKALINE PROVINCE	55
11. CONCLUSIONS.....	57
ACKNOWLEDGMENTS.....	58

APPENDIX A - ANALYTICAL TECHNIQUES.....	58
U-Pb perovskite geochronology	58
Ar-Ar mica thermochronology	59
Mineral chemistry.....	60
Whole rock geochemistry	60
Sr-Nd isotope composition	61
Oxygen and carbon isotope composition	61
APPENDIX B – SAMPLE LIST	62
APPENDIX C – GAS RELEASE SPECTRUM.....	63
REFERENCES	64
TABLES	81
FIGURES	94

ABSTRACT

Numerous ultramafic lamprophyre (aillikite, mela-aillikite, damtjernite) and subordinate dolomite-bearing carbonatite dykes occur in the vicinity of Aillik Bay (coastal Labrador) with emplacement ages of ~ 590-555 Ma. They form part of widespread alkaline carbonatitic igneous activity throughout the North Atlantic region (Laurentia and Baltica) in response to rifting and continental breakup (Rodinia) during the Late Neoproterozoic.

The Aillik Bay ultramafic lamprophyres, which host a variety of micaceous cognate low-pressure inclusions, predominantly consist of olivine and phlogopite phenocrysts in a carbonate- or clinopyroxene-dominated groundmass. Titanian aluminous phlogopites and clinopyroxenes as well as Al-enriched but Cr-Mg-poor spinels are compositionally distinct from analogous minerals in kimberlites, orangeites and olivine lamproites and show contrasting evolutionary trends. Ti-rich primary garnets (kimzeyite and schorlomite) commonly occur at Aillik Bay and are considered petrogenetically diagnostic for ultramafic lamprophyre – carbonatite suites.

The various Aillik Bay ultramafic lamprophyres and carbonatites have overlapping $^{87}\text{Sr}/^{86}\text{Sr}_i$ ratios (0.70369-0.70662) and show a narrow range in initial ϵ_{Nd} (+0.1 to +1.9) on a horizontal array implying that they are related to a single parental magma type. Aillikite is closest to the primary magma composition regarding its MgO (~ 15-20 wt.%) and Ni (~ 200-574 ppm) content; the abundant groundmass carbonate has $\delta^{13}\text{C}_{\text{PDB}}$ (-5.7 to -5 ‰) and $\delta^{18}\text{O}_{\text{SMOW}}$ (9.4-11.6 ‰) values typical for mantle-derived carbonate-rich material.

Proto-aillikite magma reached the surface only after coating the upper mantle and crustal conduits with “glimmerite” material, which caused minor alkali-loss. At intrusion level, carbonate separation from this aillikite magma occasionally occurred resulting in fractionated dolomite-bearing carbonatites and carbonate-poor mela-aillikite residues. Where alkali-loss by glimmerite precipitation did not occur, proto-aillikite magma was prone to unmix into conjugate damtjernite and calciocarbonatite liquid presumably at uppermost mantle depths. It is speculated that calciocarbonatite forms minor intrusions in a central complex, which is currently sea covered as inferred from the convergence of the satellite dykes.

Extensive melting of a metasomatized carbonate- and phlogopite-rich garnet peridotite source region at ~ 4-6 GPa can account for the volatile-bearing, potassic, incompatible trace element

enriched and MgO-rich nature of the proto-aillikite magma. It is argued that potassic-carbonatitic melts/fluids from upwelling asthenosphere infiltrated the cold base of the extending North Atlantic craton lithosphere and solidified as veins. Continued lithospheric extension and progressive upwelling of the asthenosphere beneath the developing rift in the present-day Labrador Sea area caused remelting of the metasomatic veins and volatile-fluxed melting in the host fertile garnet peridotite.

Enhanced radiogenic Sr in-growth but no apparent change in Nd isotope composition of the magma source can be explained by phlogopite concentrated in mantle veins. The low MgO/CaO ratios of aillikites in combination with positively correlated CaO versus CO₂ indicate that calcite was the mantle carbonate phase and therefore must have been part of the vein assemblage, which formed at conditions where magnesite is the stable carbonate in peridotite. Trace element concentrations indicate that other likely metasomatic phases include apatite, titanates and baddeleyite.

1. INTRODUCTION

The ultramafic lamprophyres (UML; Rock, 1986) are a widely recognized group of alkaline rocks associated with continental extension, but their origin is poorly understood. Although they are rare components of continental volcanism, they are of fundamental significance for our understanding of deep melting events during the initial stages in the development of continental rifts. UML typically occur as dyke swarms and in central complexes (Rock, 1991) but their genesis has commonly been discussed as though they are varieties of kimberlites (Dawson, 1971; Griffin & Taylor, 1975; Raeside & Helmstaedt, 1982; Alibert & Albarede, 1988; Dalton & Presnall, 1998) mainly due to a similar macroscopic appearance and problematic identification within existing classification schemes (Tappe *et al.*, 2005). However, compositional differences and the lack of spatial coexistence of contemporaneous ultramafic lamprophyres and kimberlites (Rock, 1991; Mitchell, 1995) suggest that they are derived from distinct magma types. UML magma occurrence is largely confined to stretched continental blocks and is commonly associated with carbonatite magmatism. Additionally, it occasionally forms part of flood basalt provinces (Leat *et al.*, 2000; Riley *et al.*, 2003) or occurs on oceanic islands (Nixon *et al.*, 1980; Neal & Davidson, 1989). In contrast, kimberlites occur exclusively within areas of stable Archean cratons or in surrounding Proterozoic mobile belts (Mitchell, 1986; Janse & Sheahan, 1995). As for kimberlites,

ultramafic lamprophyre magmas may contain diamonds (Hamilton, R., 1992; Mitchell *et al.*, 1999; Digonnet *et al.*, 2000; Birkett *et al.*, 2004), indicating that the depth of melting can be in excess of 150 km (> 5 GPa) and may not be the crucial petrogenetic difference.

Large areas of Labrador, adjacent northeastern Quebec and western Greenland are comprised of Archean blocks surrounded by Paleoproterozoic mobile belts (Fig.1) stabilized at ~1900-1700 Ma (Wardle & Hall, 2002). Continental rifting affected this cratonic area repeatedly during Mesoproterozoic (~1350-1140 Ma; Romer *et al.*, 1995; Upton *et al.*, 2003), Neoproterozoic (~620-550 Ma; Gower *et al.*, 1986; Kamo *et al.*, 1989; Murthy *et al.*, 1992) and Mesozoic times (Emeleus & Andrews, 1975; Hansen, 1980; Larsen & Rex, 1992) eventually causing the breakup of the North Atlantic craton and opening of the Labrador Sea at ~90 Ma (Roest & Srivastava, 1989).

All of these rifting episodes were accompanied by volatile-rich alkaline igneous activity (Larsen & Rex, 1992), but the most productive in terms of UML magma generation was the Late Neoproterozoic episode, which was distally associated with initiation of the Iapetus ocean (Tappe *et al.*, 2004). Neoproterozoic UML dykes related to this incipient rifting occur in the Frederikshåb and Sisimiut-Sarfartoq-Maniitsoq areas of western Greenland (Andrews & Emelous, 1971; Scott, 1981; Thy *et al.*, 1987; Larsen & Rex, 1992; Mitchell *et al.*, 1999), the Torngat Mountains in northern Quebec and Labrador (Digonnet *et al.*, 2000; Tappe *et al.*, 2004), the Otish Mountains region in central-north Quebec (Heaman *et al.*, 2004), single occurrences along the northern Labrador coast at Hebron, Saglek, Eclipse Harbour, Iselin Harbour and Killinek Island (Tappe *et al.*, in prep.), and Aillik Bay in central-east Labrador (Malpas *et al.*, 1986; Foley, 1989a) with plenty of potential for new discoveries (Fig.1).

Here, we report the results of a petrologic and geochemical study, combined with radiometric age determinations, on a diverse suite of UML and associated carbonatites from the Aillik Bay area on the Labrador Sea coast. One of the main issues to be addressed is whether the great compositional diversity reflects mantle source heterogeneity, variability in the melting process or relates to modification of a single parental UML magma by low-pressure processes, such as liquid immiscibility and devolatilization. Additionally, we specify and emphasize fundamental differences in the characteristic and genesis between UML and other ultramafic magma types such as kimberlites. Late Neoproterozoic UML magma production

occurred throughout the North Atlantic region so that it has to be discussed within a geodynamic scenario of rifting events distally related to continental breakup.

2. GEOLOGICAL FRAMEWORK OF THE AILLIK BAY AREA

2.1. Makkovik-Ketilidian belt

The Aillik Bay area is situated within the Paleoproterozoic Makkovik orogen at the southern edge of the Archean North Atlantic craton (NAC; Fig.1). Reworked Archean orthogneisses (protolith age 3260-2800 Ma) equivalent to the adjacent NAC are exposed along the western margin of the Makkovik Province (Fig.2), whereas a juvenile high-grade magmatic arc crust dominates the central and eastern part close to the Grenville deformation front (Culshaw *et al.*, 2000a; Culshaw *et al.*, 2000b). These supracrustal units formed during a sequence of subduction and accretion events between ~ 1900-1700 Ma (Makkovikian Orogeny) and were later detached from the basement and thrust onto the edge of the NAC (Culshaw *et al.*, 2000a; Wardle & Hall, 2002; Ketchum *et al.*, 2002). Seismic data and the Nd isotope composition of widespread post-orogenic granites clearly indicate that the western part of the Makkovik orogen, including the Aillik Bay area (Fig.2), is underlain by the Archean crust of the NAC (Kerr & Fryer, 1994; Hall *et al.*, 1995; Kerr & Wardle, 1997; Kerr *et al.*, 1997).

The Makkovik orogen of Labrador shares a similar structure and evolution with the Ketilidian orogen of south Greenland (Fig.1) representing a once-continuous mobile belt formed by the pre-1800 Ma collision of the NAC with an arc-type terrane (Kerr *et al.*, 1996). Mesoproterozoic continental rifting (1350-1140 Ma, Gardar rifting) affected this stabilized belt, but associated alkaline magmatism has only been reported from south Greenland (Upton *et al.*, 2003). Extensive lithospheric thinning occurred throughout eastern North America along the former Laurentian margin during the Late Neoproterozoic (Bond *et al.*, 1984; Kamo *et al.*, 1995; Torsvik *et al.*, 1996; Cawood *et al.*, 2001), resulting in continental breakup and subsequent opening of the Iapetus ocean. In central Labrador, this episode of continental stretching is recorded by remnant graben structures forming the eastward continuation of the prominent St. Lawrence valley rift system (Gower *et al.*, 1986; Murthy *et al.*, 1992). However, Neoproterozoic rift branches that parallel the present-day Labrador Sea seem to have been erased entirely by ocean basin formation during Late Mesozoic rifting (Roest & Srivastava, 1989; Srivastava & Roest, 1999).

2.2. Alkaline magmatism and previous age constraints

Late Neoproterozoic UML and carbonatite dykes occur in an area at least 30 by 30 km around Aillik Bay (Fig.2; Appendix). These dykes are narrow (up to 3-m-wide) and dominantly steeply dipping; flat lying sheets also occur. Recognized UML types are aillikite, mela-aillikite and damtjernite following the scheme devised by Tappe *et al.* (2005). The subvertical dykes are roughly N-S oriented and converge to a hypothetical intrusive centre in the Labrador Sea (Fig.2). Flow banding, back-veining and internal chill-bands are often seen, whereas fluidized autolithic breccias are rare. Individual members of this dyke swarm have been emplaced into common fracture systems and cut each other in a rather arbitrary manner. Some aillikite sheets grade laterally into carbonatite and/or mela-aillikite (Fig.3). A weighted K-Ar mica age of 570 Ma, obtained on a poorly described ultramafic dyke rock from Aillik Bay (Leech *et al.*, 1962), provided the only age constraint for this rift-related magmatism when our study was initiated.

UML magmatism was preceded by several Mesoproterozoic lamproites, which form subvertical N-S oriented (340-030°), 0.2-2 m wide, fine-to-medium grained dykes within the same area (Tappe *et al.*, in prep.). The youngest record of alkaline igneous activity around Aillik Bay is a Mesozoic suite of melilitite, nephelinite and basanite dykes (Tappe *et al.*, in prep.), which is related to the poorly exposed Ford's Bight intrusion (King & McMillan, 1975). The Mesozoic age of this intrusion was constrained by microfossils from a breccia bed (King & McMillan, 1975) and by whole-rock K-Ar dating of narrow dykes (145-129 Ma; Umpleby, 1979), which have been shown to be olivine melilitites (Tappe *et al.*, in prep.).

3. GEOCHRONOLOGY

3.1. U-Pb dating of ultramafic lamprophyres

Aillikite, mela-aillikite and damtjernite dykes were selected from all parts of the Aillik Bay area for U-Pb perovskite dating (Fig.2). Analytical details can be found in Appendix A. Results are reported in Table 1 and displayed in concordia diagrams (Fig.4). Two perovskite fractions of aillikite dyke ST123 from the east shore of Kaipokok Bay yielded similar $^{206}\text{Pb}/^{238}\text{U}$ dates of 560.7 ± 2.4 and 564.5 ± 3.0 Ma, respectively. Hence, a weighted average $^{206}\text{Pb}/^{238}\text{U}$ date of 562.2 ± 1.9 Ma is considered the best age estimate for emplacement of dyke ST123. A similar $^{206}\text{Pb}/^{238}\text{U}$ date of 569.2 ± 1.8 Ma was obtained from mela-aillikite dyke

ST114A exposed on the west shore of Aillik Bay. The emplacement age of aillikite dyke ST228 from the southern shore of Makkovik Bay was determined to be 576.3 ± 1.3 Ma (weighted average $^{206}\text{Pb}/^{238}\text{U}$ date of two perovskite fractions 574.4 ± 1.8 Ma and 578.6 ± 2.0 Ma). The emplacement age of aillikite dyke ST220II from West Turnavik Island is 589.6 ± 1.3 (weighted average of 589.4 ± 1.4 and 590.5 ± 2.8 Ma).

The youngest perovskite ages obtained from damtjernite dykes are 555.0 ± 1.8 Ma (ST211A; Main Turnavik Island) and 563.9 ± 2.5 Ma (ST256; east shore of Makkovik Bay). Perovskites from damtjernite dyke ST174 (Pigeon Island) yielded a $^{206}\text{Pb}/^{238}\text{U}$ date of 574.6 ± 1.6 Ma. Strikingly similar weighted average ages of 581.9 ± 2.3 Ma (582.5 ± 4.8 and 581.9 ± 2.6 Ma) and 582.5 ± 2.1 Ma (582.8 ± 3 and 582.1 ± 2.2 Ma) were obtained from the damtjernites ST140A (east shore of Aillik Bay) and ST188A (Red Island), respectively.

Taken together, the high precision $^{206}\text{Pb}/^{238}\text{U}$ perovskite dates for four individual aillikite/mela-aillikite dykes and five damtjernite dykes cover a similar age range between 562-590 Ma and 555-583 Ma, respectively (Fig.4). Hence, timing of aillikite/carbonatite and damtjernite magmatism can be considered coeval over a comparably long period of time during the Late Neoproterozoic rifting at a craton margin.

3.2. Ar-Ar dating of cognate inclusion ST162I

A clinopyroxene-phlogopite inclusion recovered from aillikite dyke ST162 on the west shore of Aillik Bay (Fig.2) yielded a phlogopite Ar-Ar plateau age of 573.3 ± 3.3 Ma (Table 2), which falls within the U-Pb perovskite age range of the four dated aillikite dykes.

The plateau was calculated over ten consecutive steps, which contained 98% of the total released ^{39}Ar . The gas release spectrum is shown in Appendix C. The 3.5%, 3.9% and 4.2% laser power steps significantly overlap the plateau but have slightly older apparent ages, indicating a potential presence of excess argon. However, on an inverse isochron diagram, a regression through these three data points and the seven others included in the plateau age calculation passes through a $^{40}\text{Ar}/^{36}\text{Ar}$ value of 433.7 ± 258.2 , which is within error of the value for atmospheric air (295.5). Since the three apparently older steps have no significant effect on the overall age, they have been included in the plateau age calculation.

4. PETROGRAPHY

Rock types of the Neoproterozoic Aillik Bay UML suite include carbonatite, aillikite, mel-aillikite and damtjernite listed in order of decreasing carbonate content. Additionally, aillikite dykes host a wide variety of micaceous cognate inclusions (Fig.5). Modal mineral abundances are listed in Table 3 and mineral compositional data are given in Tables 4-10.

4.1. Carbonatite dykes

Two distinct types of carbonatite can be distinguished: (1) a *dolomite carbonatite* devoid of any mafic silicates; and (2) a mixed *dolomite-calcite carbonatite* containing minor amounts of clinopyroxene, phlogopite and olivine phenocrysts. The dolomite carbonatite mainly consists of a mosaic of equigranular Fe-rich dolomite crystals (100-300 μm). Hydroxy-fluorapatite forms abundant euhedral microphenocrysts (50-150 μm). Interstices may be filled by barite, quartz, alkali feldspar (almost pure orthoclase and albite) and/or tiny REE-carbonate crystals. Large rutile grains commonly occur (50-100 μm), whereas opaque phases including magnetite are rare.

The dolomite-calcite carbonatites exhibit a granular texture dominated by calcite grains (150-300 μm). Calcite coexists with subordinate laths of Fe-rich dolomite (Fig.6a). Zoned phlogopite laths (up to 0.5 mm) and olivine grains (up to 1.0 mm; replaced by carbonates) are observed, suggesting gradation into aillikites. However, the presence of diopside-rich clinopyroxene phenocrysts (up to 1.2 mm) contrasts with aillikites. Fresh rutile grains and apatite prisms (up to 0.4 and 1.0 mm, respectively) can be very abundant, whereas opaque oxides are rare. Secondary interstitial barite and/or fluorite may occur.

4.2. Aillikite dykes

Aillikites are texturally heterogeneous; some exhibiting an inequigranular texture due to the presence of olivine and phlogopite macrocrysts up to 7 mm in diameter, whereas others are only weakly inequigranular and have a more typical porphyritic texture (Fig.5b). A rare textural variety consists of nucleated autoliths, which are “cemented” by calcite laths resembling a fluidized breccia. The autoliths are made up of olivine and/or glimmerite kernels surrounded by concentrically arranged fine-grained aillikite matrix (Fig.5a).

Porphyritic aillikites are characterized by phenocrysts of euhedral to subhedral olivine (0.6-1.3 mm), phlogopite (0.25-0.5 mm), apatite and magnetite (0.2-0.4 mm) in a carbonate matrix. *Mela-aillikites* are distinguished from aillikites in containing more mafic silicate phases (> 70 vol.%) and less carbonate (< 10 vol.%). The change in the modal mineral proportions is gradational from aillikite to mela-aillikite. Endmember mela-aillikite contains abundant clinopyroxene prisms in the groundmass (100-300 μm ; Fig.5c), which are rare in aillikite. Both rock types carry microphenocrysts of olivine (0.25-0.5 mm), phlogopite (< 0.25 mm), apatite, opaque oxides (dominantly titanomagnetite and Mg-rich ilmenite) and perovskite or rutile (50-200 μm). Primary kimzeyitic garnet may occur (< 100 μm).

4.3. Damtjernite dykes

Damtjernites are medium to fine grained, porphyritic to intergranular rocks (Fig.5d) containing rare macrocrysts (up to 2.0 cm) of virtually Cr-free diopside-rich clinopyroxene and/or Cr-free titanian aluminous phlogopite. Modal layering, internal chill zones, felsic segregations, flow-alignment and rotation structures are common macroscopic features of these rocks, which were called “sannaites” by Foley (1984) and Malpas *et al.* (1986), but are renamed following Tappe *et al.* (2005). The phenocryst assemblage of the damtjernites consists of olivine (up to 1 mm), phlogopite (up to 5 mm), rare clinopyroxene (250-800 μm) and apatite (up to 1 mm). The modal abundance of euhedral to subhedral olivine phenocrysts may vary from 20 vol.% to only a few crystals. Phlogopite forms large plates typically enclosing clinopyroxene and apatite needles. The groundmass mainly consists of a mesh made up of clinopyroxene and apatite needles (up to 200 μm) and biotite flakes resembling the late rims on phlogopite. Sr-calcite, alkali feldspar (almost pure orthoclase and albite) and nepheline occur in variable but small modal proportions interstitial to the mica and clinopyroxene of the groundmass (Fig.5d). Additional rare felsic phases are analcime and sodalite. Pectolite is observed as a fibrous replacement product of groundmass clinopyroxene or as primary crystals in interstices. Olivine is absent in the groundmass. Abundant rutile grains and dendrites, ilmenite laths and titanomagnetite grains are the principal oxide phases in damtjernite groundmass, whereas perovskite occurs only rarely. Perovskite relicts may be enclosed by Zr-rich titanite crystals recording fluctuations in silica activity during magma evolution or slow cooling. Schorlomite and/or melanite garnet may occur in the groundmass in association with perovskite (Fig.6e).

Felsic globules and segregations (orthoclase, albite, nepheline, analcime, sodalite, calcite, Mg-ankerite) with sharp to diffuse contacts with the groundmass are a characteristic feature of the damtjernites (Foley, 1984).

4.4. Cognate inclusions

A suite of undeformed micaceous inclusions, exclusively hosted by aillikites, comprises in order of decreasing abundance (1) *glimmerite*, (2) *clinopyroxene-phlogopite* and (3) *olivine-phlogopite* nodules (Table 3).

Glimmerite nodules are typically less than 2 cm in diameter; rare examples approach 5 cm. They are usually oval and the internal structure may appear chaotic (Fig.5e). Most glimmerites consist of interlocking 20-100 μm phlogopite flakes (Fig.5f); some contain larger isolated phlogopite “clasts” (up to 500 μm). Fluorapatite fills interstices (together with rare orthoclase) or forms discontinuous bands (Fig.5e,f) that may open into radiating patches. Tiny single and/or composite spinel and ilmenite grains (< 100 μm) are scattered throughout the fine-grained matrix.

Clinopyroxene-phlogopite nodules (up to 8 cm across; Fig.5e) are similar in shape to the glimmerites but have more variable mineralogy and are coarser grained. Large poikilitic phlogopite plates and clinopyroxene prisms dominate (up to 2 mm), whereas lath-like to interstitial opaque oxides (Mg-ilmenite, chromite-titanomagnetite) and prismatic to patchy hydroxy-fluorapatite occur only as minor components (Fig.5g). The mica plates are typically darkened due to exsolution of an opaque phase and rarely enclose subhedral olivine (typically carbonated). A subtle grain size layering was observed in larger nodules. Interstitial calcic amphibole occasionally replaces clinopyroxene and phlogopite (Fig.5g; 6f), presumably as a product of melt infiltration. Subhedral titanite occurs in a single nodule (ST250C).

Rare cumulate-textured *olivine-phlogopite nodules* contain irregular olivine grains (300-800 μm) which are typically enclosed by large phlogopite plates (0.5-1.0 mm; Fig.5h). Hydroxy-fluorapatite (200-400 μm), titanomagnetite, ilmenite (200-800 μm) and rare clinopyroxene (< 300 μm) occur as intercumulus phases. Perovskite and zirconolite (< 100 μm) are rare accessories associated with titanomagnetite surrounding olivine grains.

5. MINERAL COMPOSITIONS

5.1. Olivine

Aillikite/mela-aillikite olivine phenocrysts/microphenocrysts exhibit a fairly large range in forsterite component (Fo91-82 mol%; Fig.6b; 7; Tab.4), NiO (0.5-0.05 wt.%), CaO and MnO (up to 0.9 and 0.4 wt.%, respectively). Contrasting evolutionary trends might indicate that different olivine populations are present. Olivine phenocrysts with normal zoning have core compositions of Fo87-91, decreasing towards the rim down to Fo82-85. NiO typically decreases (0.5-0.05 wt.%), whereas CaO and MnO steadily increase (0.1-0.3 wt.%). Repetition of a normal zoning pattern may occur (Fig.6b). Reverse zoning was often observed, with core compositions of Fo82-84 (NiO 0.2-0.3 wt.%) steadily increasing towards the rim (Fo87-88; NiO 0.4 wt.%). A discrete Fe-enriched overgrowth (Fo82; NiO 0.1 wt.%) with sharp contact to the inner phenocryst typically occurs. This late overgrowth can be strongly CaO-enriched (up to 0.9 wt.%).

Olivine phenocrysts in *damtjernites* are normal zoned (Fo80-86.5) and contain 0.18-0.5 wt.% NiO (Fig.7). CaO and MnO approach 0.4 wt.% at the rims. The most primitive olivine cores in *damtjernites* are more evolved than their most primitive counterparts from *aillikite/mela-aillikite* (Fo91) but have similar high NiO concentrations (Fig.7).

Few analyses obtained for the rare subhedral olivine crystals in *clinopyroxene-phlogopite nodules* show it to be normally zoned with a fairly evolved composition (Fo77-86.6; < 0.1 wt.% NiO; < 0.4 wt.% CaO; Fig.7). The MnO content is conspicuously high ranging between 0.3-0.7 wt.%. The olivine compositions (Fo80-86) in *olivine-phlogopite nodules* overlap with the low Mg/Fe end of *aillikite* phenocrysts, but are NiO-richer (up to 0.4 wt.%) at a given Fo content (Fig.7). This elevated NiO and a lower CaO content (< 0.2 wt.%) sets them apart from rare olivines in *clinopyroxene-phlogopite nodules* (< 0.1 wt.% NiO).

In general, olivine compositions in UML and associated cognate inclusions from the Aillik Bay area are less primitive (< Fo91) than those found in kimberlites and lamproites, which typically approach forsterite contents of up to 94 mol% (Mitchell, 1986; Mitchell & Bergman, 1991).

5.2. Phlogopite

Phlogopite phenocrysts from *aillikite* and *dolomite-calcite carbonatite* typically have (1) a resorbed core with 15 to 16 wt.% Al_2O_3 and up to 5 wt.% TiO_2 , (2) a broad inner rim with elevated Al_2O_3 (up to 18 wt.%) and lower TiO_2 (about 2 wt.%) and (3) a narrow outer rim with Al_2O_3 and TiO_2 falling below 10 and 1 wt.%, respectively, at constantly high MgO. This trend may culminate in virtually Al- and Ti-free tetraferriphlogopite rims in the carbonate-richest samples (Fig.6c; 8a; Tab.5). While tetraferriphlogopite is uncommon in kimberlites, the rims reported here are similar to those from orangeites but distinct from titanian tetraferriphlogopites in lamproites. Phlogopite from type *aillikite/mela-aillikite* and carbonatite is generally Ba-poor with core compositions typically below 1 wt.% BaO. Rim compositions only rarely approach 3 wt.% BaO. This is in contrast to kimberlite phlogopites which commonly show a strong Al- and Ba-enrichment and Ti-depletion toward the rim (Fig.8a). The inner zones of less extremely zoned phlogopite plates (0.5-1.0 mm) from *mela-aillikite* contain 13-15 wt.% Al_2O_3 and 3-5 wt.% TiO_2 , but a high-Al inner rim composition such as in *aillikite* is absent. As in *aillikites*, Al_2O_3 depletion (8-13 wt.%) toward the rim is common, but we generally note a rimward increase in TiO_2 (up to 6 wt.%; Fig.8a) in *mela-aillikite* micas, which contrasts with the decreasing TiO_2 trend observed in the *aillikite* phlogopites. Furthermore, micas from *mela-aillikite* follow a different Mg/Fe evolutionary trend than *aillikite* micas, with a strong increase in Fe at the expense of Mg. This leads to discrete dark-brown biotite rims.

Damtjernite phlogopite plates compositionally resemble the less extremely zoned Ba-poor phlogopite plates from *mela-aillikites* with inner zones containing 13-15 wt.% Al_2O_3 and 3-5 wt.% TiO_2 (Fig.8b). A few samples were found to contain micas approaching 8 wt.% TiO_2 in the core. In general, these micas lack the high-Al inner rim composition of *aillikite* micas, but show Al depletion toward the rim (8-13 wt.% Al_2O_3 ; Fig.8b). We note both rimward TiO_2 increase (up to 8.5 wt.% as in *mela-aillikite*) and decrease (down to 1 wt.% as in *aillikite*). Micas in *damtjernite* show a strong Fe increase at the expense of Mg. This culminates in broad dark-brown biotite overgrowths (Fig.5d).

The mica compositional range in the *clinopyroxene-phlogopite* and *olivine-phlogopite nodules* (Fig.8c) is the same as in phenocrysts from *aillikites/mela-aillikites* and *damtjernites* with the characteristically high Al_2O_3 (13-15 wt.%) and TiO_2 (1-8 wt.%) but low BaO concentrations

(< 1.0 wt.%). Fluorine concentrations are as low as in UML micas, much lower than in glimmerite phlogopite (< 1.3 wt.% vs. 1-3 wt.% F). Evolution toward either tetraferriphlogopite or biotite is typically not seen in these mica plates. Furthermore, they are distinct from primitive mica compositions reported for MARID nodules (typically < 12 wt.% Al₂O₃, Dawson & Smith, 1977; Smith *et al.*, 1978).

Glimmerite phlogopites are compositionally unlike any of the phlogopite phenocrysts, plates or groundmass flakes in aillikite, mela-aillikite, damtjernite or the other nodule types. They are primitive (Mg# 70-90), Al₂O₃- and TiO₂-poor (5-12 and 0.3-2.0 wt.%, respectively; Fig.8c), BaO-depleted (< 0.2 wt.%) but enriched in F (1-3 wt.%).

5.3. Clinopyroxene and amphibole

Phenocrystic clinopyroxenes in *dolomite-calcite carbonatite* and *damtjernite* as well as groundmass prisms in *damtjernites* and *mela-aillikites* are diopside-rich, showing an Al₂O₃ and TiO₂ enrichment towards the rim (up to 10 and 6 wt.%, respectively). However, the average atomic Al/Ti ratio of carbonatite clinopyroxenes is ~ 3, which is distinctively higher than the ratio for clinopyroxene from associated mela-aillikite and damtjernite (~ 2; Fig.9a; Tab.6). Cr₂O₃ concentrations in all these diopsides are below 0.1 wt.%. Sodium and Fe-rich clinopyroxene compositions (with up to 46 mol% aegirine component) were only found as overgrowths on the diopside-rich phenocrysts in damtjernite. Some of these phenocrysts contain rare resorbed green Fe-rich salitic clinopyroxene cores which are remarkably rich in Al₂O₃ (up to 9 wt.%).

Clinopyroxene-phlogopite nodules also contain diopside-rich clinopyroxene enriched in Al₂O₃ and TiO₂ (up to 8 and 4 wt.%, respectively), with atomic Al/Ti (~ 2) similar to the UML clinopyroxenes (Fig.9b). Slightly FeO- and Na₂O-enriched salitic core compositions (up to 9 and 3 wt.%, respectively) may occur and Cr₂O₃ concentrations are below 0.3 wt.%. *Olivine-phlogopite nodules* carry rare diopside (4 and 2 wt.% Al₂O₃ and TiO₂, respectively), which is the Cr₂O₃-richest composition (0.1-0.6 wt.%) of all clinopyroxenes from the Aillik Bay UML suite.

In general, the strong Al- and Ti-enrichment in clinopyroxene from Aillik Bay ultramafic lamprophyres and their cognate inclusions is in contrast to an almost pure diopside

composition typical for groundmass clinopyroxene in orangeites, lamproites and associated MARID-type inclusions (Mitchell & Bergman, 1991; Mitchell, 1995).

The intercumulus calcic amphibole found in *clinopyroxene-phlogopite nodules* (Fig.6f) is generally MgO- and TiO₂-rich (Mg# 73-90 and 1.9-5.0 wt.% TiO₂) and ranges from magnesiohastingsite through pargasite to rare magnesiokatophorite. Fluorine is < 0.5 wt.% and K₂O does not exceed 1.9 wt.%.

5.4. Spinel

Spinel from the Aillik Bay area UML and related micaceous inclusions generally follow a “titanomagnetite trend” (trend 2 of Mitchell, 1986) which is characterized by high Fe_T²⁺/(Fe_T²⁺+Mg) ratios greater than 0.7, increasing Fe and Ti but decreasing Mg, Al and Cr (Fig.10a;b). The most Mg-rich spinels were found in aillikites but do not exceed 13.5 wt.% MgO (Tab.7). By comparison, kimberlite spinels are more magnesian (12-20 wt.% MgO) and they follow a trend of increasing Ti at constant Fe/Mg ratios (ca. 0.5; Fig.10b), known as the “magnesian ulvöspinel trend” (trend 1 of Mitchell, 1986). Aillik Bay UML spinels have Cr/(Cr+Al) ratios less than 0.85, which is in marked distinction to Cr-rich spinel compositions in lamproites and orangeites (Cr# > 0.85), which follow a similar “titanomagnetite trend” (Mitchell & Bergman, 1991; Mitchell, 1995).

Early-stage spinels in *aillikites* are typically composed of chromite-spinel solid solutions (up to 43 wt.% Cr₂O₃, 13 wt.% MgO, 12 wt.% Al₂O₃). The rims of zoned spinel microphenocrysts and individual grains are of ulvöspinel-magnesian ulvöspinel-magnetite composition (up to 11 wt.% MgO). These titanomagnetites are remarkably enriched in Al₂O₃ (up to 11 wt.%) with low atomic Cr/(Cr+Al) ratios (< 0.3). Spinel from *mela-aillikites* may contain cores of titanian magnesiochromite-chromite solid solution (up to 12 wt.% TiO₂, 9 wt.% MgO, 25 wt.% Cr₂O₃) and of chromite-spinel solid solution, similar to their aillikite analogues. Individual titanomagnetite microphenocrysts or rims around zoned chromite grains contain less MgO and Al₂O₃ (< 5 wt.%) than in the aillikites (Fig.10a).

Spinel group minerals in *damtjernites* are dominantly titanomagnetite which rarely exhibit cores and inclusions of titanian magnesiochromite-chromite solid solution (up to 14 wt.% TiO₂, 9 wt.% MgO, 22 wt.% Cr₂O₃). Titanomagnetites in damtjernites have the lowest MgO concentration (typically < 1 wt.%) of all the Aillik Bay UML spinels (Fig.10a), and contain

similar levels of Al_2O_3 as the mela-aillikites, but significantly less than the aillikites. Individual grains show a decreasing Mg and Ti content but increasing Fe toward the rim approaching magnetite end-member composition.

Rare *glimmerite* spinels have similar compositions to the most evolved aillikite spinels with MgO and Al_2O_3 typically below 5 wt.% following a “titanomagnetite trend” (Fig.10b). Composite spinel grains in *clinopyroxene-phlogopite nodules* may contain cores of chromite (up to 43 wt.% Cr_2O_3) and/or Cr-spinel (up to 20 wt.% Cr_2O_3) typically mantled by titanomagnetite. Titanomagnetite-magnetite resembles late-stage spinels from pyroxene-rich mela-aillikites in being very close to end-member composition. They are much more depleted in MgO and Al_2O_3 (typically < 2.0 and 3.0 wt.%, respectively) than their analogues from pyroxene-free glimmerites and aillikites (Fig.10b). Titanomagnetites in *olivine-phlogopite nodules* resemble evolved aillikite spinels. They contain more MgO than spinels from clinopyroxene-rich nodules and mela-aillikite dykes (up to 7 wt.%; Fig.10b). Cr-spinel with up to 25 wt.% Cr_2O_3 rarely occurs as inclusion in olivine.

5.5. Ilmenite and rutile

Ilmenite laths in the mixed *dolomite-calcite carbonatite* contain up to 4.4 wt.% MnO but are poor in MgO (< 0.25 wt.%) and devoid of Cr_2O_3 (below detection; Tab.8). Large rutile grains, which are common to both carbonatite types, commonly contain up to 4 wt.% Fe_2O_3 and Nb_2O_5 . Groundmass ilmenite in *aillikite* is moderately enriched in MgO (0.1-12 wt.%) and MnO (0.3-2.0 wt.%) with MnO typically increasing towards the rim (up to 6.5 wt.%). Cr_2O_3 content may approach 2.2 wt.%. Tiny rutile grains which occur in perovskite-free carbonate-rich aillikites contain less than 2 wt.% Fe_2O_3 . Ilmenite in *mela-aillikites* is almost pure FeTiO_3 with less than 1.5 wt.% MgO and 0.2 wt.% Cr_2O_3 . MnO ranges between 1-2 wt.%. The hematite component is typically below 5 mol% in ilmenites from mela-aillikite but up to 10 mol% in aillikite. *Damtjernite* ilmenite is enriched in MnO (0.8-5 wt.%) but virtually free in MgO and Cr_2O_3 (< 0.05 wt.%). The hematite component in these ilmenites is typically below 3 mol%.

Tiny ilmenite grains in *glimmerite nodules* are enriched in MnO (1.5-4.8 wt.%), poor in MgO (0.6-3.7 wt.%), and devoid of Cr_2O_3 (< 0.05 wt.%). These ilmenites have a comparably large hematite component (10-14 mol%) testifying to oxidizing crystallization conditions. In

contrast, the long ilmenite laths in *clinopyroxene-phlogopite nodules* are MgO-rich (up to 12 wt.%) and contain moderate amounts of MnO and Cr₂O₃ (< 2.0 and < 0.6 wt.%, respectively). The hematite component of these ilmenites is variable between 6-14 mol%, but dominantly below 10 mol%. Ilmenite in *olivine-phlogopite nodules* is also MgO-rich but MnO-poor (8.0-12.4 and < 0.4 wt.%, respectively) and the hematite component is low (7-9 mol%). As previously noted for clinopyroxenes, Cr₂O₃ content in these ilmenites (1-3 wt.%) is much higher than in other Aillik Bay area UML or cognate inclusions.

5.6. Perovskite, titanite and Ti-rich primary garnet

Most *aillikite/mela-aillikite* perovskites, like those from kimberlite, are close to the ideal CaTiO₃ end-member composition. However, a negative correlation between atomic Ca and Na plus LREE indicates a solid-solution series between perovskite and loparite (Na_{0.5}LREE_{0.5}TiO₃) on a limited basis with Na₂O and LREE₂O₃ commonly not exceeding 1 and 8 wt.%, respectively. The SrO (0.1-0.3 wt.%) and Nb₂O₅ (< 0.8 wt.%) contents are also remarkably low in the oscillatory zoned perovskites. Despite a compositional similarity of perovskite in aillikite and *damtjernite*, the latter are slightly richer in SrO (0.3-0.6 wt.%) than their aillikite counterparts (< 0.3 wt.%) possibly due to less Sr-incorporating carbonate in the damtjernite system. Perovskite relicts in damtjernites may be enclosed by titanite crystals which have elevated Fe₂O₃ and Ce₂O₃ concentrations (up to 3 and 0.5 wt.%, respectively) and may be enriched in ZrO₂ (up to 3.5 wt.%).

Small kimzeyitic garnets are restricted to *aillikites* and have a fairly constant TiO₂ content (9-11 wt.%), whereas ZrO₂ spans a wide range between 10-17 wt.% (Tab.9). Core compositions are generally richer in Zr than the rims. Schorlomite and/or melanite garnet is rare but characteristic for *damtjernites* and observed zoning patterns are typically from Ti-rich core compositions to Fe-rich rims (1.8-18 wt.% TiO₂; 15.7-21.6 wt.% FeO). Zirconian schorlomite with up to 5 wt.% ZrO₂ in the core was rarely found. The presence of Ti-rich andradites and kimzeyitic garnets reflects the high Ca and Ti but low Al concentration of the UML magma and can therefore be regarded as characteristic for UML-carbonatite associations (Platt & Mitchell, 1979; Rock, 1986; Tappe *et al.*, 2005). These garnets do not occur in kimberlites and lamproites (Mitchell & Bergman, 1991; Mitchell, 1995).

5.7. Apatite and carbonate

Hydroxy-fluorapatite (1.5-2.6 wt.% F) in the two *carbonatite* types is slightly enriched in LREE₂O₃ and SrO (up to 0.6 wt.%) as well as SiO₂ (1.3-3.4 wt.%). *Aillikite* hydroxy-fluorapatite microphenocrysts (0.9-2.5 wt.% F) have highest F concentrations in the core decreasing towards the rim. SiO₂ (up to 2.7 wt.%) substitutes for P₂O₅; this process was enhanced towards the rim. SrO is moderately enriched ranging between 0.3-2.6 wt.%. Other minor elements such as the LREE and S approach 1.5 and 0.2 wt.%, respectively. Hydroxy-fluorapatite in *damtjernite* contains up to 2.3 wt.% F and 1.5 wt.% SiO₂. SrO is below 0.7 wt.% and LREE₂O₃ and S approach 0.5 wt.%. Fluorapatite in *glimmerite* is much F-richer than its counterpart from aillikite (2.0-3.5 vs. 0.9-2.5 wt.% F). It is also richer in SrO (0.5-3.1 wt.%) and LREE (e.g. up to 4 wt.% Ce₂O₃) but virtually free in SiO₂ and S. Hydroxy-fluorapatite (< 1.8 wt.% F) in *clinopyroxene-phlogopite* and *olivine-phlogopite nodules* is strikingly different from fluorapatite in glimmerite. SrO is only moderately enriched ranging between 0.4-0.8 wt.% and LREE₂O₃ approach 0.6 wt.%. These compositions resemble those of apatites from aillikite/mela-aillikite and damtjernite.

Fe-rich dolomite crystals in *dolomite carbonatite* contain between 2 and 9 wt.% FeO; only rarely approaching 12 wt.% towards the rim. MnO is elevated (0.2-1.2 wt.%), whereas SrO and BaO are conspicuously low (< 0.2 wt.%). Rare interstitial REE-carbonate is probably bastnäsite and contains up to 56 wt.% LREE₂O₃. Calcite in mixed *dolomite-calcite carbonatite* coexists with subordinate laths of Fe-rich dolomite (Fig.6a) which resembles its counterpart from the dolomite carbonatites (2-12 wt.% FeO and 0.2-1.2 wt.% MnO). It differs in that both calcite and dolomite contain up to 1.5 wt.% SrO. The groundmass of *aillikites* is dominated by a mosaic of Sr-calcite (up to 2 wt.% SrO), whereas dolomite containing up to 10 wt.% FeO is rare. Fe-rich dolomite seems to dominate over calcite (< 1 wt.% SrO) in the generally carbonate-poor groundmass of *mela-aillikites*. Carbonate in the *damtjernite* groundmass is Sr-calcite with up to 4.8 wt.% SrO.

5.8. Alkali feldspar, feldspathoids and pectolite

Coexisting orthoclase and albite in the *damtjernite* groundmass are close to end-member composition (Tab.10) indicating low-temperature crystallization. Fe₂O₃ and BaO concentrations in orthoclase are typically below 1 wt.%, which is in marked contrast to lamproitic orthoclase (up to 5 wt.% Fe₂O₃). Damtjernite nephelines contain up to 7.5 wt.%

K₂O and 2 wt.% Fe₂O₃ but are poor in CaO (< 0.5 wt.%). Rare examples show almost pure sodalite overgrowths with up to 7.5 wt.% Cl. The rare pectolite, occurring in those damtjernites with the least modal carbonate, contain some minor FeO (< 1.5 wt.%), MnO and Al₂O₃ (< 1 wt.%; Tab.10).

6. PRESSURE ESTIMATES FOR COGNATE INCLUSIONS

Diopside-rich clinopyroxene and rare calcic amphibole of the clinopyroxene-phlogopite nodules allow qualitative pressure estimates. The clinopyroxene barometer of Nimis & Ulmer (1998) requires an independent temperature estimate, which we obtained using the clinopyroxene thermometer of Kretz (1982). The uncertainty in temperature is 60°C (1σ) and results in large errors in pressure estimates (0.3 GPa, 1σ). Nevertheless, the crystallization pressure of clinopyroxenes from several clinopyroxene-phlogopite nodules can be bracketed between 0.8-1.5 GPa, corresponding to ~ 25-45 km depth. Two clinopyroxene-phlogopite nodules yielded higher pressures between 1.8-2.3 GPa. Rare clinopyroxene from an olivine-phlogopite nodule gives a pressure estimate of 0.9-1.7 GPa, which is similar to most clinopyroxene-phlogopite nodules.

Calcic amphibole in clinopyroxene-phlogopite nodules yielded the lowest crystallization pressures of 0.4-0.7 GPa (Al-in-hornblende barometer of Hammarstrom & Zen, 1986), corresponding to ~10-20 km depth. This agrees with textural relations indicating late melt/fluid infiltration into the nodule material (Fig.6f). No pressure estimate can be given for the glimmerite nodules but the low-Ba mica compositions may be a reflection of comparably high crystallization pressures (Guo & Green, 1990).

7. MINERALOGICAL CONSTRAINTS ON CRYSTALLIZATION CONDITIONS AND THEIR IMPLICATIONS FOR MANTLE SOURCE CHARACTERISTICS

7.1. Oxygen fugacity estimates from olivine-spinel and ilmenite-magnetite pairs

Olivine and Cr-spinel are the earliest phases crystallized from aillikite magma and may be used to constrain the oxygen fugacity conditions during early stages in UML magma evolution. We applied the FeMg₁ exchange thermometer of O'Neill & Wall (1987) and the olivine-orthopyroxene-spinel oxybarometer of Ballhaus *et al.* (1991). Ferric iron in spinel was

calculated assuming stoichiometry (Ballhaus *et al.*, 1990). Since ultramafic lamprophyres are not saturated in orthopyroxene, the oxybarometer of Ballhaus *et al.* (1991) yields maximum fO_2 -values, which can be corrected for the appropriate silica activity of a melt as outlined by Fedortchouk & Canil (2004). The perovskite-titanite reaction (Nicholls *et al.*, 1971) rather than the monticellite-diopside reaction as chosen by Fedortchouk & Canil (2004) for kimberlite was considered as the upper limit of silica activity controlling UML magma evolution at Aillik Bay. This assumption is consistent with the observation that perovskite and diopside-rich clinopyroxene frequently occur in the groundmass of these rocks. Some damtjernites contain perovskite and titanite in reaction relationship, indicating that crystallization occurred along this buffer. We assumed an equilibration pressure for olivine-spinel pairs of 1 GPa: pressure has only a minor influence on the calculation of the equilibrium olivine-spinel crystallization temperature ($20^\circ\text{C}/\text{GPa}$) and oxygen fugacity ($0.03 \log\text{-bar units}/\text{GPa}$).

The olivine-spinel equilibration temperatures for the aillikite magma, which range from $912\text{-}1300^\circ\text{C}$ are illustrated in Figure 11. The relative oxygen fugacity varies from FMQ -0.03 to FMQ $+2.43$ ($\log\text{-bar unit deviation from fayalite-magnetite-quartz buffer}$) with most pairs recording fO_2 slightly above the FMQ buffer. An olivine-spinel pair from a damtjernite (1253°C ; FMQ $+1.84$), and from an olivine-phlogopite cognate inclusion (1002°C ; FMQ $+1.83$) fall within this fO_2 -T range calculated for aillikites (Fig.11).

The relative oxygen fugacity during UML groundmass crystallization was estimated from late ilmenite-magnetite pairs (0.2 GPa; QUILF-95 program; Andersen, D.J. *et al.*, 1993). It also scatters around the FMQ buffer (FMQ -1.81 to FMQ -0.03 for aillikite; FMQ -1.98 to FMQ $+1.89$ for cognate inclusions; Fig.11). Lower equilibration temperatures calculated for these ilmenite-magnetite pairs than for olivine-spinel phenocrysts are in keeping with the distinct crystallization stages represented by the phases involved. Ilmenite-magnetite temperatures for aillikites and micaceous cognate inclusions range between $868\text{-}641^\circ\text{C}$ and $849\text{-}556^\circ\text{C}$, respectively. Temperatures for damtjernite are at the lower end of this range ($662\text{-}525^\circ\text{C}$) and the few fO_2 values for damtjernites show the greatest negative deviation from FMQ (FMQ -3.35 to FMQ $+1.37$) presumably reflecting sub-solidus re-equilibration (Fig.11).

The estimated oxygen fugacity values for UML from Aillik Bay are significantly higher than those for diamondiferous Slave craton kimberlites (Fig.11; $< \text{FMQ } -2.0$; Fedortchouk &

Canil, 2004), which lie close to the D/GCO buffer of Frost, D.J. & Wood (1997). Highly reduced crystallization conditions were also calculated for kimberlites from the Kaapvaal craton (Mitchell, 1973). Since the redox state of a primitive mafic magma has the potential to preserve that of its source (Carmichael, 1991), it can be inferred that the UML magma was derived from a fairly oxidized mantle portion beneath the rifted North Atlantic craton in contrast to comparatively reduced sources for kimberlites within a stable cratonic mantle.

7.2. Hydrogen fluoride fugacity estimates from phlogopite-apatite pairs

Estimates of crystallization temperature and relative hydrogen fluoride (HF) fugacity in the UML were obtained from coexisting apatite and phlogopite crystals (Fig.12). Equilibrium is assumed based on textures and mode of occurrence; e.g. apatite inclusions in phlogopite (Fig.5f; g). Equilibrium pressure is negligible and was set at a minimum of 0.2 GPa.

The biotite-apatite geothermometer recalibrated by Zhu & Sverjensky (1992) yields rough temperature estimates in the range 1250 to 500°C for aillikites and damtjernites from the Aillik Bay area (mean error = $\pm 50^\circ\text{C}$ at 1σ). The micaceous cognate inclusions from aillikites and macrocrysts from damtjernites fall within this temperature range. High temperatures of the UML phlogopites at low crystallization pressures are also indicated by their high TiO_2 concentrations (Forbes & Flower, 1974; Robert, 1976; Righter & Carmichael, 1996). Apatite inclusions in olivine phenocrysts indicate early crystallization of apatite.

Estimates of the relative HF fugacity, $\log(f_{\text{HF}}/f_{\text{H}_2\text{O}})$, based on Andersen, T. & Austrheim (1991) using the apatite-phlogopite equilibrium temperature yield values between -4 and -7 ± 0.15 for Aillik Bay UML and associated cognate inclusions (Fig.12). The correlation between HF fugacity and temperature displays a relatively shallow (slow) cooling trend internally buffered by phlogopite rather than apatite, consistent with mica being the dominant phase.

There is considerable overlap between relative HF fugacities recorded by Aillik Bay aillikite and damtjernite phenocrysts; and cognate clinopyroxene-phlogopite and olivine-phlogopite inclusions also fall within this range. Interestingly, the glimmerite inclusions record higher relative HF fugacities than aillikites, damtjernites and the remainder of the cognate inclusions from Aillik Bay at a given equilibration temperature (Fig.12).

In summary, apatite and phlogopite equilibrated throughout the crystallization sequence of the UML magma, spanning a wide interval from near liquidus to near solidus temperatures. Aillik Bay aillikites, damtjernites and cognate clinopyroxene-phlogopite/olivine-phlogopite inclusions experienced a similar evolution in terms of volatile fugacities. However, glimmerite nodules crystallized under higher relative HF fugacity conditions over a similar wide temperature range. The estimated relative HF fugacity of the Aillik Bay area ultramafic lamprophyres is considerably lower than reported for carbonatites (Fig.12), i.e. from the Fen complex (Andersen, T. & Austrheim, 1991), but compares well with carbonate-rich UML from the Torngat Mountains and the Delitzsch complex, Germany (Seifert *et al.*, 2000). The generally F-poor, OH-rich nature of phlogopites in Aillik Bay UML (< 1 wt.% F) may result from highly oxidizing crystallization conditions (Foley, 1989b), which is in marked contrast to the high F content in lamproitic micas (1-7 wt.%; Mitchell & Bergman, 1991), which were experimentally shown to be derived from F-rich reduced mantle sources (Foley *et al.*, 1986). Oxidizing crystallization conditions might also be responsible for the elevated Al-content of the UML micas (atomic K/Al < 1 vs. > 1 in lamproite micas at similarly strong bulk rock Al-depletion). The pronounced substitution of Mg by Ti leading to octahedral site vacancies is also in keeping with a redox control (Arima & Edgar, 1981; Foley, 1989b).

8. GEOCHEMISTRY AND ISOTOPIC COMPOSITION

8.1. Major and compatible trace elements

Extreme SiO₂-undersaturation, Al-depletion, strong Ca-enrichment and a potassic character is the hallmark of all members of the Aillik Bay UML suite (Fig.13; Tab.11). The *aillikites* contain between 17 and 29.4 wt.% SiO₂ and 11 to 20.4 wt.% MgO (Fig.14). Mg# ranges between 60-77 and Al₂O₃ concentrations are below 3.5 wt.%. CaO is high but variable (13-24.7 wt.%) and TiO₂ is elevated (2.5-3.8 wt.%) compared to kimberlites (Fig.13). Moderately high K₂O concentrations (1.3-2.4 wt.%) but extreme Na₂O-depletion (< 0.7 wt.%) are characteristic for aillikites. P₂O₅ (0.9-3.2) and CO₂ (10.1-20.8 wt.%) concentrations are higher in aillikites than in *mela-aillikites* (P₂O₅ = 0.2-1.3 wt.%; CO₂ = 2-9.9 wt.%; Fig.13; 15). The latter have elevated SiO₂ (30.7-36 wt.%), TiO₂ (3.7-5.8 wt.%), Al₂O₃ (3.7-4.8 wt.%) and K₂O (up to 3.1 wt.%) but much lower CaO (7.4-12.4 wt.%) concentrations, a reflection of the loss of the carbonate fraction. Cr and Ni contents are high in aillikites (210-574 ppm Ni; 322-857 ppm Cr) and even higher in mela-aillikites (572-787 ppm Ni, 705-1150 ppm Cr; Fig.14).

Damtjernites have higher SiO₂ (29.3-38 wt.%), TiO₂ (3.5-6.9 wt.%), Al₂O₃ (3.6-9.9 wt.%) and Na₂O (0.2-4.3 wt.%) than aillikites (Fig.13), reflecting less primary carbonate and the occurrence of clinopyroxene plus a felsic mineral in the groundmass. MgO varies considerably between 5.5-16 wt.% (Fig.14), which translates into a wide Mg# range (40-67). *Damtjernites* have Ni and Cr concentrations which range from values typical for mantle-derived primitive magmas to low values close to the detection limit (22-517 ppm Ni; < 10-586 ppm Cr; Fig.14). There is some overlap with the major element composition of melaaillikites (which lack the felsic groundmass component), but evolved *damtjernites* approach significantly higher levels of Si, Al and Na (Fig.13). K₂O and P₂O₅ concentrations can be high (0.9-3.5 and 0.7-3.6 wt.%, respectively), as is the amount of CO₂ (0.2-10.9 wt.%).

Carbonatites typically contain less than 18 wt.% SiO₂ but may approach 22 wt.% SiO₂ (Fig.13). These carbonatites straddle the boundary between magnesio- and ferrocarbonatite (Woolley & Kempe, 1989). In the Aillik Bay UML suite, they are the rock types with lowest concentrations of TiO₂ and Al₂O₃ (< 2.6 and 3.3 wt.%, respectively). CaO (17-38.4 wt.%), MgO (6.3-16.8 wt.%), Fe₂O₃ (5.3-11.9) and MnO (up to 0.6 wt.%) concentrations are high in both dolomite-calcite carbonatite and dolomite carbonatite. The CO₂ content of the dolomite carbonatite, which does not contain mafic silicates, is higher (32.2-39.5 wt.%) than in the silicate-bearing calcitic carbonatites (17.3-30.5 wt.%; Fig.13). K₂O and P₂O₅ contents approach 2.5 and 4.5 wt.%, respectively. Dolomite carbonatite is Ni and Cr depleted (< 60 ppm), but concentrations in dolomite-calcite carbonatite may be up to 300 and 750 ppm, respectively.

8.2. Incompatible trace elements

Primitive mantle-normalized incompatible element abundances and their distribution are displayed in Figure 16. *Aillikites* are strongly enriched in Cs, Ba, Th, U, Nb, Ta and LREE with normalized concentrations of up to 600 x primitive mantle. Relative depletions are apparent at Rb, K, Pb, Sr, P, Zr, Hf and the HREE which can be as low as 3 x primitive mantle (Fig.16a). REE fractionation is extreme with La/Yb_N between 70-136 (Fig.13) and Sm/Yb_N between 18-30. The strong relative Zr-Hf depletion in aillikites, quantified by a (Zr+Hf)/(Zr+Hf)* ratio of 0.15-0.41, whereby (Zr+Hf)* is interpolated between neighbouring Nd and Sm, is only surpassed by the carbonatites. Low Zr/Nb ratios (1.2-4) are an expression of the strong incompatible trace element enrichment. *Mela-aillikites* have lower incompatible

element abundances than aillikites but exhibit a similar pattern (Fig.16a). However, the relative Zr-Hf depletion (0.47-0.87) and LREE/HREE fractionation ($\text{La/Yb}_N = 33-84$) are less pronounced.

Damtjernites exhibit similar enrichments in Th, U, LFSE and LREE to aillikites. However, marked differences between the two UML variants are apparent in the elevated Nb, Ta, Zr, Hf and HREE concentrations of the damtjernites (Fig.15a,b;16b). Interestingly, the intra-HFSE fractionation is similar between the two UML types as exemplified by similar Zr/Nb ratios of damtjernites (2-4) and aillikites (1.2-4; Fig.13). The relative Zr-Hf depletion (0.33-0.55) of damtjernites is similar but often less pronounced than in aillikites (< 0.41). The REE are less fractionated in the damtjernites than in aillikites, as indicated by their lower La/Yb_N (45-62; Fig.13) and Sm/Yb_N (11-17) ratios.

Incompatible elements in the carbonatites are extremely fractionated with strong Ba, Th and REE enrichment but Rb, K, Zr, Hf and Ti depletion (Fig.16c). While the patterns of the mixed *dolomite-calcite carbonatites* ($\text{La/Yb}_N = 13-89$) have some resemblance to those of aillikites, those for *dolomite carbonatites* ($\text{La/Yb}_N = 36-377$) greatly fluctuate with LREE concentrations $> 1000 \times$ primitive mantle but strong Zr-Hf depletions (0.01-0.02).

8.3. Sr-Nd isotope composition

Bulk rock Sr and Nd isotope compositions are listed in Table 12. Carbonatites, aillikites, mela-aillikites and damtjernites show overlapping compositions on a horizontal array in Sr-Nd isotope space close to Bulk Earth (Fig.17). Age corrected $\epsilon_{\text{Nd}(582)}$ values (+0.1 to +1.9) fall within a narrow range, whilst the $^{87}\text{Sr}/^{86}\text{Sr}_{(i)}$ ratios (0.70369-0.70466) show stronger variation across the Bulk Earth line. Two samples, the dolomite-calcite carbonatite ST126 and the damtjernite ST256, have a more radiogenic Sr isotope composition (0.70579 and 0.70662, respectively) defining the high $^{87}\text{Sr}/^{86}\text{Sr}_{(582)}$ -end of the horizontal array (Fig.17). Since these samples do not show any other “anomalous” features compared to the other samples, we consider their Sr isotope composition to be primary. The clinopyroxene-phlogopite nodule ST162I falls within the Sr-Nd compositional range of the UML and carbonatites ($^{87}\text{Sr}/^{86}\text{Sr}_{(i)} = 0.70393$; $\epsilon_{\text{Nd}(i)} = +0.25$).

8.4. Carbon and oxygen isotope composition of the bulk rock carbonate fraction

The bulk rock carbonate fraction of *aillikites* varies relatively little in $\delta^{13}\text{C}_{\text{PDB}}$ (-5 to -5.7 ‰) and $\delta^{18}\text{O}_{\text{SMOW}}$ (9.4-11.6 ‰) with sample ST220II being exceptional in approaching $\delta^{13}\text{C}$ of -4 ‰ (Fig.18; Tab.13). The *dolomite-calcite carbonatites* have a “heavier” carbon isotope composition (-3.3 to -3.7 ‰ $\delta^{13}\text{C}$) than the associated *aillikites*, with only sample ST199 being less ^{13}C -enriched (-4.8 ‰) close to values typical for *aillikites*. The oxygen isotope composition (9.6-10.8 ‰ $\delta^{18}\text{O}$) is within the range of the *aillikites*. Only sample ST231A (13.0 ‰ $\delta^{18}\text{O}$), which presumably experienced carbonate recrystallization, falls outside this narrow range. The *dolomite carbonatites* have the isotopically “heaviest” carbon composition with $\delta^{13}\text{C}$ between -2.7 and -2.8 ‰ (n=2). The oxygen isotope composition (10.8-11.5 ‰ $\delta^{18}\text{O}$) covers the higher end of the *aillikite* range, slightly elevated in comparison to the calcite-bearing carbonatites. There is no correlation between C and O isotope composition of carbonates from *aillikite* and carbonatite (Fig.18) as well as stable isotope and Sr-Nd isotope ratios. *Damtjernites* contain a composite carbonate fraction (groundmass and segregations) which is highly variable in its carbon isotope composition varying between -7 and -3 ‰ $\delta^{13}\text{C}$ (the range observed from *aillikite* to *dolomite carbonatite*) at a fairly constant $\delta^{18}\text{O}$ of 9.9-11.4 ‰ which is within the range of *aillikites* (Fig.18).

9. DISCUSSION

Field relations, age determinations and radiogenic isotope signatures imply that the various UML and carbonatite types as well as their micaceous cognate inclusions are coeval and related to a single parental magma. In order to evaluate the petrogenesis of UML in the Aillik Bay area, it is necessary to unravel the effects of low-pressure modification of the primary magma, thus clearing the way for constraining the nature of the UML magma source and the geodynamic conditions under which melting occurred.

9.1. Modification of the parental UML magma

9.1.1. Role of contamination and fractionation processes

Extensive interaction of the UML magma with continental crustal material can be ruled out by the strong Si and Al undersaturation, high Ce/Pb ratios (> 25), positive $\epsilon_{\text{Nd}(582)}$ values and fairly unradiogenic Sr isotope composition ($^{87}\text{Sr}/^{86}\text{Sr}_{(582)}$ typically < 0.7045). The continental

crust of the North Atlantic craton is characterized by extremely unradiogenic Nd and radiogenic Sr isotope compositions and therefore cannot have modified the primary UML magma (e.g. Makkovik Province gneisses $\epsilon_{\text{Nd}(582)} \sim -30$; Saglek block gneisses $^{87}\text{Sr}/^{86}\text{Sr}_{(582)} > 0.73$; Collerson *et al.*, 1989; Kerr & Fryer, 1993). There is no correlation between UML/carbonatite isotope composition and chemical parameters such as Si, Al, K and Pb, which are typically elevated in continental crustal rocks.

Fine-grained microporphyritic aillikites with high Mg-numbers, Ni and Cr contents may represent near-primary mantle-derived magma compositions following the criteria of Frey *et al.* (1978); Mg# > 68 and Ni > 320 ppm. Furthermore, they resemble experimentally produced higher-degree melts of synthetic carbonated garnet peridotite in a simple CMAS-CO₂ system close to 5 GPa (Fig.19a,b; Gudfinnsson & Presnall, 2005). Note that the accumulation of olivine macrocrysts typical of kimberlites (Mitchell, 1986, 1995) is seen in only few aillikite samples (L2, ST225) and is not considered significant. Damtjernites cannot be interpreted unequivocally as near-primary magmas using the criteria of Frey *et al.* (1978), although these rely on melts being in equilibrium with dry peridotite and not with metasomatized source materials. The most primitive olivine-rich members approach "primary" Mg#, Ni and Cr contents, but more evolved types are almost olivine-free resulting in a conspicuous bimodal distribution in terms of MgO, Ni and Cr content (Fig.14a;b). The cumulate textures formed by large subhedral olivine and rare composite clinopyroxene crystals within the fine-grained groundmass imply that the majority of these crystals formed much earlier and more likely represent cognate high-pressure phases. Clinopyroxene crystallization pressure ranges between 0.8-1.5 GPa (method of Nimis & Ulmer, 1998), similar to estimates for the clinopyroxene-bearing cognate inclusions. An unrealistically high amount of ~ 30 to 40 wt.% olivine removal ($D_{\text{MgO}}=2.56$; $D_{\text{Ni}}=4.9-6.5$; following Herzberg & O'Hara, 2002) together with minor amounts of Cr-spinel would be required to relate these two groups of damtjernites (Fig.14b), which have an identical olivine-free groundmass. On the basis of the large damtjernite sample suite examined (n=35), we can rule out a continuous fractionation series, leading us to favour a role for a silicate-carbonate unmixing process in their petrogenesis (see section on immiscibility).

Major and selected trace element variation diagrams using either MgO or SiO₂ as fractionation index show no gradation between aillikites and damtjernites (Fig.13;14), implying that they experienced different evolutionary histories (Fig.19). There is no

petrologically sound mineral assemblage that could relate the two contrasting rock types by crystal fractionation. Fractional crystallization of olivine and Cr-spinel, however, can account for some of the intra-group variation in aillikites and damtjernites, as illustrated by the distinct Ni and Cr versus MgO trends (Fig.14). Our field observation that carbonatites, aillikites and mela-aillikites are intimately related is supported by the strong compositional continuum in Si, Ti, Al, Ca, Mn, P, CO₂, Cr, Ni, Nb and LREE contents. On variation diagrams, they define well correlated trends from which damtjernites are typically displaced (Fig.13;14;15). These trends are controlled principally by a relative separation of carbonate and a 2/1 to 1/2 mix of olivine/phlogopite (Fig.13; 19a). The most likely process is devolatilization of CO₂-rich liquids/fluids from aillikite magma which caused the compositional shift to either side of these trends with carbonatite and mela-aillikite being close to the separated end-members.

9.1.2. Linking aillikites, mela-aillikites and carbonatites by a devolatilization process

Several lines of evidence indicate that the two distinct types of carbonatite occurring at Aillik Bay do not represent primary magma compositions. From a petrological point of view, the dolomite carbonatite is the more likely candidate for a primary magma composition (Sweeney, 1994; Harmer & Gittins, 1997; Lee & Wyllie, 1998), but the constituting Fe-rich dolomite is highly evolved in terms of Fe/Mg distribution. Furthermore, the conspicuous lack of mafic silicate phases such as olivine and phlogopite in combination with texture and extremely fractionated incompatible element distributions, indicate that the dolomitic carbonatites cannot represent liquids (Wyllie & Tuttle, 1960), but are more likely the product of a carbonate extraction process.

In contrast, the dolomite-calcite carbonatite contains mafic silicates compositionally resembling those of the aillikites (Fig.8a), suggesting these are close to a liquid composition. Although the analyzed dolomite-calcite carbonatite and aillikite samples were collected from discrete subvertical dykes, lateral gradations between both rock types within single sills (Fig.3) have been described from Cape Makkovik (Malpas *et al.*, 1986; Foley, 1989a). Field relations imply that the carbonatite phase of the flat lying sheets may represent a carbonatite liquid with associated fluid that was moving ahead of the more viscous silicate-rich aillikite magma as a “carbonate front” opening fissures during dyke/sill emplacement. Additional support for such a devolatilization process comes from fluidized autolith breccias (Fig.5a), which clearly demonstrate that a CO₂-rich liquid/fluid was expelled from aillikite magma.

Our stable isotope results are consistent with a fractionation relationship between aillikite and carbonatite. Groundmass carbonate from type aillikite is isotopically the most “primitive” straddling the compositional fields for primary mantle-derived carbonatite (Taylor, H.P. *et al.*, 1967; Clarke *et al.*, 1994) in a conventional $\delta^{13}\text{C}_{\text{PDB}}-\delta^{18}\text{O}_{\text{SMOW}}$ diagram (Fig.18). The carbonatites contain isotopically heavier carbon than the aillikites with an increase in $\delta^{13}\text{C}$ from aillikite through dolomite-calcite carbonatite to dolomite carbonatite in the order of $\sim 3\%$, so that they fall outside the fields for primary carbonatite. Post-magmatic processes have been shown to have only little effect on the C isotopic composition but may produce major changes in O isotopes (Deines, 1989; Santos & Clayton, 1995), which is not seen in the Aillik Bay samples.

The identical “mantle-like” Sr-Nd isotope composition of aillikites and carbonatites (Fig.17) indicate that their distinct carbon isotope composition (Fig.18) does not reflect derivation from different sources, and also that hydrothermal alteration did not play a major role, as most of the Sr resides in the carbonates. We conclude that Rayleigh fractionation of a common parent magma best explains the strong ^{13}C enrichment seen from aillikites towards dolomitic carbonatites. This may be caused by release of a CO_2 -rich liquid (enriched in ^{13}C ; Deines, 1989) by diffusive separation from carbonate-rich aillikite magma as a result of decompression. This liquid/fluid moved ahead of the crystal- and inclusion-laden aillikite magma and opened cracks for UML dyke emplacement. It eventually crystallized to form ^{13}C -enriched dolomite-calcite carbonatite and rare dolomite carbonatite preferentially at UML dyke terminations. Co-precipitation of calcite and dolomite has been experimentally demonstrated to occur from 880°C down to 650°C at 0.2 GPa in the $\text{CMS-CO}_2\text{-H}_2\text{O}$ system (Otto & Wyllie, 1993) with an expanded dolomite stability field toward the low temperature end. Changes in oxygen isotope ratios are governed by a number of other components such as H_2O , silicate and oxide phases in addition to CO_2 which may counterbalance each other (Deines, 1970).

Quantifying this Rayleigh fractionation process, a typical aillikite sample would have to release more than 90 vol.% of its carbonate fraction to cause an increase in $\delta^{13}\text{C}$ by more than 1‰ approaching observed values for the carbonatites. This rather large amount of expelled CO_2 -rich liquid would leave a residual magma (carrying early olivine and phlogopite phenocrysts) that on further cooling crystallizes a groundmass assemblage compositionally distinct from that of carbonate-rich aillikite, but resembling mela-aillikite (Fig.5b;c), which

contains abundant clinopyroxene, biotite, Mg- and Mn-depleted spinels/ilmenites (Fig.8a; 9a; 10a) but less than 10 vol.% carbonate. This model is consistent with the occurrence of composite aillikite/carbonatite and aillikite/mela-aillikite dykes, further implying that this fractionation process operated at shallow intrusion levels.

9.1.3. A role for liquid immiscibility in the genesis of damtjernites?

Fractional crystallization and partial melting cannot relate the distinct mineral assemblage and chemical composition of contemporaneous and isotopically identical aillikites and damtjernites, leading us to invoke an unmixing process. Although immiscible silicate-carbonate liquids are reported from natural mantle-derived xenoliths (Amundsen, 1987; Kogarko *et al.*, 1995; Chalot-Prat & Arnold, 1999; van Achtebergh *et al.*, 2004), they have been experimentally produced predominantly at crustal pressures (Freestone & Hamilton, 1980; Kjarsgaard & Hamilton, 1989; Kjarsgaard *et al.*, 1989; Lee & Wyllie, 1997a; Lee & Wyllie, 1997b). One of the major findings of these experiments was that primitive CO₂-bearing mantle-derived alkaline magmas do not intersect the miscibility gap and that only their evolved derivatives approach the silicate limb of the solvus. However, immiscible carbonate-silicate liquids were found in high pressure run products (3 GPa) from melting experiments on primitive olivine melilitite (Brey & Green, 1976).

Aillikite and damtjernite are unlikely to represent conjugate liquids given their rather small compositional differences (Fig.13), which would require a very small miscibility gap. It is more reasonable to consider an intermediate role for aillikite magma as the carbonated silicate parent that underwent immiscibility, but aillikite compositions do not fall in any published experimentally determined silicate-carbonate miscibility gap (Fig.20a), which mainly deal with nephelinitic systems (e.g. Lee & Wyllie, 1997a).

However, fairly large immiscibility gaps have been found in a CO₂-saturated SNAC-CO₂ system between ~ 1225-1325°C at 1.5 to 2.5 GPa (Fig.20a; Brooker & Kjarsgaard, in prep.; Brooker, 1998). Although damtjernites fall along the 1275°C/1.5 GPa immiscibility solvus, aillikite compositions are too alkali-poor to enter the miscibility gap. However, it is reasonable to assume that aillikites found at the surface have lost alkalis; their high pressure equivalents may lie in the miscibility gap (Fig.20a). The glimmerite nodules, which are present in every aillikite dyke examined, may provide a link to a more alkaline proto-aillikite magma which was able to exsolve a damtjernite liquid and a conjugate calciocarbonatite

liquid. Sövitic carbonatites are not seen at the coastal exposures around Aillik Bay, probably due to the fact that access to the radial dyke swarm is limited to its southern periphery and the centre of a hypothetical complex is covered by the sea (Fig.2). Examples for UML – carbonatite complexes with such a central sövitic core are the Fen (Andersen, T., 1988; Andersen, T. & Austrheim, 1991; Dahlgren, 1994) and Alnö complexes (Kresten, 1980; Vuorinen & Skelton, 2004) in Scandinavia, and the Callander complex in Ontario (Ferguson & Currie, 1971), which are of similar Late Neoproterozoic age as the Aillik Bay UML suite.

Proto-aillikite magma may have started to line the conduits with glimmerite material causing a loss of alkalis, Si, Al and Mg thereby lowering the Mg/Ca but elevating the Si/Al ratios of the melt (Fig.19b; 20a). These subtle but critical compositional modifications (see Lee & Wyllie, 1997a) may have prevented the derivative magma from approaching the miscibility gap (Fig.20a), enabling its direct ascent to the surface as glimmerite-laden aillikite. This explains the absence of glimmerite inclusions in damtjernite, which formed below the unmixing level (Fig.21). Furthermore, it explains similar core compositions of phlogopite phenocrysts in aillikite and damtjernite as being derived from a common magma, but later following contrasting evolutionary paths (Fig.8a;b). That the immiscible damtjernite separation from proto-aillikite magma occurred when the latter was already slightly evolved is further indicated by the lower forsterite content of “early” olivines in damtjernites (< Fo86) than in aillikites (Fo91). The damtjernite olivine compositions match the Mg# of olivines in cumulate olivine-phlogopite nodules recovered from aillikites (Fig.7).

Trace element modelling is also consistent with the proposed relation between damtjernite and aillikite by liquid immiscibility. Using partitioning data from Hamilton, D.L. *et al.* (1989); Jones *et al.* (1995); Veksler *et al.* (1998), which were determined for nephelinitic systems at pressures of up to 1 GPa but should be applicable for more potassic systems, we have calculated the budget of crucial trace elements for a hypothetical carbonatite magma conjugate to damtjernite (Fig.20b). These trace element distribution patterns resemble those of immiscible carbonatites, i.e. Oldoinyo Lengai (Bizimis *et al.*, 2003), and the trace element abundances of aillikites are indeed transitional between the damtjernite and carbonatite conjugate pairs. This demonstrates that a proto-aillikite magma could have been the parental liquid to damtjernite and that trace element partitioning between immiscible carbonate-silicate liquids can fully account for the observed differences in the LILE, HFSE and HREE budget of rock types (Fig.16b;20b). Note that the immiscibility process outlined here is not that

described by Foley (1984), which is a later unrelated process occurring within some damtjernites.

Ferguson & Currie (1971) interpreted lamprophyric intrusives from the ~ 560-580 m.y. old Callander carbonatite complex of the St. Lawrence Valley Rift system in Ontario as the chilled remains of two immiscible liquids, as we suggest for some of the Aillik Bay area damtjernites. This implies that low-pressure processes during alkaline igneous activity operated on a regional scale along the rifted Laurentian margin.

9.1.4. Petrogenetic significance of cognate inclusions in aillikites

The mineralogy of clinopyroxene-phlogopite and olivine-phlogopite inclusions in aillikites resembles both aillikites (e.g. Mg-ilmenite, Cr-spinel) and damtjernites (e.g. Ti-Al-rich clinopyroxene, titanite) but also shows individual peculiarities (e.g. high Mn-olivine, zirconolite). These inclusions may be genetically related, representing different components in a continuum of compositions. The constituent minerals seem to have been crystallized from a highly alkaline carbonated silicate melt (isotopically similar to aillikite and damtjernite) at uppermost mantle to lower crustal depths (25-45 km). The presence of a CO₂-rich phase is witnessed by the common olivine replacement by carbonate. A cumulate origin is also indicated by the banded structure of larger nodules. It is likely that this material lines the conduits of the alkaline intrusions beneath Aillik Bay (Fig.21) and was disrupted by later batches of carbonate-rich aillikite magma. The parental magma to these nodules presumably never reached the surface but clearly shows UML affinity. This multi-stage model, which is broadly similar to the suggested origin for phlogopite clinopyroxenite nodules from high-K lavas of western Italy (Giannetti & Luhr, 1990), is consistent with the 35 m.y. time span (~ 590-555 Ma) of Aillik Bay area UML magmatism.

Glimmerites are probably the product of a similar wall-rock coating process, but there are strong indications that they are genetically related to carbonate-rich proto-aillikite. While clinopyroxene-phlogopite and olivine-phlogopite nodules are in equilibrium with their host aillikite magma and with damtjernites regarding volatile fugacities (see also similar mica compositions; Fig.8), the distinctively higher relative HF-fugacity of phlogopite-apatite pairs in glimmerites indicates disequilibrium with the host aillikite (Fig.12). This difference in HF-fugacity, combined with the observation that glimmerite phlogopite coexists with pure orthoclase suggests that glimmerites crystallized in CO₂-rich, but H₂O-poor conditions.

9.2. Mantle source characteristics and melting processes

9.2.1. Identification of the parental UML magma

Amongst the UML rock types from Aillik Bay, aillikite is considered to be closest to a primary magma composition. In contrast, damtjernites have many non-primary features, so we do not consider them during subsequent discussions on mantle processes. Aillikite is the only rock type carrying cm-sized cognate inclusions (Fig.4e) testifying to rapid magma ascent although mantle peridotite xenoliths have not been found yet. This is surprising in view of the occurrence of abundant garnet- and spinel-facies peridotites in their western Greenland analogues (Scott, 1981; Larsen & Rønsbo, 1993; Bizzarro & Stevenson, 2003). However, this may be merely a function of exposed intrusion level and/or lower viscosity of the very carbonate-rich aillikite magma from the type locality.

Compositional modification by crystallization of glimmerite at deep crustal or upper mantle levels caused insignificant deviations from primary compositions (Fig.19b). Recalculation of aillikite sample ST164 for a loss of up to 10 wt.% glimmerite material (95/5 phlogopite/apatite) would lower SiO₂ (1.5 wt.%), K₂O (0.8), Al₂O₃ (0.5) and MgO (0.5) but elevate CaO (1.5) and FeO (0.6) relative to the hypothetical proto-aillikite magma.

9.2.2. Constraints on the mineralogy and location of the source region

The high MgO and CO₂ content as well as the potassic nature of aillikite has to be explained in terms of partial melting of a carbonate-rich peridotitic source with essential contribution from a K-bearing phase. Partial melting can be expected to have occurred under pressures greater than 5 GPa, presumably not much greater than 6 GPa, as indicated by the rare occurrence of diamonds in aillikites from the North Atlantic region (Mitchell *et al.*, 1999; Digonnet *et al.*, 2000). High pressure melting experiments by Dalton & Presnall (1998) and Gudfinnsson & Presnall (2005), conducted on synthetic carbonated peridotite material (CMAS-CO₂ system), are the only studies available which may be applicable to the genesis of aillikite. Indeed, these authors have produced near-solidus carbonate-rich liquids between 3-8 GPa which bear resemblance to natural primary carbonatites, and carbonate-rich ultramafic magmas such as aillikite and kimberlite at slightly higher degrees of melting. The most primitive aillikites from Aillik Bay resemble those melts which segregated significantly above the carbonate-bearing solidus close to 5 GPa in the Gudfinnsson & Presnall (2005) experiments (Fig.19). However, it must be stressed that the co-occurrence of aillikite and

carbonatite at Aillik Bay cannot be interpreted in terms of a melting continuum, but that they are related by a low-pressure fractionation process (Fig.19).

The high MgO and Ni content of aillikite requires a major contribution from an olivine-rich peridotitic mantle. Furthermore, the strong LREE/HREE fractionation of aillikites can only be explained in terms of melting in the presence of residual garnet. The abundant carbonate in aillikite is isotopically consistent with mantle derivation ($\delta^{13}\text{C} \sim -5$, Deines, 2002) and bulk rock CO_2 correlates positively with CaO but not with MgO (Fig.15c), an observation also made for many kimberlites (Bailey, 1984). This implies that the mantle carbonate that contributed to aillikite magma was calcite rather than dolomite or magnesite, although melting in excess of 5 GPa must have occurred in the magnesite stability field (Brey *et al.*, 1983). Given that the most primitive aillikites have MgO/CaO ratios between 1-1.3 (Fig.19b), much lower than in experimentally produced near-solidus melts of magnesite-bearing peridotite (up to 25; Brey *et al.*, 1983), calcite is considered the most likely source of the carbonate and therefore must have been part of a non-peridotitic vein assemblage.

Aillikite magma clearly segregated from a mantle source that contained an early melting hydrous K-bearing phase. Phlogopite and K-richterite are known from metasomatized mantle assemblages (Dawson & Smith, 1977; Waters, 1987; Ionov & Hofmann, 1995; Grégoire *et al.*, 2002, 2003), both being stable to pressures far above 6 GPa (Sudo & Tatsumi, 1990; Foley, 1991; Konzett *et al.*, 1997; Konzett & Ulmer, 1999). Phlogopite is considered the most likely K-bearing phase in the melting assemblage because of its potential to produce silica-undersaturated melts with extremely high K/Na ratios. In contrast, K-richterite was demonstrated to melt out close to the solidus of ultramafic assemblages yielding SiO_2 -rich melt compositions which are more akin to lamproites (Foley *et al.*, 1999). The impact of residual source phlogopite on the incompatible element patterns of aillikites (Fig.16a) is clearly seen at the pronounced troughs at K and Rb but the relative Cs-enrichment owing to a D_{Rb} (5.2) which is an order of magnitude higher than D_{Cs} (0.6; Foley *et al.*, 1996). Ba is strongly scattered and less meaningful for evaluating the role of phlogopite in the presence of mantle carbonate. Because K is a stoichiometric component in phlogopite, its content in the melt will be near-constant as long as phlogopite is residual, varying only as a function of the proportion to which phlogopite enters the melt. The K content of a melt in equilibrium with mantle phlogopite which melts to an extent of ~ 20 -50 % (Greenough, 1988) is ~ 1.6 -5 wt.%. The average K-content of aillikite (1.8 ± 0.3 wt.%) is at the lower end of this range, which is

consistent with lower K-saturation levels in undersaturated melts produced under CO₂-rich conditions (Rogers *et al.*, 1992). Alternatively, it may relate to our earlier proposition that proto-aillikite might have lost up to 1 wt.% K₂O by wall-rock coating with glimmerite material.

Apatite seems to be an essential constituent of the source region given the high P₂O₅ concentrations in aillikite (2.2 ± 0.7 wt.%; Fig.13). The imprint of residual apatite on the incompatible element patterns may be seen at the Sr-P trough and probably at the U-spike (Fig.16a) given its potential for fractionating Th ($D_{Th} \sim 17$) from U ($D_U \sim 1.7$; Luhr *et al.*, 1984).

Although the comparably high TiO₂ (3.4 ± 0.5 wt.%) concentrations of aillikite can be explained by melting Ti-rich phlogopite, it is more likely that a Ti-rich oxide phase controlled the HFSE budget during melting given the extremely high Nb-Ta abundances (181 ± 28 ppm Nb). Interestingly, the relative Zr-Hf depletion in aillikites is decoupled from Ti and Nb-Ta (Fig.16a) and therefore unlikely to be the effect of a residual titanate. It can be inferred from our data that the relatively low but variable Zr-Hf concentrations in aillikite are not inherited from the mantle source carbonate, which is typically depleted in Zr and Hf (Ionov, 1998; Moine *et al.*, 2004), since there is no negative correlation between absolute Zr-Hf abundances and aillikite/carbonatite CO₂ content (Fig.15b). A residual Ti-free oxide phase such as baddeleyite, which was found as mantle xenocrysts in the Ile Bizard alnöite (Heaman & LeCheminant, 2001) and has been synthesised as part of a carbonate-bearing metasomatic vein assemblage under upper mantle conditions by Meen *et al.* (1989), can account for the observed Zr-Hf troughs in the aillikite trace element spectra (Fig.16a).

An important constraint on the location of the mantle source region comes from the thermal stability of the required source mineralogy. We have pointed out that phlogopite and carbonate are essential in the melting assemblage and both phases are not stable at the temperatures of convecting upper mantle or upwelling thermal plumes from the deep mantle ($\sim 1480^\circ\text{C}$; McKenzie & Bickle, 1988). They are stable at P-T conditions of the cold mantle lithosphere (Wendlandt & Egger, 1980; Mengel & Green, 1989; Sweeney *et al.*, 1993; Dalton & Wood, 1995; Ulmer & Sweeney, 2002) and this restricts aillikite generation to lithospheric portions of the cratonic mantle. It does not, however, rule out a contribution from the convecting asthenospheric upper mantle, i.e. as metasomatizing agents (Fig.21). We

favour a veined lithospheric mantle source over pervasively metasomatized peridotite for the genesis of aillikite since it can account for the occurrence of minerals that are not in equilibrium with peridotite.

9.2.3. Isotopic constraints on the age and style of mantle metasomatism

The Nd isotope composition of aillikites, close to present-day Bulk Earth (Fig.17), does not advocate a long-term enrichment of the UML mantle source in incompatible trace elements. On the contrary, it indicates that LREE enrichment must have occurred shortly prior to melting without subsequent aging to produce negative ϵ_{Nd} values. Assuming that the parent/daughter ratios of the Sm/Nd isotope system were not disturbed during the 555-590 Ma melting episode, the Sm-Nd isotope systematics give Nd extraction ages from a depleted mantle reservoir of 1.0-1.1 Ga. Although such model ages have to be interpreted with care, it seems likely that the enrichment event did not precede UML magmatism by more than ~ 400 m.y., which is roughly 300 m.y. after the Mesoproterozoic lamproite magmatism had occurred in this region (Tappe *et al.*, in prep.).

The Sr-Nd data from Aillik Bay UML samples define a horizontal array (Fig.17), which may be explained by enhanced radiogenic Sr in-growth in the source region due to extremely high Rb/Sr ratios of phlogopite concentrated in veins, whereas there is no phase present which could cause such a rapid change of the Nd isotope composition. If representative Rb and Sr concentrations for mantle phlogopites (45-300 and 14-175 ppm, respectively; Grégoire *et al.*, 2003) are considered, then only ~50-200 m.y. would be needed to alter an initial asthenospheric $^{87}Sr/^{86}Sr$ ratio of 0.7029 (Zindler & Hart, 1986) to the maximum values measured for the Aillik Bay UML (0.7066). Such a “phlogopite signature” can therefore be produced within only a few tens of m.y. prior to magmatism and is reported from other UML and olivine melilitite occurrences (Rogers *et al.*, 1992; Andronikov & Foley, 2001; Riley *et al.*, 2003). The fact that carbonatites follow the Nd-Hf mantle array led Bizimis *et al.* (2003) to conclude that their carbonated mantle source regions underwent rapid re-melting given the potential of mantle carbonate to produce radiogenic Hf while leaving Nd isotopes unaffected. Taken together, this reinforces our argument that the metasomatic carbonate-phlogopite assemblage that gave rise to the production of Late Neoproterozoic UML magmas was short-lived and presumably formed a vein network at the base of the cratonic lithosphere (Fig.21).

It is interesting to note that type aillikite is not as HREE-depleted as kimberlites and lamproites (Fig.16a), which all form as small-degree partial melts at pressures within the garnet stability field, most likely from veined mantle sources (Mitchell & Bergman, 1991; Foley, 1992b, 1993; Mitchell, 1995). This might indicate that the peridotitic part of the UML mantle source region beneath Aillik Bay did not undergo extensive depletion prior to carbonate metasomatism, as required for the strong HREE depletion of kimberlites (Tainton & McKenzie, 1994). This assumption is supported by the only moderately high forsterite component in aillikite olivine phenocrysts ($< \text{Fo}_{91}$; Fig.7) and by their Al-rich spinel inclusions ($< \text{Cr}\#85$), which are indicative of a relatively fertile peridotitic mantle component (Arai, 1994; Barnes & Roeder, 2001).

10. PETROGENESIS OF PARENTAL AILLIK BAY UML MAGMA AS PART OF THE NORTH ATLANTIC ALKALINE PROVINCE

A number of rifting episodes affected the cratonic North Atlantic region during Middle to Late Proterozoic times and eventually led to the opening of the Iapetus Ocean and the breakup of the supercontinent Rodinia. Associated alkaline and carbonatitic igneous activity occurred from the St. Lawrence Valley Rift system (Gittins *et al.*, 1967; Doig & Barton, 1968; Ferguson & Currie, 1971; Gittins *et al.*, 1975) to the Scandinavian Peninsula (Griffin & Taylor, 1975; Kresten, 1980; Brueckner & Rex, 1980; Dahlgren, 1994; Meert *et al.*, 1998) with the Aillik Bay UML suite forming an integral part of this North Atlantic alkaline province (Doig, 1970). Deep melting events at around 1400-1200 Ma produced lamproites, and can be placed within intact long-term enriched subcontinental lithospheric mantle (strongly negative ϵ_{Nd} and highly unradiogenic Pb; Tappe *et al.*, in prep.; Nelson, 1989), whereas the widespread Late Neoproterozoic UML magmas (~ 600 -550 Ma), such as those from Aillik Bay, show an imprint from juvenile asthenosphere-derived enriched material (positive ϵ_{Nd} coupled to incompatible trace element enrichment). This indicates that progressive continental stretching resulted in lithospheric thinning with the protrusion of hotter asthenosphere to shallow levels beneath the large rift zone (Fig.21). Due to this rift-related heating, the cratonic geotherm was displaced to higher temperatures more typical of that of rift margins (Thompson & Gibson, 1994). Additionally, a depression of the former lithosphere solidus by oxidation and volatile fluxing (Foley, 1988; Taylor, W.R. & Green, 1988) within the rifted mantle triggered small-degree melting under CO_2 -bearing conditions. The depth interval of initial melting in the asthenosphere is considered to have been slightly

in excess of 5 GPa given the presence of diamonds in the overlying cratonic lithosphere. The small melt fraction produced had carbonatite-like characteristics (Wyllie, 1980; Green & Wallace, 1988; Dalton & Presnall, 1998) and during ascent quickly encountered the cold base of the cratonic lithosphere where they solidified due to their low heat capacity (Spera, 1984, 1987; McKenzie, 1989; Meen *et al.*, 1989) producing carbonate-phlogopite dominated veins with minor apatite and oxide phases such as rutile, ilmenite and baddeleyite. Such veining is to be expected at the transition from the porous to a channelized flow regime, which may roughly coincide with the asthenosphere-lithosphere boundary (McKenzie, 1985; Foley, 1988, 1992a). Continued lithospheric extension further moved the asthenosphere-lithosphere boundary upwards and outwards (indicated as steps 1-2-3 in Fig.21) so that a newly adjusted geotherm enabled re-melting of the vein assemblage, a mechanism outlined in detail by Foley (1992a). The resulting potassic-carbonate melts infiltrated into and interacted with the partially molten garnet peridotite wall-rock eventually erupting as carbonate-rich UML. While high incompatible trace element contents and in turn Sr-Nd isotope compositions of aillikites are dominated by the vein melt, the high MgO and compatible trace element concentrations are controlled by extensive volatile-fluxed melting in the surrounding peridotite.

Diversification of the proto-aillikite parental magma by low-pressure processes such as liquid immiscibility and devolatilization at uppermost mantle to crustal depth led to the variety of carbonatite and UML types seen at the surface (Fig.21). In general, the production of less carbonate-rich primitive UML such as alnöite in other areas may be merely a function of the vein to wall-rock proportions during melting (Foley *et al.*, 2002) and/or of heteromorphic low-pressure reactions (Rock, 1991). A multi-stage veined mantle melting model for UML magma production beneath a progressively rifted cratonic area (Fig.21) not only accounts for the chemical and isotopic composition of aillikites, but also explains the relatively large magma volumes (larger than in most kimberlite provinces; see Tappe *et al.*, 2004) and the long time span of UML magmatism in the Aillik Bay area (~ 35 m.y.). This also applies to other Neoproterozoic UML localities on both sides of the Labrador Sea, and throughout the North Atlantic alkaline province (~ 60 m.y.).

11. CONCLUSIONS

Ultramafic lamprophyre and carbonatite dykes from the Aillik Bay area range in age between ~ 590-555 Ma, and represent the oldest record of deep-seated alkaline rift-related magmatism in the southern part of the Labrador Sea area. The UML suite forms part of alkaline carbonatitic igneous activity which occurred throughout the North Atlantic region in response to extensional tectonics linked to the breakup of the Neoproterozoic supercontinent Rodinia.

The wide variety of rock types can be related to a single parental magma given their overlapping Sr and Nd isotope composition. We consider a carbonate-rich proto-aillikite magma as the most likely candidate for this primary liquid and its generation requires a garnet peridotite source region veined with carbonate-phlogopite rich assemblages. The metasomatic volatile-rich phases were out of equilibrium with the surrounding peridotite and therefore must be concentrated in veins, which most likely formed at the base of the cratonic lithosphere. A rifting cratonic area in which ancient cold lithosphere is successively replaced by upwelling hotter asthenosphere-derived material is an ideal setting for recurrent mantle veining and its subsequent re-melting at high pressure during rift propagation, a geodynamic scenario which is fundamentally different from typically short-lived kimberlite volcanism in the interior of stable cratons. An extensive vein-plus-wall-rock melting mechanism best accounts for the strong incompatible trace element enrichment but time-integrated isotopic depletion (asthenosphere-derived vein material) combined with high MgO content and HREE depletion (lithospheric wall-rock garnet peridotite) of the proto-aillikite magma.

Various low-pressure processes led to the diversification of proto-aillikite magma with aillikites being least modified. They have experienced only minor alkali loss due to coating of conduits with glimmerite material which enabled rapid ascent through the uppermost mantle and crust. Devolatilization processes in response to decompression close to the surface gave rise to separation and fractionation of dolomite-bearing carbonatite leaving a residual melanaillikite liquid. Where alkali-loss by glimmerite precipitation did not occur, proto-aillikite magma was prone to silicate-carbonate liquid immiscibility and exsolved a damtjernite liquid. The conjugate immiscible carbonatite liquid was not found in the Aillik Bay area but may form a central complex currently covered by the sea as indicated by the convergence of the satellite UML dykes. Abundant clinopyroxene- and/or olivine-bearing micaceous inclusions sampled by aillikites are interpreted as low-pressure cumulates from blind UML injections

given their similar age (~ 573 Ma), Sr-Nd isotope composition and mineral compositional trends.

ACKNOWLEDGMENTS

We are indebted to Bruce Ryan and Dejan Prelevic for helpful discussions that ensued during this study. Randy Edmunds, Lori Dyson and Mike Bishop are thanked for logistical support in the wilderness of Labrador; and Ralf Tappert and Michel Gorniak for their hospitality in Edmonton. Stacey Hagen, Judie Schulz, Kendra Siemens and Nancy Joyce ably assisted the geochronology work. Burkhard Schulz-Dobrick is thanked for keeping the electron microprobe facility in Mainz in excellent running condition. Comments by Roger Mitchell, Lotte Larsen, Teal Riley and Marjorie Wilson on an early version of this manuscript are gratefully acknowledged. This project is funded by the German Research Foundation (DFG grant Fo181/15) and a NSERC operating grant to GAJ and LMH. This publication is Geological Survey of Canada contribution #2005-xxx.

APPENDIX A - ANALYTICAL TECHNIQUES

U-Pb perovskite geochronology

Nine ultramafic lamprophyre hand specimens were processed through standard crushing and mineral separation procedures (Wilfley Table, Methylene Iodide, Frantz Isodynamic separator) at the University of Alberta (Canada) following the techniques described in Heaman & Kjarsgaard (2000). Perovskite recovery was best in the 40-120 μm range. Fresh euhedral crystals devoid of inclusions were individually selected, collected as morphologic fractions and dissolved as such in a mix of HF and HNO₃ (usually more than 100 grains per fraction to obtain > 50 μg perovskite). Uranium and lead were isolated and concentrated from perovskite using the HBr anion exchange chromatography technique outlined in Heaman & Machado (1992). The isotopic composition of these elements was measured on a VG354 thermal ionization mass spectrometer operating in single Faraday or analogue Daly mode.

All isotopic data reported in Table 1 were corrected for mass discrimination (+0.09%/amu Pb and +0.16%/amu U), tracer and blank contribution; uncertainties are reported at 1σ . Furthermore, a correction for the presence of initial common lead was applied to the $^{206}\text{Pb}/^{238}\text{U}$ ratios using the crustal evolution model of Stacey & Kramers (1975). The

$^{206}\text{Pb}/^{238}\text{U}$ perovskite ages were shown to be most robust because they are least sensitive to initial common lead corrections (Heaman, 1989; Heaman & Kjarsgaard, 2000). All perovskite analyses are concordant and thus allow for the calculation of multi-fraction ages using a weighted mean approach (Ludwig, 1998).

Ar-Ar mica thermochronology

The clinopyroxene-phlogopite nodule ST162I was processed for $^{40}\text{Ar}/^{39}\text{Ar}$ analysis of phlogopite plates by standard mineral separation techniques, including hand-picking of inclusion-free unaltered crystals in the size range 0.5 to 1 mm. The phlogopite crystals were loaded into an aluminum foil packet and arranged radially in an aluminum canister (40×19 mm), which contained the flux monitor PP-20 hornblende (Hb3gr equivalent) with an apparent age of 1072 Ma (Roddick, 1983). The canister was irradiated for 120 hours in position 5c at the research reactor of McMaster University (Hamilton, Ontario) in a fast neutron flux (3×10^{16} neutrons/cm²).

Laser $^{40}\text{Ar}/^{39}\text{Ar}$ step-heating analysis of the irradiated sample was carried out at the Geological Survey of Canada in Ottawa. The sample was loaded into a 1.5 mm diameter hole in a copper planchet and stepwise heated under vacuum using a Merchantek MIR10 10W CO₂ laser equipped with a 2 x 2 mm flat-field lens. The released Ar gas was cleaned over getters for ten minutes before isotope analysis using a VG3600 gas source mass spectrometer. Details of data collection protocols can be found in Villeneuve *et al.* (2000). Error calculation on individual steps follows numerical error analysis routines outlined in Scaillet (2000), whereas error analysis on grouped data follows algebraic methods of Renne *et al.* (1998). Neutron flux gradients were evaluated by analyzing the PP-20 flux monitors, which were interspersed among the sample packets throughout the sample canister, and by interpolating a linear fit against calculated J-factor and sample position. The error on the J-factor value reported in Table 2 is conservatively estimated at $\pm 0.6\%$ (2σ).

Blanks were measured prior to and after the sample analysis and levels varied between $^{40}\text{Ar} = 1.4\text{-}1.5 \times 10^{-6}$ nm, $^{39}\text{Ar} = 1.2\text{-}1.4 \times 10^{-9}$ nm, $^{38}\text{Ar} = 0.7\text{-}1.2 \times 10^{-9}$ nm, $^{37}\text{Ar} = 0.4\text{-}0.5 \times 10^{-9}$ nm, $^{36}\text{Ar} = 4.6\text{-}5.7 \times 10^{-9}$ nm, all at $\pm 20\%$ uncertainty. Nucleogenic interference corrections are $(^{40}\text{Ar}/^{39}\text{Ar})_{\text{K}} = 0.025 \pm 0.005$, $(^{38}\text{Ar}/^{39}\text{Ar})_{\text{K}} = 0.011 \pm 0.010$, $(^{40}\text{Ar}/^{37}\text{Ar})_{\text{Ca}} = 0.002 \pm 0.002$,

$(^{39}\text{Ar}/^{37}\text{Ar})_{\text{Ca}} = 0.00068 \pm 0.00004$, $(^{38}\text{Ar}/^{37}\text{Ar})_{\text{Ca}} = 0.00003 \pm 0.00003$, $(^{36}\text{Ar}/^{37}\text{Ar})_{\text{Ca}} = 0.00028 \pm 0.00016$. All errors are quoted at the 2σ level of uncertainty.

Mineral chemistry

Mineral chemistry data were obtained using a JEOL JXA 8900 RL electron microprobe at Mainz University, Germany. Operating voltage for most silicates and carbonates was 15 kV with a beam current of 12 nA and 8 nA, respectively. Opaque oxides, perovskite, rutile, titanite and garnet were analysed with an accelerating voltage of 20 kV and a beam current of 20 nA. The beam diameter varied between 1 and 10 μm depending on the volatile abundance in the mineral of interest. Counting time for common silicates was between 15 and 20 seconds on the peak, whereas trace element rich accessories were measured for up to 50 seconds on the peak. International standards of natural materials were used for calibration and all data were reduced with a CITZAF procedure, except for the carbonates where a ZAF correction was applied.

The JEOL JXA 8900 RL microprobe at Göttingen University (Germany) was used for high-precision halogen determination in apatite-phlogopite pairs in order to calculate an equilibrium fluorine distribution. Fluorine was calibrated against a natural topaz standard under 15 kV and 15 nA operating conditions with a 10 μm beam spot. Hexagonal apatite cross-sections perpendicular to the crystallographic c-axis were avoided because of the variation of F and Cl X-ray intensity due to anisotropic diffusion preferably along this crystallographic direction (Stormer *et al.*, 1993).

Whole rock geochemistry

Major and selected trace elements were measured on fused discs by standard X-ray fluorescence (XRF) spectrometry at the University of Greifswald. A wide range of trace elements and REE were analysed by a combination of ICP-AES and ICP-MS after a fusion digestion and acid dissolution procedure, respectively (Activation Laboratories, Ancaster/Canada). Concentrations for elements determined by both the ICP-MS and XRF technique compare within analytical error (e.g. Sr, Ce, Y, Zr, U, Th, Pb). Volatiles were measured by a combination of loss on ignition and direct determination of CO_2 using a C-S analyser.

Sr-Nd isotope composition

Sr-Nd isotope compositions were determined on the same powders as major and trace element contents. We selected a Savillex beaker dissolution after tests on a variety of rock types dissolved by both Teflon bomb and beaker technique had confirmed that the isotope composition was identical within analytical error. The bomb dissolution was carried out in microcapsules which were placed together in an external Teflon pressure vessel heated in an oven at 160°C for 7 days. Powders dissolved in Savillex beakers were attacked in a HF/HNO₃ mixture on a hot plate for 3 days. After slow evaporation to near dryness, the samples were taken up in 6 N HCl and heated again for 1 day repeating this step up to three times until a clear solution was obtained. Sr and Nd were separated and concentrated using Biorad AG50W cation and Eichrom Ln-Spec anion exchange resin, respectively. Sr and Nd isotope compositions were measured on a VG 54-30 Sector (Ta single filaments) and Finnigan MAT 262 (Re double filaments) thermal ionization mass spectrometer, respectively, both operating in dynamic mode (GFZ Potsdam). During the measurement period, the NBS-987 Sr reference material yielded an average value for $^{87}\text{Sr}/^{86}\text{Sr}$ of 0.710265 ± 12 and the La Jolla standard yielded a $^{143}\text{Nd}/^{144}\text{Nd}$ value of 0.511850 ± 7 (2σ of 11 measurements). The initial isotopic composition was calculated for an intrusion age of 582 Ma (U-Pb perovskite age of damtjernite ST140A), using the decay constants $1.42 \cdot 10^{-11} \text{ y}^{-1}$ and $6.54 \cdot 10^{-12} \text{ y}^{-1}$ for ^{87}Rb and ^{147}Sm , respectively.

Oxygen and carbon isotope composition

The oxygen and carbon isotope composition of bulk rock carbonate fractions was measured at Göttingen University, Germany. Rock powders ($< 20 \mu\text{m}$) were reacted with anhydrous H₃PO₄ under vacuum at 25°C for ca. 24 h in order to liberate the CO₂ of the carbonates (McCrea, 1950). The volume of collected CO₂ gas was close to a 100 % of the theoretical yield so that no isotope fractionation during dissolution of dolomite- and calcite-bearing samples is expected to have occurred (Al-Aasm *et al.*, 1990). The purified CO₂ was analysed using a Finnigan MAT-251 gas source mass spectrometer and measured isotope ratios are expressed as $\delta^{13}\text{C}$ and $\delta^{18}\text{O}$ ‰ relative to PDB (Pee Dee Belemnite) and SMOW (Standard Mean Ocean Water), respectively. Reproducibility was better than 0.07 ‰ for $\delta^{13}\text{C}$ and 0.19 ‰ for $\delta^{18}\text{O}$ ‰ as determined by repeated measurements ($n=5$, 2σ) of an in-house limestone standard.

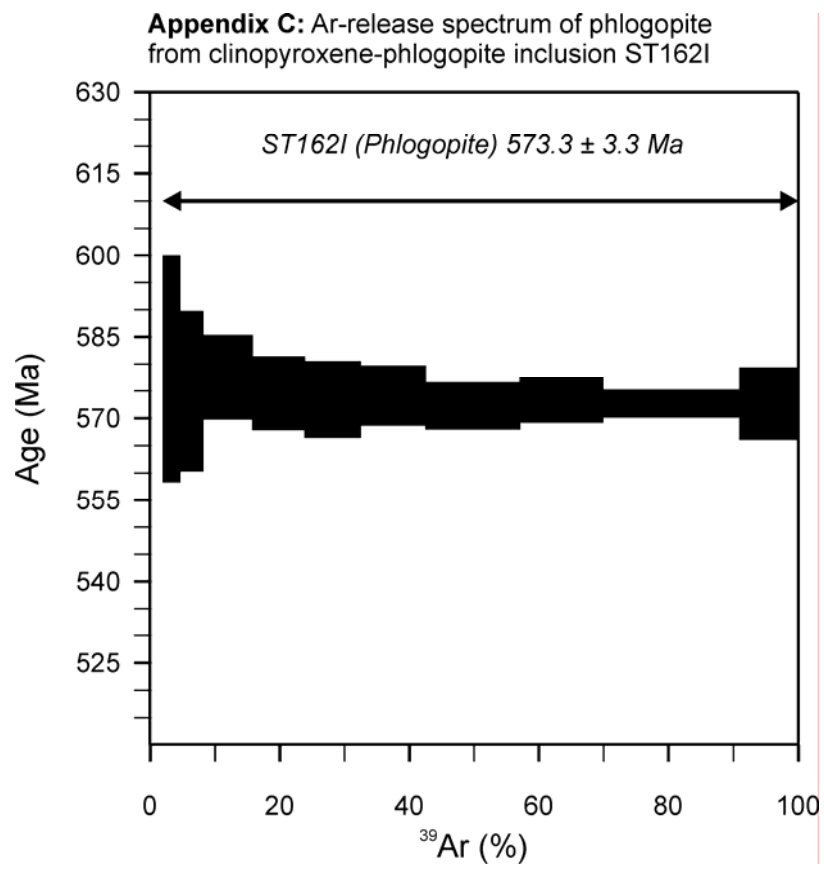
APPENDIX B – SAMPLE LIST

Appendix B: Sample list for Aillik Bay area UML and carbonatites

Sample#	rock type	*northing	*easting	location	
L2	aillikite	6122191	363469	Cape Makkovik Peninsula	Cape Makkovik
L6	aillikite	6120567	358945	Aillik Peninsula	E shore of Kaipokok Bay
L49	aillikite	6117054	357974	Aillik Peninsula	W shore of Aillik Bay
L51	aillikite	6118364	358562	Aillik Peninsula	W shore of Aillik Bay
L54	aillikite	6118210	359823	Cape Makkovik Peninsula	E shore of Aillik Bay
L60	aillikite	6122218	357310	Kranck Island	E shore of Kaipokok Bay
L61	aillikite	6131452	350216	Main Turnavik Island	northern shore
L62	aillikite	6123110	360251	Aillik Peninsula	Cape Aillik
L65	aillikite	6117091	357948	Aillik Peninsula	SW shore of Aillik Bay
L66	aillikite	6118427	358537	Aillik Peninsula	W shore of Aillik Bay
L72	aillikite	6119226	350955	Black Islands	northern island
L74	aillikite	6121921	361739	Cape Makkovik Peninsula	E shore of Aillik Bay
ST109	aillikite	6118344	359827	Cape Makkovik Peninsula	E shore of Aillik Bay
ST122	aillikite	6120567	358945	Aillik Peninsula	E shore of Kaipokok Bay
ST123	aillikite	6120662	358570	Aillik Peninsula	E shore of Kaipokok Bay
ST162	aillikite	6117091	357948	Aillik Peninsula	SW shore of Aillik Bay
ST164	aillikite	6117215	358419	Aillik Peninsula	SW shore of Aillik Bay
ST198A	aillikite	6125136	356717	Man Islands	southern island
ST220I	aillikite	6124202	349612	West Turnavik Island	western island
ST225	aillikite	6125429	350465	West Turnavik Island	main island
ST228	aillikite	6108886	362613	Ford's Peninsula	E shore of Makkovik Bay
ST250A/C	aillikite	6112669	369425	Cape Strawberry Peninsula	E shore of Makkovik Bay
ST114A	mela-aillikite	6120388	359369	Aillik Peninsula	W shore of Aillik Bay
ST147B	mela-aillikite	6120256	356729	Aillik Peninsula	E shore of Kaipokok Bay
ST196	mela-aillikite	6119731	351742	Black Islands	northern island
ST210	mela-aillikite	6128166	352171	Main Turnavik Island	southern shore
ST239A	mela-aillikite	6107253	360141	Perrets Point	E shore of Makkovik Bay
ST244B	mela-aillikite	6106492	362179	Ford's Peninsula	E shore of Makkovik Harbour
ST251B	mela-aillikite	6112987	369784	Cape Strawberry Peninsula	E shore of Makkovik Bay
L5	damtjernite	6128890	351810	Main Turnavik Island	southern shore
L7	damtjernite	6119970	361818	Cape Makkovik Peninsula	E shore of Aillik Bay
L44	damtjernite	6120101	361289	Cape Makkovik Peninsula	E shore of Aillik Bay
L45	damtjernite	6121468	361879	Cape Makkovik Peninsula	NE shore of Aillik Bay
L46	damtjernite	6122645	359406	Aillik Peninsula	Cape Aillik
L47	damtjernite	6116294	358092	Aillik Peninsula	S shore of Aillik Bay
L52	damtjernite	6119008	358674	Aillik Peninsula	W shore of Aillik Bay
L56	damtjernite	6121359	359395	Aillik Peninsula	W shore of Aillik Bay
L57	damtjernite	6121214	358972	Aillik Peninsula	W shore of Aillik Bay
L63	damtjernite	6123114	360251	Aillik Peninsula	Cape Aillik
L70	damtjernite	6121802	357601	Kranck Island	E shore of Kaipokok Bay
L76	damtjernite	6122397	362423	Cape Makkovik Peninsula	Cape Makkovik
L79	damtjernite	6122398	362424	Cape Makkovik Peninsula	Cape Makkovik
ST114B	damtjernite	6120388	359369	Aillik Peninsula	W shore of Aillik Bay
ST135	damtjernite	6120375	357559	Aillik Peninsula	E shore of Kaipokok Bay
ST140A	damtjernite	6120778	362055	Cape Makkovik Peninsula	NE shore of Aillik Bay
ST142	damtjernite	6121658	361764	Cape Makkovik Peninsula	NE shore of Aillik Bay
ST144	damtjernite	6120262	356870	Aillik Peninsula	E shore of Kaipokok Bay
ST159A	damtjernite	6117108	357764	Aillik Peninsula	SW shore of Aillik Bay
ST170	damtjernite	6124277	346865	Outside Pigeon Island	northern shore
ST174	damtjernite	6123724	346480	Outside Pigeon Island	southern shore
ST179A	damtjernite	6125780	354264	Grapnel Island	eastern shore
ST188A	damtjernite	6120846	352590	Red Islands	eastern island
ST198B	damtjernite	6125136	356717	Man Islands	southern island
ST205B	damtjernite	6124654	356897	Man Islands	southern island
ST206AI	damtjernite	6124728	357065	Man Islands	southern island
ST211A/C	damtjernite	6128219	352168	Main Turnavik Island	southern shore
ST213A	damtjernite	6129995	350069	Main Turnavik Island	southern shore
ST221II	damtjernite	6125820	351664	West Turnavik Island	main island
ST224B	damtjernite	6125106	350550	West Turnavik Island	main island
ST226	damtjernite	6126097	350956	West Turnavik Island	main island
ST230	damtjernite	6109765	363477	Ford's Peninsula	E shore of Makkovik Bay
ST246A	damtjernite	6112741	362755	Cape Makkovik Peninsula	W shore of Makkovik Bay
ST251A	damtjernite	6112987	369784	Cape Strawberry Peninsula	E shore of Makkovik Bay
ST256	damtjernite	6111995	367937	Cape Strawberry Peninsula	E shore of Makkovik Bay
L1	dol carbonatite	6121232	359678	Aillik Peninsula	W shore of Aillik Bay
ST189	dol carbonatite	6120833	352650	Red Islands	eastern island
ST203	dol carbonatite	6124730	356720	Man Islands	southern island
ST126	dol-cal carbonatite	6120646	358339	Aillik Peninsula	E shore of Kaipokok Bay
ST127	dol-cal carbonatite	6120638	358289	Aillik Peninsula	E shore of Kaipokok Bay
ST193A	dol-cal carbonatite	6119467	350946	Black Islands	northern island
ST198C	dol-cal carbonatite	6125136	356717	Man Islands	southern island
ST199	dol-cal carbonatite	6125192	356513	Man Islands	southern island
ST205AII	dol-cal carbonatite	6124654	356897	Man Islands	southern island
ST216	dol-cal carbonatite	6123843	343851	Inside Pigeon Island	eastern shore
ST231A	dol-cal carbonatite	6108158	359529	Big Island	eastern shore

*UTM coordinates (Zone 21U, NAD83)

APPENDIX C – GAS RELEASE SPECTRUM



REFERENCES

- Al-Aasm, I. S., Taylor, B. E. & South, B. (1990). Stable isotope analysis of multiple carbonate samples using selective acid extraction. *Chemical Geology* **80**, 119-125.
- Alibert, C. & Albarede, F. (1988). Relationships between mineralogical, chemical, and isotopic properties of some North American kimberlites. *Journal of Geophysical Research* **93**, 7643-7671.
- Amundsen, H. E. F. (1987). Evidence for liquid immiscibility in the upper mantle. *Nature* **327**, 692-695.
- Andersen, D. J., Lindsley, D. H. & Davidson, P. M. (1993). QUILF: a Pascal program to assess equilibria among Fe-Mg-Mn-Ti oxides, pyroxenes, olivine, and quartz. *Computers and Geosciences* **19**, 1333-1350.
- Andersen, T. (1988). Evolution of peralkaline calcite carbonatite magma in the Fen Complex, Southeast Norway. *Lithos* **22**, 99-112.
- Andersen, T. & Austrheim, H. (1991). Temperature-HF fugacity trends during crystallization of calcite carbonatite magma in the Fen Complex, Norway. *Mineralogical Magazine* **55**, 81-94.
- Andrews, J. R. & Emeleus, C. H. (1971). Preliminary account of kimberlite intrusions from the Frederikshåb district, South-West Greenland. *Report - Geological Survey of Greenland* **31**, 1-26.
- Andronikov, A. V. & Foley, S. F. (2001). Trace element and Nd-Sr isotopic composition of ultramafic lamprophyres from the East Antarctic Beaver Lake area. *Chemical Geology* **175**, 291-305.
- Arai, S. (1994). Characterization of spinel peridotites by olivine-spinel compositional relationships: review and interpretation. *Chemical Geology* **113**, 191-204.
- Arima, M. & Edgar, A. D. (1981). Substitution mechanisms and solubility of titanium in phlogopites from rocks of probable mantle origin. *Contributions to Mineralogy and Petrology* **77**, 288-295.
- Bailey, D. K. (1984). Kimberlite: "the mantle sample" formed by ultrametasomatism. In: Kornprobst, J. (ed.) *Kimberlites: Kimberlites and related rocks*. Amsterdam: Elsevier, pp. 323-333.

Ballhaus, C., Berry, R. F. & Green, D. H. (1990). Oxygen fugacity controls in the Earth's upper mantle. *Nature* **348**, 437-440.

Ballhaus, C., Berry, R. F. & Green, D. H. (1991). High pressure experimental calibration of the olivine-orthopyroxene-spinel oxygen geobarometer: implications for the oxidation state of the upper mantle. *Contributions to Mineralogy and Petrology* **107**, 27-40.

Barnes, S. J. & Roeder, P. L. (2001). The range of spinel compositions in terrestrial mafic and ultramafic rocks. *Journal of Petrology* **42**, 2279-2302.

Beard, A. D., Downes, H., Vetrin, V. R., Kempton, P. D. & Maluski, H. (1996). Petrogenesis of Devonian lamprophyre and carbonatite minor intrusions, Kandalaksha Gulf (Kola Peninsula, Russia). *Lithos* **39**, 93-119.

Birkett, T. C., McCandless, T. E. & Hood, C. T. (2004). Petrology of the Renard igneous bodies: host rocks for diamond in the northern Otish Mountains region, Quebec. *Lithos* **76**, 475-490.

Bizimis, M., Salters, V. J. M. & Dawson, J. B. (2003). The brevity of carbonatite sources in the mantle: evidence from Hf isotopes. *Contributions to Mineralogy and Petrology* **145**, 281-300.

Bizzarro, M. & Stevenson, R. (2003). Major element composition of the lithospheric mantle under the North Atlantic craton: Evidence from peridotite xenoliths of the Sarfartoq area, southwestern Greenland. *Contributions to Mineralogy and Petrology* **146**, 223-240.

Bond, G. C., Nickeson, P. A. & Kominz, M. A. (1984). Breakup of a supercontinent between 625 Ma and 555 Ma: new evidence and implications for continental histories. *Earth and Planetary Science Letters* **70**, 325-345.

Brey, G. P. & Green, D. H. (1976). Solubility of CO₂ in olivine melilitite at high pressures and role of CO₂ in the Earth's upper mantle. *Contributions to Mineralogy and Petrology* **55**, 217-230.

Brey, G. P., Brice, W. R., Ellis, D. J., Green, D. H., Harris, K. L. & Ryabchikov, I. D. (1983). Pyroxene-carbonate reactions in the upper mantle. *Earth and Planetary Science Letters* **62**, 63-74.

Brooker, R. A. (1998). The effect of CO₂ saturation on immiscibility between silicate and carbonate liquids: an experimental study. *Journal of Petrology* **39**, 1905-1915.

- Brueckner, H. K. & Rex, D. C. (1980). K-Ar and Rb-Sr geochronology and Sr isotopic study of the Alnö alkaline complex, northeastern Sweden. *Lithos* **13**, 111-119.
- Carmichael, I. S. E. (1991). The redox states of basic and silicic magmas: a reflection of their source regions? *Contributions to Mineralogy and Petrology* **106**, 129-141.
- Cawood, P. A., McCausland, P. J. A. & Dunning, G. R. (2001). Opening Iapetus: constraints from the Laurentian margin in Newfoundland. *Geological Society of America Bulletin* **113**, 443-453.
- Chalot-Prat, F. & Arnold, M. (1999). Immiscibility between calciocarbonatitic and silicate melts and related wall rock reactions in the upper mantle: a natural case study from Romanian mantle xenoliths. *Lithos* **46**, 627-659.
- Clarke, L. B., Le Bas, M. J. & Spiro, B. (1994). Rare earth, trace element and stable isotope fractionation of carbonatites at Kruidfontein, Transvaal, South Africa. In: Meyer, H. O. A. & Leonardos, O. H. (eds.) *Kimberlites, related rocks and mantle xenoliths*. Rio de Janeiro, Brazil: Companhia de Pesquisa de Recursos Minerais, pp. 236-251.
- Collerson, K. D., McCulloch, M. T. & Nutman, A. P. (1989). Sr and Nd isotope systematics of polymetamorphic Archean gneisses from southern West Greenland and northern Labrador. *Canadian Journal of Earth Sciences* **26**, 446-466.
- Connelly, J. N., van Gool, J. A. M. & Mengel, F. C. (2000). Temporal evolution of a deeply eroded orogen: the Nagssugtoqidian Orogen, West Greenland. *Canadian Journal of Earth Sciences* **37**, 1121-1142.
- Culshaw, N. G., Ketchum, J. & Barr, S. (2000a). Structural evolution of the Makkovik Province, Labrador, Canada: tectonic processes during 200 Myr at a Paleoproterozoic active margin. *Tectonics* **19**, 961-977.
- Culshaw, N. G., Brown, T., Reynolds, P. H. & Ketchum, J. W. F. (2000b). Kanairiktok shear zone: the boundary between the Paleoproterozoic Makkovik Province and the Archean Nain Province, Labrador, Canada. *Canadian Journal of Earth Sciences* **37**, 1245-1257.
- Dahlgren, S. (1994). Late Proterozoic and Carboniferous ultramafic magmatism of carbonatitic affinity in Southern Norway. *Lithos* **31**, 141-154.
- Dalton, J. A. & Wood, B. J. (1995). The stability of carbonate under upper-mantle conditions as a function of temperature and oxygen fugacity. *European Journal of Mineralogy* **7**, 883-891.

- Dalton, J. A. & Presnall, D. C. (1998). The continuum of primary carbonatitic-kimberlitic melt compositions in equilibrium with lherzolite: data from the system CaO-MgO-Al₂O₃-SiO₂-CO₂ at 6 GPa. *Journal of Petrology* **39**, 1953-1964.
- Dawson, J. B. (1971). Advances in kimberlite geology. *Earth-Science Reviews* **7**, 187-214.
- Dawson, J. B. & Smith, J. V. (1977). The MARID (mica-amphibole-rutile-ilmenite-diopside) suite of xenoliths in kimberlite. *Geochimica et Cosmochimica Acta* **41**, 309-323.
- Deines, P. (1970). The carbon and oxygen isotopic composition of carbonates from the Oka carbonatite complex, Quebec, Canada. *Geochimica et Cosmochimica Acta* **34**, 1199-1225.
- Deines, P. (1989). Stable isotope variations in carbonatites. In: Bell, K. (ed.) *Carbonatites: genesis and evolution*. London, United Kingdom: Unwin Hyman, pp. 301-359.
- Deines, P. (2002). The carbon isotope geochemistry of mantle xenoliths. *Earth-Science Reviews* **58**, 247-278.
- Digonnet, S., Goulet, N., Bourne, J., Stevenson, R. & Archibald, D. (2000). Petrology of the Abloviak aillikite dykes, New Québec: evidence for a Cambrian diamondiferous alkaline province in northeastern North America. *Canadian Journal of Earth Sciences* **37**, 517-533.
- Doig, R. (1970). An alkaline rock province linking Europe and North America. *Canadian Journal of Earth Sciences* **7**, 22-28.
- Doig, R. & Barton, J. M., Jr. (1968). Ages of carbonatites and other alkaline rocks in Quebec. *Canadian Journal of Earth Sciences* **5**, 1401-1407.
- Emeleus, C. H. & Andrews, J. R. (1975). Mineralogy and petrology of kimberlite dyke and sheet intrusions and included peridotite xenoliths from South-west Greenland. *Physics and Chemistry of the Earth* **9**, 179-197.
- Fedortchouk, Y. & Canil, D. (2004). Intensive variables in kimberlite magmas, Lac de Gras, Canada and implications for diamond survival. *Journal of Petrology* **45**, 1725-1745.
- Ferguson, J. & Currie, K. L. (1971). Evidence of liquid immiscibility in alkaline ultrabasic dikes at Callander Bay, Ontario. *Journal of Petrology* **12**, 561-585.
- Foley, S. F. (1984). Liquid immiscibility and melt segregation in alkaline lamprophyres from Labrador. *Lithos* **17**, 127-137.

Foley, S. F. (1988). The genesis of continental basic alkaline magmas: an interpretation in terms of redox melting. *Journal of Petrology* **Special Lithosphere Issue**, 139-161.

Foley, S. F. (1989a). Emplacement features of lamprophyre and carbonatitic lamprophyre dykes at Aillik Bay, Labrador. *Geological Magazine* **126**, 29-42.

Foley, S. F. (1989b). Experimental constraints on phlogopite chemistry in lamproites: 1. The effect of water activity and oxygen fugacity. *European Journal of Mineralogy* **1**, 411-426.

Foley, S. F. (1991). High-pressure stability of the fluor- and hydroxy-endmembers of pargasite and K-richterite. *Geochimica et Cosmochimica Acta* **55**, 2689-2694.

Foley, S. F. (1992a). Vein-plus-wall-rock melting mechanism in the lithosphere and the origin of potassic alkaline magmas. *Lithos* **28**, 435-453.

Foley, S. F. (1992b). Petrological characterization of the source components of potassic magmas: geochemical and experimental constraints. *Lithos* **28**, 187-204.

Foley, S. F. (1993). An experimental study of olivine lamproite: First results from the diamond stability field. *Geochimica et Cosmochimica Acta* **57**, 483-489.

Foley, S. F., Taylor, W. R. & Green, D. H. (1986). The role of fluorine and oxygen fugacity in the genesis of the ultrapotassic rocks. *Contributions to Mineralogy and Petrology* **94**, 183-192.

Foley, S. F., Musselwhite, D. S. & van der Laan, S. R. (1999). Melt compositions from ultramafic vein assemblages in the lithospheric mantle: a comparison of cratonic and non-cratonic settings. In: Gurney, J. J., Gurney, J. L., Pascoe, M. D. & Richardson, S. H. (eds.) *Proceedings of the VIIth international kimberlite conference*. Cape Town: Red Roof Design, pp. 238-246.

Foley, S. F., Andronikov, A. V. & Melzer, S. (2002). Petrology of ultramafic lamprophyres from the Beaver Lake area of Eastern Antarctica and their relation to the breakup of Gondwanaland. *Mineralogy and Petrology* **74**, 361-384.

Foley, S. F., Jackson, S. E., Fryer, B. J., Greenough, J. D. & Jenner, G. A. (1996). Trace element partition coefficients for clinopyroxene and phlogopite in an alkaline lamprophyre from Newfoundland by LAM-ICP-MS. *Geochimica et Cosmochimica Acta* **60**, 629-638.

Forbes, W. C. & Flower, M. F. J. (1974). Phase relations of titan-phlogopite $\text{K}_2\text{Mg}_4\text{TiAl}_2\text{Si}_6\text{O}_{20}(\text{OH})_2$: a refractory phase in the upper mantle? *Earth and Planetary Science Letters* **22**, 60-66.

- Fraser, K. J., Hawkesworth, C. J., Erlank, A. J., Mitchell, R. H. & Scott-Smith, B. H. (1985). Sr, Nd and Pb isotope and minor element geochemistry of lamproites and kimberlites. *Earth and Planetary Science Letters* **76**, 57-70.
- Freestone, I. C. & Hamilton, D. L. (1980). The role of liquid immiscibility in the genesis of carbonatites: an experimental study. *Contributions to Mineralogy and Petrology* **73**, 105-117.
- Frey, F. A., Green, D. H. & Roy, S. D. (1978). Integrated models of basalt petrogenesis: a study of quartz tholeiites to olivine melilitites from South eastern Australia utilizing geochemical and experimental petrological data. *Journal of Petrology* **19**, 463-513.
- Frost, B. R. (1991). Introduction to oxygen fugacity and its petrologic importance. In: Lindsley, D. H. (ed.) *Oxide minerals: petrologic and magnetic significance*. Washington, DC, United States: Mineralogical Society of America, pp. 1-9.
- Frost, D. J. & Wood, B. J. (1997). Experimental measurements of the fugacity of CO₂ and graphite/diamond stability from 35 to 77 kbar at 925 to 1650°C. *Geochimica et Cosmochimica Acta* **61**, 1565-1574.
- Giannetti, B. & Luhr, J. F. (1990). Phlogopite-clinopyroxenite nodules from high-K magmas, Roccamonfina Volcano, Italy: evidence for a low-pressure metasomatic origin. *Earth and Planetary Science Letters* **101**, 404-424.
- Gittins, J., Macintyre, R. M. & York, D. (1967). The ages of carbonatite complexes in eastern Canada. *Canadian Journal of Earth Sciences* **4**, 651-655.
- Gittins, J., Hewins, R. H. & Laurin, A. F. (1975). Kimberlitic-carbonatitic dikes of the Saguenay River valley, Quebec, Canada. *Physics and Chemistry of the Earth* **9**, 137-148.
- Gower, C. F., Erdmer, P. & Wardle, R. J. (1986). The Double Mer Formation and the Lake Melville rift system, eastern Labrador. *Canadian Journal of Earth Sciences* **23**, 359-368.
- Green, D. H. & Wallace, M. E. (1988). Mantle metasomatism by ephemeral carbonatite melts. *Nature* **336**, 459-462.
- Greenough, J. D. (1988). Minor phases in the Earth's mantle: evidence from trace- and minor-element patterns in primitive alkaline magmas. *Chemical Geology* **69**, 177-192.
- Grégoire, M., Bell, D. R. & Le Roex, A. P. (2002). Trace element geochemistry of phlogopite-rich mafic mantle xenoliths: their classification and their relationship to phlogopite-bearing peridotites and kimberlites revisited. *Contributions to Mineralogy and Petrology* **142**, 603-625.

Grégoire, M., Bell, D. R. & Le Roex, A. P. (2003). Garnet lherzolites from the Kaapvaal Craton (South Africa): trace element evidence for a metasomatic history. *Journal of Petrology* **44**, 629-657.

Griffin, W. L. & Taylor, P. N. (1975). The Fen damkjernite: petrology of a "central-complex kimberlite". *Physics and Chemistry of the Earth* **9**, 163-177.

Gudfinnsson, G. H. & Presnall, D. C. (2005). Continuous gradations among primary carbonatitic, kimberlitic, melilititic, basaltic, picritic, and komatiitic melts in equilibrium with garnet lherzolite at 3-8 GPa. *Journal of Petrology* **in press**,

Guo, J. & Green, T. H. (1990). Experimental study of barium partitioning between phlogopite and silicate liquid at upper-mantle pressure and temperature. *Lithos* **24**, 83-95.

Hall, J., Wardle, R. J., Gower, C. F., Kerr, A., Coflin, K., Keen, C. E. & Carroll, P. (1995). Proterozoic orogens of the northeastern Canadian Shield: new information from the Lithoprobe ECSOOT crustal reflection seismic survey. *Canadian Journal of Earth Sciences* **32**, 1119-1131.

Hamilton, D. L., Bedson, P. & Esson, J. (1989). The behaviour of trace elements in the evolution of carbonatites. In: Bell, K. (ed.) *Carbonatites: genesis and evolution*. London, United Kingdom: Unwin Hyman, pp. 405-427.

Hamilton, R. (1992). Geology and structural setting of ultramafic lamprophyres from Bulljah Pool, central Western Australia. *Journal of the Royal Society of Western Australia* **75**, 51-56.

Hammarstrom, J. M. & Zen, E.-A. (1986). Aluminum in hornblende: an empirical igneous geobarometer. *American Mineralogist* **71**, 1297-1313.

Hansen, K. (1980). Lamprophyres and carbonatitic lamprophyres related to rifting in the Labrador Sea. *Lithos* **13**, 145-152.

Harmer, R. E. & Gittins, J. (1997). The origin of dolomitic carbonatites: field and experimental constraints. *Journal of African Earth Sciences* **25**, 5-28.

Heaman, L. M. (1989). The nature of the subcontinental mantle from Sr-Nd-Pb isotopic studies on kimberlitic perovskite. *Earth and Planetary Science Letters* **92**, 323-334.

Heaman, L. M. & Machado, N. (1992). Timing and origin of Midcontinent Rift alkaline magmatism, North America: evidence from the Coldwell Complex. *Contributions to Mineralogy and Petrology* **110**, 289-303.

- Heaman, L. M. & Kjarsgaard, B. A. (2000). Timing of eastern North American kimberlite magmatism: continental extension of the Great Meteor hotspot track? *Earth and Planetary Science Letters* **178**, 253-268.
- Heaman, L. M. & LeCheminant, A. N. (2001). Anomalous U-Pb systematics in mantle-derived baddeleyite xenocrysts from Ile Bizard: evidence for high temperature radon diffusion? *Chemical Geology* **172**, 77-93.
- Heaman, L. M., Kjarsgaard, B. A. & Creaser, R. A. (2004). The temporal evolution of North American kimberlites. *Lithos* **76**, 377-397.
- Herzberg, C. & O'Hara, M. J. (2002). Plume-associated ultramafic magmas of Phanerozoic age. *Journal of Petrology* **43**, 1857-1883.
- Ionov, D. A. (1998). Trace element composition of mantle-derived carbonates and coexisting phases in peridotite xenoliths from alkali basalts. *Journal of Petrology* **39**, 1931-1941.
- Ionov, D. A. & Hofmann, A. W. (1995). Nb-Ta-rich mantle amphiboles and micas: implications for subduction-related metasomatic trace element fractionations. *Earth and Planetary Science Letters* **131**, 341-356.
- Janse, A. J. A. & Sheahan, P. A. (1995). Catalogue of world wide diamond and kimberlite occurrences: a selective and annotative approach. *Journal of Geochemical Exploration* **53**, 73-111.
- Jones, J. H., Walker, D., Pickett, D. A., Murrell, M. T. & Beattie, P. (1995). Experimental investigations of the partitioning of Nb, Mo, Ba, Ce, Pb, Ra, Th, Pa, and U between immiscible carbonate and silicate liquids. *Geochimica et Cosmochimica Acta* **59**, 1307-1320.
- Kamo, S. L., Gower, C. F. & Krogh, T. E. (1989). Birthdate for the Iapetus Ocean? A precise U-Pb zircon and baddeleyite age for the Long Range dikes, Southeast Labrador. *Geology* **17**, 602-605.
- Kamo, S. L., Krogh, T. E. & Kumarapeli, P. S. (1995). Age of the Grenville dyke swarm, Ontario-Quebec: implications for the timing of Iapetan rifting. *Canadian Journal of Earth Sciences* **32**, 273-280.
- Keller, J. & Hoefs, J. (1995). Stable isotope characteristics of recent natrocarbonatite from Oldoinyo Lengai. In: Bell, K. & Keller, J. (eds.) *Carbonatite volcanism: Oldoinyo Lengai and the petrogenesis of natrocarbonatites*. Berlin: Springer, pp. 113-123.

Kerr, A. & Fryer, B. J. (1993). Nd isotope evidence for crust-mantle interaction in the generation of A-type granitoid suites in Labrador, Canada. *Chemical Geology* **104**, 39-60.

Kerr, A. & Fryer, B. J. (1994). The importance of late- and post-orogenic crustal growth in the early Proterozoic: evidence from Sm-Nd isotopic studies of igneous rocks in the Makkovik Province, Canada. *Earth and Planetary Science Letters* **125**, 71-88.

Kerr, A. & Wardle, R. J. (1997). Definition of an Archean-Proterozoic crustal suture by isotopic studies of basement intersections from offshore wells in the southern Labrador Sea. *Canadian Journal of Earth Sciences* **34**, 209-214.

Kerr, A., Ryan, B., Gower, C. F. & Wardle, R. J. (1996). The Makkovik Province: extension of the Ketilidian mobile belt in mainland North America. In: Brewer, T. S. (ed.) *Precambrian crustal evolution in the North Atlantic region*. London, United Kingdom: Geological Society of London, pp. 155-177.

Kerr, A., Hall, J., Wardle, R. J., Gower, C. F. & Ryan, B. (1997). New reflections on the structure and evolution of the Makkovikian-Ketilidian Orogen in Labrador and southern Greenland. *Tectonics* **16**, 942-965.

Ketchum, J. W. F., Culshaw, N. G. & Barr, S. M. (2002). Anatomy and orogenic history of a Paleoproterozoic accretionary belt: the Makkovik Province, Labrador, Canada. *Canadian Journal of Earth Sciences* **39**, 711-730.

King, A. F. & McMillan, N. J. (1975). A Mid-Mesozoic breccia from the coast of Labrador. *Canadian Journal of Earth Sciences* **12**, 44-51.

Kjarsgaard, B. A. & Hamilton, D. L. (1989). The genesis of carbonatites by immiscibility. In: Bell, K. (ed.) *Carbonatites: genesis and evolution*. London, United Kingdom: Unwin Hyman, pp. 388-404.

Kjarsgaard, B. A., Hamilton, D. L. & Gittins, J. (1989). Carbonatite origin and diversity: discussion and reply. *Nature* **338**, 547-548.

Kogarko, L. N., Henderson, C. M. B. & Pacheco, H. (1995). Primary Ca-rich carbonatite magma and carbonate-silicate-sulphide liquid immiscibility in the upper mantle. *Contributions to Mineralogy and Petrology* **121**, 267-274.

Konzett, J. & Ulmer, P. (1999). The stability of hydrous potassic phases in lherzolite mantle: an experimental study to 9.5 GPa in simplified and natural bulk compositions. *Journal of Petrology* **40**, 629-652.

- Konzett, J., Sweeney, R. J., Thompson, A. B. & Ulmer, P. (1997). Potassium amphibole stability in the upper mantle: an experimental study in a peralkaline KNCMASH system to 8.5 GPa. *Journal of Petrology* **38**, 537-568.
- Kresten, P. (1980). The Alnö complex: tectonics of dyke emplacement. *Lithos* **13**, 153-158.
- Kretz, R. (1982). Transfer and exchange equilibria in a portion of the pyroxene quadrilateral as deduced from natural and experimental data. *Geochimica et Cosmochimica Acta* **46**, 411-421.
- Kretz, R. (1983). Symbols for rock-forming minerals. *American Mineralogist* **68**, 277-279.
- Larsen, L. M. & Rex, D. C. (1992). A review of the 2500 Ma span of alkaline-ultramafic, potassic and carbonatitic magmatism in West Greenland. *Lithos* **28**, 367-402.
- Larsen, L. M. & Rønsbo, J. (1993). Conditions of origin of kimberlites in West Greenland: new evidence from the Sarfartoq and Sukkertoppen regions. *Report - Geological Survey of Greenland* **159**, 115-120.
- Le Roex, A. P. & Lanyon, R. (1998). Isotope and trace element geochemistry of Cretaceous Damaraland lamprophyres and carbonatites, northwestern Namibia: evidence for plume-lithosphere interactions. *Journal of Petrology* **39**, 117-1146.
- Le Roex, A. P., Bell, D. R. & Davis, P. (2003). Petrogenesis of Group I kimberlites from Kimberley, South Africa: evidence from bulk-rock geochemistry. *Journal of Petrology* **44**, 2261-2286.
- Leat, P. T., Riley, T. R., Storey, B. C., Kelley, S. P. & Millar, I. L. (2000). Middle Jurassic ultramafic lamprophyre dyke within the Ferrar magmatic province, Pensacola Mountains, Antarctica. *Mineralogical Magazine* **64**, 95-111.
- Lee, W. J. & Wyllie, P. J. (1997a). Liquid immiscibility between nephelinite and carbonatite from 1.0 to 2.5 GPa compared with mantle melt compositions. *Contributions to Mineralogy and Petrology* **127**, 1-16.
- Lee, W. J. & Wyllie, P. J. (1997b). Liquid immiscibility in the join NaAlSiO₄-NaAlSi₃O₈-CaCO₃ at 1 GPa: implications for crustal carbonatites. *Journal of Petrology* **38**, 1113-1135.
- Lee, W. J. & Wyllie, P. J. (1998). Petrogenesis of carbonatite magmas from mantle to crust, constrained by the system CaO-(MgO + FeO*)-(Na₂O + K₂O)-(SiO₂ + Al₂O₃ + TiO₂)-CO₂. *Journal of Petrology* **39**, 495-517.

Leech, G. B., Lowdon, J. A., Stockwell, C. H. & Wanless, R. K. (1962). Age determinations and geological studies. *Reports Geological Survey of Canada* **4**, 116-117.

Ludwig, K. R. (1998). On the treatment of concordant uranium-lead ages. *Geochimica et Cosmochimica Acta* **62**, 665-676.

Luhr, J. F., Carmichael, I. S. E. & Varekamp, J. C. (1984). The 1982 eruptions of El Chichon Volcano, Chiapas, Mexico: mineralogy and petrology of the anhydrite-bearing pumices. *Journal of Volcanology and Geothermal Research* **23**, 69-108.

Malpas, J., Foley, S. F. & King, A. F. (1986). Alkaline mafic and ultramafic lamprophyres from the Aillik Bay area, Labrador. *Canadian Journal of Earth Sciences* **23**, 1902-1918.

McCrea, J. M. (1950). On the isotopic chemistry of carbonates and a paleotemperature scale. *J. Chem. Phys.* **18**, 849-857.

McKenzie, D. (1985). The extraction of magma from the crust and mantle. *Earth and Planetary Science Letters* **74**, 81-91.

McKenzie, D. (1989). Some remarks on the movement of small melt fractions in the mantle. *Earth and Planetary Science Letters* **95**, 53-72.

McKenzie, D. & Bickle, M. J. (1988). The volume and composition of melt generated by extension of the lithosphere. *Journal of Petrology* **29**, 625-679.

Meen, J. K., Ayers, J. C. & Fregeau, E. J. (1989). A model of mantle metasomatism by carbonated alkaline melts: trace-element and isotopic compositions of mantle source regions of carbonatite and other continental igneous rocks. In: Bell, K. (ed.) *Carbonatites: genesis and evolution*. London, United Kingdom: Unwin Hyman, pp. 464-499.

Meert, J. G., Torsvik, T. H., Eide, E. A. & Dahlgren, S. (1998). Tectonic significance of the Fen Province, S. Norway: constraints from geochronology and paleomagnetism. *Journal of Geology* **106**, 553-564.

Mengel, K. & Green, D. H. (1989). Stability of amphibole and phlogopite in metasomatized peridotite under water-saturated and water-undersaturated conditions. In: Ross, J. (ed.) *Kimberlites and related rocks*. Sydney, N.S.W., Australia: Geological Society of Australia, pp. 571-581.

Mitchell, R. H. (1973). Composition of olivine, silica activity and oxygen fugacity in kimberlite. *Lithos* **6**, 65-81.

Mitchell, R. H. (1986). *Kimberlites: mineralogy, geochemistry and petrology*. New York: Plenum Press, 442 pp.

Mitchell, R. H. (1995). *Kimberlites, orangeites, and related rocks*. New York: Plenum Press, 410 pp.

Mitchell, R. H. & Bergman, S. C. (1991). *Petrology of lamproites*. New York: Plenum Press, 447 pp.

Mitchell, R. H., Scott-Smith, B. H. & Larsen, L. M. (1999). Mineralogy of ultramafic dikes from the Sarfartoq, Sisimiut and Maniitsoq areas, West Greenland. In: Gurney, J. J., Gurney, J. L., Pascoe, M. D. & Richardson, S. H. (eds.) *Proceedings of the VIIth international kimberlite conference*. Cape Town: Red Roof Design, pp. 574-583.

Moine, B. N., Grégoire, M., O'Reilly, S. Y., Delpech, G., Sheppard, S. M. F., Lorand, J. P., Renac, C., Giret, A. & Cottin, J. Y. (2004). Carbonatite melt in oceanic upper mantle beneath the Kerguelen Archipelago. *Lithos* **75**, 239-252.

Munno, R., Rossi, G. & Tadini, C. (1980). Crystal chemistry of kimzeyite from Stromboli, Aeolian Islands, Italy. *American Mineralogist* **65**, 188-191.

Murphy, D. T., Collerson, K. D. & Kamber, B. S. (2002). Lamproites from Gaussberg, Antarctica: possible transition zone melts of Archaean subducted sediments. *Journal of Petrology* **43**, 981-1001.

Murthy, G., Gower, C. F., Tubrett, M. & Paetzold, R. (1992). Paleomagnetism of Eocambrian Long Range dykes and Double Mer Formation from Labrador, Canada. *Canadian Journal of Earth Sciences* **29**, 1224-1234.

Neal, C. R. & Davidson, J. P. (1989). An unmetasomatized source for the Malaitan alnöite (Solomon Islands): petrogenesis involving zone refining, megacryst fractionation, and assimilation of oceanic lithosphere. *Geochimica et Cosmochimica Acta* **53**, 1975-1990.

Nelson, D. R. (1989). Isotopic characteristics and petrogenesis of the lamproites and kimberlites of central West Greenland. *Lithos* **22**, 265-274.

Nicholls, J., Carmichael, I. S. E. & Stormer, J. C., Jr. (1971). Silica Activity and P_{total} in Igneous Rocks. *Contributions to Mineralogy and Petrology* **33**, 1-20.

Nimis, P. & Ulmer, P. (1998). Clinopyroxene geobarometry of magmatic rocks: Part 1, An expanded structural geobarometer for anhydrous and hydrous, basic and ultrabasic systems. *Contributions to Mineralogy and Petrology* **133**, 122-135.

- Nixon, P. H., Mitchell, R. H. & Rogers, N. W. (1980). Petrogenesis of alnöitic rocks from Malaita, Solomon Islands, Melanesia. *Mineralogical Magazine* **43**, 587-596.
- Nowell, G. M., Pearson, D. G., Bell, D. R., Carlson, R. W., Smith, C. B., Kempton, P. D. & Noble, S. R. (2004). Hf isotope systematics of kimberlites and their megacrysts: new constraints on their source regions. *Journal of Petrology* **45**, 1583-1612.
- O'Neill, H. S. C. & Wall, V. J. (1987). The olivine-orthopyroxene-spinel oxygen geobarometer, the nickel precipitation curve, and the oxygen fugacity of the Earth's upper mantle. *Journal of Petrology* **28**, 1169-1191.
- Otto, J. W. & Wyllie, P. J. (1993). Relationships between silicate melts and carbonate-precipitating melts in CaO-MgO-SiO₂-CO₂-H₂O at 2 kbar. *Mineralogy and Petrology* **48**, 343-365.
- Pearce, N. J. G. & Leng, M. J. (1996). The origin of carbonatites and related rocks from the Igaliko dyke swarm, Gardar Province, South Greenland: field, geochemical and C-O-Sr-Nd isotope evidence. *Lithos* **39**, 21-40.
- Platt, R. G. & Mitchell, R. H. (1979). The Marathon Dikes. I: Zirconium-rich titanian garnets and manganoan magnesian ulvöspinel-magnetite spinels. *American Mineralogist* **64**, 546-550.
- Price, S. E., Russell, J. K. & Kopylova, M. G. (2000). Primitive magma from the Jericho Pipe, N.W.T., Canada: constraints on primary kimberlite melt chemistry. *Journal of Petrology* **41**, 789-808.
- Raeseide, R. P. & Helmstaedt, H. (1982). The Ile Bizard Intrusion, Montreal, Quebec: kimberlite or lamprophyre? *Canadian Journal of Earth Sciences* **19**, 1996-2011.
- Renne, P. R., Swisher, C. C., Deino, A. L., Karner, D. B., Owens, T. L. & DePaolo, D. J. (1998). Intercalibration of standards, absolute ages and uncertainties in ⁴⁰Ar-³⁹Ar dating. *Chemical Geology* **145**, 117-152.
- Righter, K. & Carmichael, I. S. E. (1996). Phase equilibria of phlogopite lamprophyres from western Mexico: biotite-liquid equilibria and P-T estimates for biotite-bearing igneous rocks. *Contributions to Mineralogy and Petrology* **123**, 1-21.
- Riley, T. R., Leat, P. T., Storey, B. C., Parkinson, I. J. & Millar, I. L. (2003). Ultramafic lamprophyres of the Ferrar large igneous province: evidence for a HIMU mantle component. *Lithos* **66**, 63-76.

- Robert, J. L. (1976). Titanium solubility in synthetic phlogopite solid solutions. *Chemical Geology* **17**, 213-227.
- Rock, N. M. S. (1986). The nature and origin of ultramafic lamprophyres: alnöites and allied rocks. *Journal of Petrology* **27**, 155-196.
- Rock, N. M. S. (1991). *Lamprophyres*. Glasgow: Blackie & Son, 285 pp.
- Roddick, J. C. (1983). High precision intercalibration of ^{40}Ar - ^{39}Ar standards. *Geochimica et Cosmochimica Acta* **47**, 887-898.
- Roest, W. R. & Srivastava, S. P. (1989). Seafloor spreading in the Labrador Sea: a new reconstruction. *Geology* **17**, 1000-1003.
- Rogers, N. W., Hawkesworth, C. J. & Palacz, Z. A. (1992). Phlogopite in the generation of olivine-melilitites from Namaqualand, South Africa and implications for element fractionation processes in the upper mantle. *Lithos* **28**, 347-365.
- Romer, R. L., Schärer, U., Wardle, R. J. & Wilton, D. H. C. (1995). U-Pb age of the Seal Lake Group, Labrador: relationship to Mesoproterozoic extension-related magmatism of Laurasia. *Canadian Journal of Earth Sciences* **32**, 1401-1410.
- Santos, R. V. & Clayton, R. N. (1995). Variations of oxygen and carbon isotopes in carbonatites: a study of Brazilian alkaline complexes. *Geochimica et Cosmochimica Acta* **59**, 1339-1352.
- Scaillet, S. (2000). Numerical error analysis in $^{40}\text{Ar}/^{39}\text{Ar}$ dating. *Chemical Geology* **162**, 269-298.
- Scott, B. H. (1981). Kimberlite and lamproite dykes from Holsteinsborg, West Greenland. *Meddelelser om Grønland, Geoscience* **4**, 3-24.
- Seifert, W., Kämpf, H. & Wasternack, J. (2000). Compositional variation in apatite, phlogopite and other accessory minerals of the ultramafic Delitzsch Complex, Germany: implication for cooling history of carbonatites. *Lithos* **53**, 81-100.
- Sinclair, G. S., Barr, S. M., Culshaw, N. G. & Ketchum, J. W. F. (2002). Geochemistry and age of the Aillik Group and associated plutonic rocks, Makkovik Bay area, Labrador: implications for tectonic development of the Makkovik Province. *Canadian Journal of Earth Sciences* **39**, 731-748.

- Smith, J. V., Brennesholtz, R. & Dawson, J. B. (1978). Chemistry of micas from kimberlites and xenoliths: I. micaceous kimberlites. *Geochimica et Cosmochimica Acta* **42**, 959-972.
- Spera, F. J. (1984). Carbon dioxide in petrogenesis III: role of volatiles in the ascent of alkaline magma with special reference to xenolith-bearing mafic lavas. *Contributions to Mineralogy and Petrology* **88**, 217-232.
- Spera, F. J. (1987). Dynamics of translithospheric migration of metasomatic fluid and alkaline magma. In: Menzies, M. A. & Hawkesworth, C. J. (eds.) *Mantle metasomatism*. London, United Kingdom: Academic Press, pp. 1-20.
- Srivastava, S. P. & Roest, W. R. (1999). Extent of oceanic crust in the Labrador Sea. *Marine and Petroleum Geology* **16**, 65-84.
- Stacey, J. S. & Kramers, J. D. (1975). Approximation of terrestrial lead isotope evolution by a two-stage model. *Earth and Planetary Science Letters* **26**, 207-221.
- Stormer, J. C., Pierson, M. L. & Tacker, R. C. (1993). Variation of F and Cl X-ray intensity due to anisotropic diffusion in apatite during electron microprobe analysis. *American Mineralogist* **78**, 641-648.
- Sudo, A. & Tatsumi, Y. (1990). Phlogopite and K-amphibole in the upper mantle: implication for magma genesis in subduction zones. *Geophysical Research Letters* **17**, 29-32.
- Sun, S.-S. & McDonough, W. F. (1989). Chemical and isotopic systematics of ocean basalts: implications for mantle composition and processes. In: Saunders, A. D. & Norry, M. J. (eds.) *Magmatism in the ocean basins*. London: Geological Society of London, Spec. Publ. 42, pp. 313-345.
- Sweeney, R. J. (1994). Carbonatite melt compositions in the Earth's mantle. *Earth and Planetary Science Letters* **128**, 259-270.
- Sweeney, R. J., Thompson, A. B. & Ulmer, P. (1993). Phase relations of a natural MARID composition and implications for MARID genesis, lithospheric melting and mantle metasomatism. *Contributions to Mineralogy and Petrology* **115**, 225-241.
- Tainton, K. M. & McKenzie, D. (1994). The generation of kimberlites, lamproites, and their source rocks. *Journal of Petrology* **35**, 787-817.
- Tappe, S., Foley, S. F., Jenner, G. A. & Kjarsgaard, B. A. (2005). Integrating ultramafic lamprophyres into the IUGS classification of igneous rocks: rationale and implications. *Journal of Petrology* **in press**,

- Tappe, S., Jenner, G. A., Foley, S. F., Heaman, L. M., Besserer, D., Kjarsgaard, B. A. & Ryan, A. B. (2004). Torngat ultramafic lamprophyres and their relation to the North Atlantic Alkaline Province. *Lithos* **76**, 491-518.
- Taylor, H. P., Frechen, J. & Degens, E. T. (1967). Oxygen and carbon isotope studies of carbonatites from the Laacher See District, west Germany and the Alnö District, Sweden. *Geochimica et Cosmochimica Acta* **31**, 407-430.
- Taylor, W. R. & Green, D. H. (1988). Measurement of reduced peridotite-C-O-H solidus and implications for redox melting of the mantle. *Nature* **332**, 349-352.
- Thompson, R. N. & Gibson, S. A. (1994). Magmatic expression of lithospheric thinning across continental rifts. *Tectonophysics* **233**, 41-68.
- Thy, P., Stecher, O. & Korstgard, J. A. (1987). Mineral chemistry and crystallization sequences in kimberlite and lamproite dikes from the Sisimiut area, central West Greenland. *Lithos* **20**, 391-417.
- Torsvik, T. H., Smethurst, M. A., Meert, J. G., Van der Voo, R., McKerrow, W. S., Brasier, M. D., Sturt, B. A. & Walderhaug, H. J. (1996). Continental break-up and collision in the Neoproterozoic and Palaeozoic: a tale of Baltica and Laurentia. *Earth-Science Reviews* **40**, 229-258.
- Ulmer, P. & Sweeney, R. J. (2002). Generation and differentiation of Group II kimberlites: constraints from a high-pressure experimental study to 10 GPa. *Geochimica et Cosmochimica Acta* **66**, 2139-2153.
- Umpleby, D. C. (1979). Geology of the Labrador Shelf. *Reports Geological Survey of Canada* **79-13**, 1-34.
- Upton, B. G. J., Emeleus, C. H., Heaman, L. M., Goodenough, K. M. & Finch, A. A. (2003). Magmatism of the mid-Proterozoic Gardar Province, South Greenland: chronology, petrogenesis and geological setting. *Lithos* **68**, 43-65.
- van Achterbergh, E., Griffin, B. J., Ryan, C. G., O'Reilly, S. Y., Pearson, N. J., Kivi, K. & Doyle, B. J. (2004). Melt inclusions from the deep Slave lithosphere: implications for the origin and evolution of mantle-derived carbonatite and kimberlite. *Lithos* **76**, 461-474.
- Veksler, I. V., Petibon, C. M., Jenner, G. A., Dorfman, A. M. & Dingwell, D. B. (1998). Trace element partitioning in immiscible silicate-carbonate liquid systems: an initial experimental study using a centrifuge autoclave. *Journal of Petrology* **39**, 2095-2104.

- Villeneuve, M., Sandeman, H. A. & Davis, W. J. (2000). A method for intercalibration of U-Th-Pb and ^{40}Ar - ^{39}Ar ages in the Phanerozoic. *Geochimica et Cosmochimica Acta* **64**, 4017-4030.
- Vollmer, R., Ogden, P., Schilling, J. G., Kingsley, R. H. & Waggoner, D. G. (1984). Nd and Sr isotopes in ultrapotassic volcanic rocks from the Leucite Hills, Wyoming. *Contributions to Mineralogy and Petrology* **87**, 359-368.
- Vuorinen, J. H. & Skelton, A. D. L. (2004). Origin of silicate minerals in carbonatites from Alnö Island, Sweden: magmatic crystallization or wall rock assimilation? *Terra Nova* **16**, 210-215.
- Wardle, R. J. & Hall, J. (2002). Proterozoic evolution of the northeastern Canadian Shield: Lithoprobe Eastern Canadian Shield Onshore-Offshore Transect (ECSOOT), introduction and summary. *Canadian Journal of Earth Sciences* **39**, 563-567.
- Waters, F. G. (1987). A suggested origin of MARID xenoliths in kimberlites by high pressure crystallization of an ultrapotassic rock such as lamproite. *Contributions to Mineralogy and Petrology* **95**, 523-533.
- Wendlandt, R. F. & Egger, D. H. (1980). The origins of potassic magmas: 2. Stability of phlogopite in natural spinel lherzolite and in the system KAlSiO_4 - MgO - SiO_2 - H_2O - CO_2 at high pressures and high temperatures. *American Journal of Science* **280**, 421-458.
- Woolley, A. R. & Kempe, D. R. C. (1989). Carbonatites: nomenclature, average chemical compositions, and element distribution. In: Bell, K. (ed.) *Carbonatites: genesis and evolution*. London, United Kingdom: Unwin Hyman, pp. 1-14.
- Wyllie, P. J. (1980). The origin of kimberlite. *Journal of Geophysical Research* **85**, 6902-6910.
- Wyllie, P. J. & Tuttle, O. F. (1960). The system CaO - CO_2 - H_2O and the origin of carbonatites. *Journal of Petrology* **1**, 1-46.
- Zhu, C. & Sverjensky, D. A. (1992). F-Cl-OH partitioning between biotite and apatite. *Geochimica et Cosmochimica Acta* **56**, 3435-3467.
- Zindler, A. & Hart, S. (1986). Chemical geodynamics. *Annual Review of Earth and Planetary Sciences* **14**, 493-571.

TABLES

Table 1: U-Pb perovskite results for ultramafic lamprophyres from the Aillik Bay area

Description*	Weight (μ g)	U (ppm)	Th (ppm)	Pb (ppm)	Th/U	TCPb (pg)	$\frac{206\text{Pb}}{204\text{Pb}}$	$\frac{238\text{U}}{204\text{Pb}}$	$\frac{206\text{Pb}^{**}}{238\text{U}}$	$\frac{207\text{Pb}^{**}}{235\text{U}}$	$\frac{207\text{Pb}^{**}}{206\text{Pb}}$	apparent ages (Ma)			%Disc
												$\frac{206\text{Pb}}{238\text{U}}$	$\frac{207\text{Pb}}{235\text{U}}$	$\frac{207\text{Pb}}{206\text{Pb}}$	
ST123 (aillikite)															
1. dk brn subhed cubes/octahedrons M@0.3A (70)	60	109	746	31	6.82	179	227.368±0.620	2306.25±8.25	0.09087±20	0.74100±492	0.05914±38	560.7±1.2	562.9±2.9	572.4±13.9	2.1
2. dk brn subhed cubes/octahedrons M@0.3A (230)	169	138	892	37	6.45	575	251.696±1.226	2555.64±14.74	0.09152±25	0.74058±510	0.05869±37	564.5±1.5	562.8±3.0	565.7±13.8	-1.7
ST144A (mela-aillikite)															
1. brn/black irregular frags M@0.5A (80)	132	347	1660	77	4.79	742	373.167±1.689	3849.73±18.30	0.09232±15	0.75364±389	0.05921±29	569.2±0.9	570.3±2.3	574.8±10.6	1.0
ST228 (aillikite)															
1. black/brn frags MI@H (150)	52	86	349	18	4.08	113	249.027±1.635	2481.45±17.09	0.09319±16	0.75606±622	0.05884±47	574.4±0.9	571.7±3.6	561.3±17.2	-2.4
2. black/brn euhed cubes/octahedrons MI@H (100)	55	101	389	22	3.86	209	178.204±2.016	1708.25±21.49	0.09391±17	0.75602±733	0.05839±55	578.6±1.0	571.7±4.2	544.3±20.6	-6.6
ST220II (aillikite)															
1. black/brn irregular frags M@0.4A (95)	51	253	2002	79	7.90	188	428.111±2.626	4285.74±26.87	0.09575±13	0.79238±384	0.06002±28	589.4±0.7	592.5±2.2	604.4±9.9	2.6
2. brn flakes and frags M@0.4A	102	238	2027	78	8.54	356	425.751±1.685	4253.18±19.85	0.09592±24	0.79016±369	0.05974±24	590.5±1.4	591.3±2.1	594.3±8.5	0.7
ST211A (damtjernite)															
1. brn octahedrons M@0.5A (50)	17	85	2077	60	24.4	45	197.616±2.101	2000.07±23.44	0.08991±14	0.72407±575	0.05841±46	555.0±0.9	553.1±3.4	545.0±17.2	-1.9
ST256 (damtjernite)															
1. brn clear irregular frags M@0.5A (60)	91	79	486	24	6.15	522	96.688±0.165	861.74±1.97	0.09143±42	0.73837±1248	0.06857±103	563.9±2.5	561.5±7.3	551.3±37.9	-2.4
ST174 (damtjernite)															
1. brn frags 0.3A/NI	40	102	412	21	4.06	70	360.458±5.672	3675.34±58.61	0.09323±14	0.75200±890	0.05850±65	574.6±0.8	569.4±5.2	548.5±24.1	-5.0
ST140A (damtjernite)															
1. light brn frags M@0.5A (160)	117	45	161	10	3.57	210	167.387±0.764	1581.66±9.78	0.09458±40	0.76607±755	0.05875±56	582.5±2.4	577.5±4.4	557.7±20.6	-4.7
2. light brn frags M@0.5A (230)	184	76	279	16	3.66	471	195.384±1.086	1880.03±11.88	0.09447±21	0.76296±664	0.05888±49	581.9±1.3	575.7±3.8	551.4±18.3	-5.8
ST168A (damtjernite)															
1. brn octahedrons M@0.5A (200)	101	116	323	23	2.79	447	173.575±0.392	1646.30±4.45	0.09463±25	0.76993±672	0.05901±53	582.8±1.5	579.7±3.9	567.6±19.3	-2.8
2. dk brn euhed cubes/octahedrons M@0.5A (240)	175	131	386	25	2.95	774	193.643±0.618	1860.98±7.22	0.09450±19	0.76391±603	0.05863±46	582.1±1.1	576.3±3.5	563.4±16.9	-5.4

* dk brn - dark brown; frags - fragments; M@0.3A - non-magnetic fraction at 0.3 A (Frantz); (#) - number of grains analysed

** Atomic ratios corrected for fractionation, blank (5 pg Pb; 1 pg U), spike and initial common Pb (Stacey & Kramers, 1975)

Th concentrations calculated based on amount of ^{206}Pb present and $^{207}\text{Pb}/^{209}\text{Pb}$ date

TCPb = total common Pb

All errors reported in this table quoted at 1-sigma.

Table 2: Ar-Ar phlogopite results for clinopyroxene-phlogopite inclusion ST1621 in aillikite dyke ST162 from Aillik Bay

Power ^a [%]	volume ³⁹ Ar [10 ⁻¹¹ cm ³]	³⁶ Ar/ ³⁹ Ar	³⁷ Ar/ ³⁹ Ar	³⁸ Ar/ ³⁹ Ar	⁴⁰ Ar/ ³⁹ Ar	⁴⁰ Ar [%]	⁴⁰ Ar/ ³⁹ Ar	⁴⁰ Ar/ ³⁹ Ar	f ₃₉ ^b [%]	apparent age ^c [Ma]
2.4	0.198	0.0131±0.0427	0.384±0.033	0.137±0.012	8.377±3.602	29.3	5.921±4.663	5.921±4.663	0.3	259.26±190.27
2.8	0.306	0.0354±0.0054	1.484±0.048	0.121±0.011	13.079±2.216	16.9	10.864±2.938	10.864±2.938	0.5	450.37±107.81
3.0	0.634	0.0155±0.0029	0.143±0.010	0.081±0.012	13.181±1.066	6.3	12.348±1.467	12.348±1.467	1.1	504.00±52.25
3.5*	1.559	0.0060±0.0011	0.041±0.004	0.032±0.011	14.889±0.439	2.6	14.506±0.611	14.506±0.611	2.7	579.24±20.86
3.9*	2.093	0.0007±0.0024	0.010±0.005	0.019±0.011	14.516±0.330	0.9	14.384±0.429	14.384±0.429	3.6	575.08±14.69
4.2*	4.479	0.0003±0.0026	0.005±0.003	0.021±0.011	14.762±0.157	1.3	14.566±0.235	14.566±0.235	7.7	581.31±8.03
4.6*	4.717	0.0002±0.0010	0.008±0.001	0.020±0.011	14.454±0.164	0.4	14.401±0.188	14.401±0.188	8.1	575.67±6.43
5.0*	5.028	0.0002±0.0017	0.006±0.004	0.020±0.011	14.336±0.147	0.0	14.338±0.204	14.338±0.204	8.6	573.50±7.01
5.5*	5.866	0.0003±0.0015	0.008±0.001	0.021±0.011	14.383±0.124	0.2	14.358±0.160	14.358±0.160	10.0	574.20±5.47
6.0*	8.507	0.0001±0.0010	0.016±0.002	0.020±0.011	14.348±0.102	0.3	14.303±0.124	14.303±0.124	14.5	572.30±4.26
6.5*	7.509	0.0000±0.0012	0.013±0.002	0.020±0.011	14.383±0.097	0.3	14.333±0.118	14.333±0.118	12.8	573.33±4.05
7.5*	12.35	0.0001±0.0005	0.005±0.001	0.021±0.011	14.341±0.064	0.2	14.314±0.073	14.314±0.073	21.1	572.69±2.51
13.0*	5.296	0.0001±0.0022	0.010±0.001	0.021±0.011	14.445±0.156	0.9	14.316±0.193	14.316±0.193	9.1	572.74±6.63
plateau = 573.3±3.3										

* Denotes steps used in the calculation of the plateau age (573.3±3.3 Ma)

(a) As measured by laser in % of full nominal power (10W)

(b) Fraction ³⁹Ar as percent of total run

(c) Errors are analytical only and do not reflect error in irradiation parameter J

nominal J = 0.002610; referenced to PP-20 Hornblende (Hb3gr equivalent) = 1072 Ma (Roddick, 1983)

All errors reported in this table quoted at 2-sigma.

Table 3: Estimated modal mineral abundances (vol. %) of representative UML and carbonatite dykes and their cognate inclusions from the Aillik Bay area

Mineral Locality/rock type	Ol (pc/mc)	Phl	Cpx	Amph/Pct	Afsp/Ne	Cal/Dol	opaques	Prv/Spn	Rt/Zcl	Adr	Ap	Srp*	Br/FI	Qtz**
dyke rocks														
dol carbonatite														
L1	-/-	-	-	-/-	1/-	90	2	-/-	4/-	-	3	-	x/-	x
dol-cal carbonatite														
ST127	3/-	3	-	-/-	-/-	83	2	-/-	5/-	-	-	2	-/2	x
ST198C	-/-	3	9	-/-	-/-	72	4	-/-	8/-	-	5	-	x/-	-
ST199	-/-	11	18	-/-	-/-	60	1	-/-	5/-	-	4	-	x/-	1
ST231A	6/-	20	-	-/-	-/-	54	10	-/-	7/-	-	1	1	-/-	x
aillikite														
L60	23/-	19	4	-/-	-/-	29	13	6/-	-/-	1	x	7	-/-	-
ST109	19/2	19	-	-/-	-/-	33	13	x/-	-/-	-	6	7	-/-	-
meta-aillikite														
ST147B	19/-	22	29	-/-	-/-	7	14	1/-	1/-	x	x	5	-/-	-
ST210	22/-	22	28	-/-	-/-	10	8	-/-	4/-	-	x	6	-/-	-
ST244B	21/-	20	32	-/-	-/-	4	18	-/-	2/-	-	x	3	-/-	-
ST251B	25/2	26	18	-/-	-/-	9	9	2/-	1/-	-	2	8	-/-	-
damjernite														
ST188A	x/-	21	x	-/26	-/8	10	9	8/-	x/-	10	7	x	-/-	-
ST206AI	x/-	21	40	-/-	2/-	9	10	-/-	8/-	-	1	9	-/-	-
ST211A	x/-	20	30	-/-	-/11	7	7	15/8	x/-	-	2	x	-/-	-
ST224B	10/12	16	37	-/-	-/6	2	11	-/-	6/-	-	x	-	-/-	-
ST226	x/-	22	41	-/-	6/6	8	9	-/-	7/-	-	1	-	-/-	-
cognate inclusions														
glimmerite nodules														
	-	90-95	-	-/-	x/-	x/x	0-2	-/-	-/-	-	2-5	-	-/-	-
cpx-phl nodules														
	0-20	30-60	25-50	0-10/-	-/-	x/x	5-10	-/x	-/-	-	0-5	x	-/-	-
ol-phl nodules														
	20-70	20-50	0-5	-/-	-/-	x/x	3-10	x/-	-/x	-	0-5	x	-/-	-

pc - phenocryst; mc - macrocryst; *primary serpentine; **quartz is secondary; x = minor amounts; - = not detected;
 Symbols for minerals according to Kretz (1983) except for **Afsp** (=alkali feldspar) and **Zcl** (=zirconolite)

Table 4: Representative olivine compositions from the Aillik Bay area ultramafic lamprophyres and cognate inclusions

Rock type	ultramafic lamprophyres										cognate inclusions																							
	aillikite					mela-aillikite					damijerinite					cpx-phl nodule					ol-phl nodule													
Mineral	Ol	Ol	Ol	Ol	Ol	Ol	Ol	Ol	Ol	Ol	Ol	Ol	Ol	Ol	Ol	Ol	Ol	Ol	Ol	Ol	Ol	Ol	Ol	Ol	Ol	Ol	Ol	Ol	Ol	Ol				
Sample#	L72	L72	L72	L72	L72	ST244B	ST244B	ST244B	ST244B	ST244B	pc1	pc1	pc1	pc1	pc1	L6py	L6py	L6py	L6py	L6py	ST162ldu	ST162ldu	ST162ldu	ST162ldu	ST162ldu	L49du	L49du	L49du	L49du	L49du				
	pc2	pc2	pc2	pc2	pc2	mpc2	mpc2	mpc2	mpc2	mpc2	core	rim	core	rim	core	core	rim	core	rim	core	core1	core2	xx4	xx4	xx4	core	core	xx2	xx2	xx2				
	core1	core2	rim1	rim2	rim2	core	rim1	rim2	rim2	rim2																								
SiO ₂	39.88	40.15	39.05	39.40	39.40	40.23	39.83	39.82	39.95	39.50	39.13	39.10	39.71	38.35	39.54	39.68	39.40	39.60	39.24	38.49	39.07	39.68	39.40	39.60	39.24	38.49	39.07	39.68	39.40	39.60	39.24	38.49	39.07	
TiO ₂	0.03	0.01	0.02	0.07	0.07	0.07	0.00	0.03	0.04	0.06	0.06	0.05	0.03	0.02	0.00	0.00	0.00	0.00	0.00	0.01	0.01	0.00	0.00	0.00	0.00	0.01	0.01	0.00	0.00	0.00	0.00	0.01	0.01	
Al ₂ O ₃	0.05	0.06	0.02	0.00	0.00	0.06	0.03	0.03	0.04	0.00	0.01	0.00	0.01	0.02	0.01	0.01	0.03	0.00	0.03	0.00	0.00	0.03	0.00	0.00	0.03	0.00	0.00	0.03	0.00	0.00	0.03	0.00	0.00	
Cr ₂ O ₃	0.05	0.07	0.10	0.01	0.00	0.05	0.10	0.02	0.05	0.00	0.06	0.07	0.00	0.00	0.02	0.00	0.07	0.00	0.03	0.00	0.01	0.00	0.00	0.00	0.00	0.00	0.01	0.00	0.00	0.00	0.03	0.00	0.01	
FeO	10.15	10.61	16.32	13.71	12.05	12.05	14.25	14.47	14.89	15.81	16.38	17.80	14.05	18.12	13.33	16.03	14.93	14.42	16.40	16.61	19.03	18.86	14.05	18.12	13.33	16.03	14.93	18.86	14.05	18.12	13.33	16.03	14.93	18.86
MnO	0.17	0.14	0.15	0.22	0.09	0.09	0.15	0.24	0.11	0.18	0.18	0.25	0.55	0.39	0.70	0.34	0.23	0.16	0.42	0.35	0.25	0.22	0.55	0.39	0.70	0.34	0.23	0.22	0.55	0.39	0.70	0.34	0.23	0.22
NiO	0.45	0.38	0.27	0.12	0.43	0.43	0.21	0.14	0.44	0.19	0.43	0.28	0.03	0.02	0.00	0.08	0.42	0.37	0.26	0.19	0.22	0.27	0.03	0.02	0.00	0.08	0.42	0.27	0.03	0.02	0.00	0.08	0.42	0.27
MgO	48.75	48.19	44.12	45.55	48.45	48.45	46.52	46.85	44.83	43.83	43.89	42.34	45.87	41.77	45.86	43.89	45.50	44.47	43.86	41.82	41.83	45.87	41.77	45.86	43.89	41.82	41.83	45.87	41.77	45.86	43.89	41.82	41.83	
CaO	0.12	0.12	0.11	0.17	0.15	0.15	0.25	0.36	0.18	0.44	0.16	0.20	0.07	0.31	0.06	0.33	0.14	0.13	0.16	0.11	0.02	0.03	0.07	0.31	0.06	0.33	0.14	0.03	0.07	0.31	0.06	0.33	0.14	0.03
Na ₂ O	0.02	0.06	0.01	0.00	0.03	0.03	0.00	0.03	0.00	0.02	0.01	0.01	0.00	0.01	0.01	0.02	0.00	0.02	0.01	0.00	0.00	0.00	0.00	0.01	0.01	0.02	0.00	0.00	0.00	0.01	0.01	0.02	0.00	0.00
K ₂ O	0.00	0.00	0.01	0.02	0.02	0.02	0.01	0.03	0.01	0.00	0.01	0.01	0.01	0.02	0.01	0.01	0.01	0.00	0.00	0.00	0.00	0.02	0.01	0.02	0.01	0.01	0.01	0.02	0.01	0.02	0.01	0.01	0.01	0.02
Total	99.66	99.80	100.22	99.27	101.63	101.34	102.02	100.53	100.03	100.31	100.12	100.33	99.03	99.54	100.47	101.01	100.47	101.40	100.41	99.84	100.32	100.33	99.03	99.54	100.47	101.01	100.32	100.33	99.03	99.54	100.47	101.01	100.32	
No. oxygens	4	4	4	4	4	4	4	4	4	4	4	4	4	4	4	4	4	4	4	4	4	4	4	4	4	4	4	4	4	4	4	4	4	
Si	0.982	0.990	0.984	0.991	0.978	0.981	0.974	0.999	0.996	0.996	0.986	0.985	0.989	0.987	0.990	0.997	0.986	0.986	0.988	0.985	0.986	0.989	0.987	0.990	0.997	0.986	0.986	0.989	0.987	0.990	0.997	0.986	0.986	
Ti	0.001	0.000	0.000	0.001	0.001	0.001	0.000	0.001	0.001	0.001	0.001	0.001	0.001	0.000	0.000	0.000	0.000	0.000	0.000	0.000	0.000	0.000	0.000	0.000	0.000	0.000	0.000	0.000	0.000	0.000	0.000	0.000	0.000	
Al	0.001	0.002	0.001	0.000	0.002	0.001	0.001	0.001	0.001	0.000	0.000	0.000	0.000	0.000	0.000	0.000	0.001	0.000	0.000	0.000	0.000	0.000	0.000	0.000	0.000	0.000	0.000	0.000	0.000	0.000	0.000	0.000	0.000	
Cr	0.001	0.001	0.001	0.000	0.000	0.001	0.002	0.000	0.001	0.000	0.001	0.001	0.000	0.000	0.000	0.000	0.000	0.000	0.000	0.000	0.000	0.000	0.000	0.000	0.000	0.000	0.000	0.000	0.000	0.000	0.000	0.000	0.000	
*Fe ³⁺	0.033	0.019	0.029	0.016	0.041	0.035	0.052	0.000	0.000	0.006	0.025	0.007	0.021	0.025	0.020	0.002	0.027	0.039	0.026	0.022	0.029	0.008	0.021	0.025	0.020	0.002	0.027	0.008	0.021	0.025	0.020	0.002	0.027	0.008
*Fe ²⁺	0.176	0.200	0.315	0.272	0.204	0.259	0.244	0.311	0.327	0.327	0.320	0.371	0.272	0.365	0.260	0.335	0.283	0.261	0.315	0.327	0.379	0.394	0.272	0.365	0.260	0.335	0.283	0.394	0.272	0.365	0.260	0.335	0.283	0.394
Mn	0.003	0.003	0.003	0.005	0.002	0.003	0.005	0.000	0.002	0.004	0.004	0.005	0.012	0.009	0.015	0.007	0.005	0.003	0.005	0.007	0.006	0.005	0.012	0.009	0.015	0.007	0.005	0.005	0.012	0.009	0.015	0.007	0.005	0.005
Ni	0.009	0.008	0.006	0.002	0.008	0.004	0.003	0.009	0.009	0.004	0.009	0.006	0.001	0.000	0.000	0.000	0.000	0.000	0.000	0.000	0.000	0.000	0.001	0.000	0.000	0.000	0.000	0.000	0.001	0.000	0.000	0.000	0.000	0.000
Mg	1.790	1.771	1.656	1.707	1.756	1.708	1.709	1.671	1.648	1.648	1.649	1.606	1.703	1.603	1.712	1.645	1.685	1.703	1.651	1.647	1.596	1.590	1.703	1.603	1.712	1.645	1.685	1.590	1.703	1.603	1.712	1.645	1.685	1.590
Ca	0.003	0.003	0.003	0.005	0.004	0.007	0.010	0.005	0.012	0.004	0.004	0.006	0.002	0.009	0.001	0.009	0.004	0.003	0.004	0.003	0.000	0.001	0.002	0.009	0.001	0.009	0.004	0.001	0.002	0.009	0.001	0.009	0.004	0.001
Na	0.001	0.003	0.000	0.000	0.002	0.000	0.002	0.000	0.000	0.001	0.001	0.000	0.000	0.001	0.001	0.001	0.000	0.001	0.000	0.000	0.000	0.000	0.000	0.001	0.001	0.001	0.000	0.000	0.000	0.001	0.001	0.001	0.000	0.000
K	0.000	0.000	0.000	0.001	0.001	0.001	0.000	0.001	0.000	0.000	0.000	0.000	0.000	0.000	0.000	0.000	0.000	0.000	0.000	0.000	0.000	0.001	0.000	0.000	0.000	0.000	0.000	0.000	0.000	0.000	0.000	0.000	0.000	0.001
Total cations	3.000	3.000	3.000	3.000	3.000	3.000	3.000	3.000	3.000	2.999	3.000	3.000	3.000	3.000	3.000	3.000	3.000	2.999	3.000	3.000	3.000	3.000	3.000	3.000	3.000	2.999	3.000	3.000	3.000	3.000	3.000	2.999	3.000	3.000
Mg#	91.1	89.9	84.0	86.3	89.6	86.9	87.5	84.3	83.4	83.8	81.2	86.2	81.5	86.8	83.1	85.6	86.7	84.0	83.4	80.8	80.1	86.2	81.5	86.8	83.1	85.6	80.1	86.2	81.5	86.8	83.1	85.6	80.1	

Mg# = 100[Mg/(Mg+Fe²⁺)] in atomic units; *calculated assuming stoichiometry; pc - phenocryst; mpc - microphenocryst; xx - crystal; Ol - olivine

Table 5: Representative mica compositions of JML, carbonatite and cognate inclusions from the Aillik Bay area

Rock type	ultramafic lamprophyres and carbonatites												cognate inclusions																			
	aillikite				mela-aillikite				damijerinite				dol-calc carbonatite				glimmerite				cpx-phl nodule				ol-phl nodule							
	Phi	Phl	L66	TFP	Phi	Phl	TFP	L66	Phi	Phl	BT	TFP	Phi	Phl	TFP	L66	Phi	Phl	TFP	L66	Phi	Phl	TFP	L66	Phi	Phl	TFP	L66	Phi	Phl	TFP	L66
Mineral	L66	L66	L66	L66	pc2	pc2	pc2	pc2	core1	core2	rim1	rim2	rim3	rim3	rim3	rim3	rim3	rim3	rim3	rim3	rim3	rim3	rim3	rim3	rim3	rim3	rim3	rim3	rim3	rim3	rim3	rim3
Sample#	41.13	37.43	39.67	40.74	40.56	38.31	38.44	36.38	37.51	37.72	37.31	37.10	34.63	35.16	35.79	38.52	41.43	41.31	38.49	38.13	38.46	38.13	38.46	38.85	38.85	38.76	39.03	39.03	38.85	38.76	39.03	39.03
SiO ₂	0.92	4.54	0.72	0.06	0.04	2.72	3.03	5.46	5.34	5.38	5.18	3.80	4.55	4.16	2.56	1.44	0.62	0.53	3.12	3.00	2.71	3.12	3.00	2.53	2.53	2.48	2.48	2.48	2.53	2.48	2.48	2.48
Al ₂ O ₃	8.43	15.30	12.85	1.84	1.88	13.29	13.40	8.49	8.01	8.14	14.27	14.13	9.56	11.28	17.91	14.19	9.37	10.40	14.33	14.83	14.36	14.33	14.83	13.74	13.74	13.60	13.75	13.75	13.74	13.60	13.75	13.75
Cr ₂ O ₃	0.01	0.02	0.07	0.08	0.02	0.03	0.01	0.03	0.08	0.06	0.05	0.04	0.09	0.04	0.02	0.04	0.06	0.01	0.06	0.00	0.05	0.06	0.00	0.06	0.06	0.04	0.63	0.63	0.06	0.04	0.63	0.63
FeO	5.05	6.99	5.80	14.77	14.09	10.25	10.05	28.41	28.84	28.19	7.76	11.29	34.97	26.51	6.25	6.23	12.72	6.92	9.46	9.68	9.81	9.46	9.68	6.27	6.24	6.11	6.11	6.11	6.27	6.24	6.11	6.11
MnO	0.04	0.04	0.09	0.24	0.16	0.13	0.05	0.35	0.29	0.37	0.03	0.22	0.73	0.44	0.02	0.20	0.32	0.08	0.06	0.10	0.10	0.06	0.10	0.02	0.00	0.00	0.00	0.00	0.02	0.00	0.00	0.00
MgO	24.55	20.93	24.87	26.59	26.59	21.05	20.76	7.44	7.78	7.62	20.44	18.68	3.28	8.79	21.50	24.24	27.31	24.41	20.46	20.35	20.75	20.46	20.35	23.06	22.90	22.91	22.91	22.91	23.06	22.90	22.91	22.91
CaO	0.00	0.02	0.15	0.20	0.20	0.03	0.05	0.20	0.14	0.15	0.02	0.00	0.07	0.67	0.21	0.21	0.46	0.02	0.09	0.04	0.10	0.09	0.04	0.14	0.05	0.16	0.16	0.16	0.09	0.04	0.10	0.10
BaO	0.02	0.42	0.47	0.06	0.07	0.00	0.08	0.04	0.08	0.00	0.55	0.50	0.18	0.40	1.42	0.62	0.09	0.04	0.67	0.84	0.60	0.67	0.84	0.29	0.42	0.32	0.32	0.32	0.29	0.42	0.32	0.32
Na ₂ O	0.37	0.40	0.33	0.08	0.14	0.86	0.89	0.42	0.52	0.50	0.48	0.49	0.11	0.17	0.46	0.43	0.28	0.05	1.02	1.09	1.05	1.02	1.09	0.99	0.94	0.75	0.75	0.75	0.99	0.94	0.75	0.75
K ₂ O	10.13	9.58	9.62	10.21	10.15	8.79	9.03	8.41	8.81	8.96	9.30	9.17	8.85	8.73	9.22	9.41	9.71	10.18	8.69	8.69	8.60	8.69	8.69	8.67	8.96	8.87	8.87	8.87	8.67	8.96	8.87	8.87
H ₂ O (calc)	3.55	3.92	3.96	3.79	3.79	3.88	3.92	3.64	3.61	3.68	3.77	3.74	3.61	3.65	3.93	3.86	3.26	3.08	3.98	3.98	3.90	3.98	3.98	3.95	3.80	3.82	3.82	3.82	3.95	3.80	3.82	3.82
F	1.26	0.51	0.49	0.56	0.57	0.51	0.51	0.44	0.26	0.31	0.77	0.71	0.03	0.26	0.46	0.66	1.74	2.25	0.29	0.28	0.46	0.29	0.28	0.51	0.80	0.78	0.78	0.78	0.51	0.80	0.78	0.78
Cl	0.00	0.00	0.00	0.00	0.00	0.00	0.00	0.00	0.00	0.01	0.01	0.01	0.01	0.01	0.00	0.00	0.01	0.00	0.02	0.01	0.02	0.02	0.01	0.01	0.01	0.01	0.01	0.01	0.02	0.01	0.01	0.01
O=F	-0.53	-0.21	-0.21	-0.24	-0.24	-0.22	-0.19	-0.11	-0.13	-0.08	-0.32	-0.30	-0.01	-0.11	-0.19	-0.28	-0.73	-0.95	-0.12	-0.12	-0.19	-0.12	-0.12	-0.21	-0.33	-0.33	-0.33	-0.33	-0.21	-0.33	-0.33	-0.33
Total	96.92	99.87	98.87	98.97	98.03	99.64	99.96	99.42	101.19	100.89	99.63	99.57	100.64	100.16	99.55	99.78	98.66	97.69	100.62	100.89	100.77	99.46	99.27	99.46	99.27	99.28	99.28	99.28	99.46	99.27	99.28	99.28
No. oxygens	22	22	22	22	22	22	22	22	22	22	22	22	22	22	22	22	22	22	22	22	22	22	22	22	22	22	22	22	22	22	22	22
Si	5.912	5.399	5.730	5.988	6.006	5.570	5.574	5.745	5.816	5.856	5.404	5.471	5.626	5.523	5.197	5.541	6.055	6.055	5.554	5.502	5.547	5.554	5.502	5.575	5.587	5.614	5.614	5.614	5.575	5.587	5.614	5.614
Al	1.998	2.601	2.188	0.318	0.328	2.277	2.290	1.580	1.464	1.489	2.436	2.456	1.830	2.088	2.803	2.406	0.327	1.648	2.437	2.498	2.441	2.437	2.498	2.324	2.311	2.331	2.331	2.331	2.324	2.311	2.331	2.331
IVFe ³⁺	0.490	0.000	0.082	1.694	1.666	0.152	0.136	0.674	0.721	0.655	0.159	0.073	0.544	0.389	0.000	0.053	1.618	0.297	0.009	0.000	0.013	0.009	0.000	0.101	0.102	0.055	0.055	0.055	0.101	0.102	0.055	0.055
[T]	8.0	8.0	8.0	8.0	8.0	8.0	8.0	8.0	8.0	8.0	8.0	8.0	8.0	8.0	8.0	8.0	8.0	8.0	8.0	8.0	8.0	8.0	8.0	8.0	8.0	8.0	8.0	8.0	8.0	8.0	8.0	8.0
Ti	0.999	0.493	0.078	0.006	0.005	0.297	0.331	0.649	0.623	0.628	0.564	0.422	0.556	0.492	0.280	0.156	0.010	0.068	0.339	0.326	0.294	0.339	0.326	0.273	0.269	0.266	0.266	0.266	0.273	0.269	0.266	0.266
VAl	0.000	0.000	0.000	0.000	0.000	0.000	0.000	0.000	0.000	0.000	0.000	0.000	0.000	0.000	0.262	0.000	0.000	0.000	0.000	0.000	0.000	0.000	0.000	0.000	0.000	0.000	0.000	0.000	0.000	0.000	0.000	0.000
Cr	0.001	0.002	0.008	0.009	0.003	0.003	0.001	0.004	0.010	0.007	0.006	0.004	0.011	0.004	0.002	0.004	0.006	0.000	0.007	0.000	0.006	0.007	0.000	0.075	0.073	0.072	0.072	0.072	0.075	0.073	0.072	0.072
Mg	5.261	4.501	5.356	5.826	5.870	4.563	4.488	1.752	1.798	1.764	4.414	4.107	0.794	2.058	4.654	5.198	5.946	5.318	4.401	4.377	4.461	4.401	4.377	4.933	4.921	4.913	4.913	4.913	4.933	4.921	4.913	4.913
Ca	0.000	0.003	0.023	0.031	0.031	0.005	0.007	0.034	0.023	0.026	0.003	0.000	0.012	0.113	0.032	0.033	0.071	0.003	0.014	0.006	0.015	0.014	0.006	0.021	0.008	0.024	0.024	0.024	0.021	0.008	0.024	0.024
Mn	0.005	0.005	0.011	0.030	0.021	0.016	0.006	0.046	0.038	0.049	0.004	0.027	0.100	0.058	0.002	0.025	0.039	0.010	0.007	0.012	0.012	0.007	0.012	0.002	0.000	0.000	0.000	0.000	0.002	0.000	0.000	0.000
Fe ³⁺	0.597	0.843	0.619	1.122	0.079	1.084	1.083	3.078	3.019	3.005	0.781	1.319	4.207	3.094	0.759	0.697	0.000	0.549	1.133	1.168	1.171	1.133	1.168	0.651	0.650	0.680	0.680	0.680	0.651	0.650	0.680	0.680
[M]	6.0	5.8	6.1	6.0	6.0	6.0	6.0	5.6	5.5	5.5	5.8	5.9	5.7	5.8	6.0	6.1	6.1	5.9	5.9	5.9	6.0	5.9	5.9	6.0	6.0	5.9	6.0	6.0	6.0	5.9	6.0	6.0
Ba	0.001	0.024	0.026	0.003	0.004	0.000	0.005	0.029	0.005	0.005	0.031	0.029	0.011	0.025	0.081	0.035	0.005	0.002	0.038	0.047	0.034	0.038	0.047	0.016	0.024	0.018	0.018	0.018	0.016	0.024	0.018	0.018
Na	0.103	0.111	0.093	0.022	0.040	0.242	0.251	0.129	0.157	0.151	0.135	0.141	0.034	0.052	0.128	0.121	0.078	0.013	0.285	0.304	0.292	0.285	0.304	0.274	0.264	0.209	0.209	0.209	0.274	0.264	0.209	0.209
K	1.958	1.753	1.773	1.914	1.917	1.631	1.671	1.694	1.743	1.775	1.719	1.725	1.834	1.749	1.708	1.727	1.809	1.898	1.600	1.600	1.582	1.600	1.600	1.567	1.648	1.628	1.628	1.628	1.567	1.648	1.628	1.628
[A]	1.961	1.898	1.892	1.940	1.962	1.873	1.926	1.825	1.904	1.925	1.865	1.895	1.880	1.826	1.917	1.882	1.893	1.913	1.922	1.950	1.909	1.922	1.950	1.878	1.935	1.854	1.854	1.854	1.878	1.935	1.854	1.854
Total cations	15.9	15.7	15.0	16.0	16.0	15.9	15.8	15.4	15.4	15.4	15.7	15.8	15.6	15.6	15.9	16.0	16.0	15.9	15.8	15.9	15.9	15.8	15.9	15.8	15.9	15.8	15.8	15.8	15.8	15.9	15.8	15.8
F	0.576	0.230	0.223	0.261	0.268	0.237	0.202	0.130	0.152	0.098	0.352	0.331	0.016	0.132	0.213	0.302	0.809	1.047	0.006	0.002	0.004	0.006	0.002	0.231	0.363	0.357	0.357	0.357	0.231	0.363	0.357	0.357
Cl	0.000	0.000	0.000	0.000	0.000	0.000	0.000	0.000	0.000	0.000	0.002	0.003	0.002	0.003	0.000	0.000	0.															

Table 6: Representative clinopyroxene compositions from Aillik Bay area ultramafic lamprophyres, carbonatites and cognate inclusions

Rock type	ultramafic lamprophyres and carbonatites										cognate inclusions									
	aillikite			_mela-aillikite			damtjernite			dol-cal carbonatite			cpx-phl nodule			ol-phl nodule				
Mineral	Di	Di	Di	Di	Di	Di	Di	Di	Di	Di	Di	Di	Di	Di	Di	Di	Di	Di		
Sample#	L66	L66	ST244B	ST244B	ST244B	ST244B	ST244B	ST246A	ST246A	ST199	ST199	ST199	L74py	L74py	L74py	ST162III	ST162III	ST162III		
	mpc2	mpc2	mpc1	mpc1	rim2	rim1	rim1	core	rim	mpc6	mpc6	rim	pc12	pc12	rim	xx1	xx1	xx4		
	core	rim	core1	core2	rim1	rim2	rim	core	rim	core1	core2	rim	core1	rim1	rim2	core1	core2	rim		
SiO ₂	51.47	53.44	48.83	48.09	44.35	43.06	49.26	45.92	50.20	49.60	47.93	46.10	48.71	49.95	46.68	53.55	53.78	53.48		
TiO ₂	0.87	0.46	2.78	3.05	4.96	5.41	2.94	5.03	2.40	2.98	2.43	3.17	2.30	2.21	2.42	0.49	0.36	0.46		
Al ₂ O ₃	1.63	0.20	2.98	3.29	5.85	6.77	3.02	5.03	2.28	1.31	4.45	5.95	4.05	2.41	5.37	1.05	0.83	0.97		
Cr ₂ O ₃	0.00	0.00	0.05	0.01	0.00	0.00	0.00	0.00	0.02	0.04	0.03	0.07	0.06	0.00	0.07	0.56	0.32	0.48		
FeO	4.51	2.97	5.98	6.03	7.40	7.29	6.12	7.26	6.75	22.29	8.01	8.13	7.48	4.89	4.75	4.08	4.07	3.90		
MnO	0.11	0.20	0.16	0.11	0.08	0.06	0.11	0.11	0.12	0.54	0.09	0.11	0.13	0.08	0.04	0.05	0.10	0.12		
NiO	0.00	0.00	0.00	0.00	0.00	0.01	0.00	0.00	0.00	0.04	n.a	n.a	n.a	0.00	0.03	0.00	n.a	n.a		
MgO	15.79	16.63	14.71	14.62	12.94	12.39	15.14	13.39	14.74	3.47	12.77	12.04	12.61	15.32	13.68	16.62	16.76	16.68		
CaO	24.91	25.16	23.99	23.76	23.90	23.53	23.93	23.31	23.10	12.34	23.41	23.53	23.47	23.26	23.14	22.89	22.61	22.98		
Na ₂ O	0.22	0.23	0.33	0.32	0.43	0.43	0.30	0.65	0.81	6.82	0.88	0.69	0.88	0.32	0.38	0.81	0.77	0.76		
K ₂ O	0.01	0.00	0.00	0.00	0.03	0.00	0.00	0.00	0.02	0.04	0.00	0.00	0.00	0.00	0.00	0.01	0.02	0.00		
Total	99.52	99.29	99.82	99.32	99.93	98.95	100.83	100.70	100.44	99.47	100.00	99.79	99.68	98.18	97.56	100.11	99.62	99.83		
No. oxygens	6	6	6	6	6	6	6	6	6	6	6	6	6	6	6	6	6	6		
Si	1.896	1.963	1.810	1.792	1.658	1.628	1.807	1.701	1.846	1.904	1.7813	1.7242	1.8162	1.896	1.768	1.948	1.965	1.951		
Ti	0.024	0.013	0.078	0.086	0.139	0.154	0.081	0.140	0.066	0.086	0.0679	0.0892	0.0645	0.058	0.062	0.013	0.010	0.013		
Al	0.071	0.009	0.130	0.145	0.258	0.302	0.131	0.220	0.099	0.059	0.1949	0.2623	0.1780	0.075	0.106	0.045	0.036	0.042		
Cr	0.000	0.000	0.002	0.000	0.000	0.000	0.000	0.000	0.001	0.001	0.0010	0.0019	0.0016	0.000	0.001	0.016	0.009	0.014		
Fe ^{3+(a)}	0.105	0.055	0.116	0.123	0.180	0.165	0.115	0.146	0.134	0.469	0.1688	0.1591	0.1228	0.039	0.058	0.073	0.061	0.072		
Fe ^{2+(b)}	0.034	0.036	0.069	0.065	0.052	0.066	0.073	0.079	0.073	0.246	0.0801	0.0952	0.1105	0.115	0.091	0.051	0.064	0.047		
Mn	0.003	0.006	0.005	0.004	0.003	0.002	0.004	0.003	0.004	0.017	0.0029	0.0036	0.0040	0.003	0.001	0.001	0.003	0.004		
Ni	0.000	0.000	0.000	0.000	0.000	0.000	0.000	0.000	0.000	0.001	n.a	n.a	n.a	0.000	0.000	n.a	n.a	n.a		
Mg	0.867	0.911	0.813	0.812	0.721	0.699	0.828	0.739	0.808	0.199	0.7075	0.6713	0.7009	0.857	0.854	0.901	0.913	0.907		
Ca	0.983	0.990	0.953	0.950	0.957	0.953	0.941	0.925	0.910	0.507	0.9322	0.9430	0.9377	0.935	0.928	0.892	0.885	0.898		
Na	0.016	0.016	0.024	0.023	0.031	0.031	0.022	0.047	0.058	0.508	0.0633	0.0502	0.0638	0.023	0.027	0.057	0.054	0.054		
K	0.001	0.000	0.000	0.000	0.001	0.000	0.000	0.000	0.001	0.002	0.0000	0.0000	0.0000	0.000	0.001	0.001	0.001	0.000		
Total cations	4.0	4.0	4.0	4.0	4.0	4.0	4.0	4.0	4.0	4.0	4.0	4.0	4.0	4.0	4.0	4.0	4.0	4.0		
Al/Ti	2.9	0.7	1.7	1.7	1.3	2.0	1.6	1.6	1.5	0.7	2.9	2.9	2.8	1.3	1.7	3.4	3.6	3.3		
Mg#	96.2	96.2	92.1	92.6	93.3	91.4	91.9	90.3	91.7	44.6	89.8	87.6	86.4	88.2	90.4	94.7	93.5	95.1		

Mg# = 100[Mg/(Mg+Fe²⁺)] in atomic units; (a) - dlopsiide; Aeg - aegirine; pc - phenocryst; mpc - microphenocryst; gm - groundmass; xx - crystal; n.a. = not analyzed

Table 7: Representative spinel compositions from Aillik Bay area ultramafic lamprophyres and their cognate inclusions

Rock type	ultramafic lamprophyres												cognate inclusions														
	aillikite				mela-aillikite				damijerinite				glimmerite				cpx-phl nodule				ol-phl nodule						
	Cr-Spl L60	Cr-Spl mpc4	Ti-Mag L60	Ti-Mag rim2	Cr-Spl ST251B	Cr-Spl mpc5	Ti-Mag ST162II	Ti-Mag pc1	Cr-Spl ST251B	Cr-Spl mpc5	Ti-Mag ST251B	Ti-Mag rim1	Cr-Spl ST211A	Cr-Spl mpc5	Ti-Mag ST211A	Ti-Mag rim2	Cr-Spl L74gl	Cr-Spl xx2	Ti-Mag L74gl	Ti-Mag core	Cr-Spl L74py	Cr-Spl xx1	Ti-Mag L74py	Ti-Mag xx1	Cr-Spl L6du	Cr-Spl xx2	Ti-Mag L6du
SiO ₂	0.12	0.12	0.09	0.08	0.10	0.08	0.11	0.12	0.13	0.12	0.10	1.42	0.88	0.18	0.06	0.15	0.00	0.01	0.01	0.00	0.01	0.01	0.01	0.00	0.00	0.03	0.06
TiO ₂	8.88	15.95	20.84	11.10	3.84	12.33	8.78	6.63	6.51	16.52	15.62	3.68	4.63	2.65	8.44	8.57	8.44	8.58	10.16	9.90	8.58	10.16	9.90	16.29	19.95		
Al ₂ O ₃	7.35	5.67	4.42	9.05	6.68	7.00	3.19	9.37	8.99	2.82	2.29	0.67	0.23	0.04	0.26	1.00	0.59	0.55	0.50	4.35	4.35	0.50	4.35	4.03	3.48		
Cr ₂ O ₃	31.67	14.18	0.24	0.05	0.09	0.02	0.05	32.14	33.50	0.42	0.25	0.04	0.05	0.04	0.02	0.03	15.59	15.19	9.78	12.39	6.92	4.39					
V ₂ O ₃	0.17	0.12	0.02	0.02	0.00	0.00	0.00	0.17	0.18	0.15	0.21	0.22	0.20	0.27	0.19	0.21	0.40	0.40	0.42	0.46	0.20	0.21					
FeO*	39.34	49.07	62.57	65.34	75.64	64.60	73.11	39.45	38.47	72.69	74.78	84.97	85.81	90.02	80.19	78.16	64.84	65.67	68.24	61.19	58.49	61.14					
MnO	0.39	0.90	0.92	1.03	0.67	0.87	1.02	0.35	0.35	0.98	0.93	0.32	0.42	0.67	0.69	0.63	0.62	0.63	0.56	0.40	0.65	0.73					
NiO	0.17	0.09	0.04	0.02	0.00	0.06	0.08	0.15	0.16	0.14	0.13	0.00	0.02	0.05	0.00	0.01	0.20	0.18	0.19	0.27	0.26	0.27					
MgO	11.76	13.12	7.94	10.92	7.07	10.25	6.87	11.08	10.84	1.55	1.04	0.12	0.03	0.05	4.58	5.12	4.77	4.32	4.90	6.21	6.82	5.34					
Total	99.85	99.22	97.08	97.61	94.08	95.20	93.20	99.46	99.13	95.38	95.35	91.44	92.28	93.97	94.56	93.75	95.51	95.53	94.75	95.07	93.68	95.56					
No. oxygens	32	32	32	32	32	32	32	32	32	32	32	32	32	32	32	32	32	32	32	32	32	32	32	32	32		
Si	0.031	0.032	0.024	0.021	0.029	0.022	0.032	0.030	0.035	0.036	0.031	0.445	0.274	0.056	0.017	0.043	0.000	0.003	0.003	0.000	0.003	0.003	0.000	0.009	0.018		
Ti	1.751	3.145	4.366	2.203	0.811	2.529	1.903	1.306	1.291	3.711	3.529	0.866	1.085	0.610	1.899	1.871	1.877	1.901	2.256	2.115	3.564	4.353					
Al	2.271	1.752	1.451	2.815	2.212	2.252	1.082	2.893	2.794	0.993	0.811	0.247	0.086	0.016	0.091	0.349	0.204	0.190	0.174	1.471	1.382	1.190					
Cr	6.565	2.940	0.052	0.011	0.021	0.003	0.011	6.656	6.985	0.099	0.059	0.011	0.013	0.008	0.004	0.007	3.619	3.538	2.283	2.811	1.592	1.007					
V	0.038	0.025	0.005	0.003	0.000	0.000	0.000	0.036	0.039	0.035	0.050	0.054	0.051	0.067	0.045	0.049	0.094	0.095	0.099	0.106	0.047	0.049					
Fe ^{3+(t)}	3.563	4.929	5.712	8.724	12.087	8.641	11.037	3.743	3.530	7.380	7.960	13.066	13.133	14.577	12.028	11.766	8.330	8.370	8.927	7.383	5.833	5.013					
Fe ^{2+(t)}	5.063	5.830	8.866	5.695	5.694	6.098	6.592	4.899	4.954	10.776	10.827	9.170	9.230	8.457	7.732	7.505	7.589	7.808	7.919	7.289	8.397	9.821					
Mn	0.087	0.199	0.217	0.229	0.158	0.201	0.250	0.078	0.077	0.247	0.236	0.083	0.112	0.174	0.173	0.158	0.154	0.156	0.139	0.097	0.159	0.178					
Ni	0.036	0.020	0.009	0.005	0.000	0.014	0.018	0.032	0.034	0.034	0.031	0.000	0.004	0.011	0.000	0.002	0.047	0.042	0.044	0.053	0.060	0.062					
Mg	4.596	5.128	3.297	4.295	2.961	4.168	2.954	4.326	4.261	0.689	0.466	0.057	0.013	0.024	2.012	2.250	2.087	1.897	2.156	2.656	2.958	2.309					
Total cations	24.0	24.0	24.0	24.0	24.0	23.9	23.9	24.0	24.0	24.0	24.0	24.0	24.0	24.0	24.0	24.0	24.0	24.0	24.0	24.0	24.0	24.0	24.0	24.0	24.0		
Mg#	47.6	46.8	27.1	43.0	34.2	40.6	30.9	46.9	46.2	6.0	4.1	0.6	0.1	0.3	20.6	23.1	21.6	19.5	21.4	26.7	26.0	19.0					

Mg# = 100[Mg/(Mg+Fe²⁺)] in atomic units; *, FeO as total Fe; (a) - calculated assuming stoichiometry

Cr-Spl - chromian spinel; Ti-Mag - titanomagnetite; Mag - magnetite; mpc - microphenocryst; pc - phenocryst; xx - crystal

Table 8: Representative ilmenite compositions from Aillik Bay area ultramafic lamprophyres, carbonatites and cognate inclusions

Rock type	ultramafic lamprophyres and carbonatites												cognate inclusions											
	aillikite			mela-aillikite			damijerite			dol-calc carbonatite			glimmerite			cpx-phl nodule			ol-phl nodule					
	lim	lim	lim	lim	lim	lim	lim	lim	lim	lim	lim	lim	lim	lim	lim	lim	lim	lim	lim	lim	lim			
Mineral	L54	L54	L65	ST244B	ST244B	ST244B	ST206A	ST206A	ST211A	L49cab	L49cab	L49cab	L74gl	L74gl	L74gl	L74py	L74py	L74py	L54py	L54py	L54py	ST250B	ST250B	
Sample#	mpc2	mpc2	mpc1	mpc1	mpc1	mpc1	mpc4	mpc4	mpc6	mpc1	mpc1	mpc1	core	rim1	rim2	core1	xx3	xx3	core	xx3	xx3	core	xx3	
	core	rim	core	core1	core2	core3	core	rim	core2	core	rim	rim	core	rim1	rim2	core1	core2	rim	core	rim	rim	core	rim	
SiO ₂	0.05	0.02	0.03	0.16	0.24	0.07	0.07	0.07	0.25	0.13	0.11	0.11	0.04	0.01	0.07	0.04	0.02	0.06	0.01	0.03	0.03	0.04	0.04	3.36
TiO ₂	50.08	46.84	50.94	51.62	50.78	51.74	51.42	51.63	50.42	50.85	52.41	52.41	47.56	44.00	44.49	51.60	51.09	46.72	48.62	45.58	45.58	52.08	46.78	
Al ₂ O ₃	0.17	0.16	0.34	0.01	0.04	0.00	0.01	0.01	0.04	0.02	0.00	0.00	0.03	0.12	0.10	0.04	0.04	0.12	0.00	0.08	0.08	0.66	0.03	
Cr ₂ O ₃	0.23	0.28	0.74	0.03	0.04	0.01	0.04	0.05	0.02	0.00	0.03	0.03	0.00	0.06	0.02	0.41	0.38	0.17	0.32	0.29	0.29	0.97	0.51	
V ₂ O ₅	0.15	0.12	0.13	n.a.	n.a.	n.a.	n.a.	n.a.	n.a.	0.14	0.00	0.00	0.05	0.01	0.02	0.10	0.05	0.00	0.07	0.01	0.01	n.a.	n.a.	
FeO*	36.10	46.03	33.17	46.25	47.04	46.26	43.50	42.13	43.53	41.96	41.63	41.63	43.92	47.29	47.25	32.60	35.11	45.48	38.46	46.71	46.71	32.38	41.79	
MnO	0.65	2.03	0.66	3.77	1.18	1.12	3.37	4.42	4.16	3.97	3.96	3.96	2.08	1.82	2.18	0.65	0.75	1.18	0.98	1.86	1.86	0.41	1.68	
NiO	0.00	0.01	0.05	0.03	0.00	0.01	0.01	0.03	0.00	0.00	0.01	0.01	0.00	0.00	0.00	0.10	0.06	0.03	0.05	0.02	0.02	0.06	0.00	
MgO	10.59	1.51	11.66	2.45	1.37	1.18	0.00	0.03	0.06	0.25	0.19	0.19	3.73	1.46	0.65	12.15	10.59	4.08	8.61	1.20	1.20	12.06	2.95	
Total	98.02	96.99	97.71	100.63	100.52	100.38	98.42	98.38	98.48	97.31	88.34	88.34	97.41	94.78	94.77	97.69	98.09	97.85	97.12	95.77	95.77	98.65	97.09	
No. oxygens	6	6	6	6	6	6	6	6	6	6	6	6	6	6	6	6	6	6	6	6	6	6	6	
Si	0.002	0.001	0.001	0.008	0.012	0.003	0.003	0.004	0.013	0.007	0.006	0.006	0.002	0.001	0.004	0.002	0.001	0.003	0.001	0.002	0.002	0.002	0.002	
Ti	1.778	1.802	1.800	1.923	1.895	1.936	1.983	1.991	1.938	1.978	2.012	2.012	1.790	1.728	1.761	1.820	1.815	1.743	1.767	1.779	1.779	1.815	1.760	
Al	0.010	0.009	0.019	0.001	0.002	0.000	0.001	0.001	0.003	0.001	0.000	0.000	0.002	0.007	0.006	0.002	0.002	0.007	0.000	0.005	0.002	0.006	0.002	
Cr	0.009	0.011	0.027	0.001	0.002	0.000	0.002	0.002	0.001	0.000	0.001	0.001	0.000	0.002	0.001	0.015	0.014	0.007	0.012	0.012	0.012	0.035	0.020	
V	0.005	0.005	0.005	n.a.	n.a.	n.a.	n.a.	n.a.	n.a.	0.006	0.000	0.000	0.002	0.001	0.001	0.004	0.002	0.000	0.003	0.000	0.000	n.a.	n.a.	
Fe ^{3+(a)}	0.416	0.370	0.347	0.136	0.182	0.120	0.026	0.007	0.094	0.024	0.000	0.000	0.413	0.533	0.463	0.335	0.350	0.493	0.449	0.422	0.422	0.294	0.122	
Fe ^{2+(a)}	1.009	1.599	0.956	1.622	1.780	1.805	1.839	1.800	1.767	1.792	1.777	1.777	1.425	1.533	1.617	0.943	1.038	1.394	1.106	1.606	1.606	0.961	1.627	
Mn	0.026	0.088	0.026	0.050	0.049	0.047	0.146	0.192	0.180	0.174	0.171	0.171	0.088	0.081	0.097	0.026	0.030	0.050	0.040	0.082	0.082	0.016	0.071	
Ni	0.000	0.000	0.002	0.000	0.001	0.000	0.001	0.001	0.000	0.000	0.000	0.000	0.000	0.000	0.000	0.004	0.002	0.001	0.002	0.001	0.002	0.002	0.000	
Mg	0.745	0.115	0.817	0.101	0.087	0.087	0.000	0.002	0.004	0.019	0.014	0.014	0.278	0.115	0.051	0.849	0.746	0.302	0.620	0.093	0.093	0.833	0.220	
Total cations	4.0	4.0	4.0	4.0	4.0	4.0	4.0	4.0	4.0	4.0	4.0	4.0	4.0	4.0	4.0	4.0	4.0	4.0	4.0	4.0	4.0	4.0	4.0	
Mg#	42.5	6.7	46.1	5.4	4.7	4.6	0.0	0.1	0.2	1.1	0.8	0.8	16.3	7.0	3.0	47.4	41.8	17.8	35.9	5.4	5.4	46.4	11.9	

Mg# = 100[Mg/(Mg+Fe²⁺)] in atomic units; * - FeO as total Fe; (a) - calculated assuming stoichiometry

lim - ilmenite; mpc - microphenocryst; xx - crystal; n.a. - not analyzed

Table 3: Representative garnet compositions from the Ailik Bay area ultramafic lamprophyres

Rock type	ultramafic lamprophyres																					
	aillikite				damtjernite				Zr-Srl													
Mineral	Kim	Kim	Kim	Kim	Kim	Kim	Kim	Mit	L70	Mit	L70	Mit	Srl	Mit	Zr-Srl	ST188A	Zr-Srl	ST188A	Zr-Srl	ST188A	Zr-Srl	
Sample#	L60	L66	L66	L66	ST162II	ST162II	ST164	ST164	ST140A	ST140A	ST140A	ST140A	ST188A	ST188A	ST188A	ST188A	ST188A	ST188A	ST188A	ST188A	ST188A	ST188A
	gm4	gm2	gm2	gm2	gm1	gm1	gm8	gm8	gm2	gm2	gm2	gm2	gm3	gm3	gm3	gm3	gm4	gm4	gm4	gm4	gm4	gm4
	core	rim	core	rim	core1	core1	core	core	core	rim	core	rim	core	rim	core	rim	core1	core2	core1	core2	core1	rim
SiO ₂	24.90	25.71	22.93	23.39	23.48	21.74	24.67	25.51	31.46	33.96	33.22	33.68	30.22	30.90	34.77	28.31	28.01	28.96				
TiO ₂	9.99	9.81	10.07	9.82	10.15	10.76	9.82	10.78	11.83	5.36	5.50	3.68	13.98	12.48	3.47	15.29	15.25	15.25				
ZrO ₂	14.98	13.69	16.51	15.92	16.06	17.17	14.83	12.51	0.40	0.15	0.30	0.31	1.11	0.60	0.05	4.93	3.86	2.99				
HfO ₂	0.31	0.27	0.36	0.27	0.28	0.28	0.25	0.17	0.00	0.00	0.04	0.03	0.12	0.12	0.03	0.16	0.13	0.13				
Al ₂ O ₃	2.14	1.47	3.26	2.55	2.58	2.96	2.22	1.53	1.39	2.21	1.89	2.02	0.53	0.63	1.71	0.29	0.29	0.28				
Cr ₂ O ₃	n.a	n.a	n.a	n.a	n.a	n.a	n.a	n.a	0.00	0.03	n.a	n.a	n.a	n.a	n.a	n.a	n.a	n.a				
FeO	12.07	12.92	11.98	12.54	12.31	12.25	12.32	13.34	18.27	20.26	18.78	20.42	17.15	18.20	21.58	15.75	16.20	16.81				
MnO	0.32	0.34	0.20	0.19	0.17	0.15	0.22	0.26	0.18	0.10	0.13	0.11	0.31	0.22	0.10	0.38	0.36	0.35				
MgO	3.32	3.21	2.93	2.85	2.91	2.55	3.21	3.03	1.22	1.06	1.71	1.36	1.18	1.22	0.91	0.99	0.93	0.90				
CaO	29.62	29.98	29.85	30.08	30.18	29.99	30.36	30.90	32.75	33.45	33.97	34.27	32.43	32.98	33.34	30.50	30.84	31.26				
BaO	n.a	n.a	n.a	n.a	n.a	n.a	n.a	n.a	0.04	0.05	n.a	n.a	n.a	n.a	n.a	n.a	n.a	n.a				
SiO	0.00	0.00	0.00	0.00	0.00	0.00	0.00	0.00	0.00	0.03	0.02	0.00	0.01	0.00	0.00	0.00	0.01	0.00				
Na ₂ O	0.03	0.00	0.00	0.03	0.00	0.04	0.01	0.00	0.22	0.08	0.11	0.07	0.54	0.37	0.16	1.10	1.05	0.91				
K ₂ O	n.a	n.a	n.a	n.a	n.a	n.a	n.a	n.a	0.00	0.02	n.a	n.a	n.a	n.a	n.a	n.a	n.a	n.a				
Total	97.68	97.41	98.10	97.62	98.11	97.89	97.91	98.03	97.75	96.75	95.68	95.96	97.57	97.73	96.12	97.70	97.92	97.83				
No. oxygens	12	12	12	12	12	12	12	12	12	12	12	12	12	12	12	12	12	12				
Si	2.227	2.296	2.060	2.107	2.106	1.973	2.198	2.253	2.650	2.849	2.805	2.635	2.569	2.612	2.929	2.452	2.494	2.486				
Al	0.226	0.154	0.345	0.271	0.273	0.317	0.233	0.160	0.138	0.151	0.188	0.165	0.053	0.063	0.071	0.030	0.029	0.029				
Fe ³⁺	0.547	0.549	0.595	0.622	0.621	0.710	0.569	0.587	0.212	0.000	0.007	0.000	0.378	0.325	0.000	0.519	0.477	0.486				
Ti	0.000	0.000	0.000	0.000	0.000	0.000	0.000	0.000	0.000	0.000	0.000	0.000	0.000	0.000	0.000	0.000	0.000	0.000				
[T]	3.0	3.0	3.0	3.0	3.0	3.0	3.0	3.0	3.0	3.0	3.0	3.0	3.0	3.0	3.0	3.0	3.0	3.0				
Al	0.000	0.000	0.000	0.000	0.000	0.000	0.000	0.000	0.000	0.068	0.000	0.035	0.000	0.000	0.099	0.000	0.000	0.000				
Fe ³⁺	0.356	0.416	0.305	0.323	0.303	0.219	0.349	0.398	0.919	1.422	1.320	1.437	0.829	0.917	1.520	0.622	0.688	0.721				
Ti	0.672	0.659	0.681	0.665	0.685	0.735	0.658	0.716	0.750	0.338	0.349	0.233	0.894	0.793	0.220	0.996	0.986	0.985				
Fe ²⁺	0.000	0.000	0.000	0.000	0.000	0.000	0.000	0.000	0.156	0.000	0.000	0.000	0.013	0.044	0.000	0.000	0.000	0.000				
Zr	0.653	0.596	0.723	0.699	0.703	0.760	0.644	0.539	0.017	0.006	0.012	0.013	0.046	0.025	0.002	0.208	0.162	0.125				
Hf	0.008	0.007	0.009	0.007	0.007	0.007	0.006	0.004	0.000	0.000	0.001	0.001	0.003	0.003	0.001	0.004	0.003	0.003				
Mg	0.281	0.296	0.266	0.287	0.290	0.261	0.324	0.323	0.109	0.132	0.215	0.171	0.104	0.141	0.115	0.000	0.000	0.000				
Na	0.006	0.000	0.000	0.005	0.000	0.007	0.002	0.000	0.036	0.013	0.018	0.011	0.089	0.061	0.026	0.185	0.175	0.151				
[Y]	2.0	2.0	2.0	2.0	2.0	2.0	2.0	2.0	2.0	2.0	1.9	1.9	2.0	2.0	2.0	2.0	2.0	2.0				
Ca	2.839	2.869	2.873	2.904	2.901	2.916	2.898	2.924	2.956	3.007	3.074	3.091	2.954	2.987	3.010	2.830	2.841	2.875				
Mg	0.161	0.131	0.127	0.096	0.099	0.084	0.102	0.076	0.044	0.000	0.000	0.000	0.046	0.013	0.000	0.127	0.119	0.115				
Mn	0.000	0.000	0.000	0.000	0.000	0.000	0.000	0.000	0.000	0.000	0.000	0.000	0.000	0.000	0.000	0.000	0.000	0.000				
[X]	3.0	3.0	3.0	3.0	3.0	3.0	3.0	3.0	3.0	3.0	3.1	3.1	3.0	3.0	3.0	3.0	3.0	3.0				

Garnets recalculated on the basis of 12 oxygens following Munno *et al.* (1980); Kim - kimzeyite; Srl - schorlomite; Mit - melanite; gm - groundmass

n.a. = not analyzed

Table 10: Representative nepheline, sodalite, alkali feldspar and pectolite compositions of damtjernites from the Aillik Bay area

Mineral Sample#	Rock type <i>ultramafic lamprophyres</i> damtjernite																			
	Ne gm3 core	Sdl ST188B gm3 rim1	Sdl ST211C gm1 rim2	Ne ST211C gm1 core	Ne ST211C rim1	Sdl ST211C gm1 rim2	Ab ST246A gm2 core1	Ab ST246A gm2 core2	Or ST246A gm2 core3	Or ST246A gm2 core4	Or ST206A seg4 core1	Or ST206A seg4 core2	Ab ST206A seg4 core3	Ab ST206A seg4 core3	Pct ST174 gm8 core1	Pct ST174 gm8 core2	Pct ST188A gm3 core1	Pct ST188A gm3 core2	Pct ST256 gm1 core	Pct ST256 gm1 rim
SiO ₂	41.12	37.15	37.07	41.21	42.14	37.58	68.37	68.25	63.69	64.27	64.06	63.23	67.81	67.81	52.58	52.78	52.73	52.55	53.17	53.04
TiO ₂	0.00	0.00	0.01	0.02	0.03	0.03	0.00	0.00	0.01	0.04	0.02	0.06	0.03	0.03	0.20	0.21	0.06	0.08	0.11	0.20
Al ₂ O ₃	34.41	33.35	33.76	33.08	32.95	36.36	19.43	19.50	18.55	18.28	18.26	18.21	19.75	19.75	0.02	0.03	0.25	0.34	0.07	0.10
Cr ₂ O ₃	0.00	0.03	0.03	0.06	0.02	0.04	0.04	0.07	0.01	0.03	0.01	0.03	0.05	0.05	0.04	0.01	0.06	0.03	0.01	0.00
FeO	1.40	0.11	0.05	1.08	1.36	0.67	0.23	0.29	0.23	0.22	0.11	0.09	0.14	0.14	0.52	0.40	0.10	0.21	0.56	1.58
MnO	0.00	0.01	0.00	0.00	0.00	0.00	0.00	0.00	0.00	0.04	0.04	0.00	0.05	0.05	0.34	0.32	0.32	0.16	0.30	0.89
MgO	0.03	0.03	0.03	0.04	0.04	0.00	0.01	0.02	0.00	0.01	0.01	0.00	0.02	0.02	0.14	0.12	0.08	0.02	0.12	0.13
CaO	0.15	0.04	0.04	0.22	0.10	0.46	0.03	0.04	0.00	0.01	0.07	0.37	0.18	0.18	32.45	32.60	32.92	33.21	32.77	29.91
BaO	0.10	0.02	0.00	0.03	0.00	0.00	0.01	0.06	0.10	0.04	0.84	0.93	0.00	0.00	0.07	0.14	0.21	0.03	0.00	0.07
Na ₂ O	15.88	23.07	23.27	16.14	16.28	18.99	12.05	12.00	0.21	0.21	0.29	0.26	11.51	11.51	9.33	9.28	9.16	9.09	8.83	9.13
K ₂ O	7.36	0.06	0.01	6.68	6.71	0.00	0.03	0.05	16.60	16.75	15.87	16.16	0.01	0.01	0.00	0.00	0.00	0.00	0.00	0.01
F	0.09	0.00	0.00	0.00	0.01	0.00	n.a	n.a	n.a	n.a	n.a	n.a	n.a	n.a	n.a	n.a	n.a	n.a	n.a	n.a
Cl	0.00	7.40	7.42	0.01	0.01	6.30	n.a	n.a	n.a	n.a	n.a	n.a	n.a	n.a	n.a	n.a	n.a	n.a	n.a	n.a
O=Cl	0.00	-1.67	-1.67	0.00	0.00	-1.42	n.a	n.a	n.a	n.a	n.a	n.a	n.a	n.a	n.a	n.a	n.a	n.a	n.a	n.a
Total	100.54	99.60	100.03	98.56	99.65	99.01	100.20	100.28	99.39	99.90	99.58	99.33	99.54	99.54	95.68	95.90	95.88	95.71	95.94	95.06

Ne - nepheline; Sdl - sodalite; Ab - albite; Or - orthoclase; Pct - pectolite
gm - groundmass; seg - segregation; n.a. - not analyzed

Table 11: Major (wt. %) and trace element (ppm) concentrations of representative Neoproterozoic Aillik Bay area UML and carbonatites

Rock type	ultramafic lamprophyres										carbonatites															
	aillikite/mela-aillikite					damlilitite					dolomite carbonatite*					calcite carbonatite										
	L60	ST109	ST164	ST220II	ST225	ST260A	ST147B	ST196	ST244B	ST170	ST174	ST188A	ST206A1	ST224B	ST226	ST246A	ST256	L1	ST189	ST203	ST126	ST193A	ST198C	ST199		
SiO ₂	23.86	18.23	24.05	26.14	26.39	22.46	31.56	35.93	32.07	38.02	33.08	30.71	30.64	33.45	36.54	34.57	32.68	10.65	3.91	10.13	17.59	9.10	11.71	13.90		
TiO ₂	3.79	3.55	3.32	4.77	3.26	2.49	5.76	4.44	5.47	5.67	6.05	4.82	6.87	4.95	5.94	6.38	5.25	0.52	0.07	0.26	2.33	1.22	2.05	2.01		
Al ₂ O ₃	2.95	2.80	3.32	3.19	2.53	3.13	3.97	4.77	3.99	7.89	8.47	7.42	6.96	5.39	9.85	7.50	7.29	1.98	0.08	0.15	1.98	1.78	2.14	2.10		
Fe ₂ O ₃	13.46	15.98	13.16	14.97	13.24	12.17	17.52	14.66	14.73	14.32	15.80	14.37	15.73	15.82	14.77	14.46	14.98	7.27	6.17	8.56	8.44	5.28	10.36	8.28		
MnO	0.25	0.25	0.24	0.22	0.23	0.23	0.19	0.17	0.18	0.23	0.32	0.29	0.21	0.19	0.34	0.25	0.28	0.53	0.59	0.46	0.29	0.31	0.31	0.27		
MgO	19.10	15.89	18.59	16.51	20.91	20.42	16.75	22.17	20.17	6.80	5.86	6.36	7.82	15.87	6.28	6.43	7.86	11.13	16.77	12.88	10.72	7.15	8.30	8.09		
CaO	17.59	19.67	18.07	16.05	16.44	15.61	10.97	8.18	10.32	16.97	18.32	19.81	18.02	10.29	13.87	13.79	17.78	23.85	28.11	22.78	26.69	36.35	30.75	31.79		
Na ₂ O	0.30	0.15	0.20	0.68	0.16	0.18	0.63	0.48	0.65	1.29	2.23	4.29	1.08	1.68	2.09	1.94	2.14	0.37	0.70	1.12	0.23	0.24	1.36	1.10		
K ₂ O	1.64	1.79	1.96	1.50	1.40	2.06	1.92	1.68	1.88	2.08	2.42	2.60	1.99	0.88	2.30	2.78	2.56	1.24	0.20	0.22	1.41	0.96	0.81	1.51		
P ₂ O ₅	2.07	3.06	3.02	2.25	2.04	1.49	1.34	0.59	0.98	1.84	2.25	2.90	2.75	1.15	1.68	1.86	2.40	2.83	0.44	1.93	0.35	2.04	4.90	3.96		
LOI	3.18	3.84	2.47	1.4	2.2	4.67	3.38	3.86	2.98	2.48	3.61	2.92	1.84	1.84	3.03	2.96	3.35	0	2.19	0.24	2.74	1.59	0.59	1.52		
CO ₂	10.75	13.50	10.30	11.10	10.10	13.80	4.60	2.04	5.44	1.10	0.22	2.31	4.75	7.30	2.64	6.80	2.00	32.20	39.50	32.30	26.00	30.50	25.70	24.20		
Total	98.94	98.71	98.69	98.78	98.89	98.71	98.59	98.97	98.56	98.69	98.63	98.80	98.66	98.81	99.32	98.81	98.57	92.52	98.73	91.03	98.77	98.52	98.58	98.73		
Mg#	73.8	66.3	73.7	68.6	75.8	76.9	65.4	75.0	73.1	48.5	42.4	46.7	49.6	66.5	45.7	46.8	51.0	75.2	84.3	74.9	71.6	72.8	61.3	65.9		
LFSE																										
Cs	1.56	1.53	1.94	2.29	n.a.	6.13	1.56	4.97	2.83	0.57	1.18	1.38	0.94	18.40	22.81	1.37	n.a.	n.a.	n.a.	b.d.	1.06	b.d.	2.98	n.a.		
Rb	55	61	66	38	29	75	49	65	58	32	56	55	56	38	63	70	127	38	14	31	85	22	19	30		
Ba	1860	2777	1540	714	1018	1366	594	622	838	846	1583	1205	1213	635	1443	1282	1469	23578	7130	37275	1680	6958	1528	1835		
Sr	2685	1678	2784	2511	2868	1312	1330	564	1147	1074	3958	3346	1372	932	1344	1418	3296	3355	1870	2015	1005	3060	5555	3427		
HFSE																										
Th	24.07	23.99	14.90	16.99	20.11	15.49	9.18	5.76	14.86	48.66	38.66	22.99	43.39	10.02	32.82	39.21	16.03	64.00	111.04	128.77	16.69	10.84	40.14	13.44		
U	18.17	4.54	11.54	9.34	7.02	5.82	4.47	1.19	7.12	7.88	11.71	9.95	10.69	1.85	6.74	6.74	9.72	38.90	5.36	6.38	1.89	8.42	8.19	20.27		
Nb	166	203	153	177	159	184	130	109	117	205	373	316	226	94	256	218	274	434	154	94	245	207	269	233		
Ta	12.55	12.74	8.68	8.57	9.91	10.35	7.47	5.52	7.78	17.55	20.76	13.95	18.53	5.15	18.38	14.74	10.18	9.71	0.24	5.20	18.04	2.92	13.06	7.95		
Pb	13.0	11.9	8.5	7.5	9.6	9.0	4.2	b.d.	4.6	22.7	56.6	13.5	12.1	b.d.	10.0	10.0	13.0	31.5	80.9	46.5	9.0	11.3	12.5	18.2		
Zr	466	591	608	359	306	303	491	306	351	735	1247	865	666	451	849	534	838	110	35	75	325	110	443	506		
Hf	11.45	13.95	14.20	8.46	7.30	8.62	11.74	8.45	9.06	19.27	33.26	18.97	19.34	12.15	21.50	18.46	19.60	1.72	1.79	3.11	13.94	3.28	9.71	9.47		
Y	41	43	46	55	43	27	35	18	28	72	95	92	82	31	79	194	76	98	90	95	49	45	123	57		
REE																										
La	367	390	235	272	335	242	116	52	112	267	358	354	308	83	310	226	278	3920	1520	1490	215	347	564	376		
Ce	744	819	489	572	700	476	268	109	240	627	750	619	684	180	625	425	500	6780	3000	2850	431	510	1240	741		
Pr	86.3	95.8	55.1	65.5	82.3	52.4	32.7	13.1	28.4	77.0	86.9	67.4	78.5	21.8	69.0	47.5	56.6	594.2	305.3	369.6	46.4	52.1	147.3	82.3		
Nd	322	364	215	251	319	188	134	53	112	309	339	255	318	93	270	181	219	1690	1040	1030	167	185	607	314		
Sm	49.8	54.6	36.8	45.4	47.2	28.1	25.8	10.6	21.2	56.0	64.6	51.5	60.2	18.6	49.8	39.6	42.7	139	107	106	23.3	29.0	100	49.4		
Eu	12.54	13.46	10.11	12.43	12.57	7.14	7.16	3.03	6.00	15.80	18.98	15.75	17.43	5.39	14.62	11.35	13.50	26.72	22.26	20.52	5.28	7.90	27.02	13.78		
Gd	30.82	33.37	26.47	30.98	30.68	17.37	19.24	8.19	14.91	38.89	48.38	41.52	46.01	14.27	36.97	37.79	34.15	59.88	45.86	44.23	13.73	18.90	68.27	32.56		
Tb	3.14	3.30	3.02	3.64	3.38	1.91	2.24	1.04	1.83	4.67	6.18	5.61	5.82	1.83	4.77	6.23	4.86	4.72	4.22	3.39	1.61	2.24	7.71	3.81		
Dy	12.29	12.82	12.51	15.13	13.23	7.70	9.47	4.44	7.50	20.05	26.71	24.46	23.96	7.99	20.63	36.42	21.52	20.70	15.07	13.88	8.08	9.68	32.38	15.67		
Ho	1.59	1.65	1.74	2.10	1.83	1.11	1.31	0.64	1.12	2.82	3.97	3.53	3.32	1.17	3.02	7.25	3.15	3.38	2.70	2.23	1.58	1.44	4.52	2.24		
Er	3.44	3.63	3.98	4.84	4.00	2.44	2.91	1.52	2.64	6.60	8.53	8.17	7.73	2.77	7.08	20.87	7.37	9.92	12.84	6.88	5.88	3.68	10.34	5.26		
Tm	0.98	0.39	0.44	0.54	0.42	0.29	0.33	0.19	0.32	0.74	0.91	0.94	0.78	0.34	0.87	2.14	0.84	1.21	3.07	0.98	1.08	0.48	1.26	0.87		
Yb	1.95	2.05	2.26	2.77	2.19	1.47	1.82	1.10	1.68	3.81	4.91	4.85	3.92	1.73	4.49	14.43	4.44	7.47	30.52	7.43	8.07	2.79	7.04	3.37		
Lu	0.22	0.23	0.27	0.30	0.25	0.17	0.22	0.14	0.20	0.46	0.60	0.58	0.42	0.20	0.51	1.54	0.52	0.98	4.97	1.21	1.35	0.38	0.87	0.42		
Trans. Metals																										
Cr	601	520	700	606	577	734	705	1150	939	b.d.	b.d.	b.d.	25	586	58	32	52	60	b.d.	b.d.	618	139	b.d.	44		
Co	67	62	66	75	78	63	91	90	88	36	31	37	44	78	37	35	38	17	6	6	58	16	23	21		
Ni	441	211	483	493	719	487	593	749	670	43	23	61	85	513	55	46	93	40	b.d.	b.d.	204	87	33	74		
Sc	24	28	29	18	15	21	22	22	25	21	16	10	25	24	13	18	18	48	b.d.	b.d.	26	25	12	14		
V	205	267	204	242	194	197	293	267	287	318	390	328	379	289	346	380	405	85	30	73	112	168	197	298		

Mg# (minimum mg-number with Fe²⁺ as total Fe) = 100[Mg/(Mg+Fe²⁺)] in atomic units
 n.a. = not analyzed; b.d. = below detection

Table 12: Sr-Nd isotope composition of representative Neoproterozoic Aillik Bay area UML, carbonatites and a cognate inclusion

Sample#	Rb	Sr	$^{87}\text{Sr}/^{86}\text{Sr}_m$	$^{87}\text{Sr}/^{86}\text{Sr}_f$	Sm	Nd	$^{143}\text{Nd}/^{144}\text{Nd}_m$	$^{143}\text{Nd}/^{144}\text{Nd}_f$	$\epsilon_{\text{Nd}}^{**}$	$^{147}\text{Sm}/^{144}\text{Nd}_{\text{DM}}$	$^{147}\text{Sm}/^{144}\text{Nd}_{\text{DM}}$
aillikite											
L60	55.3	2685	0.704371(7)	0.70389	49.8	322	0.512264(5)	0.51191	0.4	0.51191	1.1
ST109	61.0	1678	0.704828(7)	0.70398	54.6	364	0.512253(3)	0.51191	0.3	0.51191	1.0
ST164	66.3	2784	0.704497(7)	0.70394	36.8	215	0.512314(5)	0.51192	0.6	0.51192	1.1
ST220II	37.9	2511	0.704040(7)	0.70369	45.4	251	0.512313(5)	0.51189	0.1	0.51189	1.1
ST225	28.8	2868	0.703999(7)	0.70376	47.2	319	0.512279(5)	0.51194	0.9	0.51194	1.0
ST250A	74.9	1312	0.705223(10)	0.70389	28.1	188	0.512251(6)	0.51191	0.3	0.51191	1.0
mela-aillikite											
ST147B	48.6	1330	0.704654(10)	0.70380	25.8	134	0.512335(4)	0.51189	0.1	0.51189	1.2
ST196	65.5	564	0.705967(7)	0.70325	10.6	53.4	0.512399(5)	0.51194	1.0	0.51194	1.1
ST244B	57.5	1147	0.705726(7)	0.70455	21.2	112	0.512419(5)	0.51198	1.8	0.51198	1.0
cpx-phl nodule											
ST162I	90.2	510	0.708075(7)	0.70393	6.8	29.1	0.512446(5)	0.51190	0.2	0.51190	1.4
damijerinite											
ST140	46.6	1342	0.704384(7)	0.70357	45.2	216	0.512446(5)	0.51196	1.4	0.51196	1.1
ST174	55.7	3958	0.704304(7)	0.70397	64.6	339	0.512372(8)	0.51193	0.8	0.51193	1.1
ST188A	54.6	3346	0.703984(7)	0.70360	51.5	255	0.512402(4)	0.51194	0.9	0.51194	1.1
ST206AI	56.4	1372	0.704729(7)	0.70377	60.2	318	0.512402(5)	0.51196	1.5	0.51196	1.1
ST224B	38.4	932	0.704944(7)	0.70398	18.6	92.8	0.512375(8)	0.51191	0.5	0.51191	1.2
ST226	62.9	1344	0.705013(10)	0.70392	49.8	270	0.512396(6)	0.51197	1.6	0.51197	1.0
ST246A	70.2	1418	0.705594(7)	0.70443	39.6	181	0.512454(5)	0.51195	1.1	0.51195	1.2
ST256	127	3296	0.707524(7)	0.70662	42.7	219	0.512435(5)	0.51198	1.9	0.51198	1.1
dol carbonatite											
L1	38.0	3355	0.704472(7)	0.70421	139	1690	0.512109(4)	0.51192	0.6	0.51192	0.9
ST189	14.1	1870	0.704168(7)	0.70399	107	1040	0.512189(5)	0.51195	1.3	0.51195	0.9
ST203	31.3	2015	0.705026(7)	0.70466	106	1030	0.512188(5)	0.51195	1.2	0.51195	0.9
dol-cal carbonatite											
ST126	85.4	1005	0.707782(7)	0.70579	23.3	167	0.512224(6)	0.51190	0.3	0.51190	1.0
ST193A	21.8	3060	0.704094(7)	0.70393	29.0	185	0.512282(6)	0.51192	0.6	0.51192	1.0
ST198C	19.4	5555	0.703967(7)	0.70389	100	607	0.512300(5)	0.51192	0.6	0.51192	1.1
ST199	30.3	3427	0.704142(7)	0.70394	49.4	314	0.512295(5)	0.51193	0.8	0.51193	1.0
ST231A	49.2	537	0.706439(7)	0.70429	31.2	159	0.512371(5)	0.51192	0.6	0.51192	1.2

*Initial isotope ratios calculated for an emplacement age of 582 Ma.

Initial epsilon Nd values were calculated using ^{147}Sm decay constant of 6.54×10^{-12} , $^{143}\text{Nd}/^{144}\text{Nd}_{\text{CHUR}} = 0.512638$ and $(^{147}\text{Sm}/^{144}\text{Nd})_{\text{CHUR}} = 0.1967$ *Depleted Mantle model ages $[T_{\text{DM}}]_{\text{Nd}}$ were calculated using ^{147}Sm decay constant of $6.54 \times 10^{-12} \text{ y}^{-1}$, $(^{143}\text{Nd}/^{144}\text{Nd})_{\text{DM}} = 0.513150$ and $(^{147}\text{Sm}/^{144}\text{Nd})_{\text{DM}} = 0.222$

Numbers in parentheses are 2-sigma errors of the mean for individual isotope ratio measurements; elemental abundances are ICP-MS data.

Table 13: Bulk rock carbonate C and O isotope composition of Aillik Bay area UML and carbonatites

Sample#	$\delta^{13}\text{C}_{\text{PDB}}$ (‰)	$\delta^{18}\text{O}_{\text{SMOW}}$ (‰)
<i>aillikite</i>		
L60	-5.7	9.5
ST109	-5.3	10.7
ST164	-5.2	9.4
ST164repl.1	-5.3	9.5
ST164repl.2	-5.2	9.7
ST220II	-4.0	11.6
ST250A	-5.0	11.0
ST250Arepl.1	-5.1	11.6
<i>damtjernite</i>		
ST188A	-7.0	11.4
ST206AI	-4.7	9.9
ST226	-5.9	10.4
ST246A	-3.0	11.3
<i>dol carbonatite</i>		
L1	-2.8	11.1
L1repl.1	-2.7	11.5
ST203	-2.8	10.8
<i>dol-cal carbonatite</i>		
ST126	-3.3	10.2
ST126repl.1	-3.3	10.7
ST126repl.2	-3.3	10.3
ST127	-3.7	9.6
ST127repl.1	-3.7	9.7
ST198C	-3.7	10.8
ST198Crepl.1	-3.7	10.7
ST199	-4.8	10.0
ST199repl.1	-4.7	10.0
ST231A	-4.1	13.0
ST231Arepl.1	-4.2	13.2

Replicate analysis = i.e. repl.1

FIGURES

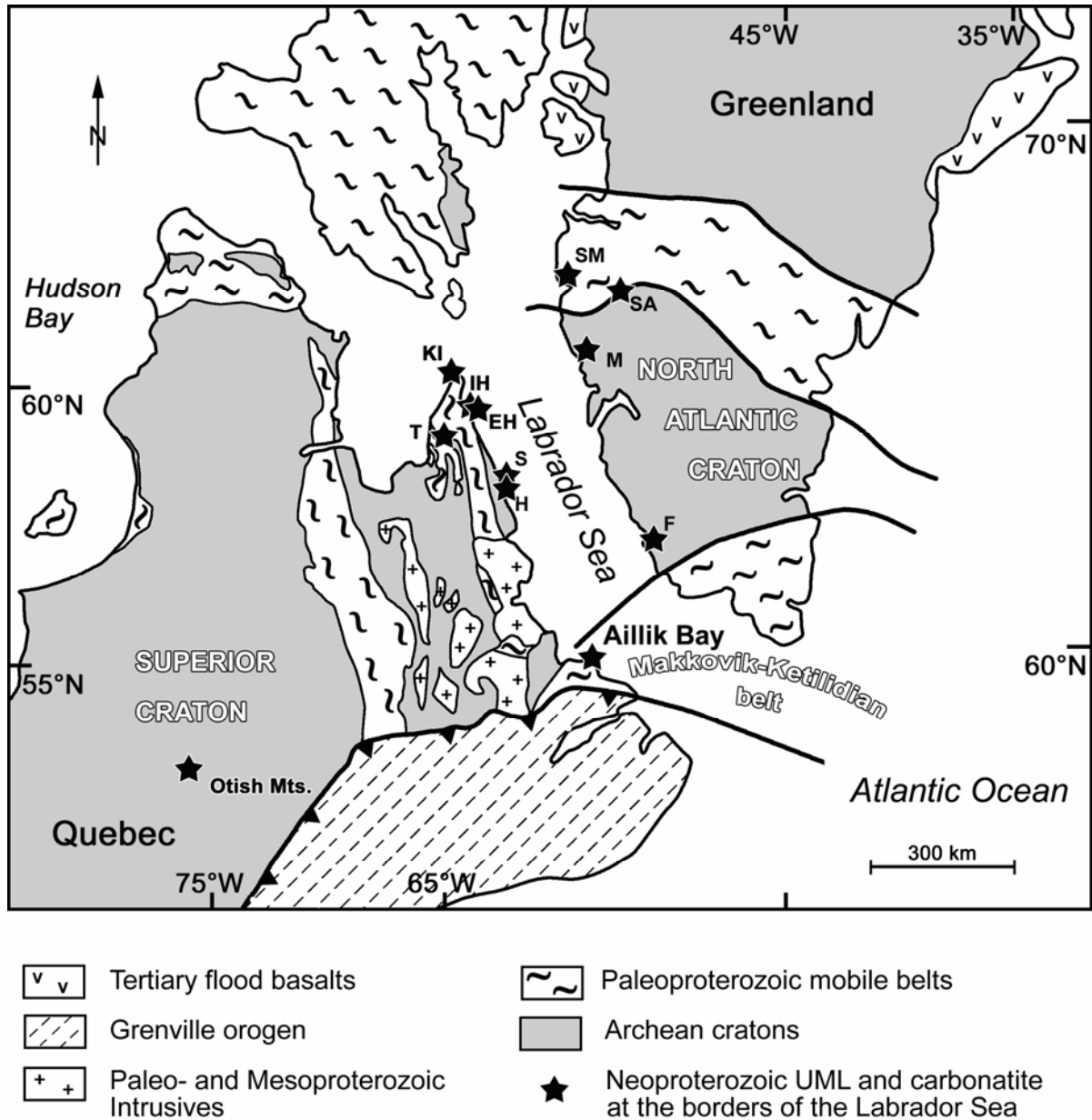


Figure 1: Simplified geology of the northeastern Canadian-Greenland Shield restored for Mesozoic drift (modified from Connelly *et al.*, 2000). A collage of Archean cratons and Proterozoic mobile belts is apparent. Abbreviations for Neoproterozoic ultramafic lamprophyre (UML) and carbonatite occurrences are: **EH** – Eclipse Harbour, **F** – Frederikshåb, **H** – Hebron, **IH** – Iselin Harbour, **KI** – Killinek Island, **M** – Maniitsoq, **S** – Saglek, **SA** – Sarfartoq, **SM** – Sisimiut, **T** – Torngat/Abloviak.

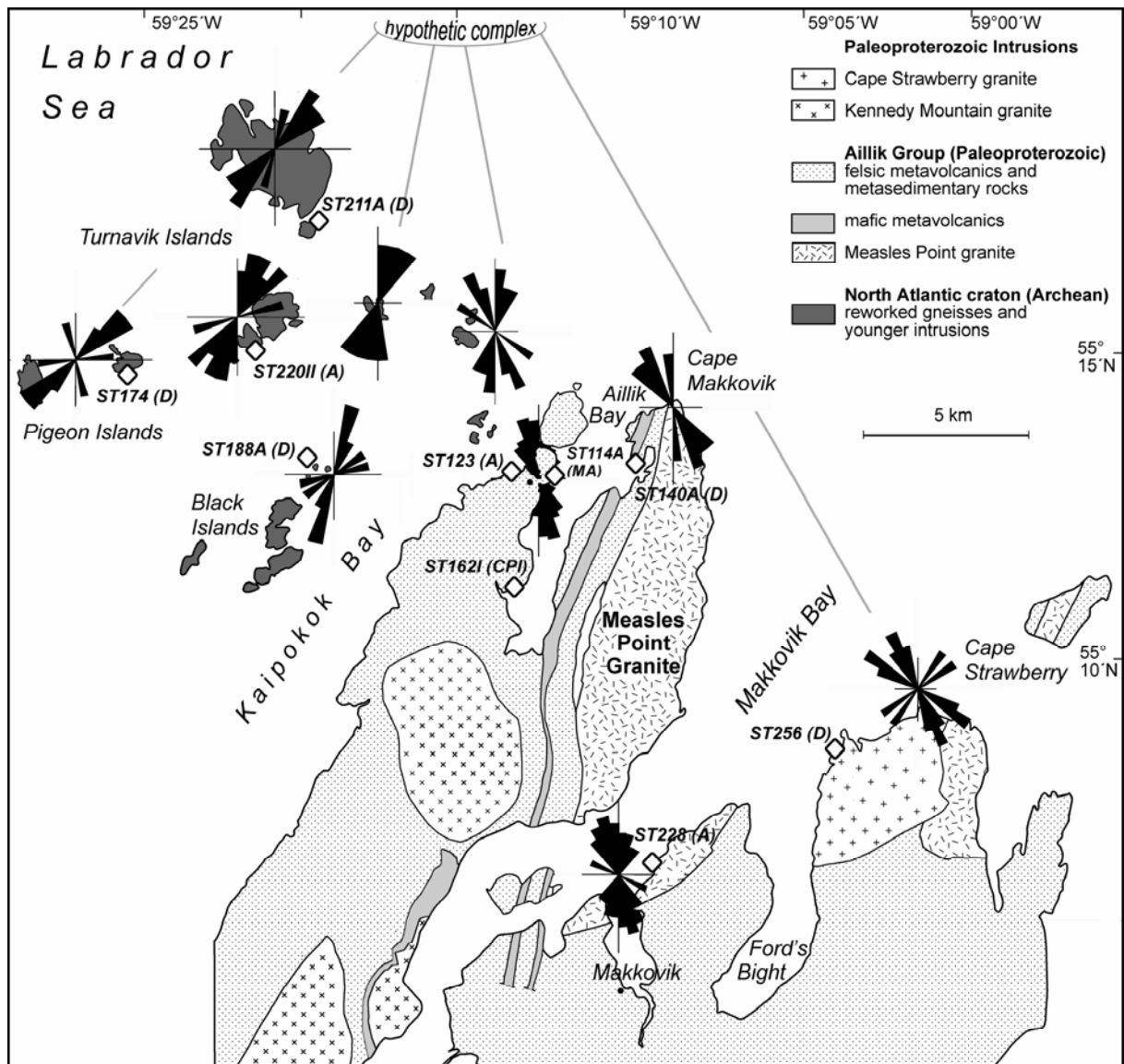


Figure 2: Simplified geologic map of the Aillik Bay area based on Sinclair *et al.* (2002). Rose diagrams illustrate the orientation of steeply dipping ($> 45^\circ$) ultramafic lamprophyre and carbonatite dykes of the Late Neoproterozoic Aillik Bay intrusive suite. Single diagrams are compiled either from longer coastal sections or neighbouring islands and imply dyke convergence to a hypothetic complex in the Labrador Sea. Open diamonds indicate sample locations for U-Pb dated aillikites (A), mela-aillikites (MA) and damtjernites (D) as well as the Ar-Ar dated clinopyroxene-phlogopite cognate inclusion (CPI).

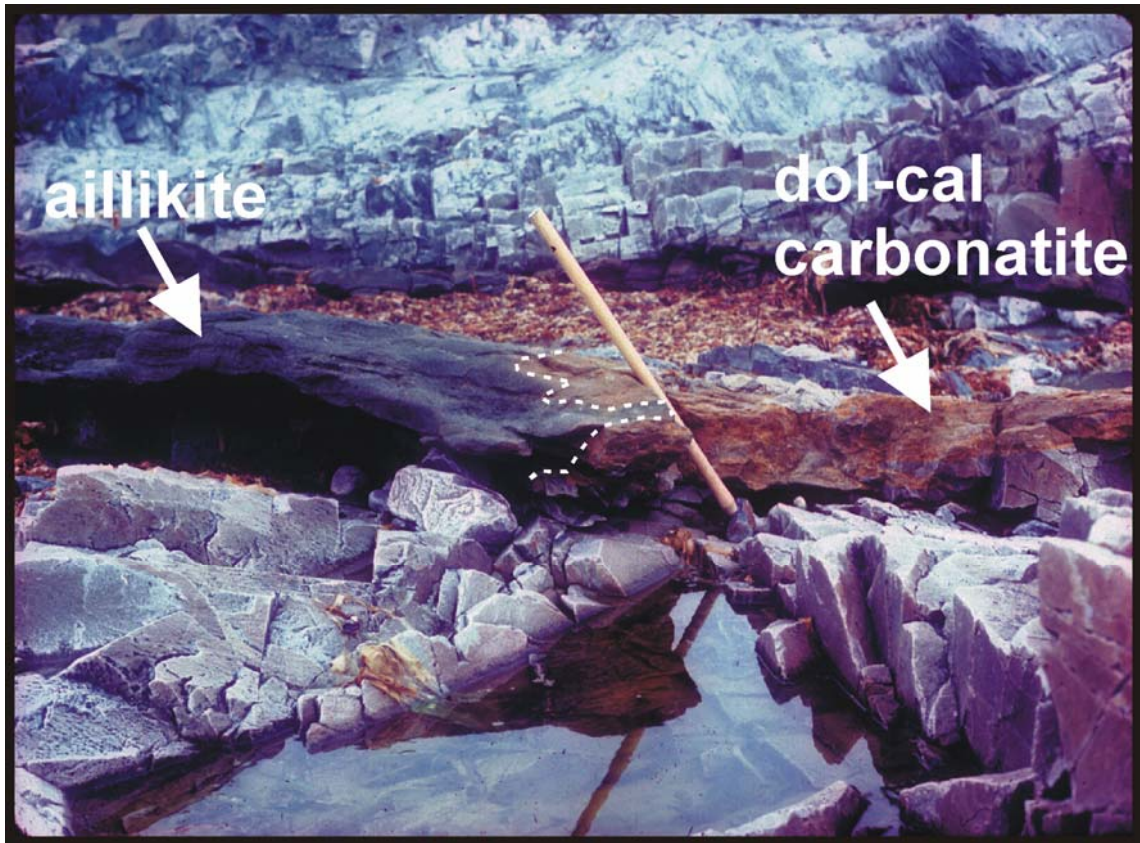
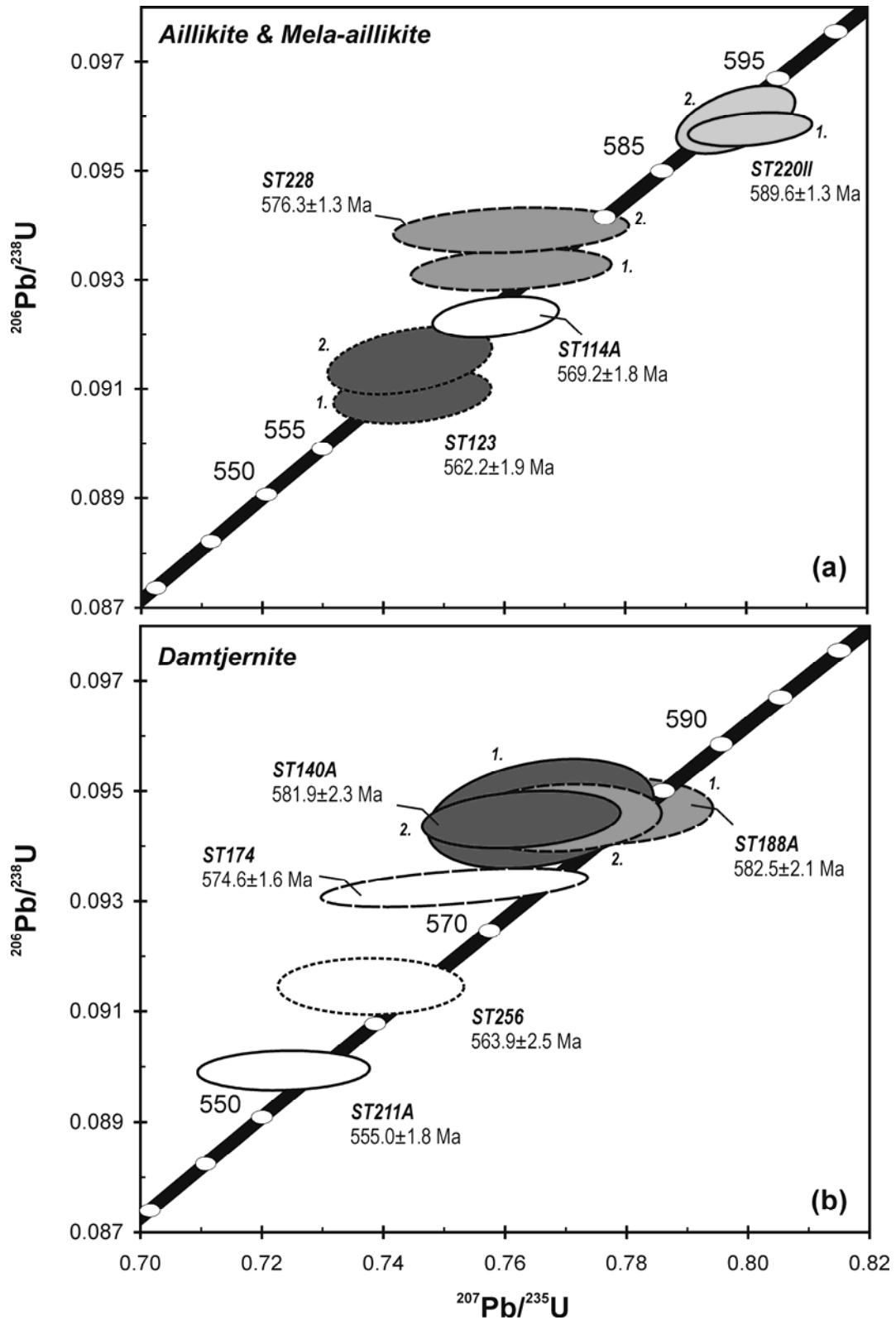


Figure 3: Flat lying aillikite sheet from Cape Makkovik. The dark-coloured aillikite at the left grades into yellowish dolomite-calcite carbonatite at the right with the hammer being close to the interface (ca. 1 metre long).

**Figure 4**

U-Pb perovskite results for (a) aillikites/mela-aillikite and (b) damtjernites from the Aillik Bay area displayed in concordia diagrams. Reported ages are $^{206}\text{Pb}/^{238}\text{U}$ dates (quoted errors and error envelopes at 2-sigma), and in cases where two perovskite fractions were analyzed the weighted average $^{206}\text{Pb}/^{238}\text{U}$ date is given (see text and Table 1 for details).

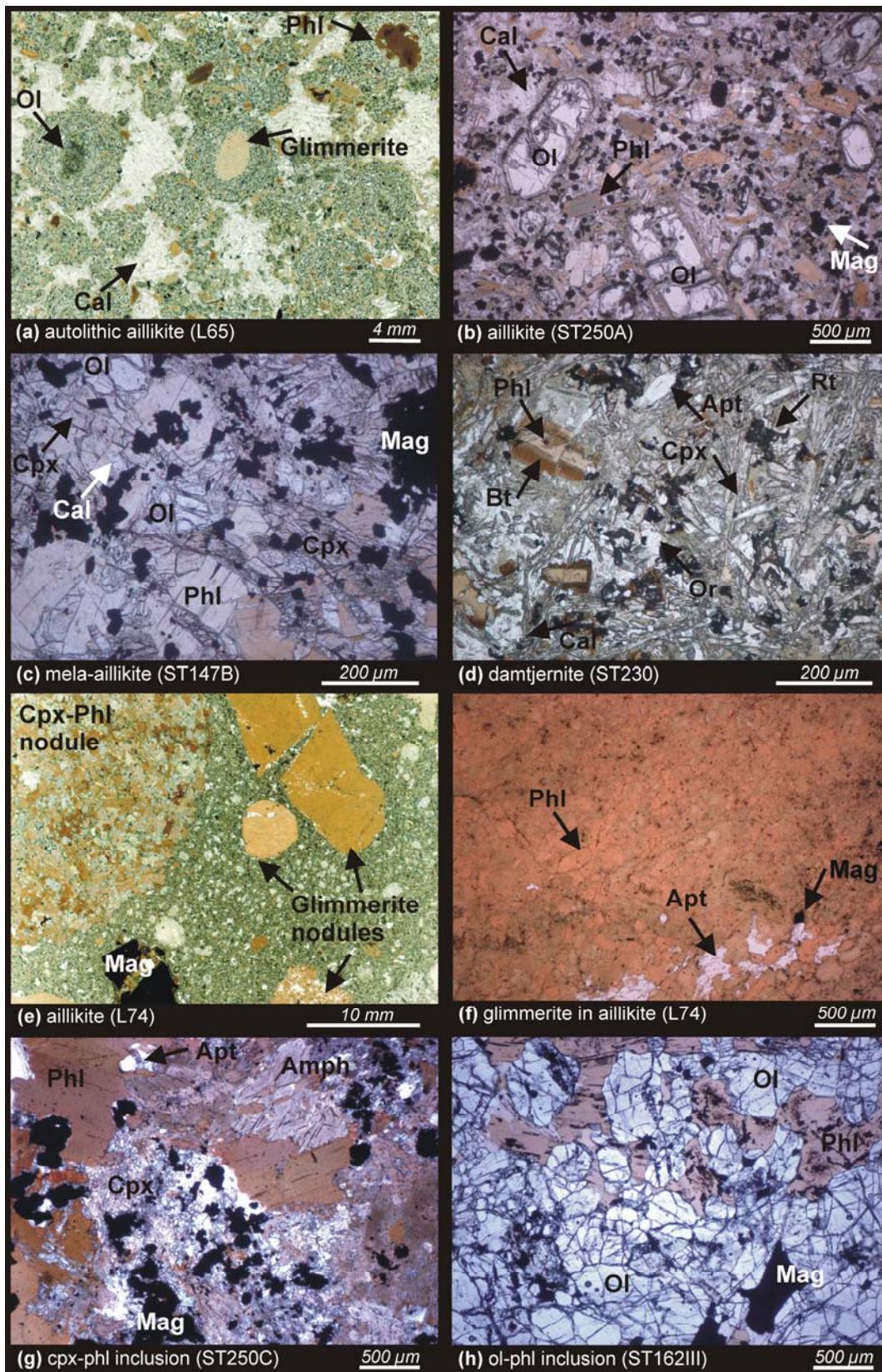


Figure 5: Photomicrographs of the Aillik Bay area UML and associated cognate inclusions: (see details on the next page)

Figure 5:

Photomicrographs of the Aillik Bay area UML and associated cognate inclusions: **(a)** Fluidized breccia consisting of nucleated aillikite autoliths cemented by calcite laths. The autoliths contain kernels of olivine and fragments from cognate inclusions surrounded by aillikite matrix. **(b)** Porphyritic aillikite containing abundant olivine, phlogopite and spinel phenocrysts which are set in a carbonate groundmass. **(c)** Intergranular mel-aillikite with abundant olivine, phlogopite, clinopyroxene and spinel. Carbonate is restricted to the interstices between the mafic silicates. **(d)** Damjernite with phlogopite phenocrysts. These are rimmed by dark biotite. Acicular groundmass clinopyroxene and apatite form a mesh with alkali feldspar, nepheline and carbonate as intercumulus phase. **(e)** Porphyritic aillikite with rounded cognate micaceous inclusions. **(f)** Glimmerite inclusion in aillikite consisting of interlocking phlogopite flakes, tiny opaque oxide grains and interstitial apatite. **(g)** Clinopyroxene-phlogopite nodule in aillikite consisting of large phlogopite plates with opaque oxide and apatite inclusions and clinopyroxene prisms, which are partly replaced by pargasitic amphibole. Calcic amphibole also occurs as larger intercumulus phase. **(h)** Cumulate-textured olivine-phlogopite cognate inclusion in aillikite.

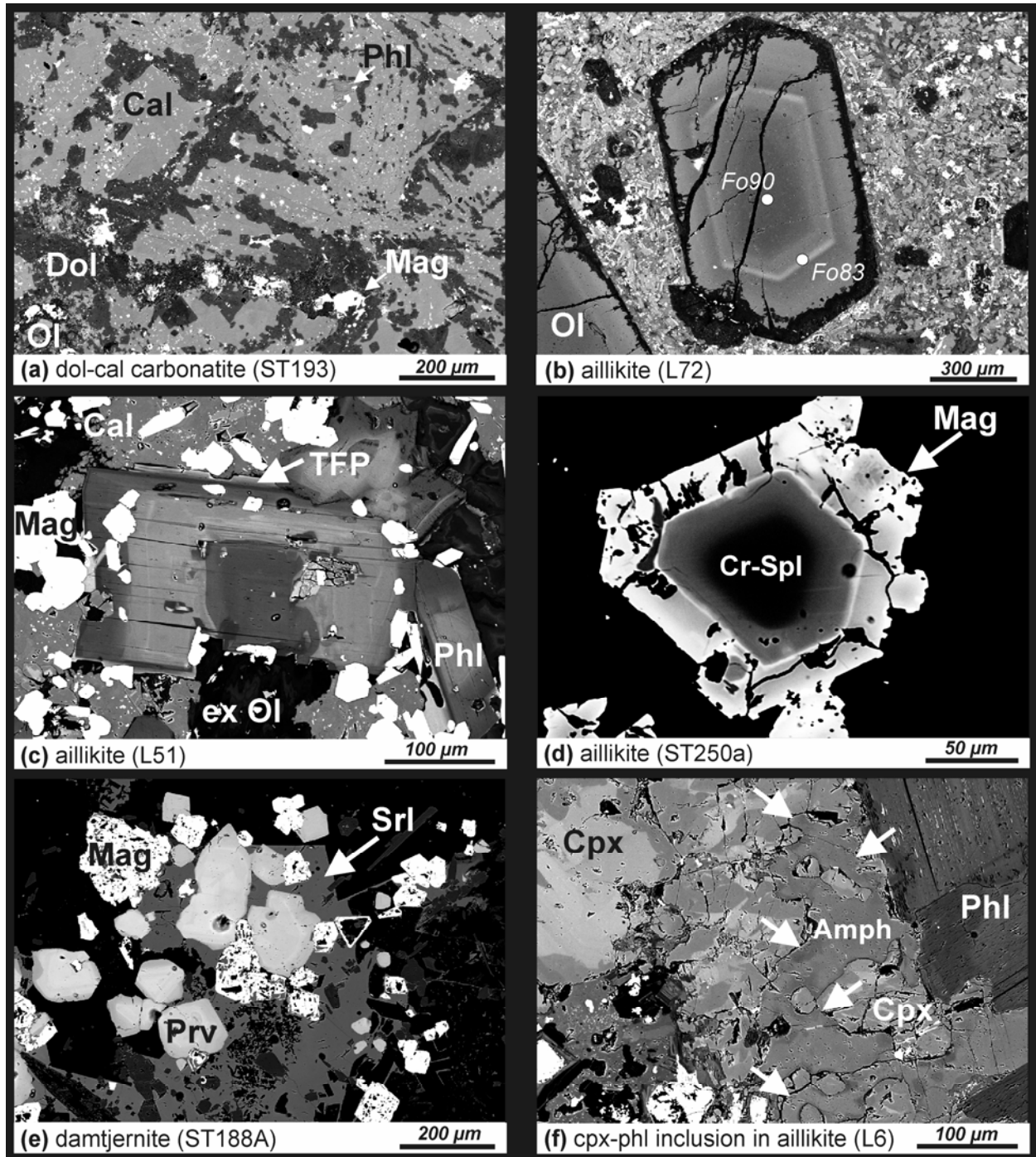


Figure 6: Backscattered electron images of Aillik Bay area UML, carbonatite and a cognate inclusion. (a) Carbonatite mainly composed of coexisting calcite (light grey) and ferroan dolomite laths (dark grey). (b) Euhedral olivine phenocryst set in aillikite matrix. Zonation is normal from a forsterite content of 91 (core) toward 83 (rim), but note the repetition of the zoning pattern. (c) Phlogopite microphenocryst in aillikite exhibiting core, inner mantle and broad rim with narrow tetraferriphlogopite overgrowth (TFP, arrow). (d) Zoned euhedral Cr-spinel microphenocryst in aillikite with titanomagnetite overgrowth. (e) Damtjernite groundmass assemblage consisting of euhedral schorlomite garnet (dark grey, arrow) which poikilitically encloses zoned perovskite (light grey) and magnetite grains (white). Note atoll-textured magnetite grain. (f) Calcic amphibole (arrows) infiltrating a cognate inclusion which is mainly composed of zoned clinopyroxene prisms and phlogopite plates. The cognate inclusion was sampled by aillikite magma.

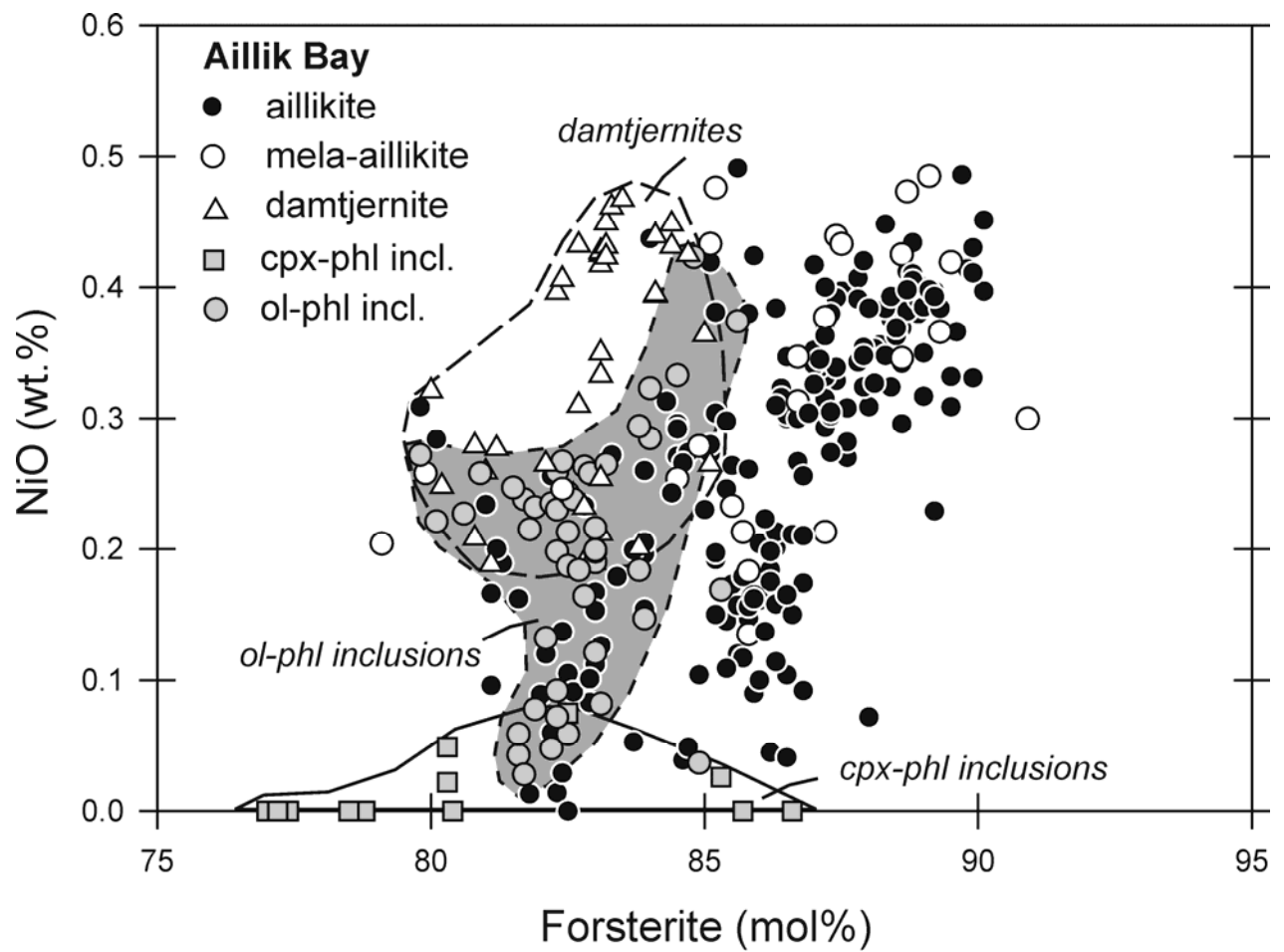


Figure 7: NiO (wt.%) vs. Forsterite (mol%) variation of olivine phenocrysts/microphenocrysts in ultramafic lamprophyres and their cognate micaceous inclusions from the Aillik Bay area. Outlines enclose olivine compositions of distinct rock types.

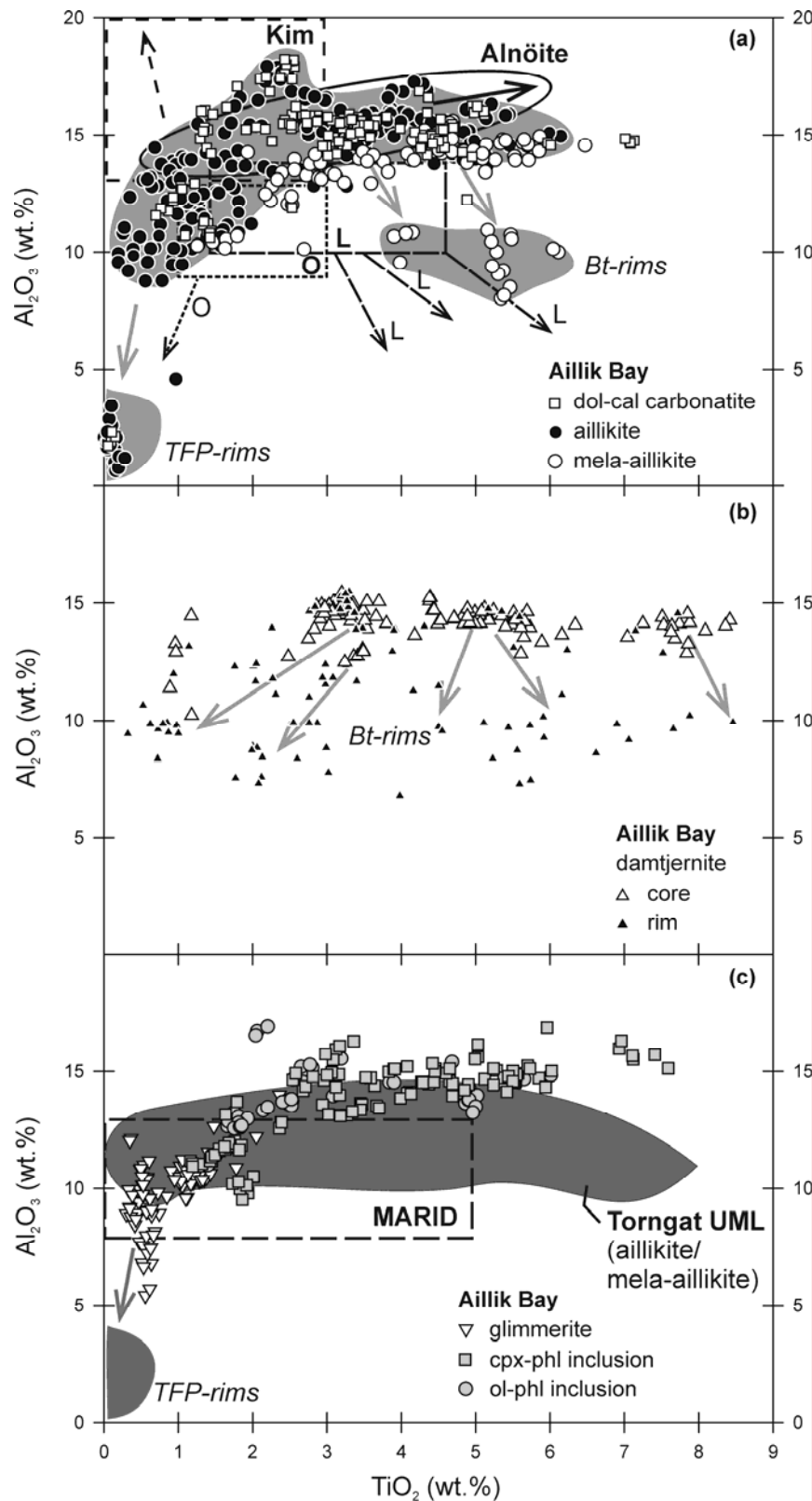


Figure 8: Al_2O_3 vs. TiO_2 (wt.%) variation of micas in carbonatites, ultramafic lamprophyres (a-b) and their cognate inclusions (c) from the Aillik Bay area. Evolutionary trends for the UML micas are superimposed by grey arrows.

Mica compositional fields and evolutionary trends for kimberlites (Kim), orangeites (O), lamproites (L) and alnöites after Mitchell (1995). MARID nodules compositional field after Dawson & Smith (1977) and Smith *et al.* (1978). Field for Torngat UML from Tappe *et al.* (2004). Bt = biotite; TFP = tetraferriphlogopite.

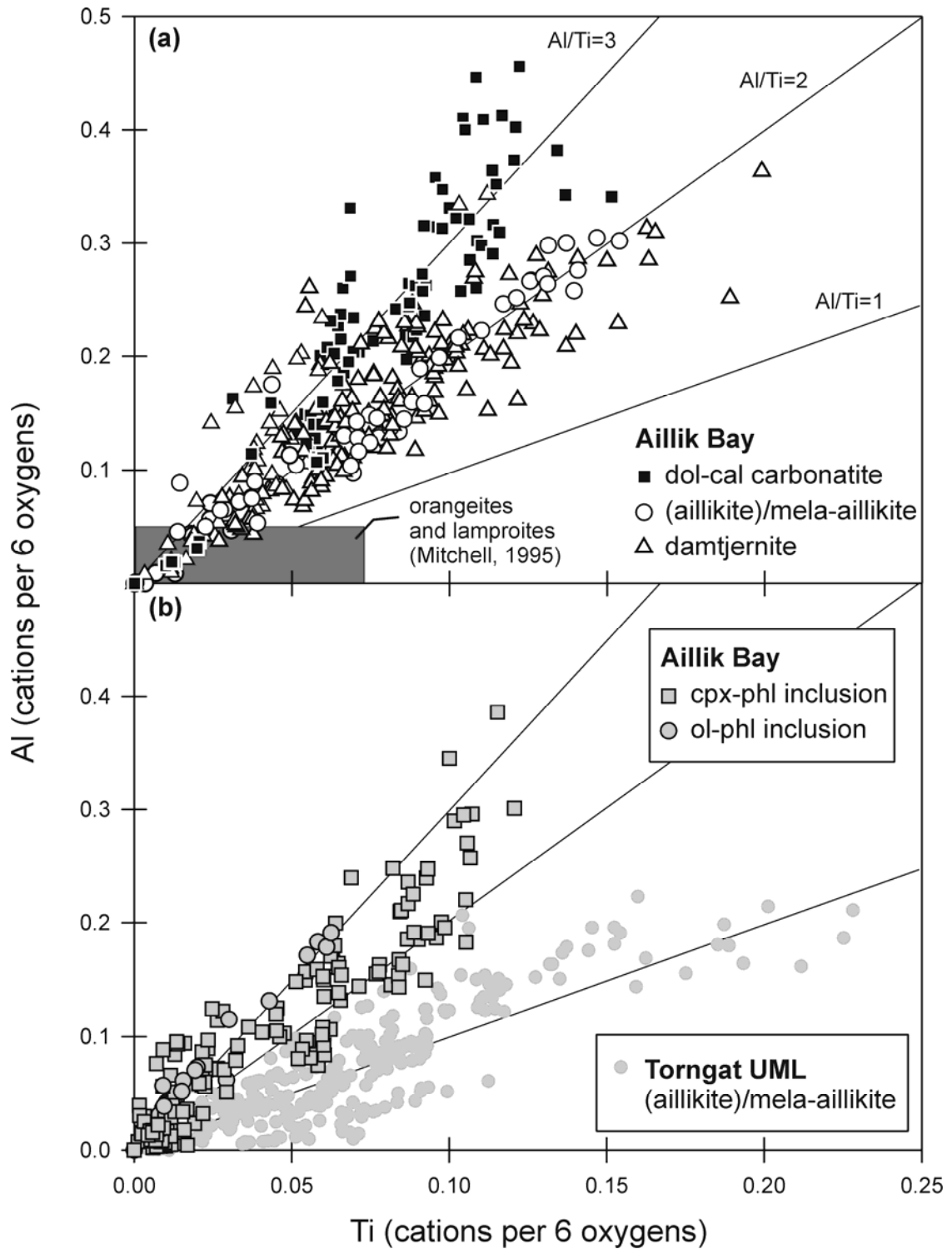


Figure 9: Atomic Al vs. Ti (cations per 6 oxygens) of clinopyroxenes in (a) carbonatites, ultramafic lamprophyres and (b) their cognate inclusions from the Aillik Bay area. The apparent Al- and Ti-enrichment of the UML clinopyroxenes is in marked distinction to almost pure diopside compositions characteristic for clinopyroxenes in orangeites and lamproites (Mitchell, 1995). Data for Torngat UML from Tappe *et al.* (2004). Lines indicate fixed Al/Ti ratios (see labels).

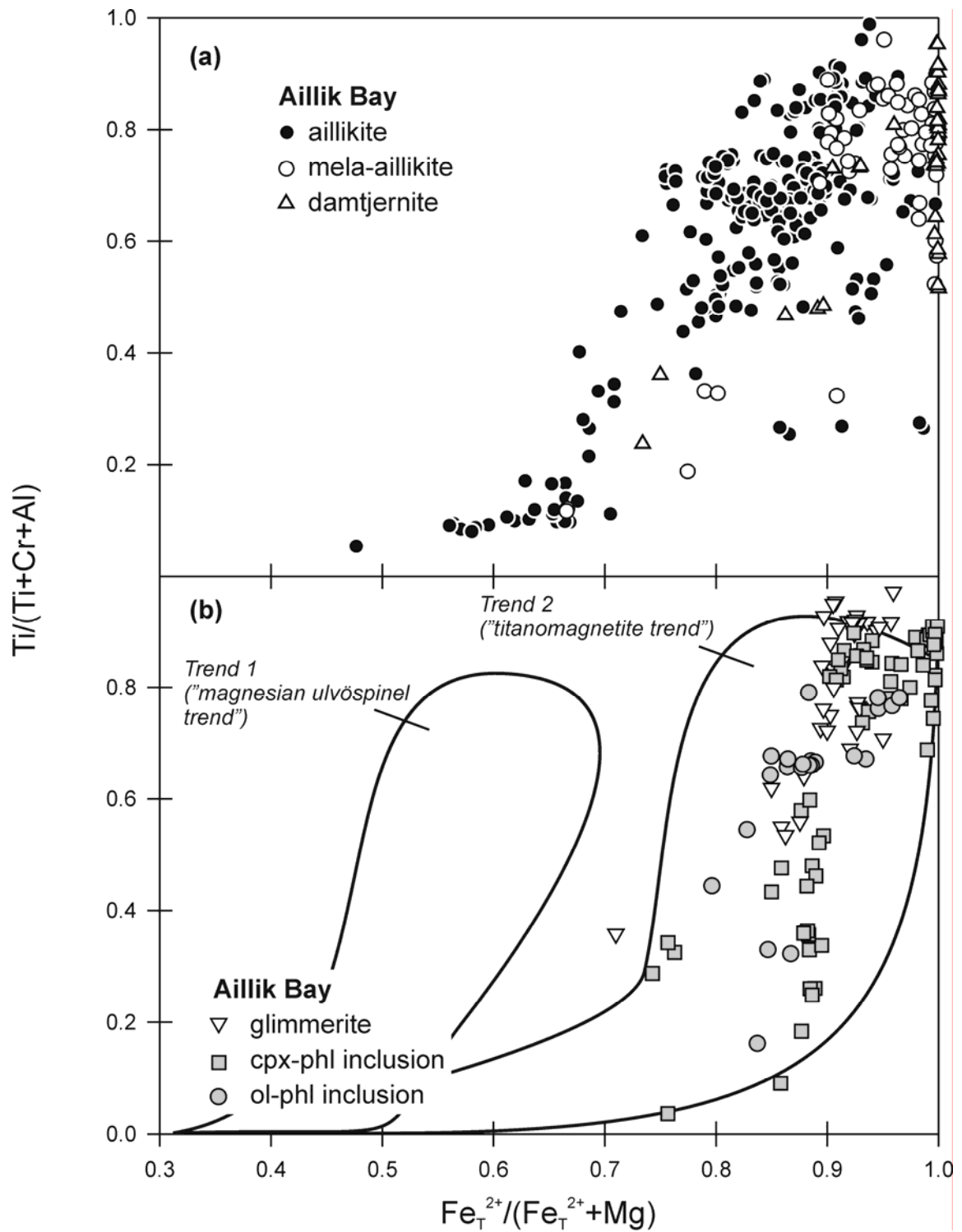


Figure 10: Atomic $Ti/(Ti+Cr+Al)$ vs. $Fe_T^{2+}/(Fe_T^{2+}+Mg)$ for spinels in (a) ultramafic lamprophyres and (b) their cognate inclusions from the Aillik Bay area. Spinels in UML dykes follow magmatic trend 2 ("titanomagnetite trend") in contrast to kimberlite spinel compositions which are rich in magnesian ulvöspinel component (magmatic trend 1 of Mitchell, 1986).

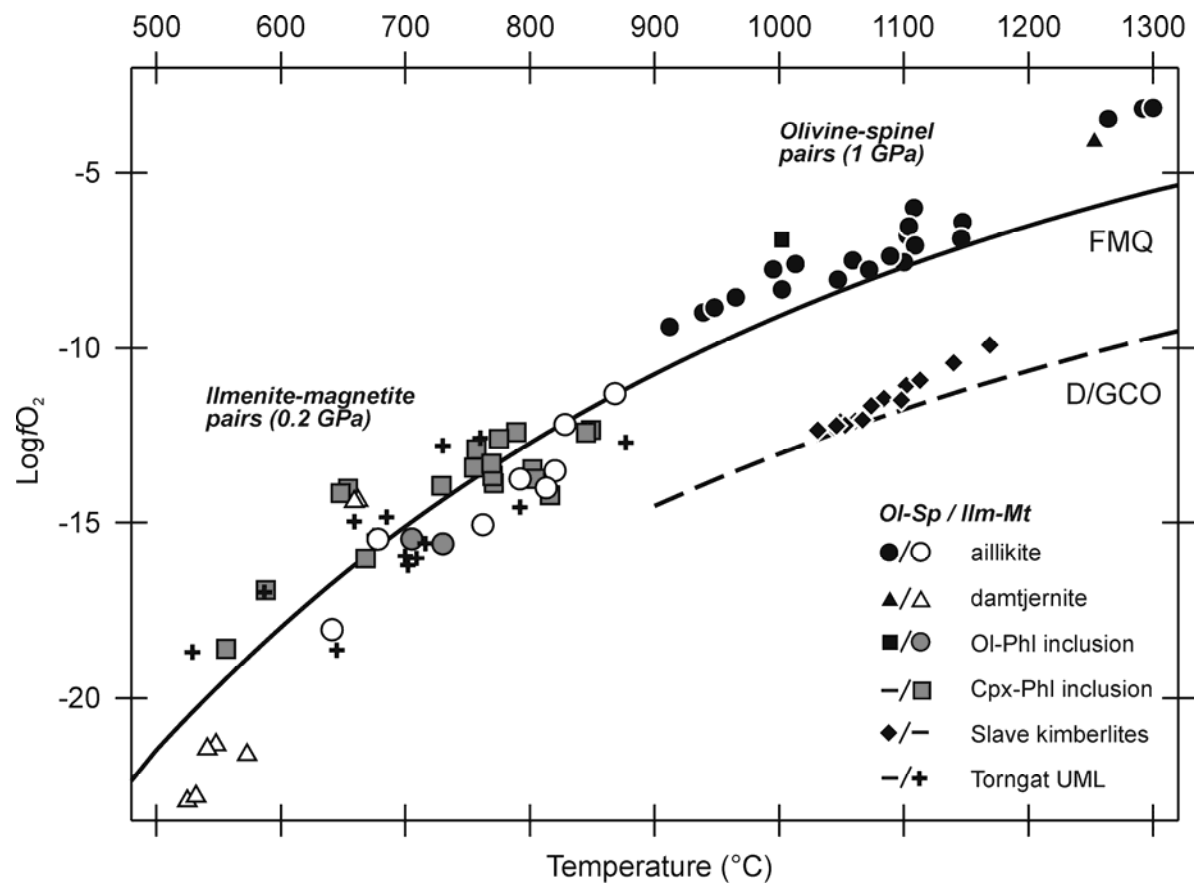


Figure 11: Log oxygen fugacity vs. equilibration temperature (°C) calculated for olivine-spinel and ilmenite-magnetite pairs (see text for explanation; note different symbols) in ultramafic lamprophyres and their cognate inclusions from the Aillik Bay area. The FMQ (fayalite-magnetite-quartz) and D/GCO (diamond/graphite-CO) buffer curves were calculated according to Frost, B.R. (1991) and Frost, D.J. & Wood (1997), respectively. Data for Slave craton kimberlites are from Fedortchouk & Canil (2004). Torngat UML ilmenite-magnetite pairs are own unpublished data from the dyke swarm described in Tappe *et al.* (2004). Symbol size is equal to the 2-sigma error.

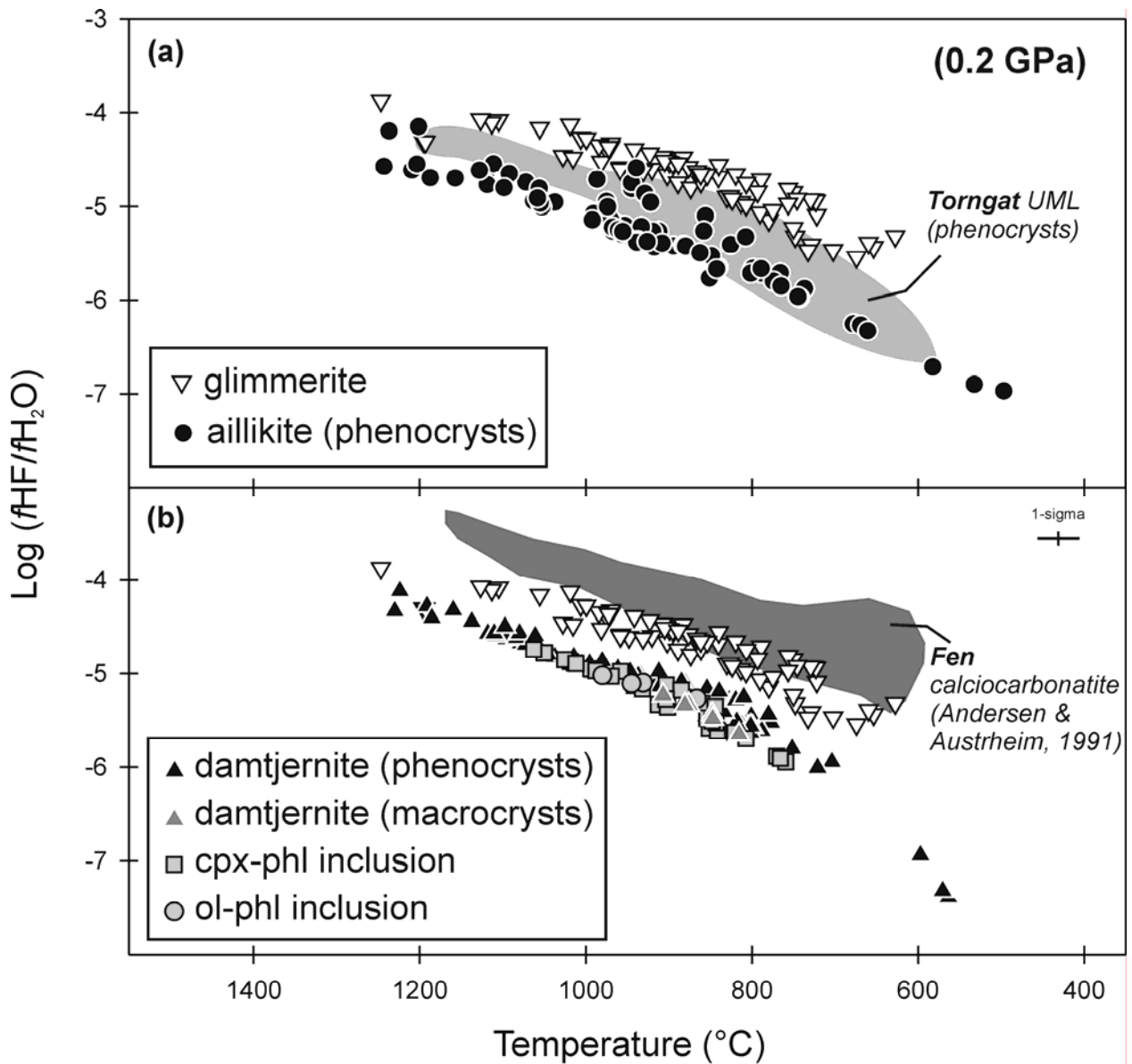


Figure 12: $\text{Log}(f_{\text{HF}}/f_{\text{H}_2\text{O}})$ vs. equilibration temperature ($^{\circ}\text{C}$) calculated for apatite-phlogopite pairs (0.2 GPa, following Andersen, T. & Austrheim, 1991) from Aillik Bay ultramafic lamprophyres and their cognate inclusions. Field for Torngat UML (aillikites/mela-aillikites) in (a) from own unpublished data from the dyke swarm described in Tappe *et al.* (2004). Glimmerite data are displayed in both (a) and (b) for easier comparison.

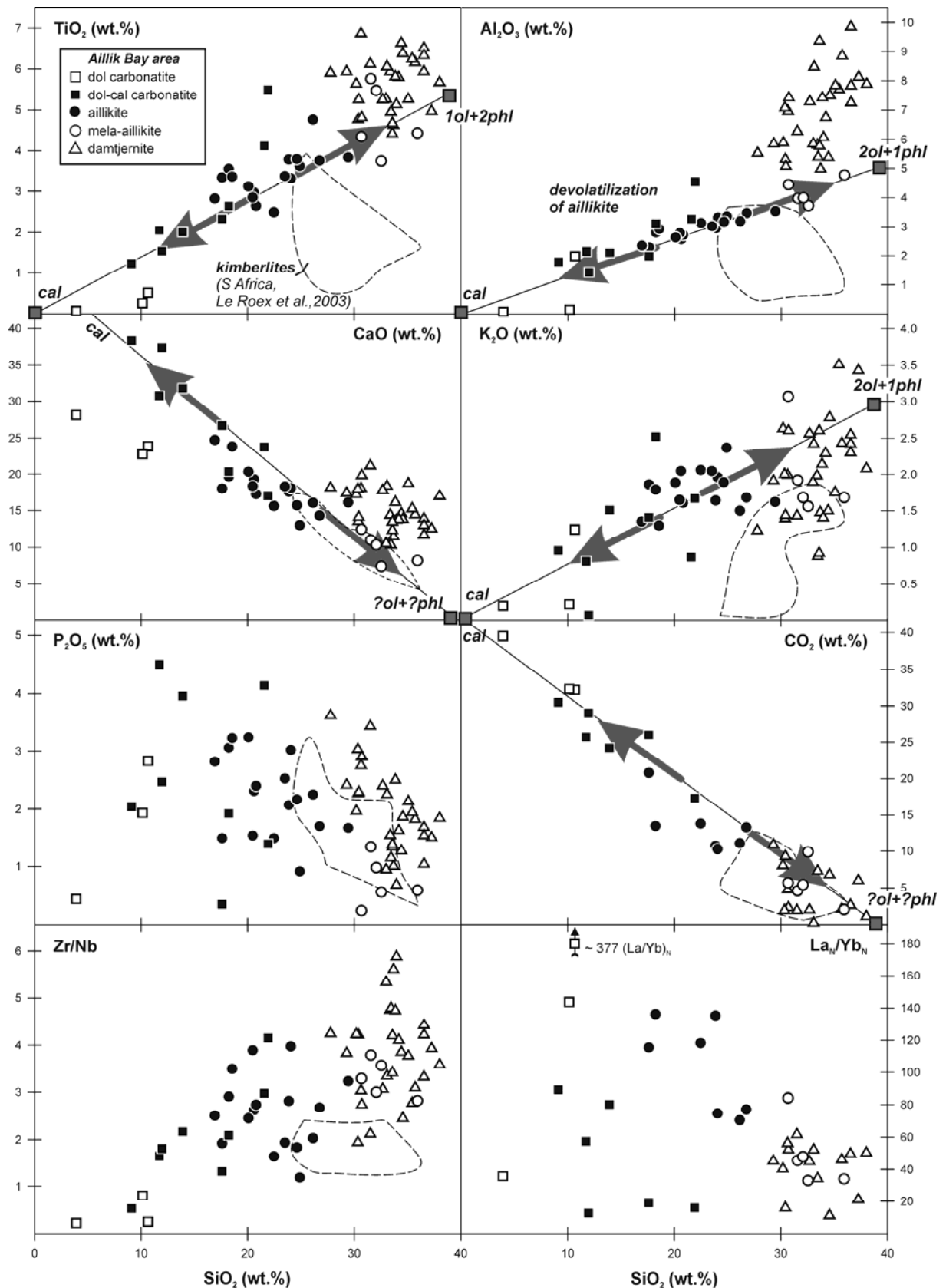


Figure 13: Major element variation and trace element ratios for Aillik Bay UML and carbonatites. Arrows and trend lines illustrate the devolatilization of aillikites leading to carbonatites and mela-aillikites. Dashed outlines display hypabyssal kimberlite compositions from Kimberley, South Africa (Le Roex *et al.*, 2003). Note the La_N/Yb_N ratios are chondrite-normalized using values from Sun & McDonough (1989).

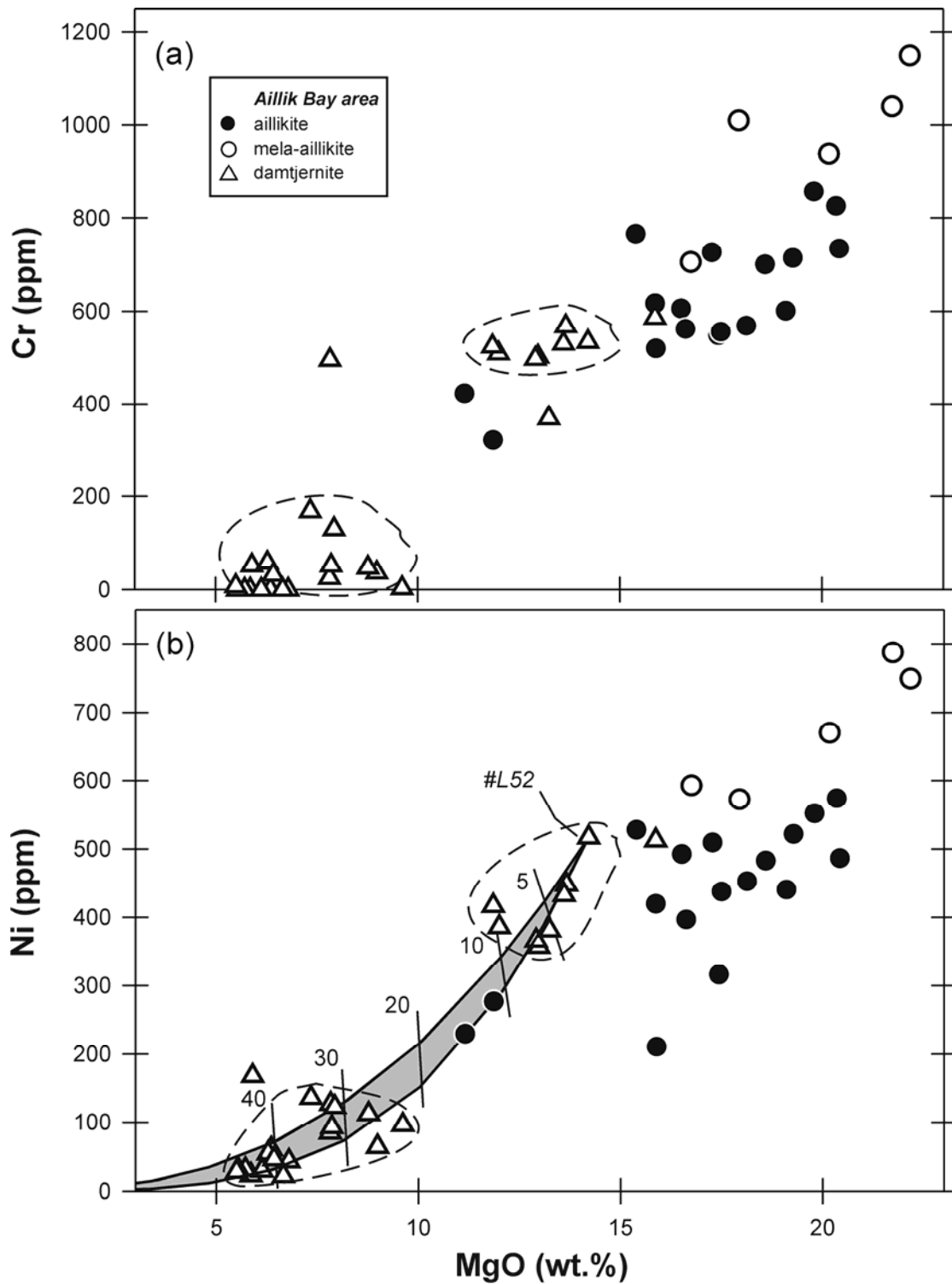


Figure 14: Cr (a) and Ni (b) content (ppm) vs. MgO (wt.%) of ultramafic lamprophyres from the Aillik Bay area. Carbonatites are not shown for clarity. The apparent bimodality of damtjernites is emphasized by the dashed outlines. Grey-shaded calculated olivine fractionation curve in (b) starts at the most primitive damtjernite (L52) with D_{MgO} set at 2.56 and a D_{Ni} -range between 4.9-6.5 following formulations of Herzberg & O'Hara (2002). Numbers at tick marks indicate amount of removed olivine (wt.%).

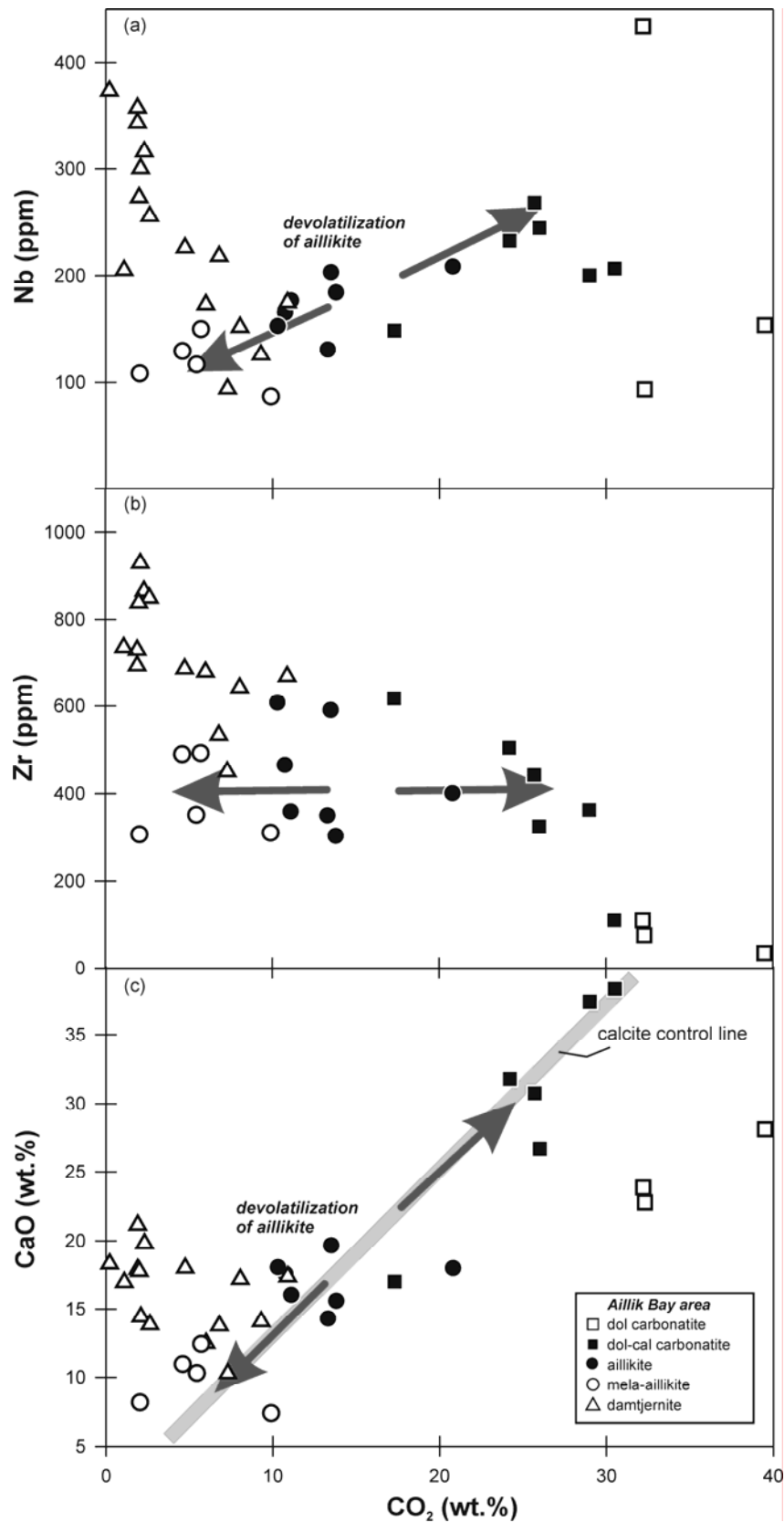


Figure 15: Nb (a), Zr (b) and CaO (c) content vs. CO₂ (wt.%) of ultramafic lamprophyres and carbonatites from the Aillik Bay area. Arrows and trend line illustrate the fractionation relationship between aillikites and carbonatites along a CaCO₃ control line leaving a mela-aillikite residue.

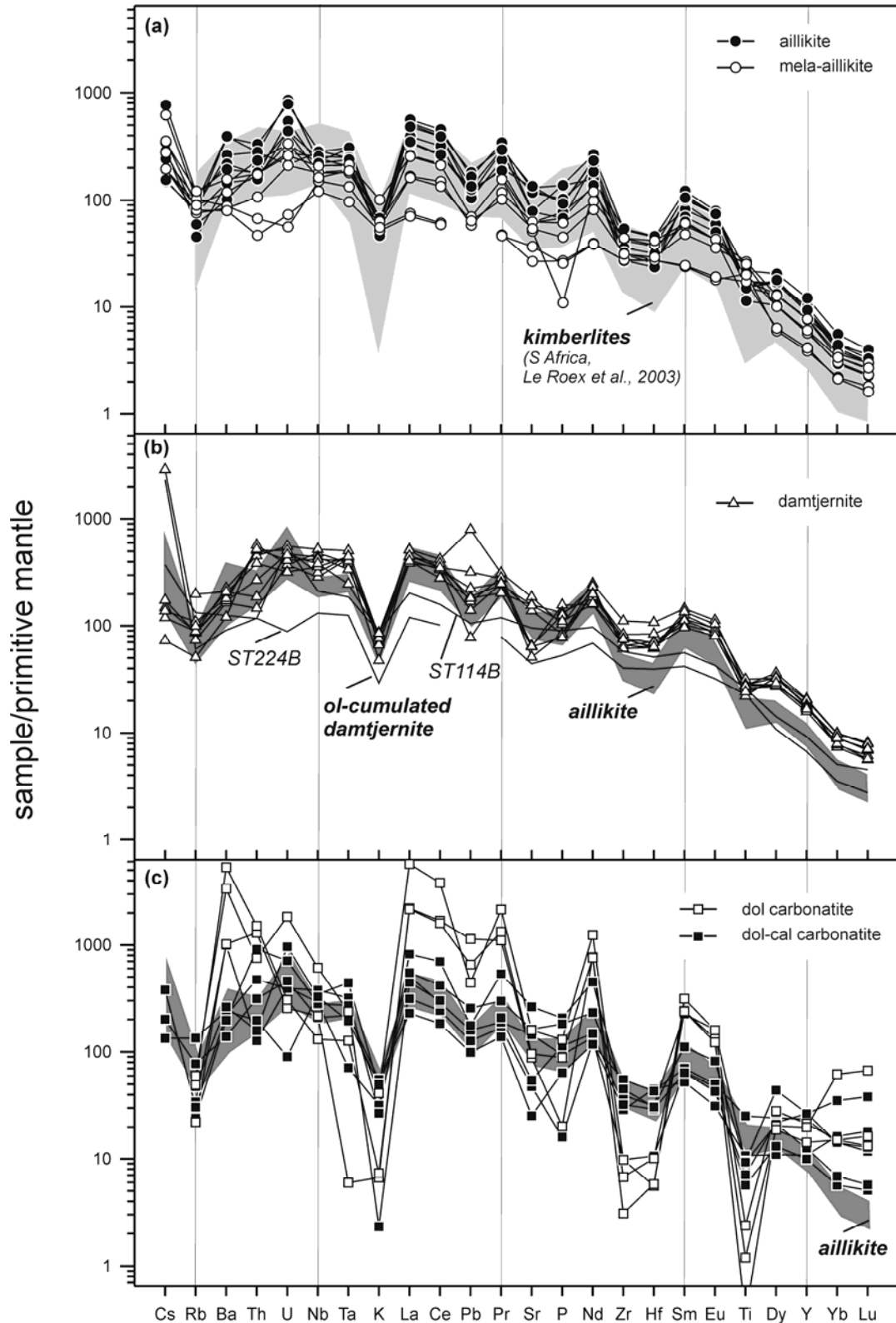


Figure 16: Primitive mantle-normalized incompatible element diagrams for (a) aillikites/mela-aillikites, (b) damtjernites, and (c) carbonatites from the Aillik Bay area. Grey-shaded area in (a) displays normalized patterns of hypabyssal kimberlites from Kimberley, South Africa (Le Roex *et al.*, 2003). Grey-shaded field in (b) and (c) represents the same aillikite composition as in (a) for easier comparison. Primitive mantle values and element sequence after Sun & McDonough (1989).

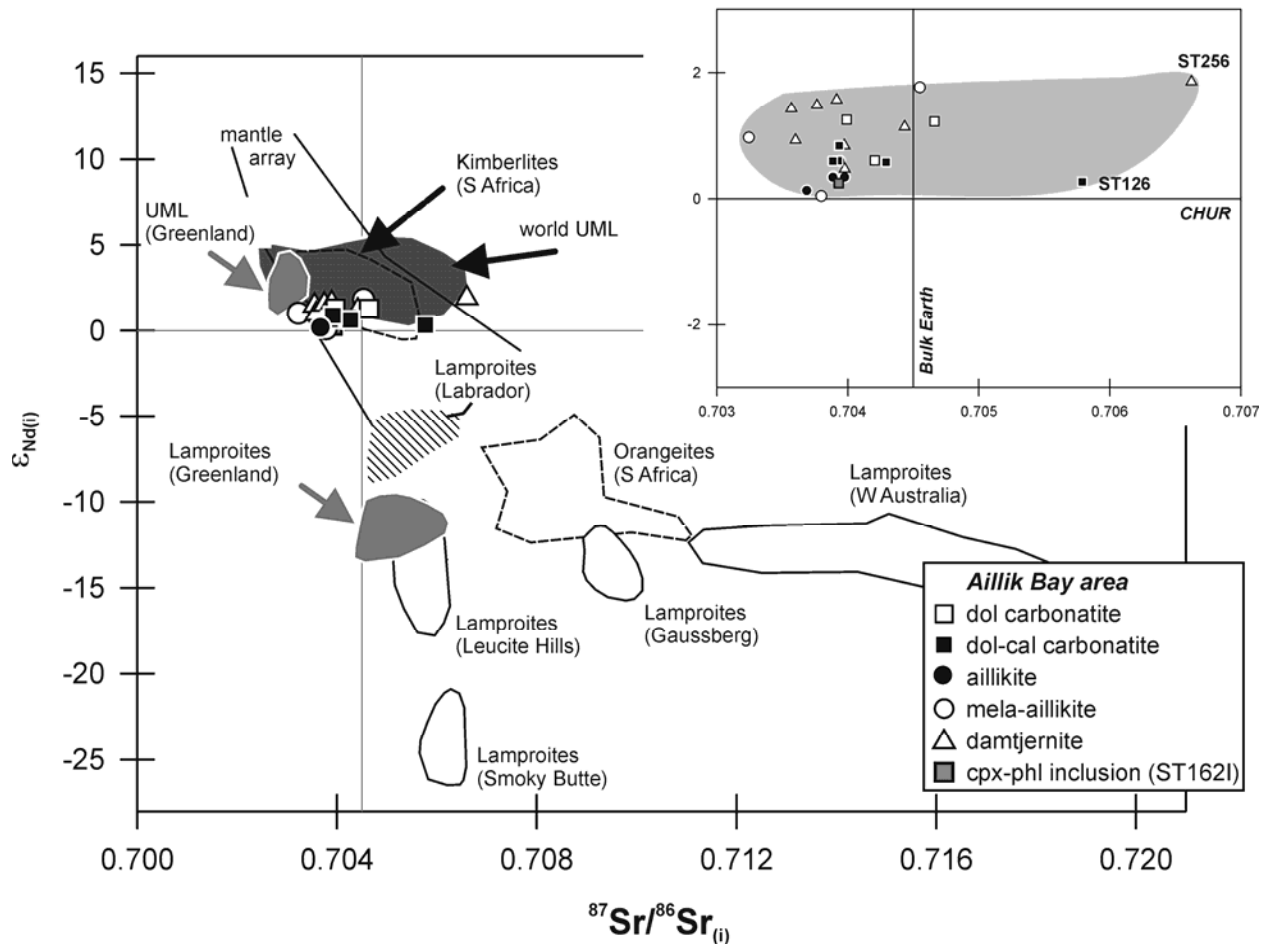


Figure 17: $\epsilon_{\text{Nd}(t)}$ vs. $^{87}\text{Sr}/^{86}\text{Sr}_i$ for Aillik Bay area UML, carbonatites and cognate inclusion ST162I (inset shows enlarged portion of Sr-Nd isotope space). Fields for Greenland UML and lamproites (Nelson, 1989), Leucite Hills, Smoky Butte and Western Australia lamproites (Vollmer *et al.*, 1984; Fraser *et al.*, 1985), Gaussberg lamproites (Murphy *et al.*, 2002), South African kimberlites and orangeites (Nowell *et al.*, 2004) and other worldwide UML occurrences (Neal & Davidson, 1989; Beard *et al.*, 1996; Pearce & Leng, 1996; Le Roex & Lanyon, 1998; Andronikov & Foley, 2001; Riley *et al.*, 2003) are shown for comparison. Field for Labrador lamproites is based on own unpublished data (Mesoproterozoic lamproites from the Aillik Bay area, see text).

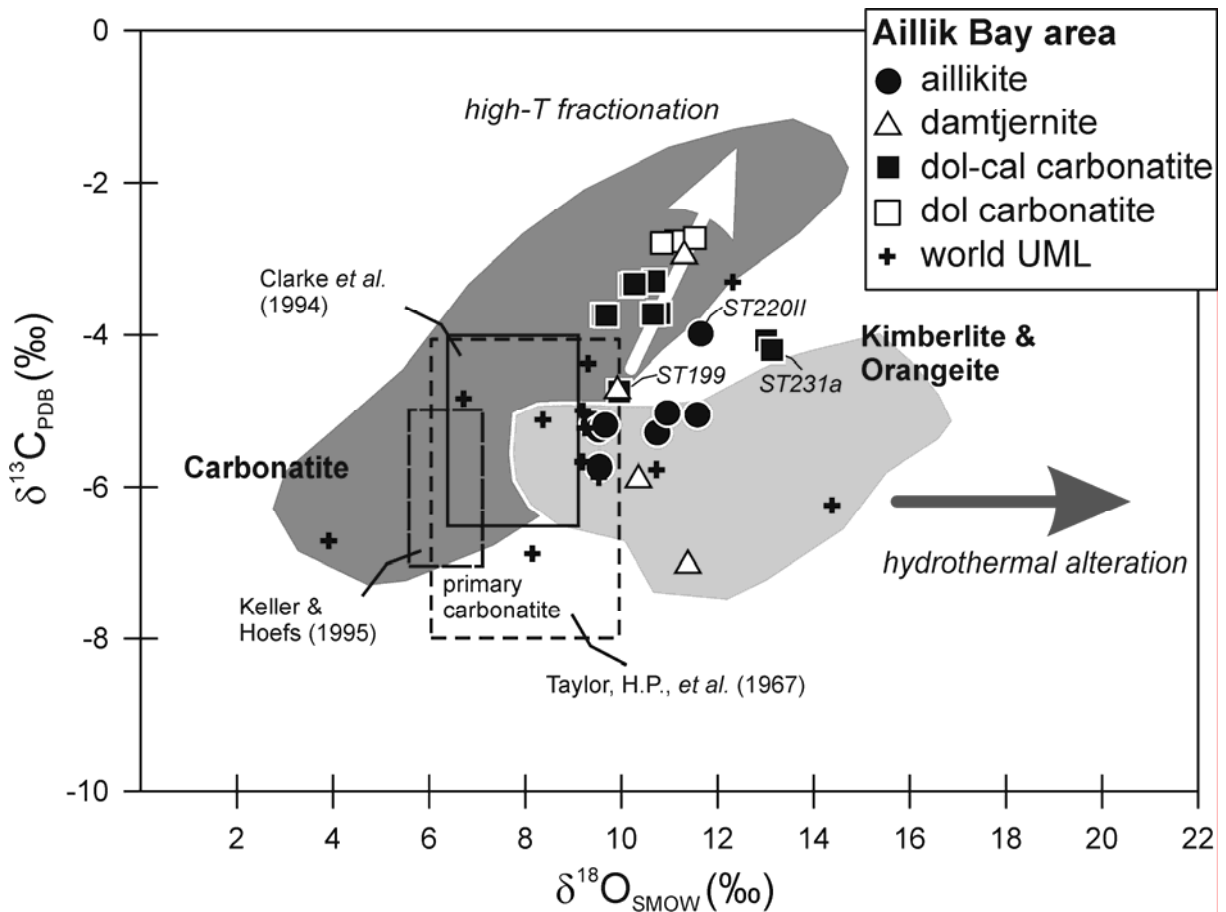


Figure 18: Carbon and oxygen isotope composition (expressed as ‰ $\delta^{13}\text{C}$ and $\delta^{18}\text{O}$ relative to PDB and SMOW, respectively) of bulk rock carbonate fractions from Aillik Bay area ultramafic lamprophyres and carbonatites. Two main petrogenetic processes which have the potential of changing the stable isotope composition are illustrated by arrows (after Deines, 1989). Fields for typical carbonatite and kimberlite compositions are compiled from worldwide occurrences and data sources are available from the senior author upon request. Data for world UML are from the same sources as in Figure 17. Symbol size is larger than the 2-sigma error.

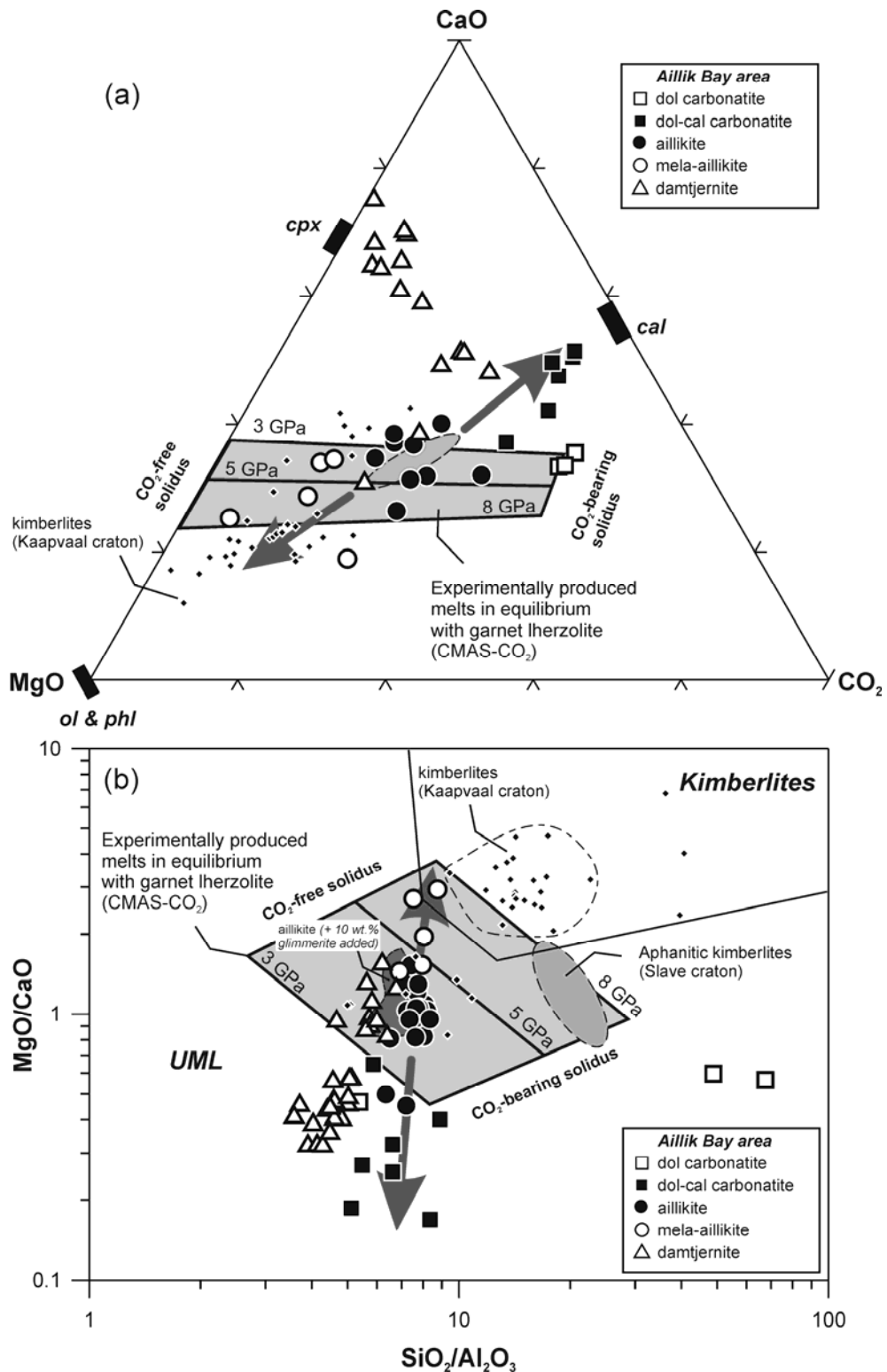


Figure 19: Aillik Bay area UML and carbonatites in (a) CaO-MgO-CO₂ space and in the (b) MgO/CaO vs. SiO₂/Al₂O₃ “UML-kimberlite-discrimination-diagram” of Rock (1991). Fields of experimentally determined melt compositions after Gudfinnsson & Presnall (2005). Arrows indicate evolutionary paths from aillikite towards mela-aillikite and dolomite-calcite carbonatite caused by devolatilization. Compositional range of calcite (*cal*), olivine (*ol*), phlogopite (*phl*) and diopside-rich clinopyroxene (*cpx*) is shown in (a). Solid diamonds represent hypabyssal kimberlites from Kimberley, Kaapvaal craton (South Africa, Le Roex *et al.*, 2003) and the light-grey ellipse displays compositions of aphanitic hypabyssal kimberlites from the Jericho pipe, Slave craton (Canada, Price *et al.*, 2000). The dark-grey field in (b) shows aillikite compositions corrected for 10 wt.% glimmerite-loss as proxy for a “proto-aillikite” composition. See text for more details.

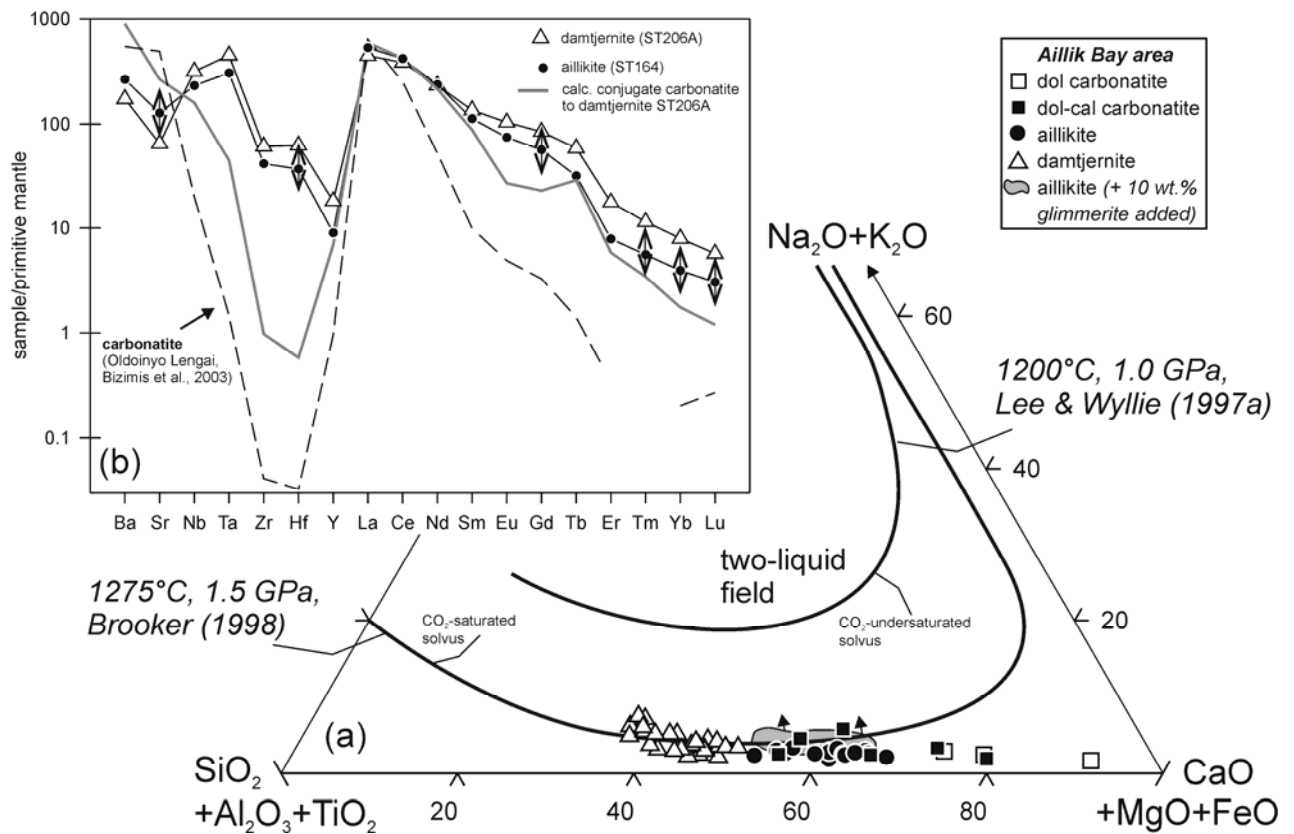


Figure 20: Illustration of a likely role for liquid immiscibility in the genesis of damtjernites. (a) Aillik Bay UML and carbonatite compositions in a multicomponent system projected from CO_2 . The grey field represents "proto-aillikite" compositions corrected for 10 wt.% "glimmerite"-loss during magma ascent. These high-pressure aillikite equivalents may thus fall into a CO_2 -saturated two-liquid field (arrows) at uppermost mantle conditions (see solvus of Brooker, 1998) and exsolve damtjernite liquids. (b) Expected trace element distribution between damtjernite ST206A and its hypothetic conjugate carbonatite liquid using partition coefficients from Veksler *et al.* (1998), except for Eu, Gd, Yb, Lu (Hamilton, D.L. *et al.*, 1989) and Ce (Jones *et al.*, 1995). The transitional composition of aillikite ST164 demonstrates the potential of proto-aillikite magma for representing the parental magma that underwent silicate-carbonate immiscibility. Primitive mantle composition after Sun & McDonough (1989).

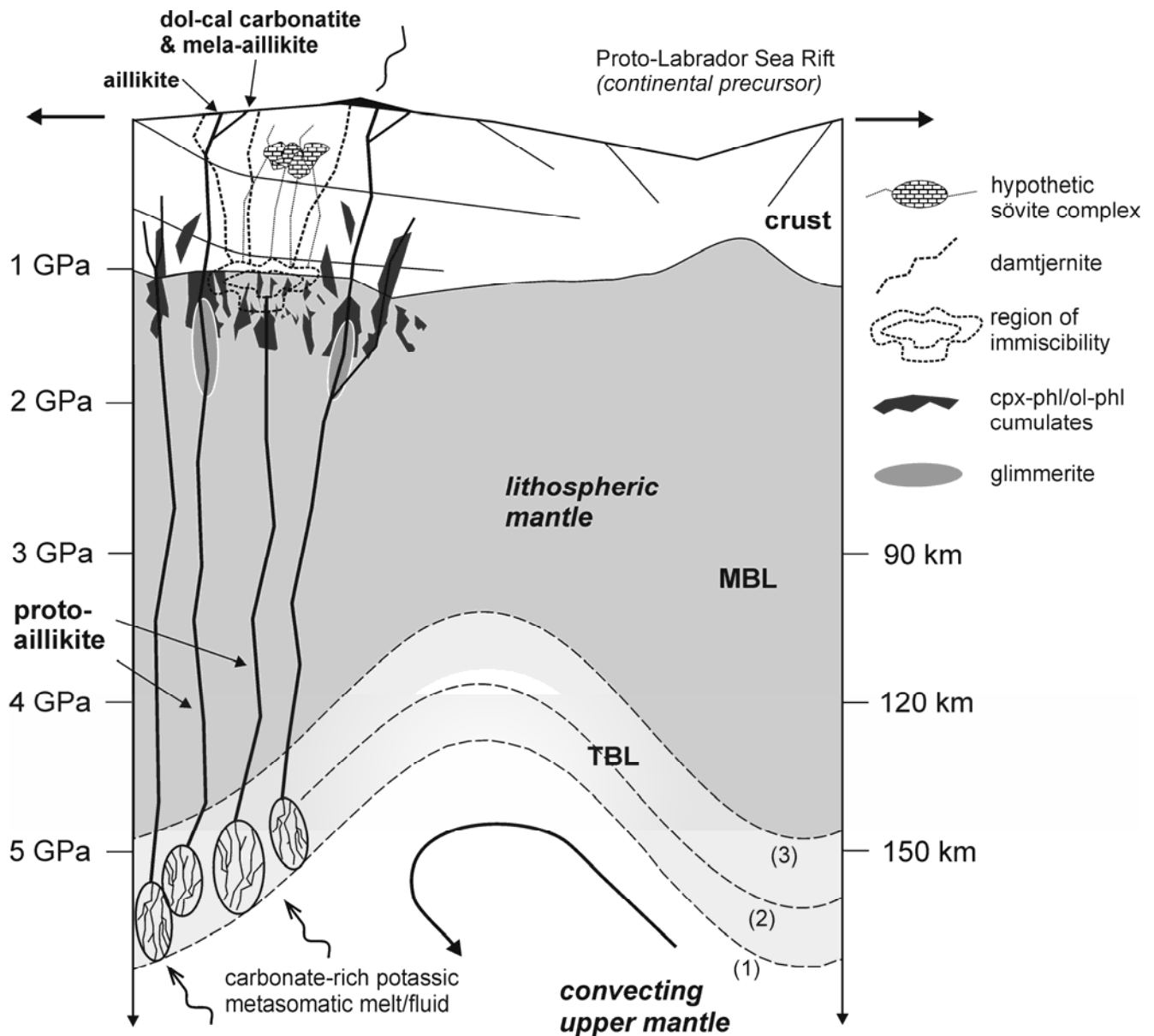


Figure 21: Petrogenetic scheme for Aillik Bay UML and carbonatites formed between ~ 590-555 Ma in response to continental extension and lithospheric thinning. Dashed lines labelled from 1 to 3 denote time-steps of progressive thermal conversion of lithospheric mantle by hot upwelling convective mantle. Metasomatic carbonate-phlogopite dominated veins formed at the base of the cold lithosphere and successively re-melted together with surrounding garnet peridotite during progressive mantle upwelling. The produced parental proto-aillikite magma was partly modified by low-pressure processes at uppermost mantle to crustal depth giving rise to the variety of UML and carbonatite types of the Aillik Bay intrusive suite. See text for further explanation. **MBL** – mechanical boundary layer; **TBL** – thermal boundary layer.

Part III

**TORNGAT ULTRAMAFIC LAMPROPHYRES AND THEIR RELATION TO THE
NORTH ATLANTIC ALKALINE PROVINCE**

S. Tappe; G.A. Jenner; S.F. Foley; L.M. Heaman; D. Besserer; B.A. Kjarsgaard & B. Ryan

ABSTRACT	118
1. INTRODUCTION	119
2. GEOLOGY AND AGE	119
2.1. Torngat Orogen	119
2.2. Ultramafic dyke swarm	120
2.3. Age	120
3. ANALYTICAL TECHNIQUES.....	121
4. PETROGRAPHY AND MINERAL CHEMISTRY	122
4.1. Main petrographic features of the Torngat dykes.....	122
4.2. Aillikites and Carbonatites	122
4.3. Mela-aillikites.....	128
5. WHOLE-ROCK COMPOSITION	131
5.1. Major elements	131
5.2. Trace elements.....	131
6. RELATIONSHIP BETWEEN AILLIKITES AND MELA-AILLIKITES	132
7. REGIONAL COMPARISONS	134
7.1. Relation to other Neoproterozoic alkaline rocks in Quebec and Labrador	134
7.2. Comparison with West Greenland occurrences.....	135

7.3. Large Scale Tectonic Implications	136
ACKNOWLEDGEMENTS	137
REFERENCES	137
TABLES	143
FIGURES	151

ABSTRACT

Geological mapping and diamond exploration in northern Quebec and Labrador has revealed an undeformed ultramafic dyke swarm in the northern Torngat Mountains. The dyke rocks are dominated by an olivine-phlogopite mineralogy and contain varying amounts of primary carbonate. Their mineralogy, mineral compositional trends and the presence of typomorphic minerals (e.g. kimzeyitic garnet), indicate that these dykes comprise an ultramafic lamprophyre suite grading into carbonatite. Recognized rock varieties are aillikite, mela-aillikite and subordinate carbonatite. Carbonatite and aillikite have in common high carbonate content and a lack of clinopyroxene. In contrast, mela-aillikites are richer in mafic silicate minerals, in particular clinopyroxene and amphibole, and contain only small amounts of primary carbonate. The modal mineralogy and textures of the dyke varieties are gradational, indicating that they represent end-members in a compositional continuum.

The Torngat ultramafic lamprophyres are characterized by high but variable MgO (10-25 wt.%), CaO (5-20 wt.%), TiO₂ (3-10 wt.%) and K₂O (1-4 wt.%), but low SiO₂ (22-37 wt.%) and Al₂O₃ (2-6 wt.%). Higher SiO₂, Al₂O₃, Na₂O and lower CO₂ content distinguish the mela-aillikites from the aillikites. Whereas the bulk rock major and trace element concentrations of the aillikites and mela-aillikites overlap, there is no fractional crystallization relation between them. The major and trace element characteristics imply related parental magmas, with minor olivine and Cr-spinel fractionation accounting for intra-group variation.

The Torngat ultramafic lamprophyres have a Neoproterozoic age and are spatially and compositionally closely-related with the Neoproterozoic ultramafic lamprophyres from central West Greenland. Ultramafic potassic-to-carbonatitic magmatism occurred in both eastern Laurentia and western Baltica during the Late Neoproterozoic. It can be inferred from the emplacement ages of the alkaline complexes and timing of Late Proterozoic processes in the North Atlantic region that this volatile-rich, deep-seated igneous activity was a distal effect of the breakup of Rodinia. This occurred during and/or after the rift-to-drift transition that led to the opening of the Iapetus Ocean.

1. INTRODUCTION

The borders of the Labrador Sea have been the site of widespread ultramafic potassic-to-carbonatitic magmatism from the Archean to the Cenozoic (Larsen & Rex, 1992). Most of the dyke and sheet intrusions were originally described as "kimberlitic". However, reclassification of some dyke occurrences (Mitchell *et al.*, 1999) and new discoveries (Marker & Knudsen, 1989; Wardle *et al.*, 1994; Pearce & Leng, 1996; Digonnet *et al.*, 2000) indicate that an appreciable amount of the alkaline magmatism is more akin to that of ultramafic lamprophyres (UML). The fact that these may also be diamondiferous, even in off-craton settings such as the Torngat Orogen (Fig.1), demands a new petrogenetic model for their origin.

We have undertaken a mineralogical and geochemical study of Late Neoproterozoic ultramafic dykes from the northern Torngat Mountains (Fig.1) in Quebec and Labrador. They occur in close proximity to Abloviak Fjord, where carbonate-rich ultramafic lamprophyres have previously been reported by Digonnet *et al.* (2000).

The samples studied in this paper cover a larger region than the Abloviak dykes, and are also more compositionally-diverse. Three closely-related rock types can be distinguished within the dyke swarm and this variability in mineral mode and composition enables us to decipher their crystallization history. U-Pb age determination of perovskite in a Torngat dyke provides an important constraint and tectonic link to related igneous activity. The relationship of volatile-rich, ultramafic potassic-to-carbonatitic magma generation in the North Atlantic region to the Late Neoproterozoic breakup of Rodinia is inferred from regional considerations.

2. GEOLOGY AND AGE

2.1. Torngat Orogen

The Torngat Mountains in northern Labrador and northeastern Quebec are part of a narrow north-south trending orogenic belt (Torngat Orogen) comprising the eastern part of the Paleoproterozoic Southeastern Churchill Province (Fig.1). This province formed during the collision of the Archean Nain (North Atlantic craton) and Superior cratons at ca. 1.9-1.7 Ga (Wardle *et al.*, 2002).

The ultramafic dykes intruded the axial part of the doubly vergent orogen, termed the Tasiuyak Domain. This metasedimentary complex is exposed over a length of more than 500 km and a width of 5-25 km. It represents the tectonic contact between the Superior Craton to the southwest and the Nain Craton to the east, which collided at about 1870-1840 Ma (Wardle *et al.*, 2002 and references therein).

2.2. Ultramafic dyke swarm

Based on airborne geophysical surveys for diamond exploration in the northern Torngat Mountains, 38 subvertical dykes were discovered between 59°01′-59°26′N and 64°42′-65°16′W. Our study of ultramafic lamprophyres is based on 34 representative samples representing 29 of these dykes.

They comprise a dyke swarm which extends from the Abloviak Fjord region at least 50 km toward the south. The individual undeformed dykes are roughly northeast oriented (360-060°) and can be traced along strike for up to 2 km (in rare cases up to 20 km). Width of the dykes ranges from a few centimetres to 3 m and the chilled contacts to the country rock appear carbonated. All the dykes are hosted within gneiss of the Tasiuyak Domain and occupy brittle fractures cutting across the regional foliation. No evidence of multiple injections in a sampled dyke was observed and flow banding only occasionally occurs. Duplicate samples from some dykes did not demonstrate significant heterogeneity. Taking these features into account, we consider our samples to be “representative”.

2.3. Age

A hand specimen of ultramafic lamprophyre dyke Q39 was selected for U-Pb perovskite geochronology and processed through standard crushing and mineral separation techniques. The analytical procedure for U-Pb perovskite age determination at the University of Alberta is reported in Heaman & Kjarsgaard (2000). A moderate yield of tiny brown perovskite fragments and cubes (< 100 µm) were recovered. The U-Pb data for a perovskite fraction consisting of 100 tiny fragments and cubes are reported in Table 1. The Q39 perovskite has a moderate uranium concentration (105 ppm) and Th/U ratio (5.6). The U-Pb perovskite data are plotted on a conventional concordia diagram in Figure 2. In other examples of Neoproterozoic U-Pb perovskite ages (e.g. Heaman *et al.*, 2003), it has been shown that the $^{206}\text{Pb}/^{238}\text{U}$ ages are most robust because they are least sensitive to initial common lead

corrections. We interpret the $^{206}\text{Pb}/^{238}\text{U}$ date of 584.0 ± 3.6 Ma to be the best estimate for the timing of Q39 emplacement. The U-Pb perovskite age obtained here for ultramafic lamprophyre Q39 is slightly older than the $^{40}\text{Ar}/^{39}\text{Ar}$ phlogopite age of 550 ± 15 Ma obtained for a nearby Abloviak ultramafic lamprophyre (Digonnet *et al.*, 2000) and the U-Pb perovskite age of 550.9 ± 3.5 Ma obtained for the Lac Beaver alkaline intrusion further south in Quebec (Moorhead *et al.*, 2003).

3. ANALYTICAL TECHNIQUES

Mineral compositions were obtained using a JEOL JXA 8900 RL electron microprobe at the University of Göttingen. Operating voltage for silicates, carbonates and apatite was 15 kV with a current of 15 nA. Perovskite, rutile and titanite were measured with 20 kV and 30 nA, whereas 15 kV and 20 nA were used for opaque oxides. The beam diameter varied between 1 and 10 μm dependent on both size and content of volatile elements in the crystal of interest. All these data were reduced with a CITZAF procedure (Armstrong, 1995), except for the carbonates where a ZAF correction was applied.

Samples were slabbed and weathered surfaces removed. The crushed rock split was powdered in an agate mill in Greifswald. Powders were supplied to Activation Laboratories Ltd. (Ancaster, Ontario) for analyses by a combination of ICP-AES and ICP-MS. Major elements and selected trace elements were determined using a fusion digestion and ICP-AES. Some samples were additionally analyzed by XRF in Greifswald; results of the two methods agree within analytical error for all major elements. Rare earth elements and other trace elements (particularly Nb, Th and U) were determined by ICP-MS following an acid dissolution. Comparison of elements determined by all techniques (i.e., Sr, Zr, Y) was excellent and indicated no dissolution problems for the ICP-MS work. Typical estimates of precision and accuracy for these techniques are given in Jenner (1996). Volatiles were determined by a combination of loss on ignition and direct determination of CO_2 using a C-S analyser. In addition, $\text{Fe}^{+2/+3}$ was determined by standard titration techniques.

4. PETROGRAPHY AND MINERAL CHEMISTRY

4.1. Main petrographic features of the Torngat dykes

The Torngat dykes are melanocratic-to-holomelanocratic rocks with a colour index greater than 80. They are dominated by olivine and phlogopite and contain variable amounts of primary carbonate (Fig.3A). On the basis of their mineralogical composition and the presence of typomorphic minerals the Torngat dykes are best classified as ultramafic lamprophyres, grading into carbonatite. Three different rock varieties - carbonatite, aillikite and mela-aillikite - can be distinguished based on modal mineral abundances and textures. Table 2 lists the modal compositions of representative samples.

Dark grey-to-black macrocrystal-to-porphyritic aillikites and light grey carbonatite samples have high carbonate content (> 10 vol.%) and only rarely contain clinopyroxene (< 5 vol.%). In contrast, the dominantly grey, intergranular mela-aillikites are enriched in clinopyroxene and amphibole (up to 26 vol.%, Fig.3B), and contain only small amounts of primary carbonate (< 4 vol.%). Following the criteria of Rock (1986), we apply the prefix “mela” to those aillikites that contain more than 70 vol.% mafic silicate minerals. Furthermore, mela-aillikites have fewer opaque oxides and olivine in the groundmass than aillikites. A high-Ti mela-aillikite group can be distinguished from the mela-aillikites on the basis of bulk rock and mineral composition only.

Carbonatite, aillikite and mela-aillikite of the Torngat dyke swarm show distinct mineral compositional trends although their modal mineral content and textures are gradational, such that they represent end-members in a compositional continuum. Representative mineral compositions are listed in Tables 3 to 7.

4.2. Aillikites and Carbonatites

Olivine occurs as abundant rounded and subhedral crystals up to 10 mm in diameter (Fig.3C), giving the aillikites a macrocrystal-to-porphyritic texture. The forsterite content (Fo) of cores to these macrocrysts and phenocrysts ranges between 81-93 mol.% with some rare Fe-richer occurrences (Fo 76 mol.%). Zoning is primarily normal and increasing Mn and Ca concentrations (up to 0.3 and 0.4 wt.%, respectively) have been observed from core to rim. A reverse pattern of zoning in terms of Mg/Fe ratio has been observed in a few samples (e.g.

Q41). The Ca content of these reverse zoned olivines also increases from core to rim, indicating equilibration with the high-CaO melt and/or decreasing pressure (Stormer, 1973; Brenan & Watson, 1991). The less common suite of Fe-rich olivines (Fo < 80 mol.%) are also rimmed by Mg-richer olivine compositions and regardless of whether the zoning is normal or reversed, rim compositions converge on Fo 82-88 mol.%. The composition of euhedral microphenocrystal olivine was measured in samples Q37 and Q41, and is the same as the overgrowth rims mantling the macrocrysts and phenocrysts.

Widespread zoned **phlogopite** laths are characteristic for both aillikites and carbonatite and may be flow-oriented (Fig.3A). Fragments of older micas are often enclosed in newly-grown laths. A later phlogopite generation is set in a groundmass composed of carbonate, phlogopite flakes and minor serpentine. The micas represent solid solutions between phlogopite, tetraferriphlogopite, annite and eastonite end-members. A weak core-rim evolutionary trend toward tetraferriphlogopite with increasing Fe and strongly decreasing Al but constant Mg occurs (Fig.4). Nearly Al-free discrete tetraferriphlogopite rims occur only in aillikites (Fig.3A, C). The Ti content is comparably low, rarely exceeding 4 wt.% TiO₂, and remains essentially constant during evolution. Ba content is below 1 wt.% and correlates only weakly with TiO₂. The only sample (Q17) with BaO exceeding 1 wt.% shows a clear Ba-enrichment toward the rim at the expense of K. The F content in the microphenocrystal plates and flakes is also low (below 1.5 wt.%). The highest F content in the micas (2-3 wt.%) is from a cm-sized kinked phlogopite megacryst in sample Q26 (1.5 cm).

Clinopyroxene occurs only sporadically in the carbonate groundmass of the aillikites and is absent in carbonatite. The rare clinopyroxene crystals are nearly pure diopside (Mg# 87-100, Fig.5). **Amphibole** was found only in one sample (Q29) coexisting with diopside; it is a solid-solution between richterite and magnesiokatophorite and is remarkably low in K (Na/K > 10; Fig.6).

Small reddish- and yellowish-brown anhedral **garnet** grains may occur in the groundmass. Poikilitic inclusions of other groundmass phases, replacement of groundmass clinopyroxene by garnet and the chemical composition (low Al, high Ca, Fe and Ti) suggest the garnet is of primary origin. The groundmass garnets can be broadly classified as titanian andradites. Schorlomitic compositions with Ti greater than 0.5 atoms per formula unit corresponding to greater than 8 wt.% TiO₂ dominate. The clinopyroxene-poor aillikites Q37 and Q39 contain

zirconian schorlomite with up to 10.5 wt.% ZrO₂. Individual crystals show abrupt compositional changes with respect to Ca, Fe, Ti and Zr content with the highest kimzeyite component confined to the core. Kimzeyitic garnets have mainly been reported from carbonatites, UML (Platt & Mitchell, 1979), shoshonites (Munno *et al.*, 1980) and more recently from kamafugitic ejecta (Schingaro *et al.*, 2001).

Spinel and **ilmenite** are abundant in the groundmass of the Torngat ultramafic lamprophyres with the highest modal abundances occurring in aillikites (9-20 vol.%, Fig.3A). Members of the magnetite-ulvöspinel solid solution series dominate over ilmenite and modally less abundant but widespread Cr-spinel.

The **spinel group** minerals occur as composite crystals rather than single-phase grains. The commonest variation in individual Ti-magnetite grains is toward increasing Fe and decreasing Ti, approaching magnetite end-member composition. Tiny Cr-spinel cores grade into less chromian compositions which in turn are mantled by Ti-magnetite or magnetite. Three broad compositional groups, listed in order of increasing abundance, can be distinguished: (1) spinel-chromite solid solutions; (2) titanian (1-10 wt.% TiO₂) magnesiochromite-chromite solid solutions with typically < 5 wt.% Al₂O₃; and (3) ulvöspinel-magnesian ulvöspinel-magnetite solid solutions with < 2 wt.% Al₂O₃.

The rare resorbed or enclosed crystals representing spinel-chromite solid solutions show a Cr-Al trend and are most likely derived from disaggregated mantle peridotite. Magnesiochromite-chromite solid solutions occur as tiny crystals overgrown by Ti-magnetites. Cr content reaches up to 52 wt.% but the Al content is remarkably low (commonly < 5 wt.%). The widespread members of the ulvöspinel-magnesian ulvöspinel-magnetite series (Ti-magnetites) occur either as overgrowth around chromite crystals or as discrete subhedral microphenocrysts in the groundmass. The latter are sometimes strongly corroded and appear to have reacted with the carbonate groundmass. Ti-magnetites from the aillikites have fairly low but constant Fe/Mg ratios (Fig.7) following a kimberlite trend (Mitchell, 1995; Barnes & Roeder, 2001). The aillikitic Ti-magnetites commonly show an increase in Mg toward the rim. The MnO content in the Ti-magnetites ranges from negligible to up to 3 wt.%. Ti-magnetite lamellae exsolved from ilmenite macrocrysts are also highly manganoan (up to 3.3 wt.% MnO).

Ilmenite typically occurs as subhedral groundmass laths or irregular grains (100-500 μm) in aillikites, and may be found in contact with magnetite, Ti-magnetite and rarely with Cr-spinel, perovskite as well as rutile. Macrocrystal ilmenites (up to 5 mm) appear to be restricted to the aillikites and may host oxidation exsolution lamellae of Ti-magnetite. The ilmenites represent a solid solution series between ilmenite (FeTiO_3) and geikielite (MgTiO_3) with some solid solution toward hematite (Fe_2O_3). The calculated Fe_2O_3 content is highest in the macrocrystals (up to 24 mol.% hematite). The MnO content is variable (0.3-11 wt.%) and is intermediate between Mn-depleted ilmenites from kimberlite (Mitchell, 1977) and carbonatitic high-Mn ilmenites (Mitchell, 1978). MnO is dominantly below 4 wt.%, resulting in a low pyrophanite component ($\text{MnTiO}_3 = 1\text{-}5$ mol.%). In rare instances, rims and inclusions reach up to 23 mol.% MnTiO_3 . If compositional zoning occurs, this is toward decreasing geikielite and hematite but increasing Mn from core-to-rim. The lamprophyric ilmenites are distinct from their kimberlitic counterparts in being poor in Cr_2O_3 (< 0.2 wt.%). They share this Cr depletion with ilmenites from carbonatites.

Rutile occurs as an accessory groundmass phase in only one third of the samples but is present in all three rock types. Tiny subhedral grains predominate and only in rare instances do rutiles reach up to 200 μm in diameter. The largest rutile grains and highest modal abundances (approx. 5 vol.%) have been observed in the dolomite carbonatite Q13. In addition to these discrete crystals, rutile occurs as an intergrowth with Ti-magnetite, and the latter two phases may form rims on each other. Rutile dendrites contribute to the carbonate-rich groundmass of sample Q35. Fe_2O_3 reaches up to 1.9 wt.% in the rutiles and the highest observed Nb_2O_5 content is 1.44 wt.%, much lower than in their kimberlitic analogues. Cr content seems to be very low on the basis of reconnaissance analyses ($\text{Cr}_2\text{O}_3 < 0.1$ wt.%). Individual crystals exhibit minor compositional variation expressed as subtle changes in Nb, Fe and Ti content.

Perovskite is a common groundmass constituent of the ultramafic lamprophyres (Fig.3), and occurs in those samples devoid of rutile. The distribution of perovskite is extremely heterogeneous, thus modal abundances may vary from a few grains to up to 10 vol.%. Grain sizes of the commonly subhedral-to-rounded brownish crystals are also highly variable ranging from few microns to up to 750 μm . Perovskite is commonly found to be in contact with Ti-magnetite and can accompany olivine pseudomorphs creating a so-called "necklace" texture, as is commonly seen in kimberlites, aillikites and kamafugites (Chakhmouradian &

Mitchell, 2000; Tappe *et al.*, 2003). Another mode of occurrence is as inclusions together with Ti-magnetite in phlogopite plates.

Most of the perovskites are close to the ideal CaTiO_3 end-member composition and contain less than 10 mol.% of other end-members such as loparite ($\text{Na}_{0.5}\text{Ce}_{0.5}\text{TiO}_3$) and lueshite (NaNbO_3). The strong negative correlation between atomic Ca and atomic Na plus REE indicates a solid solution series between perovskite and loparite. In rare instances the loparite component reaches up to 19.1 mol.%. The SrO and Nb_2O_5 content from aillikitic perovskites (less than 0.4 wt.% and 0.6 wt.%, respectively) are remarkably low.

Nearly all perovskite crystals are zoned. Both a simple core-to-rim variation and a complex oscillatory zonation exist (Fig.3F). The former is characterized by decreasing LREE and Na abundances, whereas the perovskite end-member increases toward the rim. This gradational pattern is commonly referred to as a normal zonation (Chakhmouradian & Mitchell, 2000) and contrasts with the oscillatory zoning where only subtle changes in the Ca, Ti and LREE content are displayed on a very small scale. Perovskite crystals exhibiting a discrete loparite-rich overgrowth rarely occur.

Hydroxy-fluorapatite is ubiquitous in the groundmass of aillikites but is conspicuously lacking in carbonatitic samples. Apatite forms euhedral elongated prisms and tiny needles but appears also resorbed in the carbonate groundmass. Radiating sprays of acicular apatite commonly occur (Fig.3A), a feature described from the groundmass of kimberlites (Mitchell, 1986). Rarely prismatic apatite is enclosed by groundmass phlogopite. The F content of apatites is rather high (> 1.25 wt.% F), but only rarely exceeds 2 wt.%. A significant amount of Si substitutes for P in the apatites from aillikites (up to 2.7 wt.% SiO_2). The Sr content is low (< 1 wt.% SrO) in comparison to apatites from orangeites (Mitchell, 1995). Most apatites consist of distinct domains forming a patchy irregular pattern. The strongest chemical variation between domains is with respect to their P, Si and Ca content.

Carbonate occurs as coarse ferroan dolomite crystals and subordinate breunnerite forming the matrix of the carbonatite Q13. Grain size ranges between 200 and 600 μm across with some dolomite laths reaching up to 1.5 mm in length. The Fe content is remarkably high, approaching 11.6 wt.% FeO. Phlogopite flakes and rutile grains are poikilitically-enclosed by the carbonate crystals.

Carbonates are also important groundmass constituents of the aillikites (Fig.3A). They occur as: a mosaic of calcite crystals; interlocking groundmass grains intergrown with serpentine; as pseudomorphs after olivine; in mica-rimmed globules or serpentine-carbonate segregations; and as secondary cross-cutting veins filling cracks. Sometimes fine-grained dispersed carbonate forms schlieren, in particular close to wall-rock contacts. Calcite dominates over dolomite in aillikites, and is near ideal CaCO_3 with only small contents of MgO and MnO (< 1 wt.%), as well as FeO (< 1.4 wt.%). The SrO content is generally lower than 1.5 wt.% not exceeding 3 wt.%, and usually decreases rimward. BaO is dominantly below 0.3 wt.% and only rarely approaches 0.7 wt.%. Rare dolomite in the groundmass of aillikites is Fe-poor and was observed to coexist with calcite.

Sulphides are common in the groundmass of the ultramafic lamprophyres and can reach significant abundances. Pyrite was most often observed forming laths and cubes and occasionally occupying the cleavage trace of phlogopite plates. Chalcopyrite occurs subordinately. Pyrite is generally low in Ni and Co but in rare instances contents up to 2.8 and 0.6 wt.%, respectively, were measured. The formation of rare nickel sulphide with up to 5 wt.% Co seems to be related to serpentinization as was demonstrated for various kimberlite occurrences (Akella *et al.*, 1979; Mitchell, 1986).

Serpentine is widespread as a product of olivine alteration and rarely occurs in coexistence with carbonate in the mesostasis. This latter mode of occurrence develops local segregations, interpreted as being of late-stage primary origin. The Al_2O_3 content of the groundmass serpentine ranges between 1.5 and 2.8 wt.%, but is not as high as would be expected from serpentinized mica. The lowest observed Al_2O_3 content is 0.8 wt.% and NiO may fall below the detection limit of the microprobe, supporting the primary nature. Furthermore, the groundmass serpentine is notably Fe-rich reaching up to 18 wt.% FeO.

Quartz may sporadically occur as component of the mesostasis as is also reported from kimberlites and carbonatites (Mitchell, 1986; Woolley & Kempe, 1989). It is noteworthy that groundmass quartz has only been found in the carbonate-rich aillikites as well as carbonatites (Q13, Q27, Q35). In the carbonatite sample Q13 the carbonate-quartz intergrowth clearly points to a late-stage primary origin.

4.3. Mela-aillikites

Olivine dominates the macro- and phenocrysts in the predominantly intergranular textured mela-aillikites (Fig.3B). Composition and zoning patterns are the same as observed in the aillikites.

Phlogopite is ubiquitous and forms large poikilitic plates up to 5 mm in size. All the enclosed phases such as olivine, clinopyroxene, opaques, perovskite and rutile are also set between the mica plates (Fig.3B). Groundmass laths are only present in samples Q31, Q32 and Q33 resulting in an intersertal rock fabric. Kink-banded, unzoned macrocrysts occur rarely.

Micas from mela-aillikites are solid solutions between the same end-members as in the aillikites, although there is a tendency for them to be richer in Ti (Fig.4A). Most of the phlogopites have TiO₂ contents greater than 4 wt.% and the highest (up to 8 wt.%) were measured in laths from samples Q31, Q32, Q33. An evolutionary trend toward biotite rather than tetraferriphlogopite is characteristic for the micas from mela-aillikites with increasing Fe and decreasing Mg but nearly constant Al (Fig.4B). Discrete dark brown biotite rims were found only in the mela-aillikites, sometimes altered to Fe-Mg chlorite.

The modal proportions of **clinopyroxene** are significantly higher than in aillikites reaching up to 26 vol.% (Fig.3D). In general, clinopyroxene is restricted to the groundmass, mostly forming prismatic-to-acicular crystals measuring up to 500 µm in length (Fig.3E). Smaller euhedral microphenocrysts are commonly enclosed by phlogopite plates. Complex zoning patterns are common (Fig.3D). Diopsides in the mela-aillikites have highly variable Mg/Fe²⁺ ratios approaching salitic composition (Mg# 68-100). These are characterized by high (relative to those in aillikites) contents of Al and Ti (Fig.5) leading to a high proportion of Ca-Ti-Tschermaks molecule (up to 19 mol.%). The most Fe-rich clinopyroxenes are ferrosalitic (hedenbergitic; Mg# down to 28), and were found in samples Q31, Q32, Q33. These samples also contain aegirine-augite in the groundmass. Near pure aegirine crystallized in the vicinity of carbonate segregations in sample Q16. The clinopyroxenes are commonly extensively-zoned and display normal trends of rimward Na and Fe enrichment and Mg depletion (up to 19 mol.% aegirine). In rare instances reversed zonation occurs.

Some mela-aillikites contain a pale brown richteritic **amphibole** (Fig.3B) which may equal the modal abundance of coexisting clinopyroxene. The late amphibole overgrows/replaces the

clinopyroxene (e.g. Q15, Q23, Q36 and Q38), and additionally forms poikilitic plates and prisms. Amphibole rims around clinopyroxene and phlogopite are quite common (Fig.3E), whereas clinopyroxene overgrowing amphibole has only rarely been observed (e.g. Q12). An intergrowth with groundmass apatite indicates the late occurrence of amphibole in the crystallization sequence.

Compositions of the anhedral poikilitic groundmass plates and subhedral grains range between the end-members magnesiokatophorite and richterite (Fig.6A). In contrast to typical lamproitic and orangeitic richterites, Na dominates over K (0.12-2.66 wt.% K₂O, atomic Na/K >3, Fig.6B). The Ti content is high (0.4-5.5 wt.% TiO₂), a common characteristic of all these potassic rock types, and F is homogeneously low (<0.8 wt.%). Compositional zoning trends are the same as for coexisting clinopyroxene with an increase in Al, Ti and Fe but decreasing Mg content from core to rim.

Titanian andradite **garnet** occurs in the groundmass of mela-aillikites. Replacement of clinopyroxene was observed in Q28, as in aillikites. These garnets can be classified as andradite, schorlomite, zirconian schorlomite and kimzeyite. In sample Q28 schorlomite (TiO₂ up to 31.1 wt.%) is overgrown by nearly pure andradite (TiO₂ down to 0.3 wt.%). Zirconium content reaches its maximum in sample Q18 (17.2 wt.% ZrO₂).

The **spinel** and **ilmenite** assemblage and their composition in the mela-aillikites is broadly similar to that in the aillikites. The mela-aillikites contain generally less opaques (6-13 vol.%) than the aillikites (9-20 vol.%). Furthermore, the groundmass Ti-magnetites show a trend of increasing Fe³⁺ and Fe²⁺/(Mg²⁺+Fe²⁺) that curves up towards pure magnetite end-member composition (Fig.7). This so-called Fe-Ti trend is slightly distinctive from the kimberlite trend exhibited by aillikitic spinels, where the Fe²⁺/(Mg²⁺+Fe²⁺) ratio is nearly constant over a wide range in Fe³⁺.

The **perovskite-rutile** incompatibility (they seem to be related by a reaction) observed in aillikites is also apparent in the mela-aillikites. Perovskite in the mela-aillikites has higher Sr and Nb content (up to 1.7 and 2.1 wt.%, respectively) than in aillikites, which differ nearly by an order of magnitude.

Titanite is restricted to some mela-aillikites but may reach appreciable modal abundances (up to 9 vol.%). It shows rhombic-or-sphenoidal cross-sections up to 250 μm across but can also be found filling groundmass interstices or forming spongy cores of Ti-magnetite crystals. In general, titanite does not coexist with perovskite or rutile and occurs only in the carbonate-poorest samples. Tiny relict rutile or perovskite crystals in sample Q36 and Q38 are overgrown by titanite, which almost entirely replaces the oxides. The Fe_2O_3 content of the titanites approaches 5.4 wt.% and Na_2O up to 0.6 wt.%. Alumina is generally low but exceptionally reaches 1 wt.%. The LREE contents reach up to 1.5 wt.% Ce_2O_3 .

Mela-aillikitic **apatite** has the same mode of occurrence as its aillikitic analogue but is more common (up to 5 vol.%). The F content is slightly higher (up to 3 wt.%), than in apatite from aillikites and there is less Si substituting for P in mela-aillikites than observed in aillikites. An appreciable amount of sulphur (up to 1 wt.%) was only found in apatite from mela-aillikites.

Carbonate occurs isolated in the interstices between mica plates, apatite and/or clinopyroxene prisms, or in ocelli-like segregations, never exceeding 5 vol.%. Calcite laths up to 200 μm long have been found in sample Q15. Sample Q43 shows a well-developed segregation texture composed of cm-sized globular structures with calcite margins along serpentine cores rimmed by quenched titanite, clinopyroxene and apatite needles. Compositions are broadly similar to aillikitic carbonates, but there is a tendency for calcite from the mela-aillikites to be slightly richer in MgO than its aillikitic analogues. Rare dolomite was found to coexist with breunneritic MgCO_3 - FeCO_3 solid solutions.

Groundmass **sulphides** are more abundant in mela-aillikites than in aillikites/carbonatites. Pyrite and chalcopyrite occur frequently and pyrrhotite has been detected only in mela-aillikites, where all three phases coexist. Pyrrhotite contains constantly high Ni content with up to 0.8 wt.% Ni and was found to be rimmed by chalcopyrite in sample Q19.

In addition to **serpentine**, dark green **chlorite** can rim phlogopite plates in the mela-aillikites (Fig.3B, Q18, Q36, Q38). This is a pseudomorphic replacement of the previously described biotite rims.

Near pure **albite** together with acmite fills the ocelli-like structures in sample Q31. **Zeolites** are rare and mostly concentrated in secondary carbonate veins cross-cutting the dyke rocks.

5. WHOLE-ROCK COMPOSITION

5.1. Major elements

In general, the ultramafic lamprophyres are characterized by high but varying MgO (10-25 wt.%), CaO (5-20), TiO₂ (3-10) and K₂O (1-4) but low SiO₂ (22-37) and Al₂O₃ (2-6) contents (Tab.8 and Fig.8). The mela-aillikites are distinguished from the aillikites by higher SiO₂ (> 30 wt.%), Al₂O₃ (> 4 wt.%), Na₂O (> 0.3 wt.%) and lower CO₂ (< 6 wt.%). High modal amounts of olivine macrocrysts result in scatter in major oxide variation diagrams. This is more pronounced in aillikites, where the amount of primary carbonate is also high (Fig.8). The TiO₂ content is remarkably high in comparison to other alkaline ultramafic rocks and reaches its maximum in the mela-aillikites. A high-Ti group can be distinguished from the remaining mela-aillikites, with a somewhat arbitrary boundary at 7 wt% TiO₂ (Fig.8 and Fig.10). Most samples have Fe₂O₃/FeO ratios > 1 with the aillikites being conspicuously richer in ferric iron (1.3-2.3) than the mela-aillikites (0.6-1.7). Both aillikites and mela-aillikites have MgO/CaO and SiO₂/Al₂O₃ ratios that are transitional between the low ratios for UML and higher ratios for kimberlite (cf. Rock, 1991). In summary, the dykes with their variably high *mg*-numbers (71.8-90) represent primitive potassic melts undersaturated with respect to silica. The range of compositions is consistent with those noted by Rock (1991) for ultramafic lamprophyres.

5.2. Trace elements

The concentrations of compatible trace elements such as Sc, V, Cr and Ni are high but variable demonstrating the primitive nature of the lamprophyric rock suite. Cr (290-1570 ppm) and Ni (229-1110 ppm) abundances are comparable to those found in primary or primitive mantle-derived mafic/ultramafic rocks.

Incompatible trace element concentrations of all samples are extremely high and there are only subtle differences between carbonatite/aillikite and mela-aillikite. Both aillikite/carbonatite and mela-aillikite have a common, less-fractionated primitive mantle-normalized incompatible element distribution pattern (Fig.9). Troughs or negative anomalies occur at K, Sr-P and occasionally at Zr-Hf. The Zr-Hf anomaly is of variable size and quantified by the (Zr+Hf)/(Zr+Hf)* ratio, whereby (Zr+Hf)* is interpolated between neighbouring Nd and Sm. This relative Zr-Hf depletion is strongest for the carbonatite (Q13)

and aillikites (0.25-0.77) and decreases within the mela-aillikites (0.46-0.93), where the Zr-Hf anomaly can be absent in the high-Ti group (Fig.9).

The rare earth elements (REE) are strongly fractionated, showing steep chondrite-normalized distribution patterns with highly-enriched LREE and depleted HREE. La and Ce approach chondrite-normalized values greater than 1000, whereas Yb and Lu are typically lower than 10 times chondrite. The shape of the REE distribution patterns is similar for all rock types but there is a wide range of fractionation ($La_N/Yb_N = 58-204$), undoubtedly resulting from the diverse modes of the numerous REE-bearing phases.

6. RELATIONSHIP BETWEEN AILLIKITES AND MELA-AILLIKITES

The mineralogically-distinct members of the Torngat dyke swarm represent a compositional continuum with overlapping bulk major element and comparably high trace element abundances with similar normalized distributions. This implies their parental magmas are related.

The range of composition cannot be explained in terms of fractional crystallization. Subordinate olivine and Cr-spinel fractionation, as indicated by the positive correlation between Ni, Cr and MgO, only accounts for the intragroup variation of aillikites and mela-aillikites. More-evolved olivine microphenocrysts than phenocrysts and normal zoning patterns in the latter clearly point to olivine fractionation.

The overall similarity of the incompatible trace element distribution patterns implies that fractionation of minerals rich in these elements has not been a major factor in the evolution of these rocks. The variation in the Zr-Hf anomaly is decoupled from other HFSE such as Nb-Ta and Ti (Fig.9) and therefore unlikely to be produced by fractionation of a titanate. A Ti-free Zr-Hf phase has not been observed in the Torngat dykes implying that the Zr-Hf depletion was caused during partial melting and relates to source characteristics.

The Torngat rocks do not contain xenoliths of crustal derivation. That their composition is nominally unaffected by crustal contamination is indicated by low Si and Al concentrations and a high compatible trace element content. Furthermore, Zr/Hf (30-50) and Nb/Ta (10-18) ratios have constant nearly chondritic values reflecting the source composition. Additionally,

negative correlation between Th and Zr rules out significant crustal contamination of the UML magma.

The variation in mineralogical mode and trends between the members of the Torngat dyke swarm has to be explained in terms of crystallization conditions. Amongst the vast number of constituent minerals, many incomplete reaction relations have been observed, for example; phlogopite-olivine, amphibole-clinopyroxene, carbonate-clinopyroxene, schorlomite-clinopyroxene, titanite-rutile, titanite-perovskite and rutile-perovskite. This suggests that aillikite/carbonatite and mela-aillikite crystallized from a common magma type but under different pressure, temperature and more importantly volatile conditions, with the failure of reactions to proceed to completion as the magma moved toward the surface.

Mela-aillikites seem to have crystallized over a greater temperature range than the aillikites as is implicated by Fe-Ti oxide and apatite-phlogopite equilibration temperatures. Both temperature estimates tend to be lower for mela-aillikites (500°C and 600°C, respectively) than for aillikites (650°C and 700°C, respectively). The occurrence of interstitial titanite in coexistence with olivine might be in response to temperatures falling below 650°C (Xirouchakis *et al.*, 2001). The observed perovskite-titanite reaction (Carmichael *et al.*, 1970) in the Torngat UML was controlled by changing silica activity but cooling promoted late titanite crystallization in the mela-aillikites.

The nature of the volatile component during crystallization of mela-aillikites and aillikites was different, as is implicated by their contrasting modal phlogopite, amphibole and carbonate contents. The CO₂/H₂O ratio was much higher in the aillikites than in the mela-aillikites.

An interesting observation is that the CaO content of both rock types is identical despite the higher modal carbonate abundances in the aillikites (Fig.10). This is best explained by CO₂ loss (degassing) in the mela-aillikites. The low CO₂ but high H₂O conditions promoted the crystallization of clinopyroxene and amphibole incorporating most of the Ca, whereas the CO₂-rich conditions during aillikite solidification suppressed the precipitation of clinopyroxene. It seems that clinopyroxene and amphibole crystallized at the expense of olivine and Ti-magnetite in the groundmass of mela-aillikites. Other than in the aillikites, the late-stage Ti-magnetite of the mela-aillikites tends to be Mg-free (Fig.7). This might be a

consequence of exchange with coexisting pyroxene, an effect favoured in slowly cooled rocks as pointed out by Barnes & Roeder (2001). The Mg content is also lower in phlogopite from mela-aillikites than from aillikites.

There are indications that late crystallization of aillikites occurred under more oxidizing conditions than in mela-aillikites. Ferric Fe-bearing tetraferriphlogopite rims exclusively occur in the aillikites, whereas biotite rims are restricted to the mela-aillikites. The mela-aillikites also contain late richteritic amphibole, which requires lower oxygen fugacity during crystallization (Charles, 1975). Given the similar whole-rock Fe content of the dyke rocks, it is interesting to note that aillikites have much higher ferric/ferrous Fe ratios than mela-aillikites. This is unlikely to reflect the redox conditions of the parent magma but point to the oxidation state during dyke emplacement.

Taken together, these points indicate slower cooling and a greater crystallization depth for the mela-aillikites in a less open system than is to be expected for aillikites and carbonatites. Emplacement of these CO₂-richer magmas was more violent, as is implicated by disrupted fragments of older mica enclosed in newly grown plates.

7. REGIONAL COMPARISONS

7.1. Relation to other Neoproterozoic alkaline rocks in Quebec and Labrador

Ultramafic dyke rocks have been described from the northwest part of the Abloviak Fjord in the northern Torngat Mountains (Digonnet *et al.*, 2000). They are spatially and structurally closely-related to the Torngat dykes, which occur only a few tens of kilometres to the southeast. The Abloviak dykes have a phlogopite Ar-Ar Neoproterozoic age (579-550 Ma; Digonnet *et al.*, 2000) similar to the U-Pb perovskite age of the Torngat dykes. Rock texture, mineralogy and geochemistry resemble the carbonate-richest UML of the Torngat dykes, and they have also been classified as aillikites (Fig.8). The Abloviak aillikites are diamondiferous (Digonnet *et al.*, 2000).

The common characteristics between the Abloviak and Torngat dykes suggest that they comprise a single ultramafic lamprophyre dyke swarm in the northern Torngat Mountains of Quebec and Labrador. The dykes intruded an area that is at least 1500 km² in size, thus forming one of the largest UML swarms known from North America.

A NW-SE trending mela-aillikite dyke was found at the coast of the Labrador Sea close to the mouth of Hebron Fjord during field work in 2003 (Fig.1). This UML has a strong textural and mineral chemical resemblance to the Torngat mela-aillikites. It contains abundant perovskite and a U-Pb age determination is in progress.

Aillikites have been described from the Aillik Bay intrusive suite (Malpas *et al.*, 1986; Foley, 1989), on the Labrador coast (Fig. 1). Based on a U-Pb perovskite age of 582.1 ± 1.5 Ma (own unpublished data, see part II of this thesis), these rocks are nearly identical in age to the Torngat dykes.

7.2. Comparison with West Greenland occurrences

Greenland has been the site of recurrent alkaline ultramafic magmatism from the Archean to the Tertiary (Larsen & Rex, 1992). Kimberlites, lamproites and ultramafic lamprophyres have been reported from numerous localities (Fig.1), but our emphasis is on occurrences that are of the same age as the Torngat UML. Such Neoproterozoic ultramafic dykes (607-583 Ma) have been described from the central West Greenland occurrences Sisimiut, Sarfartoq and Maniitsoq (Scott, 1981; Larsen *et al.*, 1983). They intruded the Paleoproterozoic Nagsugtoqidian mobile belt (Sisimiut) and the Archean of the North Atlantic craton (Maniitsoq) or straddle the boundary between both (Sarfartoq). They were earlier described as kimberlites (Scott, 1981; Thy *et al.*, 1987; Nelson, 1989; Larsen & Rex, 1992; Larsen & Rønso, 1993) but, in more recent studies, these carbonate-rich dykes were shown to have lamprophyric affinity (Dalton & Presnall, 1998; Mitchell *et al.*, 1999). We believe they should be classified as aillikites and this becomes clear when the whole-rock data and available mineral chemical data are compared to the Torngat dykes.

Silica (< 33 wt.%), Al_2O_3 (< 4), CaO (5-15), Na_2O (< 0.5) and K_2O (< 2.4) and the ratios of Si/Al and Mg/Ca are identical between the Neoproterozoic aillikites from central West Greenland and the Torngats (Fig.10). The Ti concentrations in the Greenlandic aillikites (< 5 wt.%) are lower than those in most Torngat samples, suggesting that the high Ti content of the Torngat rocks is a localized phenomenon. Clinopyroxenes from both Greenland and Torngat rocks are also enriched in Al and Ti (Fig.5), clearly distinct from kimberlitic rocks. Spinels from the Neoproterozoic Greenland and Torngat aillikites follow a kimberlite trend with fairly constant Fe^{2+}/Mg ratios as ferric Fe increases (Fig.7).

The mineralogy and bulk rock chemistry of micaceous ultramafic dyke rocks from the Gardar Province, originally termed mica peridotites and mica pyroxenites by Upton & Thomas (1973), is in accord with that of the Torngat mela-aillikites (e.g. Fig.5 and Fig.10). These rocks have been classified as UML by Rock (1986), who picked them as an example for the application of the prefix "mela" when describing UML with an extremely high colour index.

7.3. Large Scale Tectonic Implications

Numerous ultramafic potassic-to-carbonatitic complexes of Late Neoproterozoic age occur on both sides of the present day North Atlantic (Doig, 1970). Restoring the Laurentian part for Mesozoic-Cenozoic drift, it is apparent that the UML suite from the Torngat Mountains in Quebec and Labrador has its nearest allies in the Neoproterozoic ultramafic lamprophyre - carbonatite occurrences of West Greenland (Sisimiut-Sarfartoq-Maniitsoq, Fig.1). At least parts of the Aillik Bay intrusive suite at the coast of Labrador were also emplaced during Neoproterozoic; hence, these type aillikites also fit into the same tectonic framework.

Neoproterozoic ultramafic lamprophyre - carbonatite complexes on the European side (Baltica) of the North Atlantic region occur at Alnö Island (Sweden) and in the Fen district (South Norway). Magmatism of these classic igneous provinces was coeval and ages of 584-546 Ma (Alnö) and 578 ± 24 Ma (Fen) have been obtained (Barth & Ramberg, 1966; Welin *et al.*, 1972; Brueckner & Rex, 1980; Dahlgren, 1994; Andersen, 1996).

During the Vendian period (650-545 Ma) the Late Proterozoic supercontinent Rodinia started to break up and the Proto-Atlantic formed. These tectonic events were initially accompanied by voluminous continental rift-related subalkaline mafic magmatism in both eastern Laurentia and western Baltica (e.g. Kamo *et al.*, 1989; Bingen *et al.*, 1998). Torsvik *et al.* (1996) demonstrated that between approximately 600 and 580 Ma, the maximum age of the alkaline rock suites, the rift-to-drift transition occurred, whereby the Iapetus Ocean opened. It can be inferred from the emplacement ages of the alkaline complexes and the timing of Late Proterozoic tectonic processes in the North Atlantic region that the volatile-rich, ultramafic potassic-to-carbonatitic magmatism followed the major continental rifting stage and occurred when nearby oceanic rifting was already initiated.

ACKNOWLEDGEMENTS

We are grateful to Andreas Kronz who ably assisted with the microprobe work. Dejan Prelevic is thanked for discussions that ensued during this study. Roger Mitchell, Casey Hetman (DeBeers) and Dave Apter are thanked for their comments on this paper. This project is funded by the German Research Foundation (grant Fo 181/15) and a NSERC operating grant (GAJ). Most of the work was done whilst ST was a recipient of a scholarship from the state of Mecklenburg-Vorpommern (Germany). We acknowledge the generous contribution of samples for our study by Marum Resources Inc., Dumont Nickel Inc. and International Tower Hill Mines Ltd. This is Geological Survey of Canada contribution #2003317.

REFERENCES

- Akella, J., Rao, P. S., McCallister, R. H., Boyd, F. R. & Meyer, H. O. A. (1979). Mineralogical studies on the diamondiferous kimberlite of the Wajrakharur area, southern India. In: Boyd, F. R. & Meyer, H. O. A. (eds.) *Kimberlites, diatremes, and diamonds: their geology, petrology, and geochemistry*. Washington, D.C.: American Geophysical Union, pp. 172-177.
- Andersen, T. (1996). Sr, Nd, and Pb isotopic characteristics of the Alnö carbonatite complex, Sweden. In: Kohonen, T. & Lindberg, B. (eds.) *Nordic Geological Winter Meeting*. Turku-Åbo, Finland, pp. 11.
- Araujo, A. L. N., Carlson, R. W., Gaspar, J. C. & Bizzi, L. A. (2001). Petrology of kamafugites and kimberlites from the Alto Paranaíba Alkaline Province, Minas Gerais, Brazil. *Contributions to Mineralogy and Petrology* **142**, 163-177.
- Armstrong, J. T. (1995). CITZAF: a package of correction programs for the Quantitative electron microbeam x-ray analysis of thick polished materials, thin films, and particles. *Microbeam Analysis* **4**, 177-200.
- Barnes, S. J. & Roeder, P. L. (2001). The range of spinel compositions in terrestrial mafic and ultramafic rocks. *Journal of Petrology* **42**, 2279-2302.
- Barth, T. F. W. & Ramberg, I. B. (1966). The Fen circular complex. In: Tuttle, O. F. & Gittins, J. (eds.) *Carbonatites*. New York, United States: Interscience, pp. 225-257.

- Bingen, B., Demaiffe, D. & van Breemen, O. (1998). The 616 Ma old Egersund basaltic dike swarm, SW Norway, and late Neoproterozoic opening of the Iapetus Ocean. *Journal of Geology* **106**, 565-574.
- Brenan, J. M. & Watson, E. B. (1991). Partitioning of trace elements between carbonate melt and clinopyroxene and olivine at mantle P-T conditions. *Geochimica et Cosmochimica Acta* **55**, 2203-2214.
- Brueckner, H. K. & Rex, D. C. (1980). K-Ar and Rb-Sr geochronology and Sr isotopic study of the Alnö alkaline complex, northeastern Sweden. *Lithos* **13**, 111-119.
- Carmichael, I. S. E., Nicholls, J. & Smith, A. L. (1970). Silica activity in igneous rocks. *American Mineralogist* **55**, 246-263.
- Chakhmouradian, A. R. & Mitchell, R. H. (2000). Occurrence, alteration patterns and compositional variation of perovskite in kimberlites. *The Canadian Mineralogist* **38**, 975-994.
- Charles, R. W. (1975). The phase equilibria of richterite and ferrichterite. *American Mineralogist* **60**, 367-374.
- Connelly, J. N., van Gool, J. A. M. & Mengel, F. C. (2000). Temporal evolution of a deeply eroded orogen: the Nagssugtoqidian Orogen, West Greenland. *Canadian Journal of Earth Sciences* **37**, 1121-1142.
- Dahlgren, S. (1994). Late Proterozoic and Carboniferous ultramafic magmatism of carbonatitic affinity in Southern Norway. *Lithos* **31**, 141-154.
- Dalton, J. A. & Presnall, D. C. (1998). The continuum of primary carbonatitic-kimberlitic melt compositions in equilibrium with lherzolite: data from the system CaO-MgO-Al₂O₃-SiO₂-CO₂ at 6 GPa. *Journal of Petrology* **39**, 1953-1964.
- Digonnet, S., Goulet, N., Bourne, J., Stevenson, R. & Archibald, D. (2000). Petrology of the Abloviak aillikite dykes, New Québec: evidence for a Cambrian diamondiferous alkaline province in northeastern North America. *Canadian Journal of Earth Sciences* **37**, 517-533.
- Dimroth, E. (1970). Meimechites and carbonatites of the Castignon Lake Complex, New Quebec. *Neues Jahrbuch für Mineralogie Abhandlungen* **112**, 239-278.
- Doig, R. (1970). An alkaline rock province linking Europe and North America. *Canadian Journal of Earth Sciences* **7**, 22-28.

Dressler, B. (1975). Lamprophyres of the north-central Labrador Trough, Quebec, Canada. *Neues Jahrbuch für Mineralogie Monatshefte* **6**, 268-280.

Foley, S. F. (1989). Emplacement features of lamprophyre and carbonatitic lamprophyre dykes at Aillik Bay, Labrador. *Geological Magazine* **126**, 29-42.

Heaman, L. M. & Kjarsgaard, B. A. (2000). Timing of eastern North American kimberlite magmatism: continental extension of the Great Meteor hotspot track? *Earth and Planetary Science Letters* **178**, 253-268.

Heaman, L. M., Kjarsgaard, B. A. & Creaser, R. A. (2003). The timing of kimberlite magmatism in North America: implications for global kimberlite genesis and diamond exploration. *Lithos* **71**, 153-184.

Jenner, G. A. (1996). Trace element geochemistry of igneous rocks: geochemical nomenclature and analytical geochemistry. In: Wyman, D. (ed.) *Trace element geochemistry of volcanic rocks: applications for massive sulphide exploration*. St. John's, Canada: Geological Association of Canada, pp. 51-77.

Kamo, S. L., Gower, C. F. & Krogh, T. E. (1989). Birthdate for the Iapetus Ocean? A precise U-Pb zircon and baddeleyite age for the Long Range dikes, Southeast Labrador. *Geology* **17**, 602-605.

Kretz, R. (1983). Symbols for rock-forming minerals. *American Mineralogist* **68**, 277-279.

Larsen, L. M. & Rex, D. C. (1992). A review of the 2500 Ma span of alkaline-ultramafic, potassic and carbonatitic magmatism in West Greenland. *Lithos* **28**, 367-402.

Larsen, L. M. & Rønsbo, J. (1993). Conditions of origin of kimberlites in West Greenland: new evidence from the Sarfartoq and Sukkertoppen regions. *Report - Geological Survey of Greenland* **159**, 115-120.

Larsen, L. M., Rex, D. C. & Secher, K. (1983). The age of carbonatites, kimberlites and lamprophyres from southern West Greenland: recurrent alkaline magmatism during 2500 million years. *Lithos* **16**, 215-221.

Leake, B. E., Woolley, A. R., Arps, C. E. S., Birch, W. D., Gilbert, M. C., Grice, J. D., Hawthorne, F. C., Kato, A., Kisch, H. J., Krivovichev, V. G., Linthout, K., Laird, J., Mandarino, J. A., Maresch, W. V., Nickel, E. H., Rock, N. M. S., Schumacher, J. C., Smith, D. C., Stephenson, N. C. N., Ungaretti, L., Whittaker, E. J. W. & Guo, Y. (1997). Nomenclature of amphiboles: report of the Subcommittee on Amphiboles of the International Mineralogical Association, Commission on new minerals and mineral names. *American Mineralogist* **82**, 1019-1037.

- Malpas, J., Foley, S. F. & King, A. F. (1986). Alkaline mafic and ultramafic lamprophyres from the Aillik Bay area, Labrador. *Canadian Journal of Earth Sciences* **23**, 1902-1918.
- Marker, M. & Knudsen, C. (1989). Middle Proterozoic ultramafic lamprophyre dykes in the Archaean of the Ata area, central West Greenland. *Rapport Groenlands Geologiske Undersoegelse* **145**, 23-28.
- Mitchell, R. H. (1977). Geochemistry of magnesian ilmenites from kimberlites in South Africa and Lesotho. *Lithos* **10**, 29-37.
- Mitchell, R. H. (1978). Manganoan magnesian ilmenite and titanian clinohumite from the Jacupiranga carbonatite, Sao Paulo, Brazil. *American Mineralogist* **63**, 544-547.
- Mitchell, R. H. (1986). *Kimberlites: mineralogy, geochemistry and petrology*. New York: Plenum Press, 442 pp.
- Mitchell, R. H. (1995). *Kimberlites, orangeites, and related rocks*. New York: Plenum Press, 410 pp.
- Mitchell, R. H., Scott-Smith, B. H. & Larsen, L. M. (1999). Mineralogy of ultramafic dikes from the Sarfartoq, Sisimiut and Maniitsoq areas, West Greenland. In: Gurney, J. J., Gurney, J. L., Pascoe, M. D. & Richardson, S. H. (eds.) *Proceedings of the VIIth international kimberlite conference*. Cape Town: Red Roof Design, pp. 574-583.
- Moorhead, J., Beaumier, M., Girard, R. & Heaman, L. M. (2003). Distribution, structural controls and ages of kimberlite fields in the Superior Province of Quebec. *8th International Kimberlite Conference extended abstract*,
- Munno, R., Rossi, G. & Tadini, C. (1980). Crystal chemistry of kimzeyite from Stromboli, Aeolian Islands, Italy. *American Mineralogist* **65**, 188-191.
- Nelson, D. R. (1989). Isotopic characteristics and petrogenesis of the lamproites and kimberlites of central West Greenland. *Lithos* **22**, 265-274.
- Pearce, N. J. G. & Leng, M. J. (1996). The origin of carbonatites and related rocks from the Igaliko dyke swarm, Gardar Province, South Greenland: field, geochemical and C-O-Sr-Nd isotope evidence. *Lithos* **39**, 21-40.
- Platt, R. G. & Mitchell, R. H. (1979). The Marathon Dikes. I: Zirconium-rich titanian garnets and manganoan magnesian ulvöspinel-magnetite spinels. *American Mineralogist* **64**, 546-550.

- Rock, N. M. S. (1986). The nature and origin of ultramafic lamprophyres: alnöites and allied rocks. *Journal of Petrology* **27**, 155-196.
- Rock, N. M. S. (1991). *Lamprophyres*. Glasgow: Blackie & Son, 285 pp.
- Schingaro, E., Scordari, F., Capitanio, F., Parodi, G., Smith, D. C. & Mottana, A. (2001). Crystal chemistry of kimzeyite from Anguillara, Mts. Sabatini, Italy. *European Journal of Mineralogy* **13**, 749-759.
- Schumacher, J. C. (1991). Empirical ferric iron corrections: necessity, assumptions, and effects on selected geothermobarometers. *Mineralogical Magazine* **55**, 3-18.
- Scott, B. H. (1981). Kimberlite and lamproite dykes from Holsteinsborg, West Greenland. *Meddelelser om Grønland, Geoscience* **4**, 3-24.
- Sgarbi, P. B. A. & Gaspar, J. C. (2002). Geochemistry of Santo Antônio da Barra kamafugites, Goiás, Brazil. *Journal of South American Earth Sciences* **14**, 889-901.
- Stacey, J. S. & Kramers, J. D. (1975). Approximation of terrestrial lead isotope evolution by a two-stage model. *Earth and Planetary Science Letters* **26**, 207-221.
- Stormer, J. C. (1973). Calcium zoning in olivine and its relationship to silica activity and pressure. *Geochimica et Cosmochimica Acta* **37**, 1815-1821.
- Sun, S.-S. & McDonough, W. F. (1989). Chemical and isotopic systematics of ocean basalts: implications for mantle composition and processes. In: Saunders, A. D. & Norry, M. J. (eds.) *Magmatism in the ocean basins*. London: Geological Society of London, Spec. Publ. 42, pp. 313-345.
- Tappe, S., Foley, S. F. & Pearson, D. G. (2003). The Kamafugites of Uganda: a mineralogical and geochemical comparison with their Italian and Brazilian analogues. *Periodico di Mineralogia* **72**, 51-77.
- Thy, P., Stecher, O. & Korstgard, J. A. (1987). Mineral chemistry and crystallization sequences in kimberlite and lamproite dikes from the Sisimiut area, central West Greenland. *Lithos* **20**, 391-417.
- Torsvik, T. H., Smethurst, M. A., Meert, J. G., Van der Voo, R., McKerrow, W. S., Brasier, M. D., Sturt, B. A. & Walderhaug, H. J. (1996). Continental break-up and collision in the Neoproterozoic and Palaeozoic: a tale of Baltica and Laurentia. *Earth-Science Reviews* **40**, 229-258.

Upton, B. G. J. & Thomas, J. E. (1973). Precambrian Potassic Ultramafic Rocks: South Greenland. *Journal of Petrology* **14**, 509-534.

Walton, B. J. & Arnold, A. R. (1970). Plutonic nodules in lamprophyric carbonatite dykes near Frederikshåb, South-West Greenland. *Grønlands Geologiske Undersøgelse Bulletin* **91**, 1-26.

Wardle, R. J., James, D. T., Scott, D. J. & Hall, J. (2002). The southeastern Churchill Province: synthesis of a Paleoproterozoic transpressional orogen. *Canadian Journal of Earth Sciences* **39**, 639-663.

Wardle, R. J., Bridgwater, D., Mengel, F., Campbell, L., van Kranendonk, M. J., Hauman, A., Churchill, R. & Reid, L. (1994). Mapping in the Torngat Orogen, northernmost Labrador: Report 3, the Nain Craton (including a note on ultramafic dyke occurrences in northernmost Labrador). *Current Research, Newfoundland Department of Mines and Energy* **94-1**, 399-407.

Welin, E., Lundström, I. & Aaberg, G. (1972). Fission track studies on hornblende, biotite and phlogopite from Sweden. *Bulletin of the Geological Society of Finland* **44**, 35-46.

Woolley, A. R. & Kempe, D. R. C. (1989). Carbonatites: nomenclature, average chemical compositions, and element distribution. In: Bell, K. (ed.) *Carbonatites: genesis and evolution*. London, United Kingdom: Unwin Hyman, pp. 1-14.

Xirouchakis, D., Lindsley, D. H. & Andersen, D. J. (2001). Assemblages with titanite (CaTiOSiO₄), Ca-Mg-Fe olivine and pyroxenes, Fe-Mg-Ti oxides, and quartz: Part I., Theory. *American Mineralogist* **86**, 247-253.

TABLES

Table 1: U-Pb perovskite results for aillikite sample Q39 from the Tomgat dykes

Description*	Weight (μg)	U (ppm)	Th (ppm)	Pb (ppm)	Th/U	TC Pb (pg)	$\frac{^{206}\text{Pb}}{^{204}\text{Pb}}$	$\frac{^{238}\text{U}}{^{204}\text{Pb}}$	$\frac{^{206}\text{Pb}^{**}}{^{238}\text{U}}$	$\frac{^{207}\text{Pb}^{**}}{^{235}\text{U}}$	$\frac{^{207}\text{Pb}^{**}}{^{206}\text{Pb}}$	Model ages (Ma)		%Disc	
												$\frac{^{206}\text{Pb}}{^{238}\text{U}}$	$\frac{^{207}\text{Pb}}{^{235}\text{U}}$		
1. tiny dk brn frags/cubes M@0.5A (100)	38	105	587	29	5.6	187	150.4 ± 3.6	1399.6 ± 37.8	0.09483 ± 30	0.7976 ± 93	0.06101 ± 68	584.0 ± 1.8	595.5 ± 5.3	639.4 ± 23.8	9.1
2. tiny dk brn cubes/frags M@0.5A (246)	50	130	729	36	5.6	296	146.5 ± 0.7	1373.9 ± 7.3	0.09388 ± 32	0.7818 ± 97	0.06040 ± 74	578.5 ± 1.9	586.5 ± 5.6	617.8 ± 26.3	6.7

* dk brn - dark brown; frags - fragments; M@0.5A - non-magnetic fraction at 0.5 A (Frantz); (#) - number of grains analysed

** Atomic ratios corrected for fractionation, blank (8 pg Pb; 2 pg U), spike and initial common Pb (Stacey & Kramers, 1975)

Th concentrations calculated based on amount of ^{206}Pb present and $^{207}\text{Pb}/^{206}\text{Pb}$ date

TC Pb = total common Pb

The 2nd fraction is a new, yet unpublished analysis

All errors reported in this table quoted at 1-sigma.

Table 2: Estimated modal mineral abundances (vol.%) of representative Torngat dykes

Mineral Rock/sample#	Ol	Phl	Cpx	Amph	opaques	Prv	Spn	Rt	Adr	Cal/Dol	Ap	Srp	Chl	Qtz*
carbonatite (Q13)	7	28	-	-	1	-	-	5	-	51	-	-	-	4
aillikite	18-40	22-44	0-5	x	9-20	0-10	-	0-1	x	9-24	0-3	0-8	x	x
Q9	18	44	-	-	20	4	-	-	-	12	2	x	-	-
Q17	30	40	-	-	9	-	-	1	-	12	-	8	-	x
Q21	40	28	-	-	20	-	-	-	-	9	3	x	-	-
Q24	28	32	5	-	13	4	-	-	-	16	2	x	-	-
Q26	32	23	-	-	14	-	-	x	-	24	2	5	-	-
Q34	32	22	3	-	10	10	-	-	-	18	2	3	-	-
mela-aillikite	4-32	29-52	4-26	0-19	6-13	0-11	0-9	0-1	x	0-4	0-5	2-15	0-3	x
Q15	11	30	20	19	8	4	-	-	-	3	3	2	-	-
Q22	32	29	14	-	10	11	-	-	-	1	3	x	-	-
Q23	16	35	10	15	11	x	-	-	-	4	5	4	-	-
Q28	12	45	16	x	13	5	-	x	x	4	5	x	x	-
Q31	23	32	26	-	13	-	-	1	-	4	1	x	-	-
Q36	4	52	12	15	7	x	5	x	x	x	2	x	3	-
Q43	27	36	4	-	6	x	9	-	-	2	1	15	-	-

*quartz is secondary; x = minor amounts; - = not detected; symbols for minerals according to Kretz (1983)

Table 3: Representative olivine and clinopyroxene compositions from the Torngat ultramafic lamprophyres

Rock type Mineral Sample#	aillikite			mela-aillikite			aillikite			mela-aillikite			mela-aillikite			Ti-Di									
	Q9 pc4 core	Q9 mpc1 core	Q9 pc2 rim	Q37 pc2 core	Q37 pc2 rim	Q37 rim	Q22 pc1 core	Q22 pc1 rim	Q22 rim	Q24 gm1 core	Q24 gm1 rim	Q24 rim	Q39 gm1 core	Q39 gm1 rim	Q39 rim	Q28 gm3 core	Q28 gm3 rim	Q28 rim	Q32 gm10 core	Q32 gm10 rim	Q32 rim	Q43 gm3 core	Q43 gm3 rim	Q43 rim	
SiO ₂	38.56	40.95	41.31	39.28	39.92	40.69	39.92	40.69	55.28	52.22	52.22	52.65	51.71	51.71	53.33	46.71	46.71	47.53	42.40	42.40	42.40	52.54	52.54	45.45	45.45
TiO ₂	0.02	0.01	0.00	0.01	0.02	0.05	0.02	0.05	0.04	1.27	1.27	0.74	0.68	0.68	0.89	4.17	4.17	2.76	6.43	6.43	6.43	0.77	0.77	5.42	5.42
Al ₂ O ₃	0.02	0.01	0.00	0.02	0.01	0.03	0.01	0.03	0.03	0.91	0.91	0.63	1.30	1.30	0.50	3.29	3.29	1.36	4.35	4.35	4.35	0.95	0.95	4.28	4.28
Cr ₂ O ₃	0.00	0.02	0.00	0.01	0.04	0.05	0.04	0.05	0.04	0.00	0.00	0.00	0.00	0.00	0.00	0.01	0.01	0.01	0.00	0.00	0.00	0.03	0.03	0.02	0.02
FeO	20.74	7.67	6.94	16.28	14.38	10.92	14.38	10.92	0.99	4.89	4.89	3.61	5.54	5.54	4.86	7.33	7.33	23.60	11.50	11.50	9.42	9.42	7.23	7.23	7.23
MnO	0.27	0.17	0.08	0.16	0.25	0.19	0.25	0.19	0.13	0.17	0.17	0.14	0.29	0.29	0.13	0.14	0.14	0.59	0.12	0.12	0.23	0.23	0.18	0.18	0.18
NiO	0.03	0.34	0.34	0.26	0.34	0.33	0.34	0.33	0.00	0.03	0.03	0.03	0.00	0.00	0.01	0.02	0.02	0.00	0.00	0.00	0.00	0.00	0.00	0.00	0.00
MgO	40.66	50.68	51.12	43.11	45.46	47.95	45.46	47.95	18.11	15.70	15.70	16.41	15.22	15.22	15.70	13.71	13.71	2.33	10.43	10.43	12.00	12.00	12.88	12.88	12.88
CaO	0.03	0.00	0.01	0.10	0.06	0.21	0.06	0.21	25.65	24.63	24.63	25.18	24.75	24.75	24.24	23.10	23.10	13.69	22.62	22.62	22.00	22.00	23.01	23.01	23.01
Na ₂ O	0.01	0.00	0.01	0.00	0.01	0.00	0.01	0.00	0.02	0.49	0.49	0.23	0.26	0.26	0.41	0.58	0.58	5.70	0.76	0.76	1.67	1.67	0.55	0.55	
K ₂ O	0.00	0.00	0.01	0.00	0.00	0.02	0.00	0.02	0.01	0.00	0.00	0.02	0.01	0.01	0.00	0.00	0.00	0.02	0.00	0.00	0.00	0.00	0.00	0.00	0.00
Total	100.34	99.85	99.82	99.23	100.50	100.44	100.50	100.44	100.29	100.30	100.30	99.63	99.77	99.77	100.06	99.06	99.06	97.59	98.61	98.61	99.61	99.61	99.02	99.02	99.02
No. oxygens	4	4	4	4	4	4	4	4	6	6	6	6	6	6	6	6	6	6	6	6	6	6	6	6	6
Si	0.990	0.996	1.001	1.001	0.995	0.999	0.995	0.999	1.995	1.912	1.912	1.932	1.909	1.909	1.958	1.758	1.758	1.889	1.641	1.641	1.964	1.964	1.720	1.720	1.720
Ti	0.000	0.000	0.000	0.000	0.000	0.001	0.000	0.001	0.001	0.035	0.035	0.020	0.019	0.019	0.025	0.118	0.118	0.082	0.187	0.187	0.022	0.022	0.154	0.154	
Al	0.001	0.000	0.000	0.001	0.000	0.001	0.000	0.001	0.001	0.039	0.039	0.027	0.057	0.057	0.021	0.146	0.146	0.064	0.198	0.198	0.042	0.042	0.191	0.191	
Cr	0.000	0.000	0.000	0.000	0.001	0.001	0.001	0.001	0.001	0.000	0.000	0.000	0.000	0.000	0.000	0.000	0.000	0.000	0.000	0.000	0.001	0.001	0.001	0.001	
*Fe ³⁺	0.019	0.007	0.000	0.000	0.008	0.000	0.008	0.000	0.007	0.101	0.101	0.085	0.108	0.108	0.042	0.145	0.145	0.434	0.201	0.201	0.108	0.108	0.100	0.100	
*Fe ²⁺	0.426	0.149	0.141	0.347	0.291	0.224	0.291	0.224	0.023	0.049	0.049	0.025	0.063	0.063	0.108	0.086	0.086	0.350	0.171	0.171	0.186	0.186	0.129	0.129	
Mn	0.006	0.004	0.002	0.003	0.005	0.004	0.005	0.004	0.004	0.005	0.005	0.004	0.009	0.009	0.004	0.004	0.004	0.020	0.004	0.004	0.007	0.007	0.006	0.006	
Ni	0.001	0.007	0.007	0.005	0.007	0.006	0.007	0.006	0.000	0.001	0.001	0.001	0.000	0.000	0.000	0.001	0.001	0.000	0.000	0.000	0.000	0.000	0.000	0.000	
Mg	1.556	1.837	1.847	1.638	1.689	1.756	1.689	1.756	0.974	0.857	0.857	0.898	0.838	0.838	0.859	0.769	0.769	0.138	0.602	0.602	0.669	0.669	0.727	0.727	
Ca	0.001	0.000	0.000	0.003	0.002	0.005	0.002	0.005	0.992	0.966	0.966	0.990	0.979	0.979	0.954	0.931	0.931	0.583	0.938	0.938	0.881	0.881	0.933	0.933	
Na	0.000	0.000	0.001	0.000	0.001	0.000	0.001	0.000	0.001	0.035	0.035	0.016	0.019	0.019	0.029	0.042	0.042	0.439	0.057	0.057	0.121	0.121	0.040	0.040	
K	0.000	0.000	0.000	0.000	0.000	0.000	0.000	0.000	0.000	0.000	0.000	0.001	0.000	0.000	0.000	0.000	0.000	0.001	0.000	0.000	0.000	0.000	0.000	0.000	
Total cations	3.000	3.000	2.999	2.998	3.000	2.999	3.000	2.999	4.000	4.000	4.000	4.000	4.000	4.000	4.000	4.000	4.000	4.000	4.000	4.000	4.000	4.000	4.000	4.000	
Mg#	77.5	92.0	92.8	82.4	84.7	88.5	84.7	88.5	97.7	94.6	94.6	97.3	93.0	93.0	88.9	90.0	90.0	28.3	77.9	77.9	78.2	78.2	84.9	84.9	

Mg# = 100[Mg/(Mg+Fe²⁺)] in atomic units; *calculated assuming stoichiometry; pc - phenocryst; mpc - microphenocryst; gm - groundmass; Ol - olivine; Di - diopside; Ti-Di - Titanian diopside

Table 4. Representative compositions of mica from the Torngat dykes

Rock type Mineral Sample#	carbonate				allikite				mela-allikite				Bt			
	Phi Q13 pc1 core	Phi C13 pc1 rim	Phi Q6 pc3 core	Phi Q8 pc3 rim1	Phi Q26 mc1 core	Phi Q34 pc3 rim1	Phi Q34 pc3 rim2	Phi Q34 pc3 rim2	Phi Q30 gm2 core	Phi Q30 gm2 rim	Phi Q40 pc2 core	Phi Q40 pc2 rim	Phi Q43 gm1 core1	Phi Q43 gm1 core2	Phi Q43 gm1 rim1	Phi Q43 gm1 rim2
SiO ₂	38.10	38.10	37.31	37.89	40.25	40.19	37.68	40.64	40.50	38.14	34.86	37.08	34.96	37.11	37.30	35.73
TiO ₂	3.23	3.61	2.58	1.78	0.10	0.18	2.74	0.24	0.16	4.37	6.71	4.95	6.42	2.93	5.44	3.89
Al ₂ O ₃	13.17	13.26	13.38	12.43	0.61	11.67	12.88	8.43	2.16	12.54	10.09	13.30	7.38	11.13	11.60	10.41
Cr ₂ O ₃	0.03	0.01	0.00	0.00	0.03	0.03	0.00	0.00	0.03	0.05	0.03	0.00	0.04	0.03	0.00	0.02
FeO	7.44	7.32	6.50	7.44	16.33	10.14	5.97	7.77	13.41	7.42	28.38	7.49	34.19	14.84	9.26	23.91
MnO	0.07	0.09	0.04	0.06	0.14	0.25	0.03	0.06	0.09	0.03	0.29	0.03	0.61	0.20	0.11	0.43
NiO	0.01	0.00	0.01	0.04	0.02	0.00	0.00	0.00	0.00	0.10	0.01	0.09	0.03	0.02	0.06	0.06
MgO	22.25	22.61	22.41	24.19	25.52	21.06	22.61	26.03	26.44	21.46	5.35	21.02	2.78	17.69	19.83	11.06
CaO	0.00	0.04	0.03	0.05	0.06	0.00	0.07	0.02	0.03	0.10	0.30	0.02	0.12	0.02	0.02	0.11
BaO	0.43	0.60	0.78	0.55	0.09	0.19	0.70	0.26	0.31	0.59	0.19	0.77	0.20	0.20	0.52	0.33
SiO	0.03	0.00	0.00	0.00	0.00	0.04	0.00	0.06	0.00	0.03	0.00	0.02	0.00	0.00	0.05	0.00
Na ₂ O	0.43	0.38	0.32	0.27	0.20	0.14	0.42	0.22	0.11	0.45	0.20	0.30	0.06	0.43	0.42	0.28
K ₂ O	9.75	9.79	9.85	9.22	9.99	10.26	9.46	10.71	10.30	9.53	8.61	9.83	9.14	8.92	9.07	9.02
H ₂ O (calc)	3.93	3.88	3.86	3.85	3.75	2.84	3.88	3.90	3.96	3.56	3.62	3.70	3.51	3.60	3.70	3.64
F	0.45	0.54	0.58	0.62	0.56	2.62	0.54	0.56	0.43	1.21	0.26	0.88	0.21	0.84	0.83	0.37
Cl	0.00	0.00	0.01	0.01	0.01	0.01	0.01	0.00	0.01	0.00	0.00	0.00	0.00	0.00	0.02	0.00
O=F	-0.19	-0.23	-0.24	-0.26	-0.24	-1.10	-0.23	-0.24	-0.18	-0.51	-0.11	-0.37	-0.09	-0.35	-0.35	-0.16
Total	99.13	98.98	98.45	98.14	97.41	98.52	97.76	98.65	97.55	99.07	98.80	99.10	99.57	97.60	97.87	99.10
No. oxygens	22	22	22	22	22	22	22	22	22	22	22	22	22	22	22	22
Si	5.538	5.554	5.461	5.548	6.049	5.968	5.551	5.910	6.020	5.546	5.584	5.412	5.709	5.642	5.518	5.597
^{IV} Al	2.256	2.278	2.308	2.145	0.108	2.032	2.236	1.445	0.378	2.149	1.505	2.288	1.420	1.994	2.023	1.922
^{VI} Fe ³⁺	0.206	0.167	0.231	0.307	1.843	0.000	0.212	0.645	1.602	0.305	0.510	0.300	0.870	0.364	0.459	0.481
[T]	8.000	8.000	8.000	8.000	8.000	8.000	8.000	8.000	8.000	8.000	8.000	8.000	8.000	8.000	8.000	8.000
Ti	0.353	0.283	0.397	0.196	0.011	0.020	0.304	0.026	0.017	0.478	0.609	0.543	0.789	0.335	0.605	0.458
^{VI} Al	0.000	0.000	0.000	0.000	0.000	0.010	0.000	0.000	0.000	0.000	0.000	0.000	0.000	0.000	0.000	0.000
Cr	0.004	0.001	0.000	0.000	0.003	0.004	0.000	0.000	0.003	0.005	0.004	0.000	0.006	0.003	0.000	0.003
Mg	4.821	4.514	4.890	5.280	5.718	4.662	4.966	5.643	5.859	4.652	1.278	4.574	0.677	4.009	4.373	2.583
Ca	0.000	0.006	0.005	0.008	0.009	0.000	0.011	0.003	0.005	0.016	0.051	0.003	0.021	0.004	0.004	0.018
Mn	0.009	0.012	0.005	0.007	0.017	0.031	0.004	0.007	0.012	0.004	0.040	0.004	0.084	0.026	0.013	0.057
Ni	0.002	0.000	0.001	0.005	0.002	0.000	0.000	0.000	0.000	0.012	0.002	0.010	0.004	0.002	0.007	0.007
Fe ²⁺	0.698	0.725	0.564	0.604	0.210	1.259	0.647	0.300	0.055	0.598	3.292	0.614	3.799	1.523	0.686	2.652
[M]	5.887	5.941	5.863	6.099	5.970	5.986	5.931	5.980	5.951	5.765	5.474	5.749	5.380	5.902	5.689	5.778
Ba	0.024	0.034	0.045	0.031	0.006	0.011	0.041	0.015	0.018	0.033	0.012	0.044	0.013	0.012	0.030	0.020
Na	0.121	0.106	0.086	0.077	0.058	0.041	0.121	0.051	0.032	0.127	0.063	0.084	0.020	0.126	0.121	0.084
K	1.808	1.821	1.835	1.722	1.915	1.944	1.778	1.987	1.953	1.768	1.760	1.830	1.904	1.730	1.712	1.803
[A]	1.954	1.562	1.974	1.830	1.979	1.966	1.939	2.062	2.003	1.929	1.835	1.958	1.936	1.868	1.863	1.907
Total cations	15.841	15.503	15.836	15.930	15.949	15.982	15.870	16.043	15.954	15.694	15.509	15.708	15.316	15.771	15.552	15.685
F	0.209	0.251	0.265	0.287	0.267	1.230	0.252	0.258	0.232	0.560	0.132	0.408	0.112	0.406	0.391	0.187
Cl	0.000	0.000	0.002	0.003	0.002	0.002	0.001	0.000	0.002	0.000	0.000	0.000	0.000	0.000	0.004	0.000
OH	3.791	3.749	3.728	3.711	3.731	2.787	3.746	3.742	3.796	3.440	3.668	3.592	3.888	3.594	3.604	3.813
Total	4.000	4.000	4.000	4.000	4.000	4.000	4.000	4.000	4.000	4.000	4.000	4.000	4.000	4.000	4.000	4.000

analyses recalculated on the basis of 8 tetrahedral cations and 22 O equivalents; Phi - Phlogopite; TFP - Tetraferriphlogopite; Bt - Biotite; mc - macrocryst

Table 5: Representative amphibole compositions from the Torngat ultramafic lamprophyres

Rock type	<i>aillikite</i>		<i>mela-aillikite</i>										
	Ti-Mkt	Rcht	Ti-Mkt	Ti-Mkt	Rcht	Rcht	Ti-Mkt	Ti-Mkt	Ti-Mkt	Ti-Mkt	Rcht	Rcht	
Mineral	Q29	Q29	Q12	Q12	Q15	Q15	Q15	Q15	Q15	Q15	Q23	Q36	Q36
Sample#	gm9	gm9	gm6	gm6	gm4	gm4	gm4	gm4	gm4	gm4	gm1	gm1	gm1
	core1	core2	core1	rim1	core1	core2	rim1	rim2	rim3	core	core	core	rim
SiO ₂	51.56	54.00	46.51	46.67	56.26	55.85	50.93	50.12	51.99	47.16	52.13	50.33	
TiO ₂	2.97	1.82	4.73	4.66	0.50	0.44	2.08	2.57	1.36	3.98	3.00	3.26	
Al ₂ O ₃	1.92	1.07	4.39	4.44	0.28	0.30	2.73	2.96	2.38	4.40	0.91	1.10	
Cr ₂ O ₃	0.00	0.00	0.01	0.03	0.00	0.00	0.03	0.00	0.03	0.01	0.01	0.03	
FeO	6.13	5.04	8.09	7.70	2.61	2.80	4.32	4.61	3.67	7.57	6.00	6.93	
MnO	0.10	0.13	0.10	0.13	0.00	0.06	0.01	0.02	0.02	0.12	0.13	0.13	
NiO	0.03	0.03	0.00	0.00	0.00	0.01	0.03	0.05	0.02	0.04	0.04	0.06	
MgO	19.11	20.64	17.24	17.25	22.40	22.16	20.79	20.55	21.34	17.89	19.71	18.98	
CaO	6.26	6.29	5.75	6.46	6.19	6.35	8.06	8.10	8.35	7.48	6.10	6.13	
BaO	0.00	0.00	0.04	0.04	0.04	0.02	0.00	0.00	0.00	0.06	0.00	0.03	
SrO	0.16	0.11	0.20	0.22	0.00	0.00	0.04	0.04	0.04	0.38	0.36	0.40	
Na ₂ O	6.60	6.94	6.86	6.40	7.34	7.26	6.22	6.01	6.09	5.95	5.87	5.42	
K ₂ O	0.98	0.68	0.54	0.50	0.12	0.15	0.47	0.56	0.36	0.60	2.38	2.36	
H ₂ O (calc)	1.74	1.86	1.87	1.81	2.17	2.14	1.95	1.97	2.00	1.85	1.75	1.76	
F	0.77	0.58	0.45	0.56	0.01	0.06	0.39	0.32	0.30	0.49	0.73	0.68	
Cl	0.00	0.00	0.00	0.00	0.00	0.00	0.00	0.01	0.00	0.00	0.01	0.00	
O=F	-0.32	-0.24	-0.19	-0.23	-0.01	-0.03	-0.16	-0.13	-0.13	-0.21	-0.31	-0.29	
Total	96.58	97.32	96.59	95.05	95.77	95.46	96.10	95.92	95.95	96.14	97.37	95.85	
Si	7.462	7.654	6.886	6.922	7.914	7.904	7.312	7.225	7.440	6.926	7.517	7.427	
^{IV} Al	0.328	0.178	0.766	0.776	0.047	0.051	0.462	0.503	0.401	0.762	0.154	0.192	
^{IV} Ti	0.210	0.167	0.348	0.302	0.039	0.046	0.225	0.272	0.146	0.313	0.325	0.362	
[T]	8.000	8.000	8.000	8.000	8.000	8.000	7.998	8.000	7.987	8.000	7.997	7.981	
^{VI} Al	0.000	0.000	0.000	0.000	0.000	0.000	0.000	0.000	0.000	0.000	0.000	0.000	
^{VI} Ti	0.113	0.027	0.179	0.218	0.014	0.001	0.000	0.006	0.000	0.127	0.000	0.000	
Fe ³⁺	0.145	0.182	0.515	0.332	0.092	0.076	0.222	0.244	0.139	0.368	0.245	0.232	
Cr	0.000	0.000	0.001	0.003	0.000	0.000	0.003	0.000	0.003	0.001	0.001	0.003	
Mg	4.123	4.361	3.805	3.814	4.697	4.675	4.450	4.416	4.553	3.917	4.237	4.175	
Fe ²⁺	0.597	0.416	0.487	0.623	0.196	0.248	0.297	0.312	0.300	0.562	0.478	0.590	
Mn	0.013	0.015	0.012	0.009	0.000	0.000	0.002	0.002	0.003	0.015	0.016	0.000	
[C]	4.991	5.000	4.999	5.000	5.000	5.000	4.973	4.980	4.997	4.989	4.978	5.000	
Mg	0.000	0.000	0.000	0.000	0.000	0.000	0.000	0.000	0.000	0.000	0.000	0.000	
Fe ²⁺	0.000	0.000	0.000	0.000	0.018	0.007	0.000	0.000	0.000	0.000	0.000	0.034	
Mn	0.000	0.001	0.000	0.008	0.000	0.007	0.000	0.000	0.000	0.000	0.000	0.017	
Ca	0.971	0.955	0.912	1.027	0.933	0.963	1.240	1.251	1.280	1.177	0.943	0.969	
Na	1.029	1.043	1.088	0.966	1.049	1.023	0.760	0.749	0.720	0.823	1.057	0.980	
[B]	2.000	2.000	2.000	2.000	2.000	2.000	2.000	2.000	2.000	2.000	2.000	2.000	
Na	0.823	0.864	0.881	0.875	0.953	0.969	0.971	0.931	0.970	0.871	0.584	0.570	
K	0.180	0.123	0.101	0.095	0.022	0.027	0.086	0.104	0.065	0.112	0.438	0.444	
[A]	1.003	0.987	0.982	0.970	0.975	0.996	1.057	1.035	1.035	0.983	1.022	1.015	
Total cations	15.994	15.987	15.981	15.970	15.975	15.996	16.029	16.015	16.020	15.973	15.996	15.995	
F	0.350	0.259	0.211	0.260	0.006	0.029	0.175	0.144	0.137	0.229	0.331	0.317	
Cl	0.000	0.000	0.000	0.000	0.000	0.000	0.000	0.002	0.000	0.000	0.002	0.000	
OH	1.650	1.741	1.789	1.740	1.994	1.971	1.825	1.854	1.863	1.771	1.667	1.683	
Total	2.000	2.000	2.000	2.000	2.000	2.000	2.000	2.000	2.000	2.000	2.000	2.000	

Analyses recalculated on the basis of 23 oxygens following Leake *et al.* (1997); empirical Fe³⁺ correction after Schumacher (1991);

Ti-Mkt - Titanian Magnesiooktophorite; Rcht - Richterite

Table 6: Representative spinel and ilmenite compositions from the Torrnat dykes

Rock type Mineral Sample#	allikite						mela-allikite						allikite						mela-allikite																												
	Cr-Spl Q17	Ti-Mag Q17	Cr-Spl Q21	Ti-Mag Q21	Cr-Spl Q42	Cr-Spl Q15	Ti-Mag Q15	Ti-Mag Q15	Cr-Spl Q20	Ti-Mag Q20	Ti-Mag Q20	Cr-Spl Q35	Ti-Mag Q35	Cr-Spl Q39	Ti-Mag Q39	Cr-Spl Q39	Ti-Mag Q39	Cr-Spl Q39	Ti-Mag Q39	Cr-Spl Q39	Ti-Mag Q39	Cr-Spl Q39	Ti-Mag Q39	Cr-Spl Q39	Ti-Mag Q39	Cr-Spl Q39	Ti-Mag Q39	Cr-Spl Q39	Ti-Mag Q39																		
SiO ₂	0.04	0.06	0.07	0.08	0.05	0.00	0.03	0.04	0.00	0.19	0.04	0.02	0.59	0.00	0.51	0.02	0.00	0.02	0.00	0.02	0.00	0.00	0.01	0.06	0.04	0.06	0.07	0.08	0.05	0.00	0.03	0.04	0.00	0.19	0.04	0.02	0.59	0.00	0.51	0.02	0.00	0.02	0.00	0.00	0.01	0.06	
TiO ₂	6.94	10.27	8.05	11.44	10.34	0.06	16.05	18.93	4.34	11.33	13.00	52.15	52.05	44.11	51.39	49.22	54.30	50.60	51.12	49.22	54.30	50.60	51.12	6.94	10.27	8.05	11.44	10.34	0.06	16.05	18.93	4.34	11.33	13.00	52.15	52.05	44.11	51.39	49.22	54.30	50.60	51.12	49.22	54.30	50.60	51.12	
Al ₂ O ₃	3.29	4.17	4.56	2.26	1.31	47.23	2.16	1.48	7.01	1.77	0.92	0.02	0.04	0.04	0.00	0.12	0.00	0.00	0.00	0.12	0.00	0.00	0.00	3.29	4.17	4.56	2.26	1.31	47.23	2.16	1.48	7.01	1.77	0.92	0.02	0.04	0.04	0.00	0.12	0.00	0.00	0.00	0.12	0.00	0.00	0.00	
Cr ₂ O ₃	37.66	0.11	25.02	3.67	1.71	19.73	33.70	8.81	35.62	6.50	0.75	0.05	0.00	0.07	0.00	0.00	0.00	0.00	0.00	0.05	0.00	0.00	0.00	37.66	0.11	25.02	3.67	1.71	19.73	33.70	8.81	35.62	6.50	0.75	0.05	0.00	0.07	0.00	0.00	0.00	0.00	0.05	0.00	0.00	0.00	0.00	
V ₂ O ₅	0.11	0.05	0.15	0.09	0.13	0.12	0.10	0.12	0.09	0.15	0.21	0.40	0.07	0.24	0.00	0.06	0.08	0.07	0.20	0.40	0.07	0.24	0.00	0.11	0.05	0.15	0.09	0.13	0.12	0.10	0.12	0.09	0.15	0.21	0.40	0.07	0.24	0.00	0.06	0.08	0.07	0.20	0.40	0.07	0.24	0.00	
*Fe ₂ O ₃	18.74	48.17	26.90	43.49	45.84	2.13	21.14	31.10	29.04	37.70	40.25	6.07	0.00	19.10	0.00	12.66	4.67	4.43	1.38	6.07	0.00	19.10	0.00	18.74	48.17	26.90	43.49	45.84	2.13	21.14	31.10	29.04	37.70	40.25	6.07	0.00	19.10	0.00	12.66	4.67	4.43	1.38	6.07	0.00	19.10	0.00	
*FeO	22.62	29.28	25.80	31.84	36.34	12.57	26.42	33.73	46.15	24.72	39.79	32.04	37.89	33.08	33.96	28.39	29.73	40.84	40.69	32.04	37.89	33.08	33.96	22.62	29.28	25.80	31.84	36.34	12.57	26.42	33.73	46.15	24.72	39.79	32.04	37.89	33.08	33.96	28.39	29.73	40.84	40.69	32.04	37.89	33.08	33.96	
MnO	0.71	0.83	0.64	0.67	1.62	0.17	0.53	0.61	1.23	1.01	0.76	1.64	6.46	0.23	10.56	0.72	1.22	1.99	5.23	1.64	6.46	0.23	10.56	0.71	0.83	0.64	0.67	1.62	0.17	0.53	0.61	1.23	1.01	0.76	1.64	6.46	0.23	10.56	0.72	1.22	1.99	5.23	1.64	6.46	0.23	10.56	
NiO	0.17	0.15	0.21	0.13	0.16	0.17	0.15	0.20	0.09	0.11	0.11	0.03	0.00	0.01	0.02	0.13	0.02	0.00	0.00	0.03	0.00	0.01	0.02	0.17	0.15	0.21	0.13	0.16	0.17	0.15	0.20	0.09	0.11	0.11	0.03	0.00	0.01	0.02	0.13	0.02	0.00	0.00	0.03	0.00	0.01	0.02	
MgO	9.92	7.32	8.54	6.21	1.69	17.30	7.38	7.67	0.56	7.20	0.85	7.40	0.11	3.56	0.29	8.44	10.01	1.49	0.03	7.40	0.11	3.56	0.29	9.92	7.32	8.54	6.21	1.69	17.30	7.38	7.67	0.56	7.20	0.85	7.40	0.11	3.56	0.29	8.44	10.01	1.49	0.03	7.40	0.11	3.56	0.29	
Total	100.19	100.41	99.95	99.88	99.19	99.48	98.93	99.81	98.60	100.15	97.70	99.83	97.20	100.44	96.73	99.76	100.03	99.43	98.72	99.83	97.20	100.44	96.73	100.19	100.41	99.95	99.88	99.19	99.48	98.93	99.81	98.60	100.15	97.70	99.83	97.20	100.44	96.73	99.76	100.03	99.43	98.72	99.83	97.20	100.44	96.73	
No. oxygens	32	32	32	32	32	32	32	32	32	32	32	32	32	32	32	32	32	32	32	32	32	32	32	32	32	32	32	32	32	32	32	32	32	32	32	32	32	32	32	32	32	32	32	32	32	32	
Si	0.010	0.017	0.020	0.023	0.015	0.000	0.000	0.009	0.013	0.000	0.057	0.001	0.030	0.000	0.027	0.001	0.000	0.001	0.003	0.001	0.000	0.000	0.003	0.010	0.017	0.020	0.023	0.015	0.000	0.000	0.009	0.013	0.000	0.057	0.001	0.030	0.000	0.027	0.001	0.000	0.001	0.000	0.001	0.000	0.003	0.003	
Ti	1.431	2.173	1.676	2.469	2.340	0.010	1.574	3.422	4.314	0.898	3.022	1.880	2.009	1.638	1.997	1.767	1.916	1.914	1.966	1.880	2.009	1.638	1.997	1.431	2.173	1.676	2.469	2.340	0.010	1.574	3.422	4.314	0.898	3.022	1.880	2.009	1.638	1.997	1.767	1.916	1.914	1.966	1.880	2.009	1.638	1.997	
Al	1.053	1.383	1.488	0.765	0.466	12.191	0.724	0.496	0.449	2.274	0.336	0.001	0.002	0.002	0.000	0.007	0.000	0.000	0.000	0.001	0.002	0.002	0.000	1.053	1.383	1.488	0.765	0.466	12.191	0.724	0.496	0.449	2.274	0.336	0.001	0.002	0.002	0.000	0.007	0.000	0.000	0.000	0.001	0.002	0.002	0.000	0.000
Cr	8.163	0.025	5.478	0.833	0.407	3.416	7.579	1.975	0.233	7.751	1.547	0.002	0.000	0.003	0.000	0.000	0.000	0.000	0.000	0.002	0.000	0.003	0.000	8.163	0.025	5.478	0.833	0.407	3.416	7.579	1.975	0.233	7.751	1.547	0.002	0.000	0.003	0.000	0.000	0.000	0.000	0.002	0.000	0.003	0.000	0.000	
V	0.024	0.010	0.034	0.020	0.030	0.022	0.022	0.028	0.039	0.020	0.037	0.015	0.003	0.010	0.000	0.002	0.003	0.003	0.008	0.015	0.003	0.010	0.000	0.024	0.010	0.034	0.020	0.030	0.022	0.022	0.028	0.039	0.020	0.037	0.015	0.003	0.010	0.000	0.002	0.003	0.003	0.008	0.015	0.003	0.010	0.000	
*Fe ³⁺	3.867	10.201	5.607	9.398	10.386	0.351	4.527	6.638	6.625	4.158	8.545	4.219	4.527	4.158	4.219	4.527	4.158	4.219	4.527	4.219	4.527	4.158	4.219	3.867	10.201	5.607	9.398	10.386	0.351	4.527	6.638	6.625	4.158	8.545	4.219	4.527	4.158	4.219	4.527	4.158	4.219	4.527	4.158	4.219	4.527	4.158	4.219
*Fe ²⁺	5.187	6.889	5.975	7.643	9.146	2.301	6.284	7.997	11.695	5.690	10.020	1.285	1.626	1.366	1.468	1.133	1.167	1.718	1.740	1.285	1.626	1.366	1.468	5.187	6.889	5.975	7.643	9.146	2.301	6.284	7.997	11.695	5.690	10.020	1.285	1.626	1.366	1.468	1.133	1.167	1.718	1.740	1.285	1.626	1.366	1.468	
Mn	0.164	0.198	0.149	0.162	0.413	0.032	0.127	0.146	0.315	0.235	0.195	0.067	0.281	0.010	0.462	0.029	0.049	0.085	0.227	0.067	0.281	0.010	0.462	0.164	0.198	0.149	0.162	0.413	0.032	0.127	0.146	0.315	0.235	0.195	0.067	0.281	0.010	0.462	0.029	0.049	0.085	0.227	0.067	0.281	0.010	0.462	
Ni	0.037	0.033	0.047	0.031	0.038	0.029	0.034	0.046	0.063	0.019	0.026	0.001	0.000	0.001	0.001	0.005	0.001	0.000	0.000	0.001	0.000	0.001	0.001	0.037	0.033	0.047	0.031	0.038	0.029	0.034	0.046	0.063	0.019	0.026	0.001	0.000	0.001	0.001	0.005	0.001	0.000	0.000	0.001	0.000	0.001	0.001	
Mg	4.054	3.070	3.525	2.657	0.758	5.648	3.129	3.242	0.254	2.954	0.381	0.529	0.008	0.262	0.023	0.601	0.700	0.112	0.002	0.529	0.008	0.262	0.023	4.054	3.070	3.525	2.657	0.758	5.648	3.129	3.242	0.254	2.954	0.381	0.529	0.008	0.262	0.023	0.601	0.700	0.112	0.002	0.529	0.008	0.262	0.023	
Total cations	24.000	24.000	24.000	24.000	24.000	24.000	24.000	24.000	24.000	24.000	24.000	24.000	24.000	24.000	24.000	24.000	24.000	24.000	24.000	24.000	24.000	24.000	24.000	24.000	24.000	24.000	24.000	24.000	24.000	24.000	24.000	24.000	24.000	24.000	24.000	24.000	24.000	24.000	24.000	24.000	24.000	24.000	24.000	24.000	24.000		
Mg#	43.9	30.8	37.1	25.8	7.7	71.0	33.2	28.8	2.1	34.2	3.7	29.2	0.5	16.1	1.5	34.6	37.5	6.1	0.1	29.2	0.5	16.1	1.5	43.9	30.8	37.1	25.8	7.7	71.0	33.2	28.8	2.1	34.2	3.7	29.2	0.5	16.1	1.5	34.6	37.5	6.1	0.1	29.2	0.5	16.1	1.5	

Mg# = 100[Mg/(Mg+Fe²⁺)] in atomic units; *calculated assuming stoichiometry; mpc - microphenocryst; mc - macrocryst; ic - inclusion; xc - xenocryst; lam - exsolution lamellae; vs - in vesicles

Table 7. Representative garnet and perovskite compositions from the Torngat dykes

Mineral Sample#	allikite				mela-allikite				allikite				mela-allikite			
	Zr-Srl Q37 gm6 core1	Zr-Srl Q37 gm6 core2	Zr-Srl Q39 gm2 core	Srl Q37 gm6 rim1	Zr-Srl Q39 gm2 core	Zr-Srl Q39 gm2 rim	Zr-Srl Q18 gm1 core	Srl Q28 gm3 core1	Kim Q18 gm4 core	Srl Q28 gm3 core2	Adr Q28 gm3 rim1	Psv Q34 mpc2 core	Psv Q34 mpc2 core	Psv Q15 mpc3 core	Psv Q22 mpc1 core	Psv Q22 mpc1 rim1
SiO ₂	29.86	30.07	25.01	29.70	26.99	27.52	26.99	28.00	25.42	28.93	32.43	0.25	0.37	1.65	0.47	0.38
TiO ₂	9.16	9.98	12.57	16.74	18.66	12.51	18.66	26.23	9.87	18.22	6.65	0.00	0.03	0.00	0.18	0.01
ZrO ₂	8.70	6.06	9.99	6.69	4.25	5.90	4.25	n.a.	17.21	n.a.	n.a.	55.41	56.36	53.28	56.37	56.24
HfO ₂	0.07	0.02	0.00	0.00	0.00	0.01	0.00	n.a.	0.16	n.a.	n.a.	0.15	0.11	0.03	0.06	0.08
Al ₂ O ₃	0.04	0.02	1.01	0.00	0.02	0.01	0.02	0.02	0.04	0.03	0.21	1.25	1.24	0.73	1.18	1.08
Cr ₂ O ₃	0.02	0.06	0.00	0.05	0.02	0.02	0.02	0.03	0.00	0.03	0.03	0.54	0.28	2.44	0.25	0.54
FeO	14.69	15.32	12.74	14.98	13.63	16.65	13.63	6.27	12.74	13.26	22.34	1.45	0.59	3.93	0.46	1.17
MnO	0.00	0.10	0.13	0.23	0.23	0.38	0.23	0.41	0.21	0.25	0.13	0.21	0.05	0.32	0.38	0.05
NiO	0.00	0.03	n.a.	0.04	n.a.	n.a.	n.a.	0.02	n.a.	0.00	0.00	0.66	0.17	1.08	0.10	0.38
MgO	3.04	2.79	3.00	2.97	2.05	1.88	2.05	0.37	2.28	1.54	0.58	0.11	0.07	0.18	0.23	0.07
CaO	32.14	32.69	29.95	33.56	30.89	31.34	30.89	33.31	27.78	33.24	33.27	0.06	0.02	0.08	0.05	0.02
BaO	0.00	0.01	0.09	0.03	0.02	0.11	0.02	0.00	0.04	0.00	0.00	0.03	0.05	0.00	0.06	0.07
SrO	0.03	0.00	0.06	0.00	0.00	0.00	0.00	0.06	0.08	0.00	0.00	38.80	39.47	33.55	39.92	38.42
Na ₂ O	0.22	0.14	0.17	0.16	0.91	0.36	0.91	1.06	1.60	0.53	0.22	0.23	0.24	1.72	0.48	0.47
K ₂ O	0.01	0.00	0.01	0.00	0.00	0.02	0.00	0.00	0.00	0.01	0.00	0.45	0.31	1.86	0.91	0.49
Total	97.99	97.30	97.15	96.83	97.67	96.71	97.67	95.73	97.44	96.10	95.85	99.61	99.34	100.83	99.94	99.47
No. oxygens	12	12	12	12	12	12	12	12	12	12	12	3	3	3	3	3
Si	2.574	2.587	2.218	2.522	2.330	2.413	2.330	2.427	2.298	2.489	2.777	0.003	0.004	0.018	0.005	0.004
Al	0.004	0.002	0.105	0.000	0.002	0.001	0.002	0.002	0.005	0.003	0.021	0.000	0.001	0.000	0.000	0.000
Fe ³⁺	0.422	0.411	0.677	0.478	0.668	0.586	0.668	0.508	0.697	0.508	0.202	0.962	0.972	0.944	0.964	0.975
Ti	0.000	0.000	0.000	0.000	0.000	0.000	0.000	0.570	0.000	0.000	0.000	0.004	0.003	0.001	0.002	0.002
[T]	3.000	3.000	3.000	3.000	3.000	3.000	3.000	3.000	3.000	3.000	3.000	0.022	0.021	0.013	0.020	0.019
Al	0.000	0.000	0.000	0.000	0.000	0.000	0.000	0.000	0.000	0.000	0.000	0.005	0.002	0.021	0.015	0.005
Fe ³⁺	0.637	0.691	0.434	0.420	0.316	0.635	0.316	0.239	0.266	0.398	1.398	0.012	0.005	0.034	0.004	0.010
Ti	0.594	0.646	0.838	1.069	1.212	0.825	1.212	1.140	0.671	1.179	0.428	0.002	0.000	0.003	0.001	0.000
Fe ²⁺	0.000	0.000	0.000	0.007	0.000	0.000	0.000	0.455	0.000	0.207	0.000	0.005	0.001	0.009	0.014	0.003
Zr	0.366	0.254	0.432	0.258	0.179	0.252	0.179	n.a.	0.759	n.a.	n.a.	0.001	0.001	0.001	0.000	0.001
Hf	0.002	0.000	0.003	0.000	0.000	0.000	0.000	n.a.	0.004	n.a.	n.a.	0.001	0.000	0.001	0.000	0.000
Mg	0.360	0.358	0.238	0.380	0.122	0.190	0.122	0.048	0.000	0.197	0.074	0.001	0.002	0.000	0.010	0.002
Na	0.037	0.024	0.030	0.027	0.152	0.060	0.152	0.179	0.280	0.088	0.037	0.959	0.970	0.847	0.885	0.949
[Y]	1.996	1.973	1.931	1.931	1.981	1.964	1.981	1.821	1.980	1.911	1.937	0.003	0.003	0.023	0.007	0.006
Ca	2.969	3.013	2.846	3.053	2.858	2.845	2.858	3.094	2.691	3.065	3.052	0.020	0.014	0.085	0.041	0.022
Mg	0.031	0.000	0.154	0.000	0.142	0.055	0.142	0.000	0.307	0.000	0.000	2.000	2.000	2.000	2.000	1.999
Mn	0.000	0.000	0.000	0.000	0.000	0.000	0.000	0.000	0.000	0.000	0.000	0.000	0.000	0.000	0.000	0.000
[X]	3.000	3.013	3.000	3.053	3.000	3.000	3.000	3.094	2.998	3.065	3.052	0.000	0.000	0.000	0.000	0.000

Garnets recalculated on the basis of 12 oxygens following Munno *et al.* (1980); gm - groundmass; mpc - microphenocryst; Srl - schorlomite; Adr - andradite; Kim - kimzeyite; Psv - perovskite

Table 8: Major (wt.%) and trace element (ppm) content of representative rocks from the Torngat dyke swarm

Rock type Sample#	<i>carbonatite</i>	<i>aillikite</i>					<i>mela-aillikite</i>				
	Q13	Q9	Q17	Q24	Q26	Q42	Q22	Q23	Q28	Q36	Q43
SiO ₂	22.04	26.51	27.72	27.38	29.14	27.47	29.86	36.71	33.03	35.35	36.23
TiO ₂	4.87	5.82	2.45	5.91	4.39	3.49	9.40	4.60	7.68	9.42	3.85
Al ₂ O ₃	2.94	3.13	2.31	3.49	3.14	2.26	2.94	3.94	4.75	4.24	3.36
Fe ₂ O ₃	2.75	11.93	7.84	11.66	11.37	8.71	13.46	7.90	10.89	8.23	7.01
FeO	11.81	6.32	3.84	6.47	6.48	5.14	3.15	5.68	6.42	7.48	6.74
MnO	0.24	0.26	0.23	0.25	0.27	0.28	0.22	0.26	0.31	0.30	0.20
MgO	16.87	20.03	23.87	20.20	23.07	20.39	23.53	22.10	15.23	17.93	23.17
CaO	9.73	9.68	11.30	10.76	6.15	11.97	6.70	6.33	11.51	6.71	7.61
Na ₂ O	0.29	0.15	0.12	0.26	0.22	0.24	0.36	1.42	0.38	0.57	0.64
K ₂ O	2.42	3.14	1.40	2.55	1.76	2.06	2.53	2.28	3.09	3.49	1.74
P ₂ O ₅	0.11	0.86	0.18	0.86	0.62	1.71	0.45	0.72	1.36	0.46	0.84
LOI	3.28	5.85	8.60	5.38	7.87	7.51	5.93	6.47	3.79	4.66	6.19
CO ₂	21.70	5.30	8.90	4.45	4.30	7.30	0.37	1.39	0.48	0.07	1.28
Total	99.05	98.98	98.76	99.62	98.78	98.53	98.90	99.80	98.92	98.91	98.87
Mg#	71.8	85.0	91.7	84.8	86.4	87.6	93.0	87.4	80.9	81.0	86.0
K ₂ O/Na ₂ O	8.3	20.9	11.7	9.8	8.0	8.6	7.0	1.6	8.1	6.1	2.7
LFSE											
Rb	102.3	120.8	73.2	113.7	94.8	82.3	115.09	79.54	162.20	141.09	61.45
Ba	1418.5	1831.0	2133.5	1555.5	1033.0	910.8	835.69	911.66	1504.00	1022.50	689.15
Sr	1460.0	1450.5	1570.0	1159.5	792.5	1108.5	747.70	1223.00	1089.50	861.43	1014.00
HFSE											
Th	19.99	25.20	57.10	22.03	19.79	19.74	49.85	19.55	29.45	35.41	15.16
U	1.59	5.73	7.34	4.61	5.35	4.57	8.02	4.61	5.83	5.30	3.76
Nb	172.78	221.73	292.78	200.24	146.23	168.37	296.22	193.85	272.79	257.23	163.15
Ta	15.06	14.03	17.78	14.16	10.97	11.94	30.50	13.21	20.54	20.80	10.40
Zr	145.13	616.19	143.63	471.59	263.02	382.77	383.64	702.44	754.50	1213.00	713.55
Hf	3.15	15.67	4.66	12.92	6.74	9.18	11.15	16.71	21.70	31.08	15.10
Y	19.31	37.95	35.35	36.25	27.08	29.15	39.66	28.97	40.98	31.63	25.56
REE											
La	170.34	231.86	405.20	206.46	127.19	190.71	490.35	187.73	288.52	282.50	144.93
Ce	421.13	530.56	923.34	474.76	330.01	427.69	1030.00	415.36	643.29	673.86	301.99
Pr	42.42	51.42	92.42	45.76	39.63	46.96	100.49	39.04	60.98	64.31	31.50
Nd	159.00	192.27	330.14	170.68	157.31	175.48	359.58	138.74	218.46	231.46	112.60
Sm	24.14	30.60	44.89	27.82	27.31	27.05	51.89	20.27	33.84	32.87	16.75
Eu	6.06	8.27	10.52	7.56	7.24	7.11	13.15	5.28	9.10	8.23	4.35
Gd	15.29	21.40	26.66	19.29	19.43	17.98	35.56	13.97	23.85	20.46	11.46
Tb	1.59	2.39	2.58	2.23	2.10	1.93	3.62	1.61	2.74	2.24	1.33
Dy	6.08	10.00	10.54	9.40	8.35	8.28	14.26	7.10	11.35	9.27	6.15
Ho	0.88	1.54	1.65	1.48	1.22	1.27	2.01	1.18	1.79	1.42	1.01
Er	1.86	3.26	3.79	3.12	2.38	2.62	4.07	2.60	3.64	3.07	2.27
Tm	0.19	0.34	0.45	0.33	0.24	0.29	0.36	0.31	0.39	0.36	0.27
Yb	0.96	1.79	2.47	1.71	1.20	1.45	1.72	1.63	1.97	1.95	1.46
Lu	0.10	0.19	0.29	0.18	0.12	0.16	0.16	0.19	0.22	0.25	0.18
Transition metals											
Co	95.9	108.7	89.7	107.9	119.8	91.8	112.9	102.5	95.0	83.8	94.4
Cr	472.7	586.9	1570.0	547.5	1360.0	917.4	1260.0	1470.0	290.8	821.5	1150.0
Cu	56.7	95.6	21.6	109.7	114.4	94.7	91.5	115.0	131.6	133.7	158.2
Ga	13.1	19.0	10.6	19.1	14.4	10.5	17.2	13.8	21.1	22.6	11.4
Ni	543.5	575.5	1050.0	562.0	904.2	824.6	1010.0	1090.0	462.4	648.3	986.3
Sc	15.0	31.0	18.0	31.0	21.0	19.0	21.0	20.0	37.0	28.0	20.0
V	187.4	273.1	92.7	245.9	243.9	183.1	276.1	266.2	307.8	402.5	239.9
Zn	112.5	152.1	73.3	153.1	255.2	120.8	140.7	114.3	147.8	165.1	110.6

Mg# = 100[Mg/(Mg+Fe²⁺)] in atomic units

FIGURES

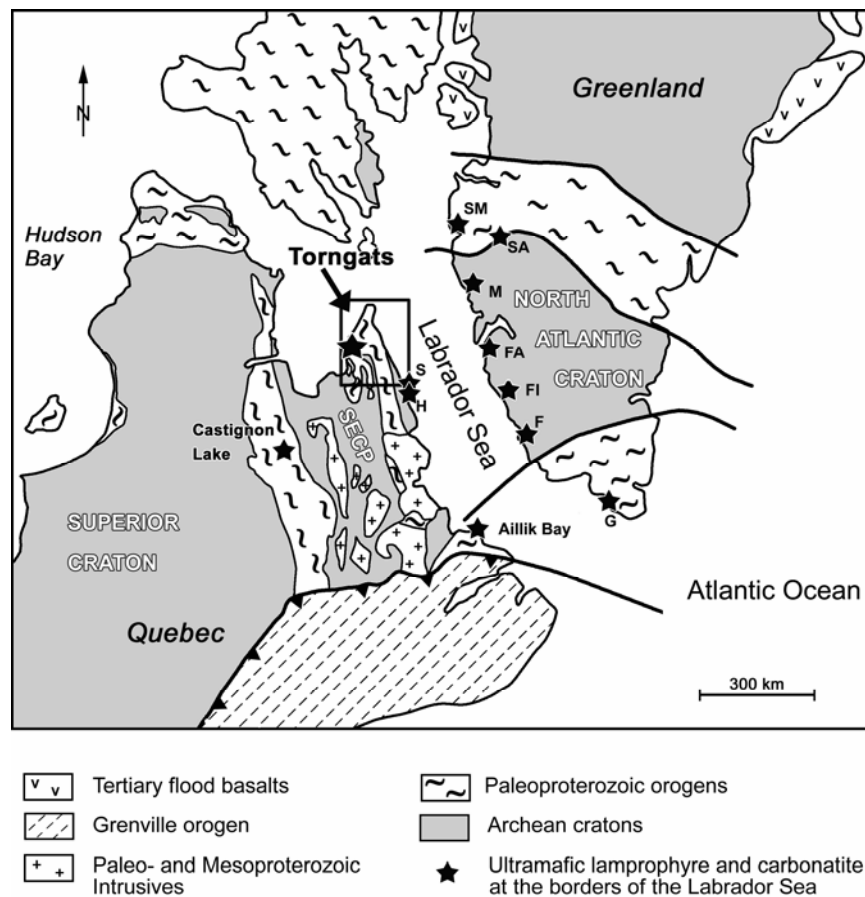


Figure 1: Simplified geology of the northeastern Canadian-Greenland Shield restored for Mesozoic drift (modified from Connelly *et al.*, 2000). A microcosm of Archean cratons and Proterozoic orogens in the once continuous structure of northeast America and Greenland is apparent. Abbreviations for ultramafic potassic to carbonatitic occurrences at the present day borders of the Labrador Sea are as follows:

F – Frederikshåb, FA – Faeringehavn, FI – Frederikshåb Isblink, G – Gardar, H – Hebron, M – Maniitsoq, S – Saglek, SA – Sarfartoq, SM – Sisimiut, SECP – Southeast Churchill Province.

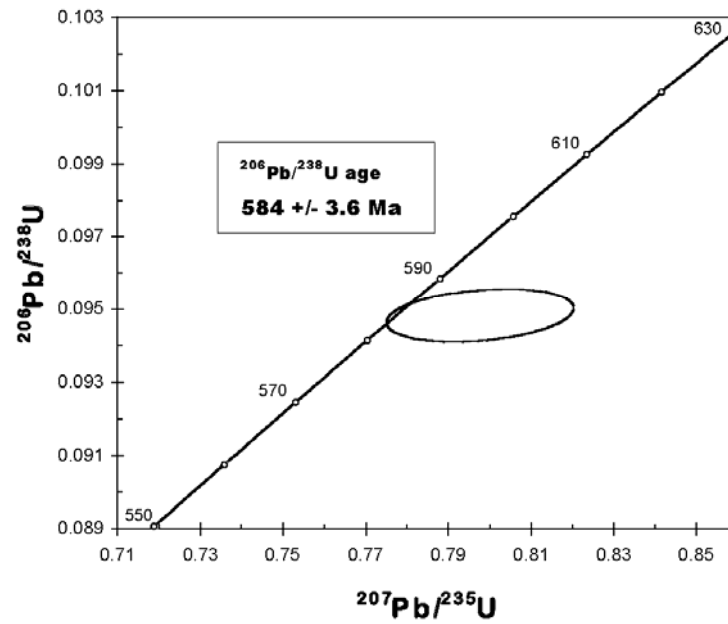


Figure 2: Perovskite analyses from aillikite sample Q39 in an U-Pb concordia diagram. The Neoproterozoic $^{206}\text{Pb}/^{238}\text{U}$ model age of 584 ± 3.6 Ma is the best estimate for the timing of Q39 emplacement. Error is quoted at 2-sigma.

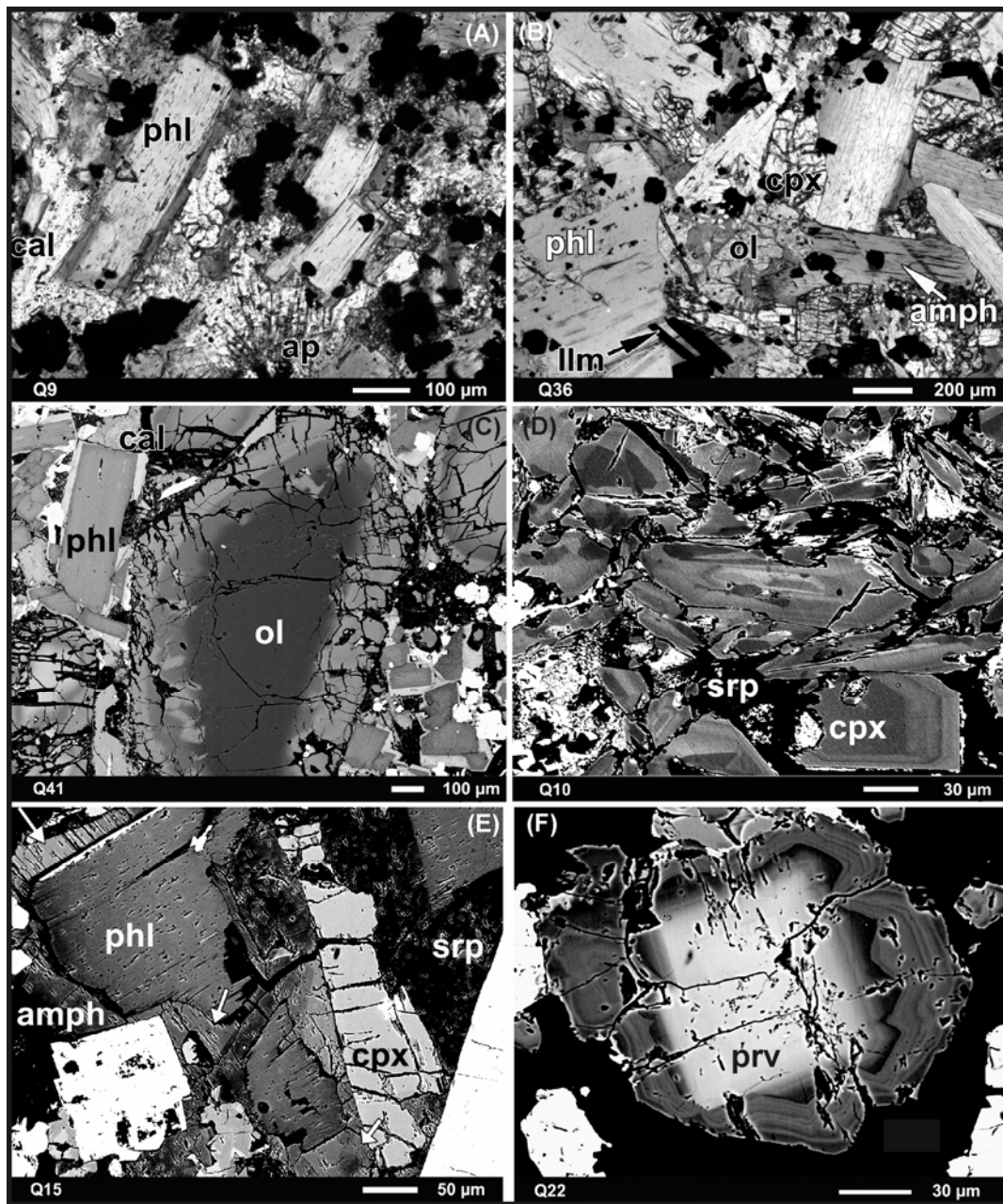


Figure 3: Photomicrographs (a-b; PPL) and backscattered electron images (c-f) from the Torngat ultramafic lamprophyres: (A) Porphyritic aillikite containing abundant phlogopite and opaque oxide microphenocrysts. Phlogopite crystals are rimmed by tetraferriphlogopite. The groundmass is dominated by carbonate and sprays of radiating apatite may occur. (B) Intergranular mela-aillikite containing abundant phlogopite, clinopyroxene and amphibole. Serpentinized olivine and opaque oxide microphenocrysts only subordinately occur. (C) Macrocrystal aillikite showing normal and reverse zonation in olivine. Phlogopite exhibits Fe-rich (bright) tetraferriphlogopite rims. (D) Zoned clinopyroxenes in mela-aillikite. The groundmass consists of a mixture of serpentine and carbonate. (E) Coexisting phlogopite, clinopyroxene and amphibole in mela-aillikite. The late amphibole (arrows) invades the crystal mush and seems to replace the other phases. (F) Perovskite microphenocryst showing an euhedral core and oscillatory zoned rim.

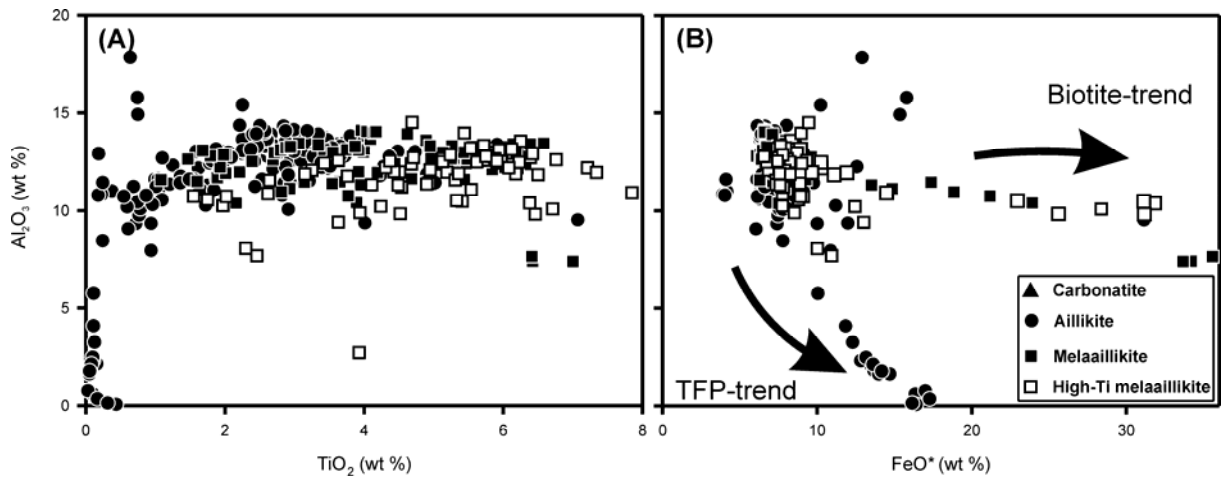


Figure 4: Al₂O₃ versus TiO₂ (A) and FeO* (B) compositional variation of micas from the Torngat UML. Aillikites show a tetraferriphlogopite trend toward the rim, whereas mela-aillikitic micas are characterized by a biotite trend.

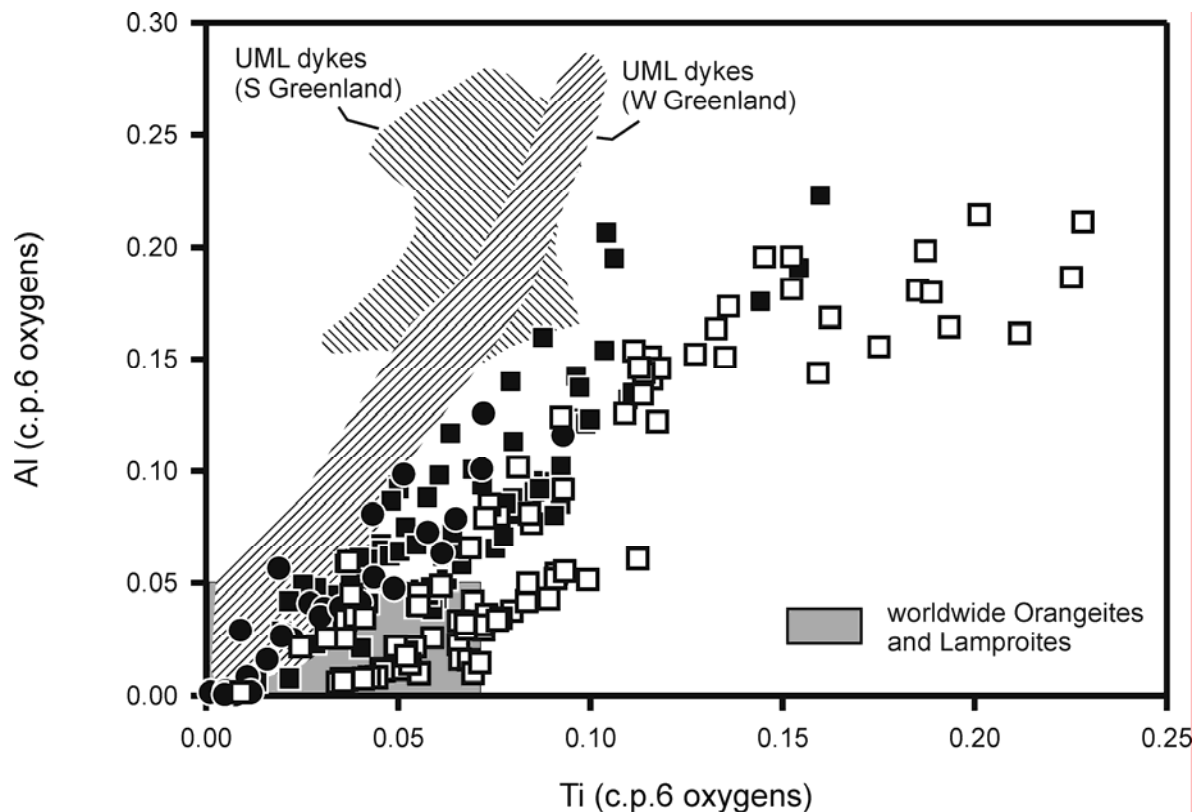


Figure 5: Atomic Al versus Ti (6 oxygens) of clinopyroxene from Torngat UML. Clinopyroxenes from Neoproterozoic aillikite dykes in West Greenland (Scott, 1981, Thy *et al.*, 1987, Mitchell *et al.*, 1999) also show a trend toward Al enrichment. High Ti but extremely enriched Al concentrations are characteristic for ultramafic dykes from the South Greenland Gardar Province (Upton & Thomas, 1973), which petrographically resemble the Torngat mela-aillikites. Field for orangeite and lamproite from Mitchell (1995). Symbols as in Fig. 4.

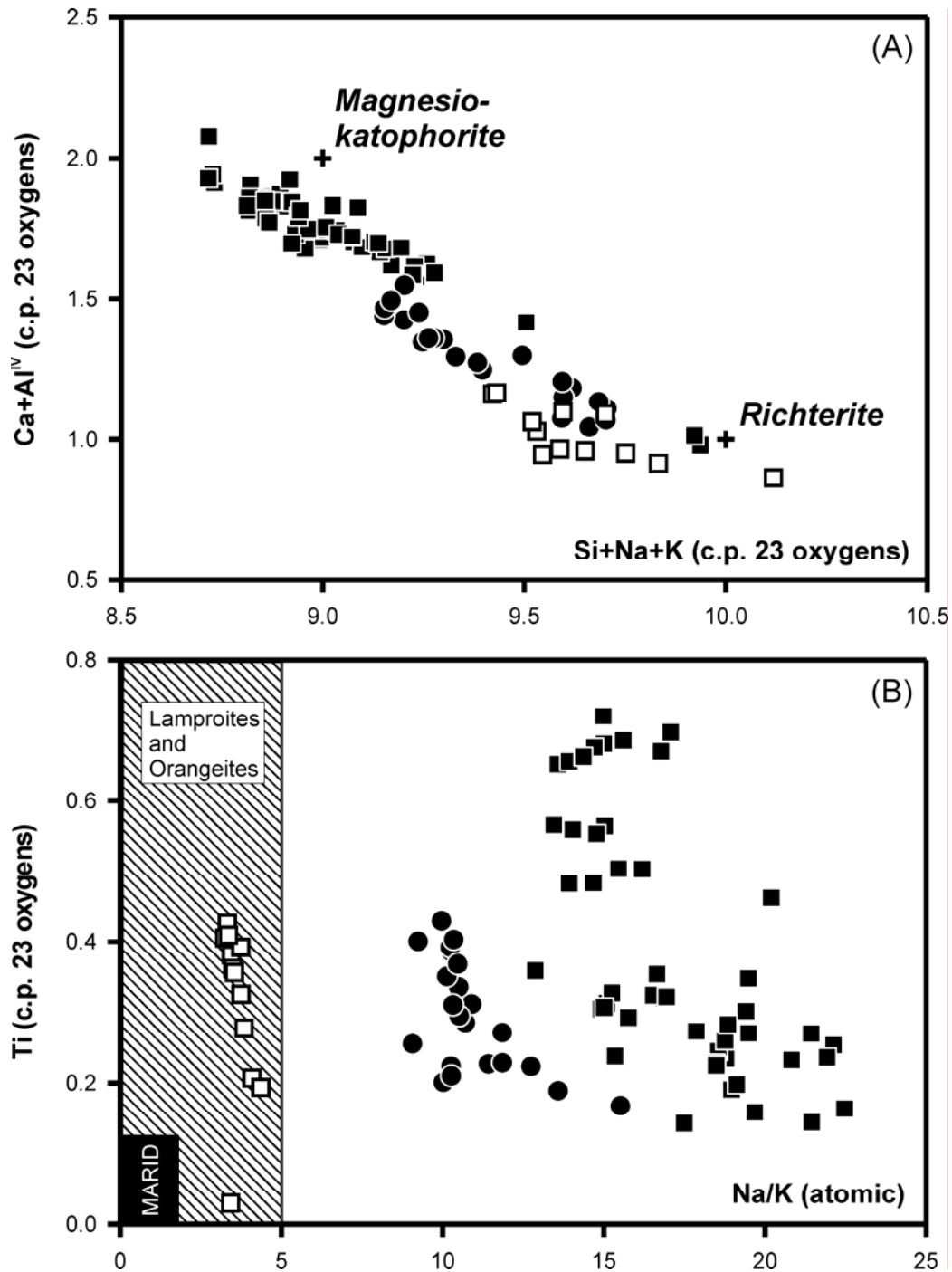


Figure 6: Composition of groundmass amphibole from Torngat UML. (A) Atomic Ca plus tetrahedral Al versus Si+Na+K (23 oxygens). Compositions are between the magnesiokatophorite and richterite end-member. (B) Atomic Ti versus Na/K. High Na/K ratios are characteristic for the Torngat amphiboles in marked distinction to amphibole from lamproites, orangeites and MARID suite xenoliths. Amphibole from aillikite is only from 1 sample, whereas mela-aillikites are represented by 4 samples. Fields for other rock types compiled by Mitchell (1995). Symbols as in Fig. 4.

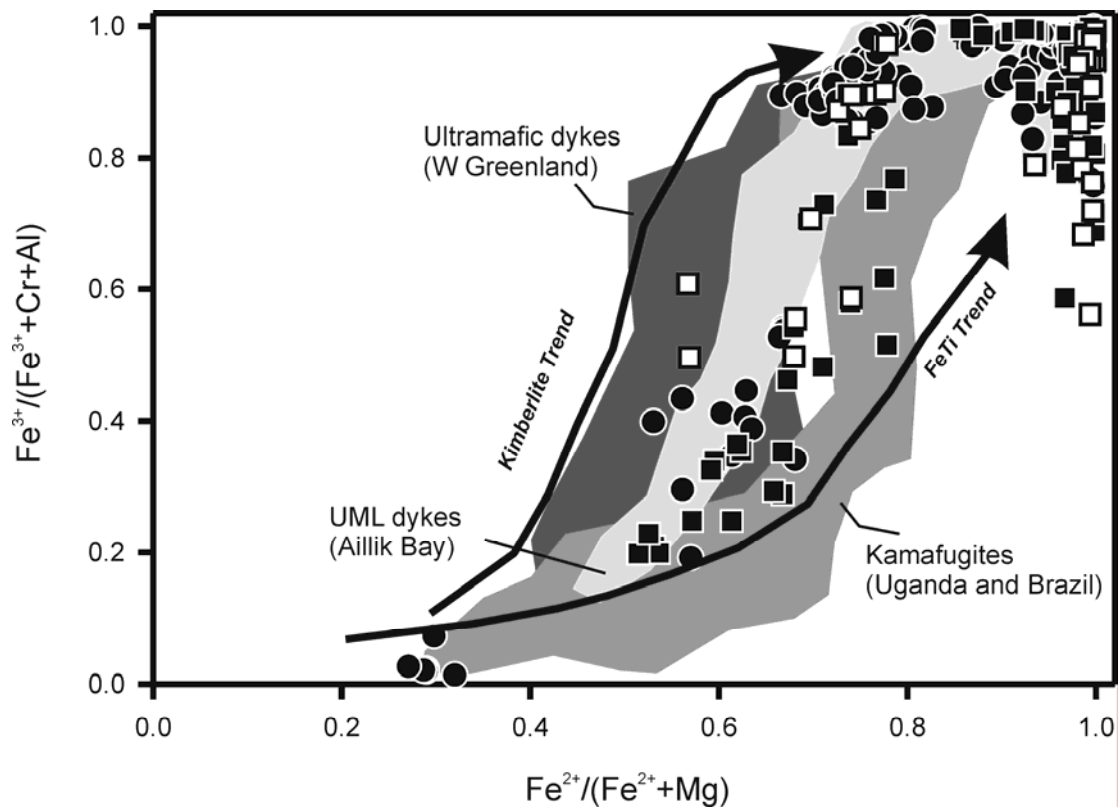


Figure 7: Compositional variation of Cr-spinels and Ti-magnetites from the Torngat UML. Aillikites follow a trend of fairly constant Fe^{2+}/Mg as Fe^{3+} increases, similar to spinels from Labrador type aillikites (own unpublished data, see part II) and West Greenland aillikites (Scott, 1981, Thy *et al.*, 1987, Mitchell *et al.*, 1999). Mela-aillikites preferably show a trend of increasing Fe^{2+}/Mg with increasing Fe^{3+} culminating in pure magnetite compositions similar to spinels from kamafugites (Araujo *et al.*, 2001; Sgarbi & Gaspar, 2002; own data). Trends are from Barnes & Roeder (2001). Symbols as in Fig. 4.

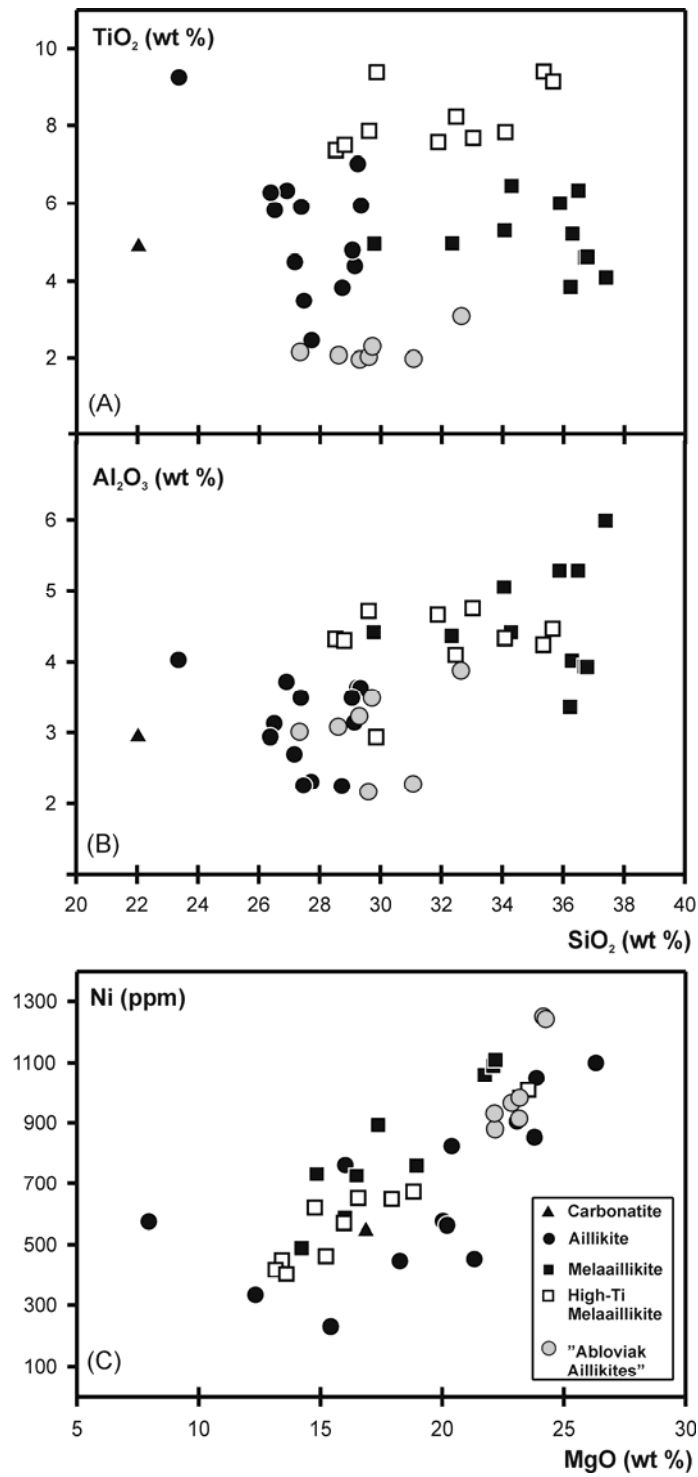


Figure 8: Bulk rock variation of TiO_2 and Al_2O_3 versus SiO_2 and Ni versus MgO for the Torngat UML. Data for Abloviak aillikites are from Digonnet *et al.* (2000).

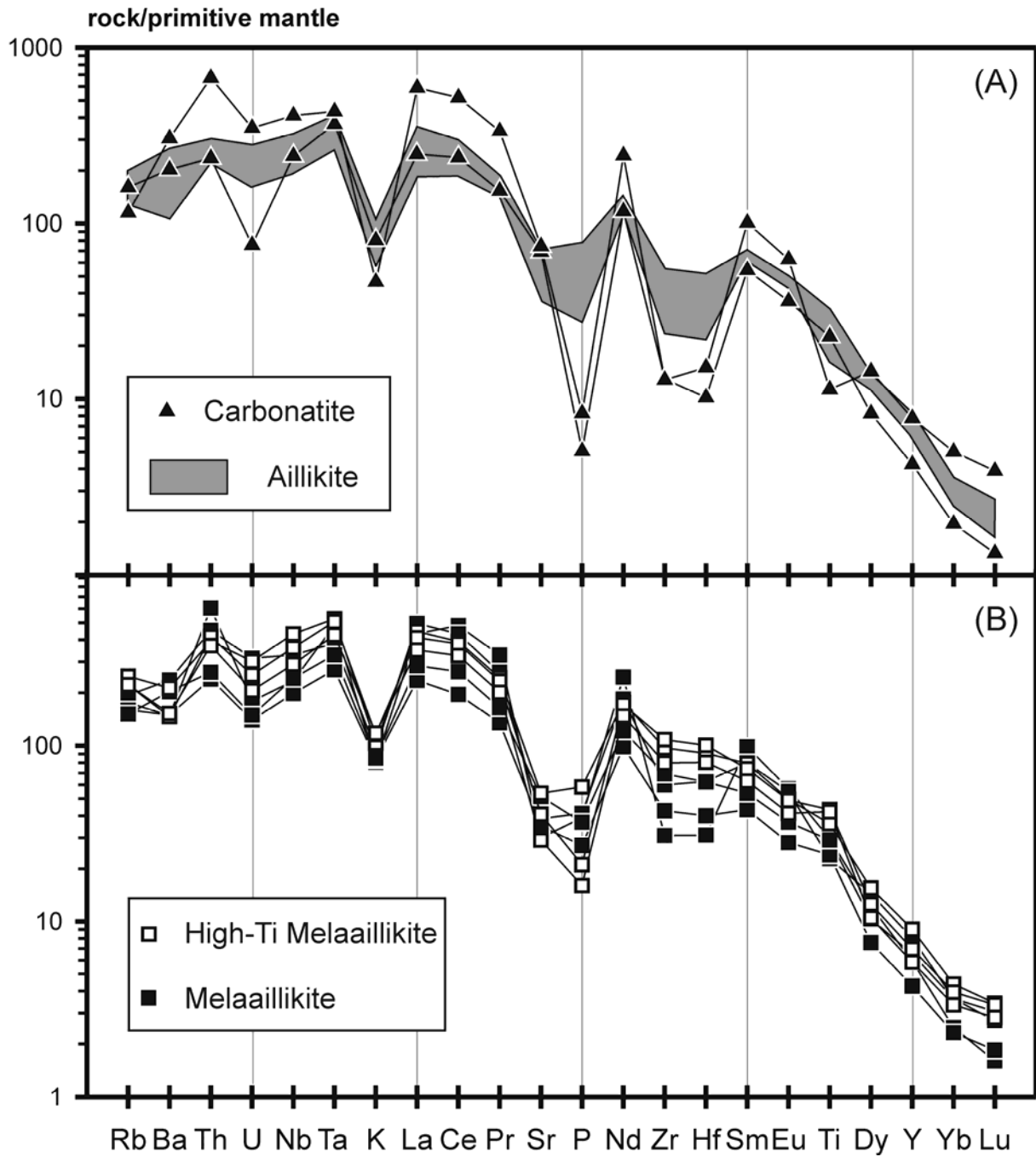


Figure 9: Primitive mantle-normalized incompatible element distribution of the (A) aillikites/carbonatites and (B) mela-aillikites from the Torngat Mountains. A high-Ti mela-aillikite group is separately displayed. Normalization values from Sun & McDonough (1989).

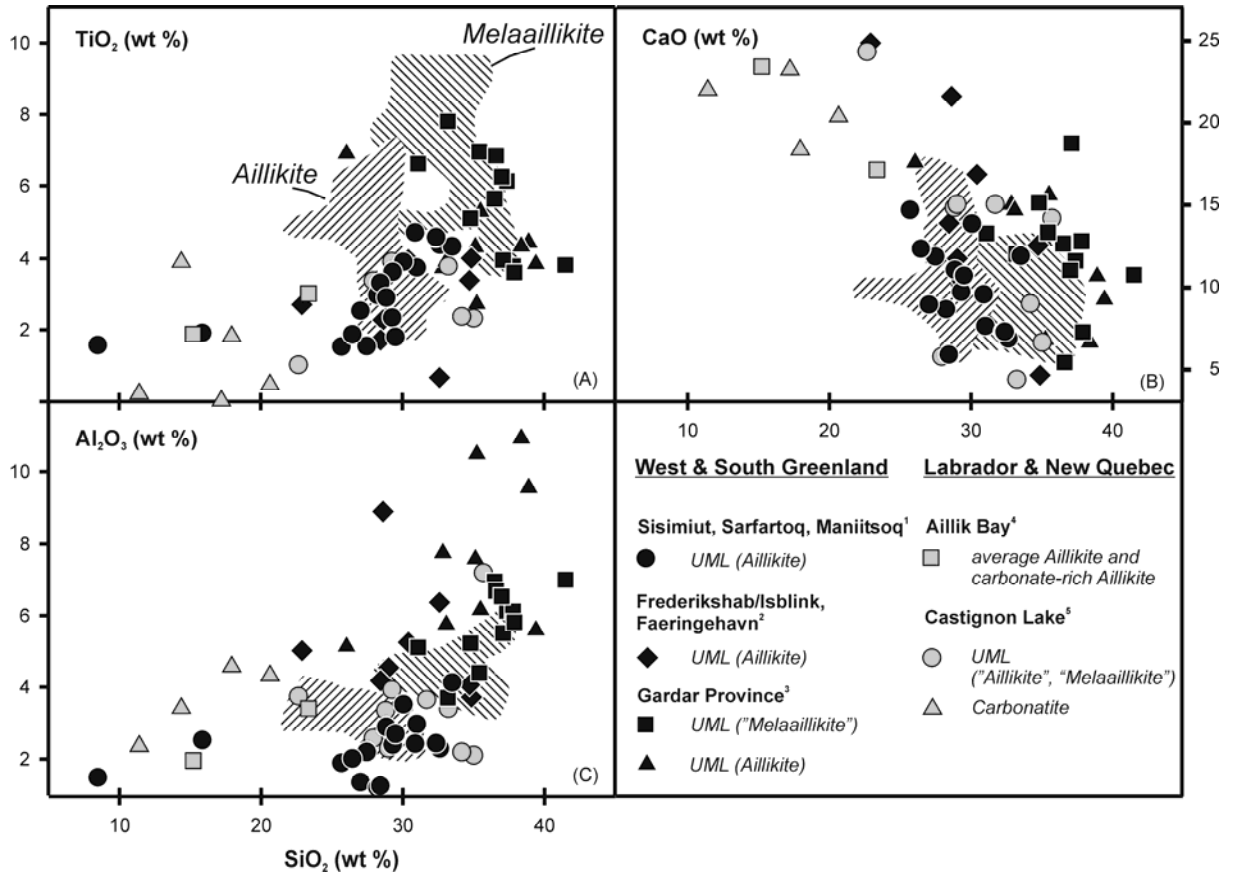


Figure 10: Bulk rock TiO_2 (A), CaO (B) and Al_2O_3 (C) versus SiO_2 for the Torngat UML (hatched fields) and UML/carbonatites from New Quebec/Labrador and West/South Greenland.

Data sources:

(1) – Scott (1981), Larsen & Rex (1992); (2) – Walton & Arnold (1970), Larsen & Rex (1992); (3) – Upton & Thomas (1973), Pearce & Leng (1996); (4) – Malpas *et al.* (1986); (5) – Dimroth (1970), Dressler (1975).